UNIVERSITY OF LONDON THESIS

Degree PhD Year 2007 Name of Author MARK SPENCER WESTMOQUETTE

Super star clusters, their environment, and the formation of galactic winds

Mark S. Westmoquette

Thesis submitted for the Degree of Doctor of Philosophy
of the University of London

Department of Physics & Astronomy
UNIVERSITY COLLEGE LONDON

February 2007

ProQuest LLC
789 East Eisenhower Parkway
P.O. Box 1346
Ann Arbor, MI 48106-1346

I, Mark Westmoquette, confirm that the work presented in this thesis is my own. Where information has been derived from other sources, I confirm that this has been indicated in the thesis.

"One sticks one's fingers into the soil to tell by the smell in what land one is: I stick my finger into existence - it smells of nothing. Where am I? Who am I? How came I here? What is this thing called the world? What does this world mean? Who is it that has lured me into this thing and now leaves me there?... How did I come into the world? Why was I not consulted?... but thrust into the ranks as though I had been bought of a kidnapper, a dealer in souls? How did I obtain an interest in this big interest they call reality? Why should I have an interest in it? Is it not a voluntary concern? And if I am compelled to take part in it, where is the director?... Whither shall I turn with my complaint?"

— Søren Kierkegaard (1813-1855)

ABSTRACT

Starbursts and starburst-driven outflows play a central role in the evolution of galaxies. However, the paucity of detailed observations of superwinds limits our current understanding of these complex systems.

To this end we have undertaken two intensive ground- and space-based observing campaigns aimed at studying the ionized gas conditions in two nearby starburst galaxies, M82 and NGC 1569. These two systems host starbursts on different scales: M82 contains densely-packed star cluster complexes that drive a large-scale bipolar superwind, whereas NGC 1569 exhibits a set of discrete superbubbles powered by only a handful of young massive clusters.

We have used long-slit spectra, obtained with the *Hubble Space Telescope* (*HST*), together with *HST* and ground-based imaging from the WIYN 3.5 m telescope, to observe M82 at optical wavelengths. The high quality *HST* spectroscopy obtained with the Space Telescope Imaging Spectrograph (STIS), have allowed us to investigate the properties of the gas across the starburst core. By combining high-resolution *HST* imaging with deep WIYN observations, we have created the most comprehensive image of the M82 superwind to date, and used it to characterise the outflow morphology.

We also observed the centre of NGC 1569 with the Integral Field Unit (IFU) of the Gemini Multi-Object Spectrograph (GMOS) on the Gemini-North telescope, and M82 with the WIYN/DensePak and SparsePak IFUs. We decomposed the observed emission-line profile shapes, and identified an underlying broad ($>$100 km s^{-1}) component across the starburst cores of both galaxies. By mapping the spatial variation of each individual line component, we have developed a new model to explain the broad emission and the state of the interstellar medium (ISM) in the central starbursts.

We have also observed the outer-wind environment of NGC 1569 with the WIYN SparsePak instrument. We find that the broad line is only found within 500–700 pc of the centre, and speculate that the boundary of this region may indicate the point at which bulk motions begin to dominate over turbulence.

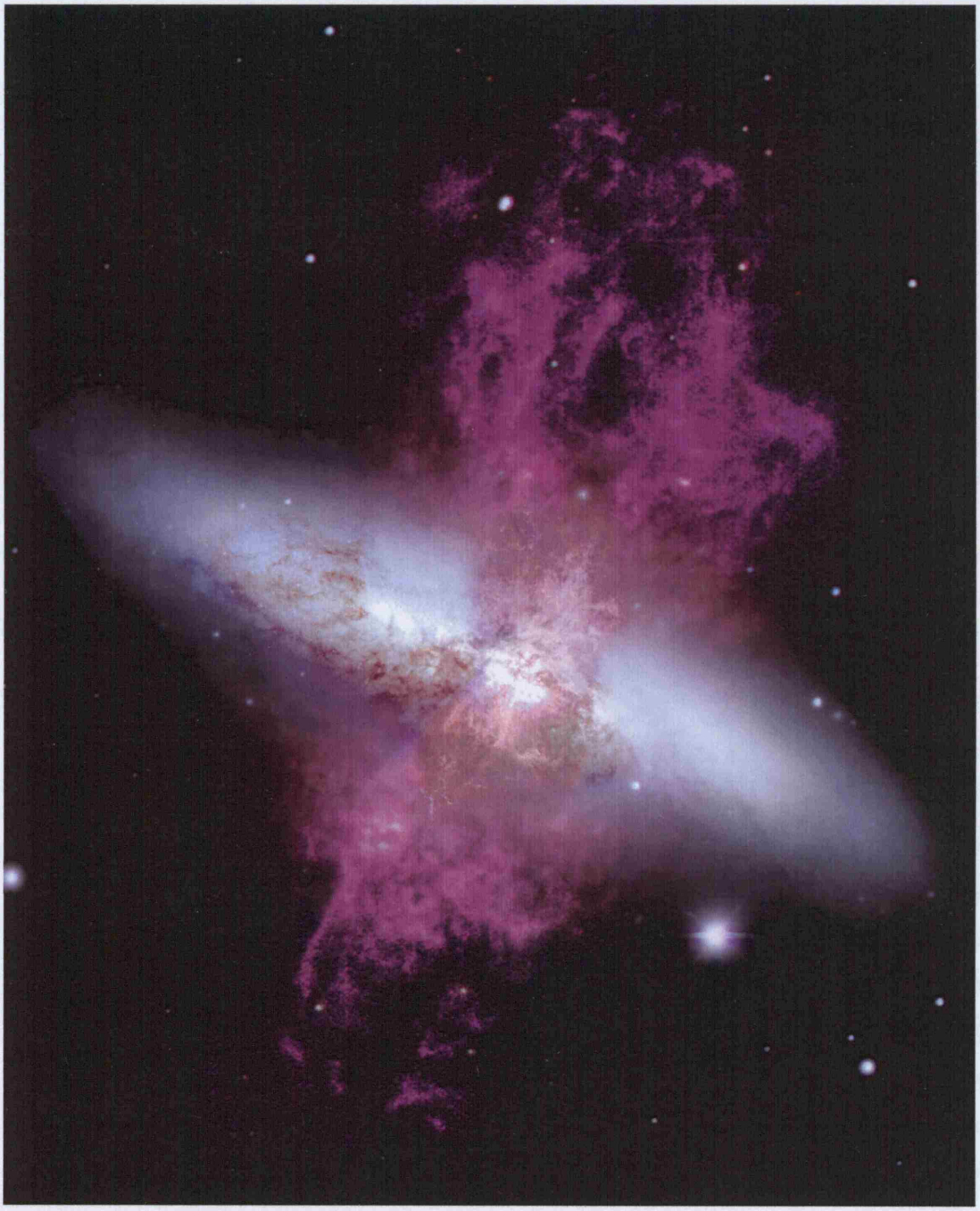

Colour-coded image of the starburst galaxy M82 oriented to show its supergalactic wind running top to bottom (north–south) and the nearly horizontal disc of stars. Broad blue, green and red filters were used to render the relatively smooth stellar disc. Purple represents emission from hydrogen.

CONTENTS

LIST OF FIGURES

LIST OF TABLES

CHAPTER 1

INTRODUCTION

Modern astronomy is concerned with understanding the evolution of the Universe. Stars are one of the prime drivers of this change, and one of the most dramatic ways of creating new stars is through a starburst.

Starbursts (Fig. 1.1) are defined as regions experiencing a rapid but unsustainable rate of star-formation. Active starburst sites are usually located in the centres of galaxies (although can be found in the outer parts) and are in the majority thought to be the result of a dynamical trigger such as a minor merger. They typically occupy between one and ten per cent of the host galaxy's volume, and can be characterized by the formation of dense stellar clusters (including so-called super star clusters; SSCs) and large-scale gas outflows. They quickly convert their large supply of interstellar gas into massive stars on the order of 10^8 yr (a few O-star lifetimes), and consequently, rate as some of the most luminous objects in the Universe.

The above paragraph contains references to many subjects concerning starbursts. We shall now explore each in turn, with an emphasis on aspects relevant to the contents of this thesis.

1.1 Starbursts

A major step towards understanding the evolution of galaxies is the ability to parametrise their star-formation history. Within this history, it is the periods of rapid, intense star-formation that have the most effect. The importance of starbursts (M82 in particular) was first recognised in the 1960s, mainly due to their peculiarity (*e.g.* Sandage 1961; Lynds &

Figure 1.1: A small-scale starburst in our own Galaxy. This figure illustrates how such a widely known phenomenon as this can be given its own corporate branding. Is this the brainchild of a university spin-off company, or a wildly successful public outreach programme?

Sandage 1963; O'Connell & Mangano 1978), and were the subject of intense study by the 1980s and 1990s (*e.g.* Telesco 1988; Heckman *et al.* 1990; Rieke *et al.* 1993; O'Connell *et al.* 1995). Following this era's detection of starbursts at high redshifts, subsequent studies have suggested that the universal star-formation rate (SFR) may have peaked at redshifts of $z \sim 1.5$ (Madau *et al.* 1998; Gómez *et al.* 2003; Heavens *et al.* 2004), beyond which many galaxies show characteristics of powerful starburst events and very high SFRs.

With the list of known starburst galaxies now fairly extensive, many theories regarding their triggering mechanisms have been proposed. In general, starbursts are thought to result from some kind of dynamical trigger, such as the merger or interaction of two galactic systems, the collision of two gas bodies, or even the passage of a spiral density wave, since the large build-up of mass needed to fuel such a period of intense star-formation requires strong gravitational perturbations. This is supported by the common observation of features indicative of interaction, such as tidal tails or disturbed H I morphologies. Theory suggests that the dissipation of energy resulting from gas-cloud collisions allows the transfer of angular momentum from the gas to stars, effecting a gas inflow towards the centre of the galaxy (Heckman 2000). A bar feature (which is also linked to gravitational triggers) can also act to transfer angular momentum outwards, driving gas towards the nucleus (Binney & Tremaine 1987). Some starburst regions, such as those found in NGC 4038/9 (the Antennae Galaxies), are quite obviously the result of a direct galaxy-galaxy collision; others such as M51, show very pronounced spiral arms thought to result from a tidal interaction; but other systems, such as NGC 253, do not show

any obvious signs of recent encounters. Furthermore starbursts are often found in galaxies exhibiting signatures of an AGN (active galactic nucleus); in fact very few starbursts have been convincingly determined not to have an AGN component. This has led to suggestions that some types of AGN can be accounted for solely through starburst activity (*i.e.* without the influence of a black-hole; Terlevich *et al.* 1987, 1992), or that black-hole activity acts to trigger starbursts or *vice-versa* (Norman & Scoville 1988; Colina & Arribas 1999).

Besides allowing advances in our knowledge of how starbursts arise and are maintained, the increase in available resolving power over the years has radically altered the supposed fundamental scale of starburst structure. Of the largest dimensions, and possibly found only in large, gas rich spirals such as M83, is the complex (collection) of giant molecular clouds (GMCs) and the star-cluster complexes (or starburst clumps; *e.g.* O'Connell & Mangano 1978). Then come the individual GMCs and the gas clumps (overdensities) within the GMCs. On the smallest scale, we now regularly detect individual star clusters representing the smallest unit of a starburst currently observable. A subject of much recent debate has been whether these classifications represent parts of the same scale-continuum or whether real distinctions exist separating them phenomenologically (Bastian *et al.* 2005, 2006*b*).

In the high-redshift Universe, starbursts are thought to have significantly contributed to the ionizing flux needed for re-ionization (Loeb & Barkana 2001), and the pollution of the inter-galactic medium (IGM) from the ejection of chemically-processed matter (*e.g.* Rupke *et al.* 2005, discussed in detail in Section 1.3.3). Furthermore, the occurrence rate of starbursts is thought to be inextricably linked to the peak in universal SFR mentioned above. Through studying local starbursts, we build up a pool of knowledge based on high-resolution, high signal-to-noise (S/N) observations, which can be applied to more distant cases. The nearest starbursts are found at distances of $D \sim 2$–3 Mpc, corresponding to angular scales of $1'' \approx 10$–20 pc, and by definition are very luminous, thus making them easy to study. Since we can now resolve structures on 10–100 milli-arcsecond scales (*e.g.* with Very Long Baseline Interferometry; VLBI, or with the *Hubble Space Telescope*; *HST*), nearby starbursts are ideal laboratories for studying a vast host of phenomena associated with intense star-formation. The effects of resolution-dependent dilution or model degeneracies can then be investigated, resulting in better input parameters for cosmological models of galaxy formation/evolution and universal structure formation.

Figure 1.2: Deep VLT/ISAAC colour composite of the massive Galactic star cluster NGC 3603. Although not technically a super-star cluster, this is the closest (6 kpc) and least obscured massive star cluster ($M \approx 10^3\ M_\odot$), and serves as a good laboratory for the study of processes that occur in more distant, more extreme environments. (Credit: ESO VLT, 1999)

1.2 The significance of super-star clusters

The existence of massive, hyper-luminous star clusters was not fully realised until the advent of high-resolution imaging by *HST* (and later with ground-based adaptive-optics systems; see Fig. 1.2). Holtzman *et al.* (1992) were the first to identify such objects in NGC 1275, followed soon after with the discovery of similar objects in the high surface-brightness clumps of M82 (O'Connell *et al.* 1995). Commonly termed super star clusters (SSCs), they have now been identified across a broad range of starburst environments, from dwarf irregular galaxies (NGC 1569, Maoz *et al.* 2001; NGC 1140, Hunter *et al.* 1994; NGC 1705, Ho & Filippenko 1996; NGC 5253, Vanzi & Sauvage 2004; M82); major mergers (NGC 7252, Miller *et al.* 1997; NGC 4038/9, Whitmore *et al.* 1999); large, gas rich 'grand-design' spirals (M83, Hadfield *et al.* 2005; M51, Larsen 2000; NGC 253, Watson *et al.* 1996) and even our own Galaxy (Westerlund 1, Clark & Negueruela 2002).

Although a universally accepted definition does not exist, a super-star cluster has come

to mean a gravitationally bound stellar association with mass, $M > 10^5\ M_\odot$, age < 100 Myr and effective radius, $R_{\rm eff} < 5$ pc. They are obviously associated with regions of intense star-formation, but not all regions of intense star-formation host SSCs. This immediately raises the question of whether the interstellar environment affects SSC production. For example, do the ambient interstellar densities need to be unusually high to produce an SSC? Conversely, do these objects simply represent the high-end of a continuous cluster mass-function? Larsen & Richtler (1999) presented a study of a large sample of star clusters in nearby face-on spiral galaxies, and found no obvious peak in the age distributions of clusters, indicating that they did not arise in single bursts, but formed in an ongoing process. An explanation for the seemingly random presence of SSCs comes from the size-of-sample effect first discussed in a meaningful way in Larsen (2002), which states that the larger the sample (*i.e.* the bigger the galaxy or the higher the SFR), the more statistically likely it is to contain a massive cluster. This supports the hypothesis that SSCs represent just one level in the 'heirarchy of star-formation'. Mirroring the mass scale discussed above, this paradigm describes that stars are formed from GMCs (governed by a stellar initial mass function; IMF), clusters form part of cluster complexes (governed by a cluster mass function), which are, in turn, formed from GMC complexes at galaxy size scales (Elmegreen *et al.* 2006). This is supported by work looking at cluster complexes in the Antennae (NGC 4038/9; Bastian *et al.* 2006*a*). These authors found the complexes to be grouped spatially at approximately the same scale as large GMCs, leading them to conclude there is a characteristic maximum scale on which coherent star formation can take place (that varies according to the individual conditions of the galaxy).

An outstanding issue which has received much recent attention is that of the connection between SSCs and globular clusters (GCs). It has long been known that GCs are ancient bound collections of stars (ages $\sim 10^{10}$ yr) and are thought to have formed coevally under nearly constant abundance conditions. However, an almost equally long-standing enigma is why we do not observe a range in ages of GCs; where are the young counterparts to GCs (the only young clusters in our Galaxy are low-mass, low-density open clusters – except for Westerlund 1)? Thus the detection of SSCs, which share the same space as GCs in a mass-radius plot (typical masses 10^5–$10^6\ M_\odot$, typical $R_{\rm eff} = 5$–10 pc), suddenly provided an appealing solution to this enigma. Do they represent newly forming GCs? To prove a connection, we must address whether SSCs are formed in such a way as to be able to survive to the typical age of a GC (a Hubble time). Since SSCs have now been detected in

many galaxies in the local Universe, we can safely assume that they were also formed in the early Universe when starbursts are thought to have been more common. However, whether their survival rates are sufficient to explain the copious numbers of GCs that we observe in old galaxies today still remains to be quantified. Clusters can be disrupted through gravitational unbinding resulting from gas expulsion by the young massive star population (Goodwin 1997; Melioli & de Gouveia dal Pino 2006), or through tidal disruption (Gnedin & Ostriker 1997), but are these effects strong enough to destroy every SSC? For a definitive answer, problems in determining cluster masses and understanding cluster disruption mechanisms must be resolved (see *e.g.* Bastian & Goodwin 2006, and references therein). SSCs are, by definition, formed in starburst regions which are typically located within a small area of the host galaxy (usually the nucleus). However, today's GCs are found in the halo of galaxies, often on highly eccentric elliptical orbits. If SSCs represent the young counterparts of old GCs, how could they form in a low-density galactic halo? and if they do form in this environment, do they form in the same way as the old GCs (*i.e.* with the same IMFs, densities and due to the same triggers)?

1.2.1 Evolutionary synthesis models

Star clusters, by their very nature, are well suited to modelling using instantaneous burst scenarios (so-called simple stellar populations; SSPs). Due to their compactness, it is assumed that the entire cluster population was formed coevally, and from a single GMC of constant metallicity. Evolutionary synthesis models have been developed over the years to predict the fundamental properties of clusters from a variety of input parameters. A set of stellar spectra (derived either from stellar atmosphere models or from observations) covering the full range of expected stellar types are used, together with a formulation of the initial mass function (IMF), metallicity, total mass, and a set of stellar evolutionary tracks (expected evolutionary paths for stars of particular mass and metallicity) to predict the full spectral energy distribution (SED), emission line flux ratios, equivalent widths, and a whole host of other observables for the integrated population as a function of age for comparison to observations. For example, Starburst99 (Leitherer *et al.* 1999) is an evolutionary synthesis code specialising in predicting the properties of very young clusters, and the synthesis code developed by Bruzual & Charlot (2003) is the state-of-the-art for older populations.

Cluster SEDs are dominated by O-stars of up to ages of ~6–8 Myr. At this time, the

most massive stars start to explode as type-II supernovae (SNe), and their contribution starts to dominate the mechanical luminosity, energy and mass output (Leitherer *et al.* 1999). Between approximately 3 and 6 Myr, the most massive O-stars evolve into the WR stage[1] (Starburst99 predicts the peak in the number of WR stars occurs at ~5 Myr), and provide a significant proportion of the stellar wind contribution to the energy and mass output. Under normal circumstances (interstellar densities of the order of 10 cm^{-3} and temperatures of a few $\times$ 10^4 K), the gas from which the cluster formed is expected to have been blown away by 6–7 Myr by the first wave of SNe explosions from the most massive stars (Weaver *et al.* 1977; Goodwin 1997).

1.2.2 Consequences of SSCs

If one massive star ($M > 50\ M_\odot$) can eject mass at a rate of 10^{-4}–$10^{-5}\ M_\odot\ yr^{-1}$ at speeds of several $10^3\ km\,s^{-1}$, and emit an ionizing flux of ~10^{49} erg s^{-1}, a $10^6\ M_\odot$ cluster can clearly have a devastating impact on it surroundings. For a young cluster, the collective effect of massive star winds (age $\lesssim$ 7 Myr), and eventually SNe (age $\lesssim$ 40 Myr), drives a 'cluster wind' into the surrounding H II region. The modelling of such cluster winds has proven very difficult due to a lack of suitable high-resolution observations (Stevens & Hartwell 2003), but as we shall see, a cluster of star clusters has a very significant and easily observable impact on their surroundings, driving a galactic-scale wind, and possibly resulting in the ejection of mass from the galaxy altogether.

1.3 Galaxy outflows and superwinds

Large-scale gas outflows have been observed in a wide range of environments, and are always associated with high-energy phenomena such as intense star-formation (starbursts) or AGN. Here we focus on starburst-driven winds; for a review of AGN-driven outflows, see Veilleux *et al.* (2005). The presence of kinematically confirmed winds has been connected to strong starbursts for a broad range of galaxy types (Heckman *et al.* 1990; Marlowe *et al.* 1995; Hunter & Gallagher 1997; Martin 1998). Most outflows have a bi-polar

[1]WR stars are the evolved descendants of massive O-type stars ($M > 30\ M_\odot$), and their high surface temperature and stellar winds produce unique emission features. As a massive star loses significant mass at the end of its life through strong stellar winds, it first reveals the CNO-burning products at its surface, followed by He-burning products. This gives rise to an evolutionary sequence from WN-type (nitrogen rich) to WC-type (carbon and oxygen rich) WR stars (Abbott & Conti 1987).

morphology, resulting from interactions with the host galaxy's disc, with typical opening angles of 10–45° at the base, widening to 45–100° above the disc. The vertical extent of galactic winds (GWs) varies between 1–20 kpc, and any tilts or asymmetries in the outflow probably reflect the distribution of the starburst population and density distribution of the disc or the halo (and on larger scales, the IGM through which the galaxy is moving). The dynamical time-scale of starburst driven outflows (derived from typical outflow radii and de-projected wind speeds) and is of the order 0.1–10 Myr and typical mass outflow rates in the range 0.1–10 $M_{\odot}$ yr^{-1} (Heckman *et al.* 1990).

In the very local Universe, large-scale expanding structures (commonly termed supershells) and gas outflows are found in many giant H II regions powered by a single star cluster, *e.g.* 30 Dor in the LMC (Chu & Kennicutt 1994), NGC 2363 in NGC 2366 (González-Delgado *et al.* 1994), and NGC 5461 in M101. However, as good as these objects are as test beds for cluster-driven dynamics, they do not exhibit large-scale winds. These can only be found in larger, more distant systems, and take on a number of different forms: uncollimated, amorphous winds (*e.g.* NGC 1569, Martin 1998, Chapter 5; NGC 4449, Summers *et al.* 2003); well-defined nuclear cones with limb-brightened morphologies (*e.g.* NGC 253, Strickland *et al.* 2002; NGC 3079, Cecil *et al.* 2001, Fig. 1.3); and large bi-polar plumes (*e.g.* M82, Shopbell & Bland-Hawthorn 1998; NGC 1482, Veilleux & Rupke 2002).

How these different morphologies result is thought to arise from differences in how the bubbles blown by individual clusters/cluster complexes within the starburst interact with one another. These may, to begin with, evolve similarly to 30 Dor-type objects, but are thought to coalesce through interactions to form one large superbubble surrounding the entire starburst region, from which a GW might form. The evolution of the initial starburst-blown superbubble behaves similarly to a single-star wind-blown bubble (Weaver *et al.* 1977; Koo & McKee 1992), where the central pressure of the hot cavity is proportional to the SFR and the radius of the starburst region. As the hot gas expands through the sonic radius (the point at which the flow becomes supersonic; sometimes called the 'critical point'), it cools adiabatically and begins to drive a shock into the surrounding interstellar medium (ISM), sweeping up a shell of shocked material. After this free-expansion stage the bubble can be described by an onion-skin structure, the first layer of which is termed the 'energy injection zone' (Schiano 1985). Determined from [S II] derived density profiles and emission line kinematics, the vertical extent of energy injection zones have been found to be fairly large (a few hundred pc; Heckman *et al.* 1990; Shopbell

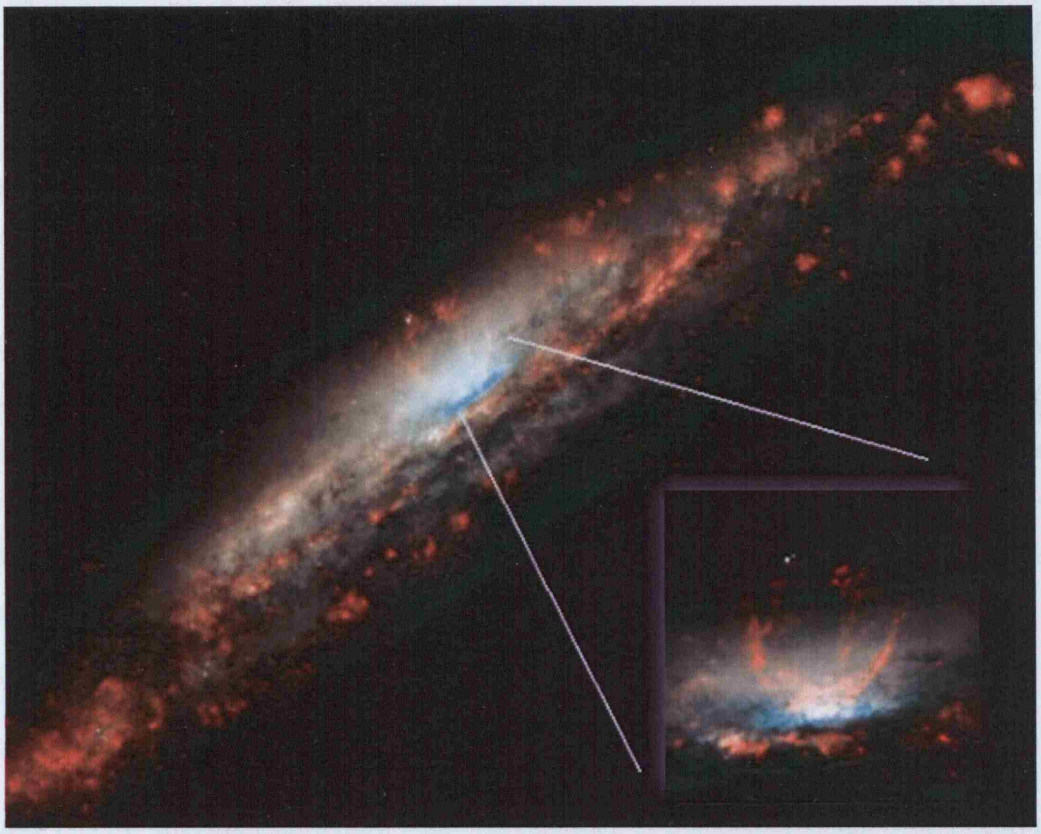

Figure 1.3: *HST* colour composite of the edge-on galaxy NGC 3079 showing (inset) the concave superbubble emitting brightly in Hα (red) (Cecil *et al.* 2001).

& Bland-Hawthorn 1998), but contamination from the foreground/background galaxy disc and structure formation through Kelvin-Helmholtz instabilities[2] results in highly uncertain measurements. Following these theoretical predictions, an important question to ask is: which part of the starburst is doing the energy injection? Is it the star clusters, or the collective effect of the non-clustered (field) stars? Answers to these questions have implications for the initial structure-formation and evolution of the wind (see Section 1.3.2). X-ray observations of NGC 1569, for example, show the wind seeming to emanate from the entire Hα disc, rather than specifically the area around the central SSCs (Martin *et al.* 2002), but the latest high-resolution studies and models indicate that hot wind gas can be vented on a very localised scale (Wills *et al.* 1999; Tenorio-Tagle *et al.* 2003, Chapter 4), and that any energy injection zones we measure in galaxies are simply averaged effects resulting from resolution dilution.

[2]In fluids, Kelvin-Helmholtz instabilities arise as the flow becomes supersonic, whereas a collimated flow moving through a medium of decreasing density will develop Rayleigh-Taylor instabilities.

Once the starburst-blown superbubble reaches the scale height, H, of the galaxy disc, its expansion re-accelerates (as the density drops) and its structure starts to fragment through growing Rayleigh-Taylor instabilities. The bubble may then 'blow out', allowing the free-flowing wind component to vent out into the halo. For a superbubble to reach this stage, a number of conditions have to be fulfilled: radiative losses must be mild enough for the bubble not to have lost too much kinetic energy (*i.e.* the cooling timescale must be much longer than the timescale for the bubble to reach H); and the velocity of the shell must be higher than the sound-speed at H (Mac Low & McCray 1988; Veilleux *et al.* 2005). The flow can be thought of as 'free' until its ram pressure equals the thermal pressure of the ambient ISM. In disc geometries, this occurs at large polar angles, and can result in circumgalactic 'ring shocks' in the disc that can help to collimate the bi-polar outflow (Tenorio-Tagle & Muñoz-Tuñón 1998).

To first order, the terminal velocity of a free-flowing wind can be approximated by

$$v_\infty \approx (2\,\xi\dot{E}/\Lambda\dot{M})^{1/2} \approx 3000\,(\xi/\Lambda)^{1/2} \quad \mathrm{km\,s^{-1}}, \tag{1.1}$$

where ξ is the thermalisation efficiency (percentage of the mechanical energy from the starburst that is converted into heat energy, and is thought to be $\lesssim$10 per cent from observations, Veilleux *et al.* 2005), making $\xi\dot{E}$ is the total energy deposition rate, and Λ is the mass-loading factor (the ratio of the total mass of heated gas to the mass that is directly ejected by SNe and stellar winds, and is also thought to be of order 10 per cent), making $\Lambda\dot{M}$ the total mass deposition rate. The temperature of the hot wind fluid can be estimated using the following (Veilleux *et al.* 2005):

$$T \approx 3 \times 10^8\,\xi\Delta^{-1} \quad \mathrm{K}. \tag{1.2}$$

For $\xi \approx \Delta \approx 10\%$ and at the predicted very low densities ($\rho < 0.1$ cm^{-3}), the wind fluid is therefore expected to be very hot and almost undetectable at any wavelength.

GWs are very complex systems; observations at all wavelength regimes often show structure down to the resolution limit of the detector (which can be <0.1 pc for *HST* images of the closest systems). To fully understand them, a multi-wavelength approach is required; indeed "the multiphase nature of GWs greatly complicates the task of estimating the energetics and mass outflow rates" (Veilleux *et al.* 2005). Historically, line and continuum emission from Hα, [N II], [S II], [O III] and [O I] in the optical, and Paα, Brγ, H_2 2.1μm in the near-infrared (IR), have been used to study GWs, together with both low-ionization

(*e.g.* Si II, C II, Fe II) and high-ionization (*e.g.* S V, O VI) ultra-violet (UV) absorption lines, and Na I D and K I optical absorption lines (Veilleux *et al.* 2005). Through these lines, the morphology and kinematics can be studied, together with the excitation mechanisms and energetics of the flow. However, a potential observer must be aware of two caveats regarding the use of line emission to probe GWs: firstly, emission can only arise through an energy drain from the outflow, caused by some factor such as cooling or interaction; and secondly, since emission intensity is proportional to ρ^2, this probe is intrinsically biassed (luminosity weighted) towards higher density regions.

Further support for a multi-wavelength approach comes from the search for molecular material from which the starburst is fuelled. In the early phase of a starburst, molecular clumps are violently eroded by the UV flux from the young stars, and a complex mixing of ionized and molecular gas takes place and almost certainly results in a certain amount of material being entrained in the wind. We will return to this important point many times in the body of this thesis. Hα emission is good at tracing the warm ionized gas, but to detect neutral material, radio observations of the emission from H I or CO are required, and to detect dust, IR or sub-mm observations are needed. Unambiguous evidence for entrained neutral gas had been detected in a number of galaxies (*e.g.* Heckman *et al.* 2000; Schwartz & Martin 2004) including M82 (Walter *et al.* 2002), and it is even thought that some winds entrain a mass of cool neutral material equal to or greater than the mass ejected from SNe. This evidence is supported by systematic kinematic variations with wind phase temperature (cool gas has lower outflow speeds than hot gas), implying that the cooler gas is being entrained into the flow (Veilleux *et al.* 2005).

The accessibility of high-resolution X-ray and IR satellites has opened up new detection possibilities for GWs, and the use of IR colours has enabled the identification of starbursts and their associated winds out to large redshifts. The IR luminosity of a galaxy is proportional to the dust temperature, which is in turn controlled by the UV photon flux, which is directly proportional to the SFR. For example, 75% of ultra-luminous IR galaxies (ULIRGS; IR luminosities $> 10^{12}\ L_{\odot}$, SFR $> 100\ M_{\odot}\ \mathrm{yr}^{-1}$) at $z < 3$ have identified winds (Rupke *et al.* 2005; Veilleux *et al.* 2005).

1.3.1 Emission line ratio plots

Motivated by the need to understand and identify the ionization mechanisms of H II and starburst, Seyfert, LINER (Low-Ionization Emission-line Regions) and AGN galaxies, Bald-

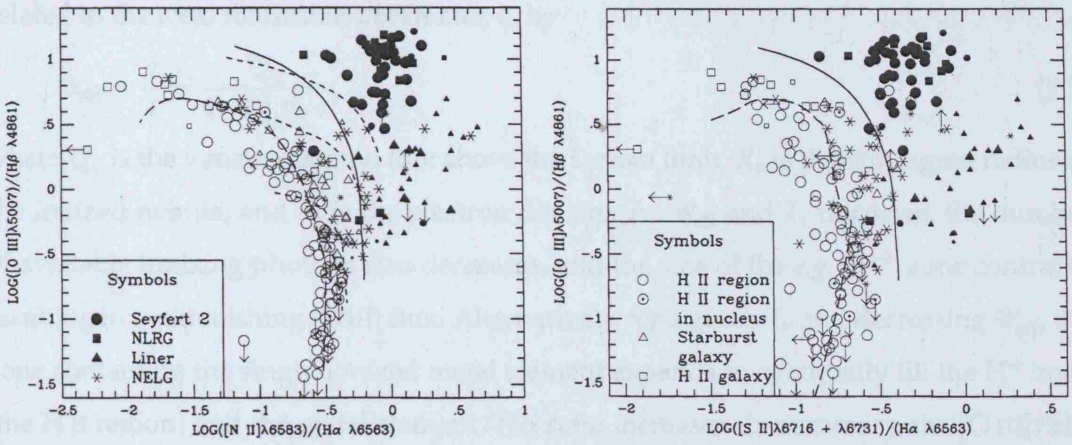

Figure 1.4: Diagnostic diagrams for [N II]/Hα and [S II]/Hα vs. [O III]/Hβ reproduced from Veilleux & Osterbrock (1987). Short and long dashed curves are H II region models, and the solid curve represents their derived threshold for dividing AGN from H II region-like objects.

win *et al.* (1981) and Veilleux & Osterbrock (1987) proposed a method to combine sets of indicators based on narrow emission lines to best distinguish which emission mechanisms applied in which galaxies. The expected ionization processes include photoionization by either OB stars or a non-thermal (power-law) continuum from the AGN component, or non-photoionization processes including shock-ionization and to a lesser extent turbulent mixing layers or changes in gas temperature (Calzetti *et al.* 2004). The indicators chosen were line flux ratios, and for practical reasons had to be composed of lines which are strong (hence easy to measure); unblended; have a small wavelength separation (to avoid reddening or flux calibration issues); are found in the optical (which at the time was the most easily accessible waveband); and are ideally ratios of a metal line and a hydrogen line (to avoid strong abundance sensitivities). Their studies concluded that comparing the ratio of [O III]λ5007/Hβ to [N II]λ6583/Hα, [O I]λ6300/Hα, and [S II]$\lambda\lambda$6717,6731/Hα gave the best results (see Fig. 1.4), and can be understood by the following argument: low-ionization forbidden-lines arise preferentially in zones of partially ionized hydrogen. For high forbidden-line fluxes, the zones need to be spatially extended, which only occurs in the presence of a large high-energy photon flux (*i.e. not* in the case of OB stars; Veilleux & Osterbrock 1987). The number of photons capable of ionizing a metal element (*e.g.* O^+) depends on T_* and $\mathscr{U}_{\rm eff}$, where T_* is the effective temperature of the ionizing source (star, star cluster or AGN) and $\mathscr{U}_{\rm eff}$ is the dimensionless effective ionization parameter. This is

related to the local ionization parameter, q, by

$$\mathscr{U}_{\rm eff} = \frac{q}{c} = \frac{Q_0}{4\pi\, R_{\rm s}^2\, n_{\rm e}\, c}, \tag{1.3}$$

where Q_0 is the ionizing photon flux above the Lyman limit, $R_{\rm s}$ is the Strömgren radius of the ionized nebula, and $n_{\rm e}$ is the electron density. As $\mathscr{U}_{\rm eff}$ and T_* decrease, the number of available ionizing photons also decreases, and the size of the *e.g.* O^{++} zone contracts, resulting in a diminishing [O III] flux. Alternatively, for a given T_* and decreasing $\mathscr{U}_{\rm eff}$, the zone containing the singly-ionized metal element expands to eventually fill the H^+ zone (the H II region) and the metal element/Hα ratio increases. In summary, the [O III]/Hβ ratio is primarily sensitive to T_* (or the hardness of the ionization field) and the [N II], [O I] or [S II]/Hα ratio is sensitive to $\mathscr{U}$. However, $\mathscr{U}$ is also expected to exhibit strong dependences on the geometric distribution of gas and the abundance (metallicity or Z). The metallicity dependence arises because at low Z, stellar atmospheres are hotter, their UV fluxes are higher, hence the O^{++} zone is larger and the *e.g.* N^+ zone is smaller as the electrons are now populate higher ionization states (Evans & Dopita 1985). Initially, as Z increases the forbidden-line flux increases, but as Z increases further, cooling by the forbidden lines lowers the electron temperature, $T_{\rm e}$, making it more difficult to collisionally excite these lines. At a certain point an increase in abundance (Z) is matched by a decrease in excitation and the line ratio begins to fall again, thus leading to a degeneracy. Considerable work has been done by the Dopita *et al.* group in calibrating these kind of emission line diagnostics with evolutionary synthesis and H II region models (Dopita *et al.* 2000, 2005), with particular emphasis on abundance measurements (Dopita *et al.* 2006).

Forbidden-line to recombination-line flux ratios can also be used to determine the significance of non-photoionization processes, including shocks and shock precursors [3] (Dopita & Sutherland 1995; Calzetti *et al.* 2004). Even a weak shock highly compresses the gas, leading to a significantly lower post-shock local ionization parameter, and traps the radiation field in a thin layer of partially ionized plasma leading to strong enhancement of [O I] emission in particular (Dopita 1997; Dopita *et al.* 2000). Furthermore, relatively cool, high-density regions forming behind a shock front can emit strongly in [S II] resulting in emission enhancement (Dopita 1997; Oey *et al.* 2000). For this reason, the ratio of [S II]/Hα has traditionally been used (by itself) as an indicator of shock excitation, even though it

[3] A shock precursor is a region in front of a shock that is ionized by the high density gas at the shock front (see Allen *et al.* 1999). Pure shock ionization (no precursor) occurs when a shock is propagating into a low-density environment, like the neutral ISM, or for a low-velocity shock.

is now realised that this can be ambiguous in some circumstances (Dopita & Sutherland 1995).

A natural upper limit to pure OB star photoionization can be described by predictions from a zero-age instantaneous starburst model (giving the hardest starburst spectrum possible). This led Kewley *et al.* (2001) to define a theoretical 'maximum starburst line', where for points to exist above this threshold, they theoretically need an additional contribution from a harder ionization source (*e.g.* shock or AGN). Points lying just below the threshold, however, are not necessarily purely photoionized, and can contain a contribution of up to 30 per cent from non-photoionization processes (Kewley *et al.* 2001). Calzetti *et al.* (2004) use these diagnostic plots to search for non-photoionized regions in starburst galaxies. Using the maximum starburst line together with a fairly conservative additional restriction on the [S II]/Hα ratio, they define areas of shock excited emission derived from ratioed *HST* WFPC2 (Wide Field and Planetary Camera 2) images. Fig. 1.5 shows two examples of their [O III]/Hβ *vs.* [S II]/Hα diagnostic plots used to define points of non-photoionized emission for NGC 3077 and NGC 4214. Points lying above and to the left of the dotted line are defined as arising from non-photoionization processes. On the right, the spatial distribution of the non-photoionized points for NGC 3077 are over-plotted on an Hα map, and are found to trace the edges of expanding shells, possibly indicating that they are caused by starburst-driven shocks. They also find a relationship between non-photoionized areas and areas of low Hα surface-brightness, resulting from the fact that shock-excited emission is intrinsically weaker than photoionized emission. Mazzuca *et al.* (2006) use similar emission line diagnostic plots to investigate the nuclear starburst ring and nuclear regions of NGC 7742, and find robust evidence for the transition from star formation in the nuclear ring to excitation by high-velocity shocks or from a non-thermal source in the nucleus.

1.3.2 Galactic wind models

The ultimate aim behind the study of GWs is to measure quantitatively the transport of energy and mass (including the metal-enrichment levels) out of star-forming galaxies. The radiation we actually measure when observing GWs is often fairly divorced from the processes that shape the wind's evolution, and can therefore be difficult to interpret. Hence, a full understanding of the mechanics of wind-formation is essential for correctly interpreting what often appear to be contradictory observations, and this can only come

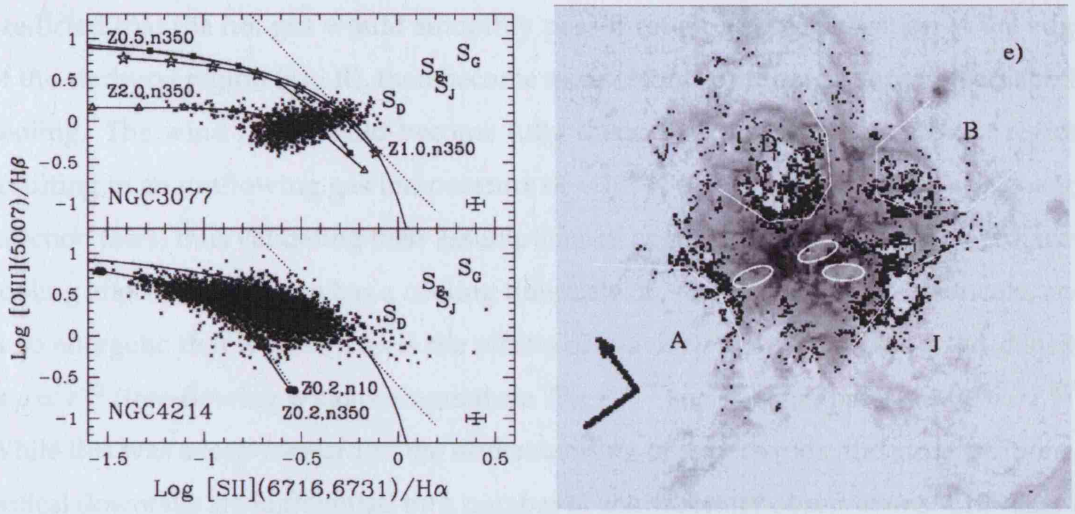

Figure 1.5: *Left:* diagnostic [S II]/Hα vs. [O III]/Hβ diagram for NGC 3077 (part of the M81/M82 system) and NGC 4214 derived from *HST* WFPC2 images. Photoionization models (labelled curves), the maximum starburst line of Kewley *et al.* (2001, solid line) and the position of shock excited emission line ratios (S) are shown. *Right:* points lying above and to the right of the maximum starburst line for NGC 3077 are over-plotted in black on the Hα image, together with the location of expanding shells (white curves) and peaks in the CO emission (white ellipses). The non-photoionized emission traces the expanding shell structures surprisingly well, possibly indicating that they are shock-driven. (Reproduced from Calzetti *et al.* 2004).

from complex analytical and hydrodynamical models.

Many GW simulations developed over the years have been modelled on the famous bi-polar outflow seen in M82. However we postpone a detailed comparison of these models and their predictions regarding this specific case to Chapter 4. Here, we discuss GW models in a more general sense.

Chevalier & Clegg (1985) developed a basic analytical model in the first attempt to understand the formation and evolution of starburst-driven winds. It contains many of the essential foundations of GW theory, but just as importantly, has a number of critical downfalls. It is essentially an extension of the Weaver *et al.* (1977) model for a stellar wind-driven expanding ionized shell, but applied to a larger scale. Their basic assumptions of spherical symmetry, negligible gravitational forces, and one large starburst region injecting a constant energy and mass from SNe with negligible radiative cooling, allowed them to model fairly accurately the radial dependence of temperature (T), density (ρ), pressure (P) and wind velocity using a number of simple adiabatic energy equations. Their model

predicted that the hot gas would smoothly pass through a sonic transition at the edge of the starburst region ($r = R$), then become a supersonic outflow undergoing adiabatic cooling. The wind flow would become fully thermalised within the starburst region, resulting in an outflowing gas temperature of $\sim 10^8$ K (for reasonable mass and energy injection rates) thus validating their assumptions of negligible gravitational and radiative cooling effects (a 10^8 K gas has a cooling timescale of $\sim 10^9$ yr $\gg$ outflow timescale, and is so energetic that it hardly feels the effects of gravity). For $r \gg R$, the wind density is $\rho \propto r^{-2}$ (free-flowing wind), temperature $T \propto r^{-4/3}$ and thermal pressure $P_{\rm th} \propto r^{-10/3}$. While this was a leap forward in the understanding of superwinds, the aforementioned critical downfalls are highlighted by a number of contradictory observations. Chevalier & Clegg (1985) themselves mentioned that the model struggled to reproduce contemporary X-ray observations, noting that unrealistic values for the fraction of SN energy and mass deposited in the gas outflow were needed to reproduce the measured X-ray properties of the wind. This point was raised again in Strickland *et al.* (1997), who reported that the density and temperature gradients derived from their X-ray spectra of the M82 wind differed greatly from those predicted by Chevalier & Clegg (1985). If radiative cooling is indeed negligible, a free wind would expand adiabatically and hence with constant entropy. However Strickland *et al.* (1997) showed that their observations of the temperature and density of M82's southern outflow were incompatible with an isentropic flow to the 95 per cent confidence level, thus effectively ruling out the Chevalier & Clegg model.

The issue of correctly predicting the measured X-ray properties (both energetics and morphologies) has proved to be a 'make-or-break' point for GW models as observations have become more readily available. A particularly difficult thing to predict has been the striking similarities between the Hα-emitting filaments and the soft X-ray morphology, seen on both small and large scales (0.01–10 kpc; Cecil *et al.* 2002; Strickland *et al.* 2002; Stevens & Hartwell 2003; Strickland *et al.* 2004). Strickland *et al.* (2002) list a variety of simple models that can simultaneously explain this correlation on the medium- to large-scales, and describe the possible physical origin of the components in each case. Fig. 1.6 contains four schematics from their paper showing possible situations that give rise to spatially correlated X-ray and Hα emission. The first scenario (Fig. 1.6a) was employed by Lehnert *et al.* (1999) to explain a particular feature in the M82 wind structure (see Chapters 2 and 4). Here, an expanding superwind impacts pre-existing neutral clouds of denser material in the halo, resulting in shock heating (Williams & Dyson 2002), raising

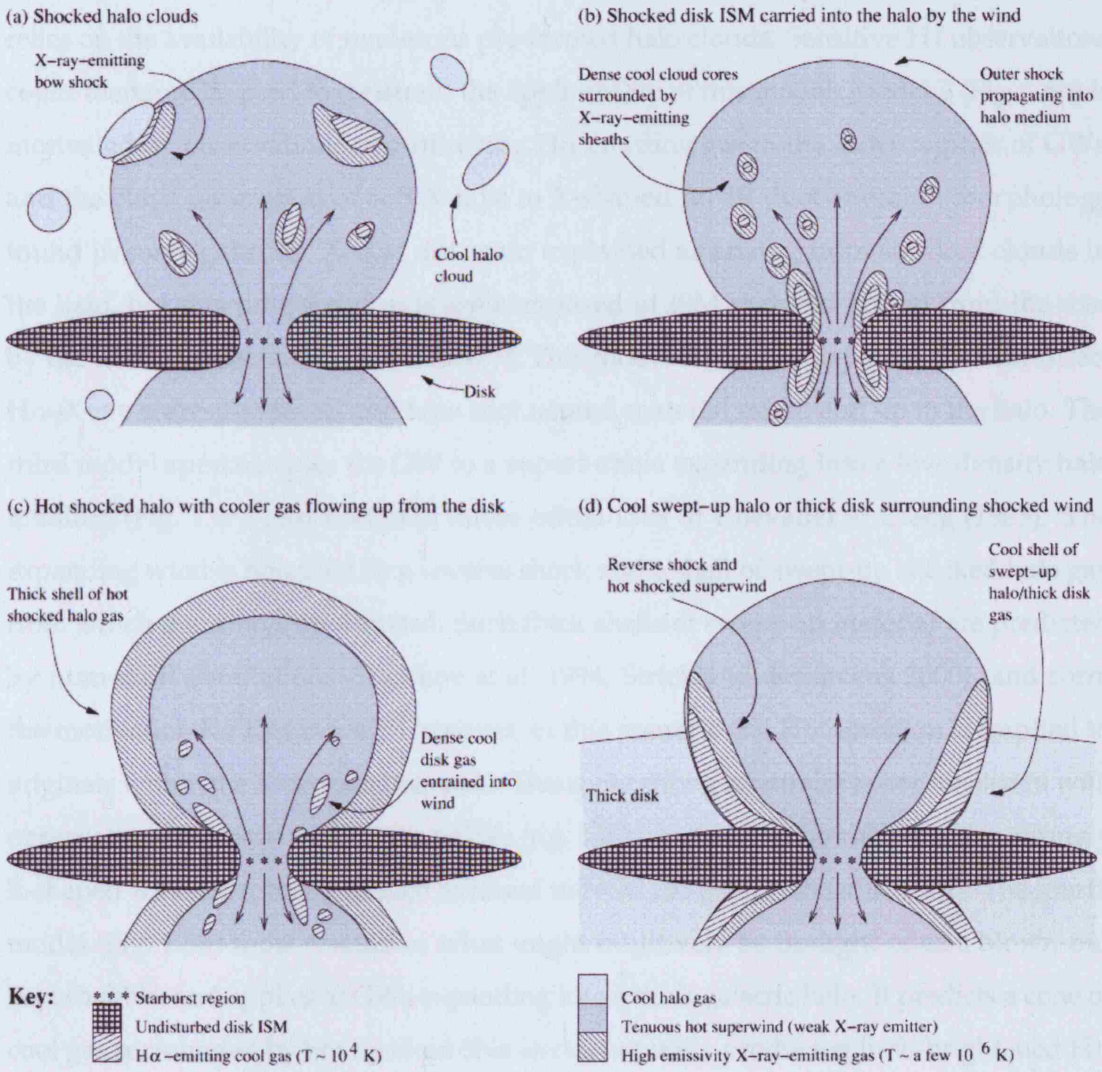

Figure 1.6: Schematic representation of possible wind models giving rise to spatially correlated Hα and X-ray emission in the halos of starburst galaxies (reproduced from Strickland *et al.* 2002). The four scenarios are described and discussed in the text.

the temperature to 10^4 K for dense gas (to produce optical emission) and 10^{6-7} K for less dense gas (producing soft X-ray emission), and meaning that the Hα emission would originate slightly downstream from the initial interaction as the highest energy photons are used up at the cloud face. This type of model is strongly favoured by two-dimensional hydrodynamic models of GWs (*e.g.* Tomisaka & Ikeuchi 1988; Suchkov *et al.* 1994), but relies on the availability of numerous pre-formed halo clouds. Sensitive H I observations could therefore be used to constrain the applicability of this model. Model 2 (Fig. 1.6b) is motivated by observations of outflowing Hα emitting gas in the inner regions of GWs, and the close association of soft X-rays to X-shaped far-IR dust emission morphology found in some galaxies. X-rays are again explained as arising from shocked clouds in the halo, but this time the clouds are composed of ISM material driven from the disc by the wind (*i.e.* entrained by the flow [4]). This model efficiently explains both the direct Hα–X-ray correspondence, and how cool neutral material might end up in the halo. The third model approximates the GW to a superbubble expanding into a low-density halo medium (Fig. 1.6c), and is closest to the initial idea of Chevalier & Clegg (1985). The expanding wind is bounded by a reverse shock and a shell of swept-up shocked halo gas, from which the X-rays are emitted. Such thick shells of swept-up material are predicted by numerical simulations (Suchkov *et al.* 1994; Strickland & Stevens 2000), and form the motivation for this model. However, in this scenario the Hα emission is implied to originate within the X-ray emitting shell. This quite strong constraint is not consistent with observations of many well studied GWs (*e.g.* M82), but cannot be ruled out for strongly X-shaped wind morphologies such as found in NGC 253 (Strickland *et al.* 2002). The fourth model (Fig. 1.6d) most resembles what might intuitively be thought of as a blown-out superbubble, and applies to GWs expanding into a thick galactic halo. It predicts a cone of cool gas surrounded by hot shocked SNe ejecta, naturally producing limb-brightened Hα emission just exterior to soft X-ray emission. For the shocked halo to cool enough to emit in Hα, the shock velocity must be low, and the halo density high. A key observational constraint is the prediction of strong O VI emission from the cooling region behind the outer shock. H I observations can also help to constrain the mass and density of the halo, hence how appropriate this model is.

The next step after defining these simple toy models was taken by Strickland & Stevens

[4]We take 'mass-entrainment' to mean material dragged along with the flow, whereas the more specific term 'mass-loading' to mean material which has been evaporated and incorporated into the flow.

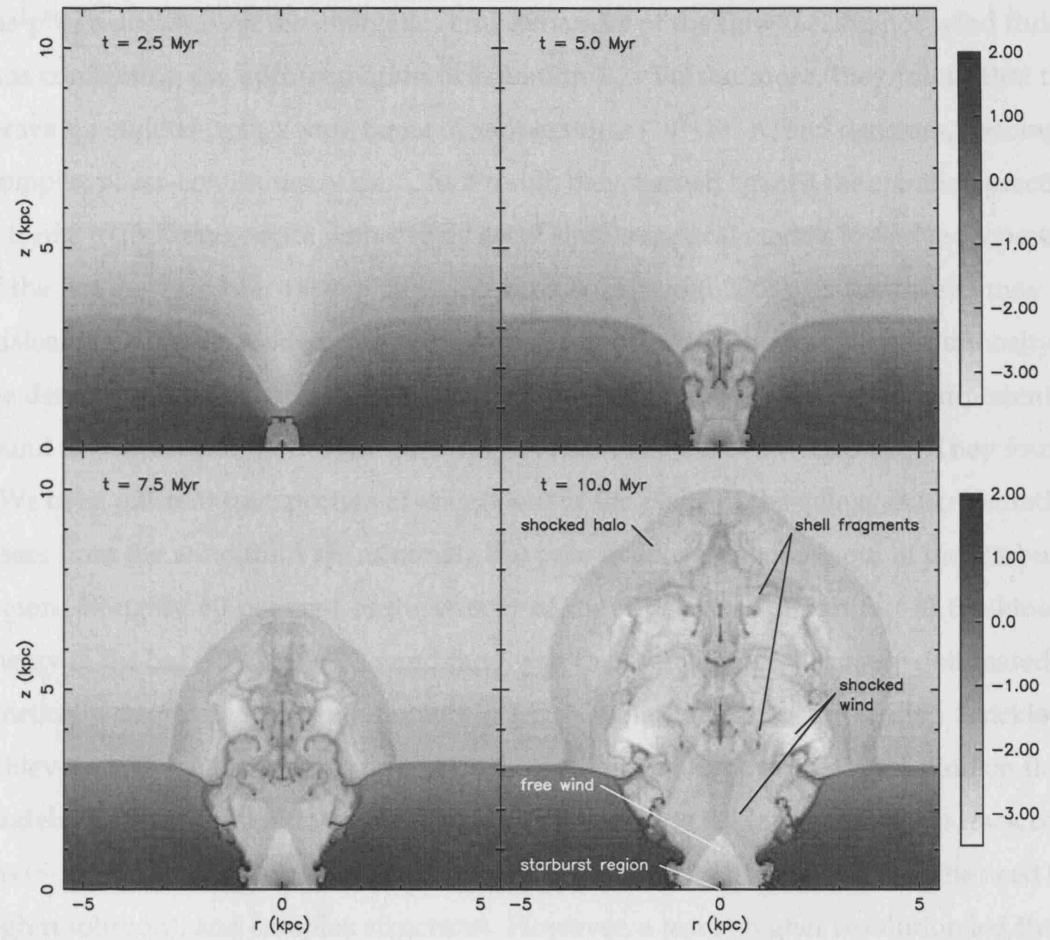

Figure 1.7: Logarithmic density cuts through the thick disc hydrodynamic wind model of Strickland & Stevens (2000) at four epochs, showing the time evolution of a starburst-driven superwind. Important features of the wind are labelled in the final panel. (Figure reproduced from Strickland & Stevens 2000).

(2000). These authors performed extensive hydrodynamical modelling of starburst-driven GWs with the aim of exploring in detail how the wind dynamics, morphology and X-ray emission depend on the ISM distribution of the host galaxy, the star-formation history and rate, and the presence and distribution of mass-loading. Fig. 1.7 shows an example of one of their hydrodynamical models for an instantaneous burst forming 10^8 $M_\odot$ of stars within a spherical starburst region of diameter 150 pc, with no mass-loading (assuming cylindrical symmetry about the z-axis). Significantly, they found that the soft X-ray emission from GWs originates from low filling-factor (≤ 2 per cent) gas which contains less than 10 per cent of the mass and energy of the wind (regardless of the mass-loading factor). This implies that X-ray observations *do not* directly probe the

gas-phase dominating the energetics and dynamics of the flow (*i.e.* the hot wind fluid), thus confirming the approximation of Equation 1.2. Furthermore, they found that the X-rays are emitted from a wide range of temperatures (10^5–10^8 K) and densities, forming a "complex phase-continuum of gas". As a result, they warned against the common practice of trying to fit X-ray spectra with a small set of simple spectral models to derive properties of the hot gas (*e.g.* Martin *et al.* 2002; Stevens & Hartwell 2003), as the results may be misleading. In their models, the primary variable affecting the soft X-ray luminosity is the density and distribution of the ambient ISM gas, and the hard X-ray component is found to originate from the starburst region itself, not the hot wind fluid. They found GWs to be efficient transporters of energy out of the plane of the galaxy (since radiative losses from the wind fluid are minimal), but poor at conveying mass out of the starburst region. Roughly 60 per cent of the energy of the superwind is manifest in the kinetic energy of the hot ($10^{6.5}$–$10^{7.5}$ K) wind fluid, and the change from thermally-dominated to kinetically-dominated energetics occurs when the wind breaks out of the disc. Strickland & Stevens also included a detailed analysis of the effect of numerical resolution on their models and find that the most significant consequence is the lack of ability to track cool gas ($\sim 10^4$ K; cooling is usually associated with steep density gradients, hence the need for high resolution), and complex structures. However, a test at higher resolution led them to believe that complex structuring (albeit at large scales and radii $\gtrsim 2$ kpc; see Fig 1.7) would arise naturally from their models if the necessary resolution could be achieved. A discussion of this model would not be complete without mentioning that one of its main failings is the large predicted size of the superwind region compared to the actual size of developed winds such as in M82. This is clearly seen in Fig. 1.7, where at 10 Myr it occupies an unrealistic volume, $\sim$8 kpc wide and $\sim$10 kpc high.

In all probability, the dominant effects producing the observed morphology and dynamics act to differing degrees of importance in every superwind, perhaps depending on evolutionary stage, energy injection rate and/or the mass injection/entrainment/loading rate. Indeed, "...collimation, mass loading, and confinement by the ambient gas depend primarily on the amount and distribution of the gas in the disc and halo of the galaxy... Since [energy/mass deposition rates] may be significantly different even in galaxies with the same level of SN activity, we may easily envision very different scenarios for the development of galactic winds..." (Suchkov *et al.* 1996). Furthermore, the morphology and flow-dynamics of a wind will differ substantially between a confined flow (*e.g.* the Galaxy;

Bland-Hawthorn & Cohen 2003), and a blow-out scenario (*e.g.* M82, NGC 253, NGC 3079) where the gas is venting into the halo.

While there is no doubt that hydrodynamical models such as Strickland & Stevens (2000) do a increasingly good job at modelling the kpc-scale energetics and dynamics of GWs, there is a need for models that accurately predict the intricately structured morphology of GWs on sub-kpc scales. Tenorio-Tagle *et al.* (2003) developed an alternative approach by assuming energy deposition does not arise from single region of order several tens or hundreds of parcecs in diameter, but from multiple discrete luminous concentrations of stars (SSCs), and has proved successful in reproducing the small-scale structure seen in the inner-wind of M82 (Tenorio-Tagle *et al.* 2003, Chapter 4). They set up hydrodynamical models to investigate what effect the interaction of several strong winds emanating from a collection of nearby SSCs would have on each other, and whether this could explain the highly structured inner morphology of superwinds. Starting with an already evacuated medium (following the commencement of a free-wind stage), they found cluster wind–wind interactions to cause the development of an extended region in which crossing shocks act to collimate outflow at small radii, while giving rise to soft X-ray emission at large radii. A more detailed description of this approach and its application to the M82 superwind is given in Chapter 4.

1.3.3 Cosmological implications

It is expected that the hot, chemically-enriched wind fluid has sufficient energy to escape the gravitational potential of all but the most massive of galaxies (Heckman *et al.* 1990; Martin 1998), thereby depositing energy into the intra-cluster and inter-galactic media (ICM and IGM, respectively) and polluting them with metals. Nearby galaxy clusters are observed to be pervaded by a hot, X-ray emitting gas with a metallicity of $\sim$0.3–0.5 $Z_{\odot}$ (Aguirre *et al.* 2001*a*). The observed IGM also shows substantial metal enrichment (0.01–0.1 $Z_{\odot}$) at all redshifts yet measured, and the integrated column density of absorbing species (related to the abundance) appears to be constant over the interval $1 < z < 5$ (Pettini *et al.* 2003; Kulkarni *et al.* 2005). Observations of the IGM are achieved through looking at the myriad absorption lines that arise on sight-lines through slight overdensities in the matter distribution within the IGM. As these clouds are located at a large range of distances (hence velocities), and since the Lyα resonance line is the dominant transition, they are collectively known as the Lyα-forest. However, the mere detection of metals in the

IGM raises important questions about the evolution of the Universe. Metals can only form in stars, which are all bound to galaxies with deep gravitational wells. The IGM should therefore represent a pristine environment comprised only of elements nucleosynthesized in the Big Bang. How, then, have metals been able to escape these potential wells and into the IGM? GWs from distant starbursts or Lyman-break galaxies (distant, rapidly star-forming galaxies with a strong Lyman-jump, so named through their method of detection; see Giavalisco 1998) offer an enticing possibility, and indeed powerful winds have already been observed in Lyman-break-type galaxies at $z > 1$, implying that superwinds do play an important role in the evolution of the IGM (Aguirre *et al.* 2001*b*; Pettini *et al.* 2001; Adelberger *et al.* 2003; Rupke *et al.* 2005). Although other equally plausible explanations for the ejection of metals have been proposed, including tidal stripping, ram pressure stripping, and radiation-driven ejection of dust (followed by thermal sputtering to release the metals), simulations suggest that these methods alone cannot account for the observed metallicity of the Lyα-forest (Aguirre *et al.* 2001*a*). Some authors even suggest that the majority of the IGM metals are already in place through SNe-driven flows by $z \sim 5$ (Qian & Wasserburg 2005).

Another important unknown in cosmology is the origin of the ionizing photons that effected the re-ionization of the Universe. It can be shown that the contribution of ionizing photons from quasars and galaxies to the intergalactic radiation field is roughly equal at $z \sim 3$ (Hunt *et al.* 2004; Shapley *et al.* 2006, inferred from the Lyα-forest optical depth), and is thought that Lyman-continuum radiation from star-forming galaxies becomes increasingly important at higher redshifts (Fan *et al.* 2001; Spergel *et al.* 2003). However, estimating the contribution from galaxies directly is extremely hard due to the inherent difficulties of observing the Lyman-break spectral region and determining reddening corrections, *etc.* Moreover, it is very difficult to model, let alone observationally derive, the value of $f_{\rm esc}$, the escape fraction of ionizing photons from the ISM of a star-forming galaxy. For instance, Shapley *et al.* (2006) recently observed 14 Lyman-break galaxies with Keck in the rest-frame UV with an average integration time of 10–20 hrs per object, and found only two with significant emission below the Lyman limit. From this, they derived a sample averaged escape fraction of $f_{\rm esc} = 14$ per cent, in rough agreement with previous observations. Since only a modest column density of gas results in a galaxy becoming fairly opaque to outgoing ionizing photons, GWs have been proposed as a method for carving channels in galaxy halos through which these ionizing photons could escape to

large radii (Loeb & Barkana 2001; Fujita *et al.* 2003).

A full discussion of the cosmological implications of GWs is outside the scope of this introduction, but hopefully these brief paragraphs are enough to make it obvious that investigation of starbursts and superwinds in close-by, easily studied systems, including the level of metal-enrichment of ejected gas, and the effect of winds on the porosity of interstellar media in galaxies, is essential to further understand high-z systems. Even though the determination of the observational parameters is notoriously difficult due limited spatial/spectral resolution and the poorly understood nature of the interaction between the gas phases, it is important to continue pushing the boundaries of wind observations and modelling techniques. Potentially anything we discover may have important implications for our understanding of the Universe as a whole.

Galactic winds: summary

The study of GWs is in its infancy, but with increasing access to high-resolution observations in every part of the electromagnetic spectrum, a proper understanding of arguably the dominant feedback mechanism in galaxy formation and evolution is beginning to form. Here we summarise the most important points of this section.

- The dynamical time-scales of GWs (derived from their typical radii and wind speeds) are of the order 1–10 Myr, and so are very dependent on the current state of the starburst (size, SFR, distribution and density of ISM gas and galaxy halo, *etc.*).
- The wind is dominated energetically by the fast flowing ($v_\infty \sim 10^3$ km s^{-1}) SNe-ejected wind fluid, which is almost undetectable due to its high temperatures ($T \sim 10^7$–10^8 K), low densities and filling factor ($\lesssim 2$ per cent). Detection is only made possible through its interaction with higher density ambient material (whether that be material entrained into or swept up by the flow, or pre-existing halo gas).
- Optical diagnostic ratios can be used successfully to search for the dominant ionization mechanisms in the flow (OB star photoionization, non-thermal black-hole powered ionization, shocks, *etc.*), and by comparing to ionization models, characteristics such as the ionizing source temperature (T_*), ionization parameter ($\mathscr{U}$), and gas abundances can be estimated.

- GWs are thought to entrain considerable quantities of cool neutral material, equalling or greater than the mass of material ejected by SNe.
- High resolution hydrodynamical models currently do a fairly good job at predicting the large-scale morphology and energetics of GW flows as long as an accurate account of mass-loading and ISM distribution is taken into account. Models that assume energy deposition from multiple discrete sources represent a promising solution to predicting small-scale structure in the inner-wind (see also Chapter 4).
- Besides studying GW for the purposes of evaluating their effect on galaxy evolution in the local Universe, is has become apparent in recent times that they may have played a significant role in the early Universe. As well as being thought to be the dominant mechanism for pollution of the IGM with metals, they may also have contributed to the re-ionization of the Universe.

1.4 Integral Field Spectroscopy

With our increasing desire and capability to observe and understand ever more complex systems in the Universe, the requirement for spatially resolved spectroscopy has become very apparent. Since this thesis is based on a significant number of observations making use of integral field spectroscopy (IFS), it is now prudent to include a short introduction to the technologies used.

IFS (sometimes known as 3D spectroscopy) is distinct from multi-object spectroscopy (MOS) by the fact that a continuous spatial area is observed, rather than discrete points across the field. IFS can be achieved using a number of instruments employing different techniques, including scanning Fabry-Pérot devices or integral field units (IFUs). An IFU is designed to split the whole field-of-view (FoV) into individual sections for re-imaging by a spectrograph. The number of techniques developed for dividing up the FoV are numerous, but since their characteristics are what define the resolution and capabilities of an IFU, we briefly describe the main ones below.

IFS technologies result in data-products containing three dimensions and usually formatted as a data-cube (two spatial dimensions for every wavelength slice). 3D data-cubes have been used by the radio community ever since detectors were developed with spatial resolution capabilities (the techniques used are very similar to that of the scanning

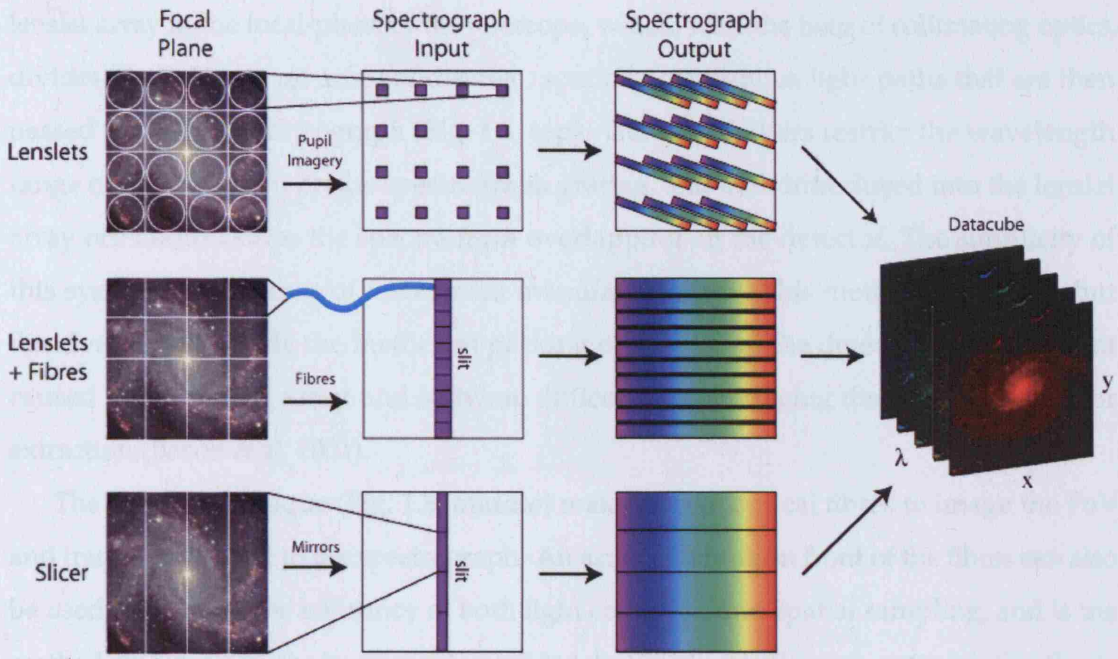

Figure 1.8: Cartoon diagram depicting the three main designs of integral-field units. *Top:* the FoV is split using a lenslet array, and through pupil imagery, the light is transmitted to the spectrograph. The individual spectra have to be tilted to avoid overlap on the detector. *Middle:* a lenslet array coupled to optical fibres reformats the FoV into a pseudo-slit at the entrance to the spectrograph. Fig. 1.9 shows a real image of the spectra as seen by the detector after reformatting by the fibre array. *Bottom:* a set of angled mirrors slices up the FoV and the subsequent optics reformat the slices into a pseudo-slit before the light enters the spectrograph. In all three methods, the information on the original spatial arrangement of the spectra can be used to reconstruct the data into a set of x-y images for each wavelength unit. (Adapted from Allington-Smith *et al.* 1998)

Fabry-Pérot interferometer). However, with the advent of modern large-format IFUs and the high volume of data output from even a single observing run, there has been considerable effort (and alas confusion) put into the development of standard data-cube formats and common data-reduction routines (Kissler-Patig *et al.* 2004; Sánchez 2004, 2006, European Commission's Euro3D research training network; Euro3D RTN).

1.4.1 Integral Field Units (IFUs)

As described above, an IFU is defined by the method it uses to split up the available FoV for re-imaging by a spectrograph. A cartoon representation of the three main techniques is shown in Fig. 1.8 (Allington-Smith *et al.* 1998). The simplest method involves placing a

lenslet array in the focal-plane of the telescope, which, with the help of collimating optics, divides the FoV into an array of discrete, spatially contiguous light paths that are then passed through a spectrograph (Fig. 1.8, top). The use of filters restrict the wavelength range of light incident on the spectrograph grating, and a tilt introduced into the lenslet array orientation stops the spectra from overlapping on the detector. The simplicity of this system and the ease of instrument manufacture make this method appealing, but disadvantages include the inefficient packing of spectra on the detector, scattered light caused by the lenslet array, and software difficulties with tracing the angled spectra for extraction (Bacon *et al.* 2001).

The second technique (Fig. 1.8, middle) makes use of optical fibres to image the FoV and transmit the light to the spectrograph. An array of lensets in front of the fibres can also be used to increase the efficiency of both light collection and spatial sampling, and is the method employed by the instruments used to take the observations presented in this thesis. The advantage of this technique is that the spatial format of the spectra can be re-formatted (in any order) by the fibres into a pseudo-slit at the entrance aperture of the spectrograph (*i.e.* all the fibres are arranged such that they line up in a row forming the shape of a slit). Fig. 1.9 shows an example of a CCD image showing a sub-set of spectra taken with the GMOS-IFU, focussing on the Hα and [N II] spectral region. As can be seen, a separation sufficient to avoid contamination between individual spectra and to enable them to be easily traced along the length of the detector must also be made when re-arranging the fibres into the pseudo-slit (Allington-Smith *et al.* 2002). Nevertheless, this method is much more efficient at making use of the available space on the detector than the first technique, and software routines for extraction of the individual spectra from the final CCD image can be simpler (since the spectra are not angled). Furthermore, it is trivial to design an instrument that takes simultaneous observations of the sky background, since fibres can easily be placed anywhere within the FoV. Disadvantages of this technique include difficulties of manufacturing an array that precisely couples fibres to lenslets (especially for the significant number of elements – often 1000s – required for good spatial resolution and coverage), multiple reflections within the fibre causing focal ratio degradation, and the fact that it is very difficult to make a fibre transmissive to wavelengths < 4500 Å, or that delivers a high throughput (Allington-Smith *et al.* 1998).

Image slicing techniques are the third option (Fig. 1.8, bottom), and involve an array of angled mirrors that 'slice' the FoV into sections. These sections are then reformatted by the

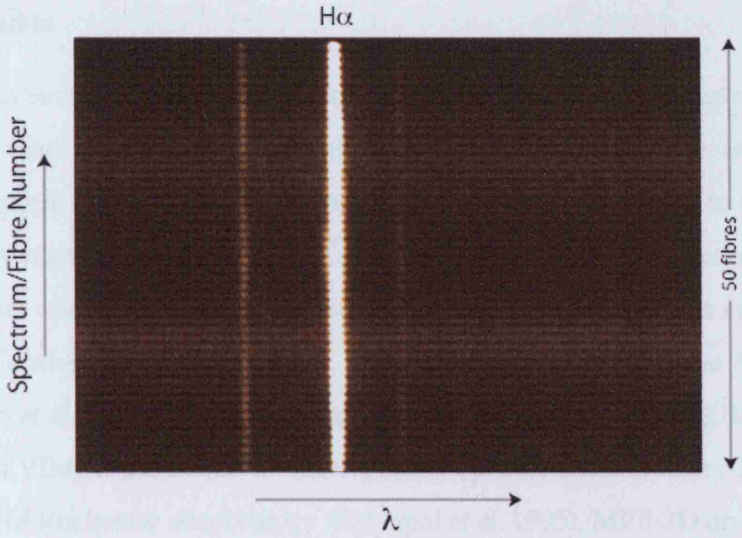

Figure 1.9: An example of a sub-set of 50 spectra as imaged onto a CCD detector after having been re-formatted by a lenslet+fibre IFU array. Hα and [N II] emission is evident together with some faint continuum emission.

Table 1.1: Examples of currently operating IFUs for each of the three techniques.

Technique	Instrument	Telescope	Notes
Lenslet array	SAURON	WHT	1600 square lenslets giving a spatial coverage of $33'' \times 44''$
Lenslets+Fibres	DensePak	WIYN	91 fibres covering $30'' \times 45''$ including 4 separated sky fibres
	GMOS-IFU	Gemini-N&S	500 object fibres covering $5'' \times 3.''5$, and a separate array of 250 sky fibres
	VIMOS	VLT	6400 fibres covering $27'' \times 27''$
Slicer	UIST	UKIRT	18 slices giving a $3.''3 \times 6.''0$ FoV
	GNIRS IFU	Gemini-S	33×21 slices giving a $3.''15 \times 4.''46$ spatial coverage
	NIRSPEC IFU	JWST	proposed instrument

optics to lie end-to-end (again forming a pseudo-slit) for re-imaging at the spectrograph. The main advantages of this system are its ability to attain high spatial-resolution through conserving spatial information in the direction parallel to the slit (no clear space is needed between spatial elements on the pseudo-slit, so resolution is essentially limited by the plate-scale of the detector), and a high light throughput. However, this technique has so far been hindered by limitations in current optical design, and the difficulty of incorporating a small enough slicer into a preexisting spectrograph. For a more detailed review of current slicer technology see Content (1998).

Table 1.1 lists a number of integral field units in current operation on telescopes around the world which make use the three techniques.

IFS and starbursts

As alluded to in Sections 1.1 and 1.3, the complexity of starburst and superwind systems requires innovative and novel approaches to investigating their inner-workings. Since IFS gives you both spatial and spectral resolution, it is ideally suited to studying these phenomena. A number of integral field spectrographs have been successfully used to study starbursts and GWs in the past, including the HIFI Fabry-Pérot system at CFHT (Shopbell & Bland-Hawthorn 1998), the TAURUS Fabry-Pérots on the AAT and WHT (Muñoz-Tuñón *et al.* 1996; Veilleux & Rupke 2002), DensePak and SAURON (Mazzuca *et al.* 2006), and VIMOS (Bastian *et al.* 2006*a*) in the optical, and the Fabry-Pérot system at the University of Rochester observatory (Satyapal *et al.* 1995), MPE-3D on Calar Alto and the WHT (Förster Schreiber *et al.* 2001) and CIRPASS on the WHT and Gemini-S (de Grijs *et al.* 2004) in the IR, to name just a few.

Studies such as (Bastian *et al.* 2006*a*) show the true power of IFU observations when investigating emission-line regions. In particular, their fig. 12 illustrates how you can isolate an arbitrary section of the spectrum (in this case the blue WR bump) and map its intensity over the whole IFU field to reveal the location of objects that would otherwise be very hard to identify. Although similar results can be achieved using narrow-band filters (*e.g.* Fig. 1.5), not all spectral lines have filters explicitly made for them, and when observing at a significant redshift, narrow-band filters become ineffectual as lines they are designed for become shifted out of the filters' response functions.

1.4.2 Interpretation and visualisation

Historically, IFS data-products have been notoriously hard to reduce and calibrate. This is the reason that Fabry-Pérot devices have fallen out of favour in recent times, with (in some ways) the more traditional approach offered by IFUs taking its place. The 3D aspect inevitably results in very large data files which have proven difficult to process until the recent availability of cheap and powerful computer hardware. Furthermore, flat-fielding and throughput-correction (the correction for individual throughput differences between different spatial elements) have proven challenging. A considerable effort has been made in the last decade to standardise and simplify the use of IFS techniques (through initiatives such as the Euro3D RTN and other smaller-scale programmes at the

institution/observatory-level, such as the SAURON project[5]), but as work presented in this thesis might betray, there is a considerable way yet to go.

After the hurdles of data reduction have been overcome, next come the issues regarding interpretation of such large data-sets. The complexity of the data-products, coupled with the inevitable complexity of the astronomical system being observed, means that sophisticated visualisation techniques are required to fully comprehend IFS data. Past problems are again linked to the lack of available hardware and software, but even now, problems of projecting inherently 3D data onto a 2D screen or printed page persist.

1.5 Structure of this thesis

Motivated by the many questions arising from the work presented in this introduction, the following chapters contain work based on the approaches I have taken to address these problems. A full introduction to the prototypical starburst galaxy M82 is given in Chapter 2 as a primer for the following two chapters. Chapter 3 presents and discusses observations of the inner environment of the M82 starburst taken with *HST*/STIS (Space Telescope Imaging Spectrograph), including the first ever spectral analysis of the SSC we denote M82-A1. Further observations of the M82 starburst taken with the DensePak IFU are given in Chapter 4, together with SparsePak observations of the outer-wind.

Chapter 5 contains an introduction to the dwarf starburst NGC 1569, preceding the analysis and discussion of a large set of IFU data taken with the GMOS and SparsePak instruments of the NGC 1569 wind in Chapters 7 and 8. Chapter 6 contains a description of the reduction and visualisation software developed for the analysis of the data contained in the these two chapters.

Conclusions derived from the whole body of work are given in Chapter 9, together with a discussion of the points raised and possible future directions for research into the starburst–galactic wind connection.

[5]http://www.strw.leidenuniv.nl/sauron/

CHAPTER 2

INTRODUCTION TO M82

The following pages contain an introduction to the enigmatic galaxy M82, focussing on its famous starburst and galactic wind. Following this, in Sections 2.2 and 2.3, are descriptions of the observations obtained to further study M82's star-cluster population and its large-scale superwind. The data-reduction methods are described here, but the analysis and discussion of the data-sets are left to the subsequent chapters.

2.1 Overview of the galaxy, the starburst and the superwind

M82 (NGC 3034), one of the most studied galaxies after the Milky Way, is famous for its intense starburst and prominent superwind. It is an obvious candidate for studies of galaxy evolution due to its proximity (3.6 Mpc; Freedman *et al.* 1994) and the sheer variety of interesting, resolvable phenomena throughout the galaxy. Originally classified as a dwarf (6×10^9 $M_\odot$; Sofue *et al.* 1998) irregular type-II (Sandage & Brucato 1979) galaxy, it has been recently re-classified as a late type spiral (~SBc) with the discovery of a bar (Telesco *et al.* 1991; Achtermann & Lacy 1995) and arm structure in the disc (Mayya *et al.* 2005). The confusion stems from the fact that M82 is inclined to the line-of-sight by ~80°, and suffers from a large amount of optical obscuration.

2.1.1 The starburst

M82 is the brightest extragalactic source in the infrared (IR) due to the large-scale on-going starburst (galaxy-wide star-formation rate ~10 $M_\odot$ yr^{-1}; Förster Schreiber *et al.* 2003).

Table 2.1: Basic observed and derived properties of M82

Parameter	Value	Reference
Designations	M82, NGC 3034, Arp 337, UGC 5322, 3C 231	1
Coordinates (J2000)	$9^h55^m54'$, $69°40'57''$	2
Distance (Mpc)	3.6	3
Position angle	65° (major axis)	2
Inclination	80°	4
B magnitude	9.3 ± 0.1 mag	2
Systemic velocity ($km\,s^{-1}$)	+200	1, 5, this work
Galactic extinction (mag)	$A_B = 0.13$	2
H I mass ($M_\odot$)	6×10^9	6
Metallicity ($Z_\odot$)	~1	7
Star formation rate ($M_\odot\ yr^{-1}$)	10–30	8

(1) Shopbell & Bland-Hawthorn (1998); (2) de Vaucouleurs *et al.* (1991); (3) Freedman *et al.* (1994); (4) Lynds & Sandage (1963); (5) McKeith *et al.* (1993); (6) Sofue *et al.* (1998); (7) Förster Schreiber *et al.* (2001); (8) Förster Schreiber *et al.* (2003)

Observations and models of the H I gas distribution surrounding M82 have led to the conclusion that the current starburst was triggered by an interaction with M81 2–5 $\times$ 10^8 yr ago (Brouillet *et al.* 1991; Yun *et al.* 1993, 1994), which may have resulted in the formation of a bar, thus channelling gas into the nucleus and triggering the intense star-formation episode (Wills *et al.* 2000; Greve *et al.* 2002*b*). Achtermann & Lacy (1995) find evidence for an ionized ring in [Ne II], just interior to the molecular ring detected by Telesco *et al.* (1991) at 2 μm, the appearance of which is very similar to other galaxies with bars.

The current active starburst region extends over 500 pc centred on the nucleus, and is defined optically by the high surface brightness regions or clumps denoted A, C, D and E by O'Connell & Mangano (1978). O'Connell *et al.* (1995) identified over one hundred candidate super-star clusters (SSCs[1].) within these clumps from *HST*/Planetary Camera imaging, while more recently Melo *et al.* (2005) catalogued a total of 197 young massive clusters in the starburst core from *HST*/WFPC2 observations. O'Connell *et al.* (1995) find that the cluster complexes correspond to known sources at X-ray, infra-red (IR) and radio wavelengths, and argue that on this basis, regions A, C, D and E represent the parts of the starburst core which are the least obscured along the line-of-sight. Region A is the most prominent of the starburst clumps and contains an impressive number of SSCs (Melo *et al.* 2005 associated 86 of their total to region A alone) together with very high continuum and emission-line surface brightnesses (O'Connell & Mangano 1978; O'Connell *et al.* 1995).

The evolutionary state of the M82 starburst has been modelled extensively in the past.

[1]As a guide, SSCs are usually defined as having half-light radii of $\leq$ 5 pc, ages of $\leq$ 500 Myr, and total masses $\geq 10^5\ M_\odot$

In a seminal paper, Rieke *et al.* (1993), and later Förster Schreiber *et al.* (2003), find that two spatially separate bursts are needed to reproduce the integrated observational properties of the galaxy's central regions. These authors find the bursts occurred $\sim$10 and 5 Myr ago with a duration of a few million years each. The first episode took place throughout the disc, but was particularly intense in the core (central few tens of pc). This burst is observationally represented by a population of red supergiants inferred from a strong IR continuum and a large CO absorption index (Rieke *et al.* 1993; Satyapal *et al.* 1997; Förster Schreiber *et al.* 2001). The second burst occurred mainly in the circumnuclear regions and along the stellar bar, consistent with the on-going consequences of the gravitational interaction with M81. This burst is responsible for the current generation of young, massive stars emitting a strong Lyman continuum flux. The data presented by Förster Schreiber *et al.* (2003) imply burst durations of few$\times 10^6$ Myr for individual burst sites, which each have typical scales of 10 pc or less. These values imply strong local and global negative feedback effects on starburst activity. M82 hosts the only large-scale starburst which can be investigated at this resolution.

An alternative probe for determining the star-formation history of a galaxy is through its star-cluster population. Gallagher & Smith (1999) derived ages of 60 ± 20 Myr for two SSCs, M82-F and L, located 440 pc south-west of the nucleus. Photometric age-dating of the extended "fossil" starburst region B, located 0.5–1 kpc north-east of the nucleus, shows that the peak of the star formation episode occurred $\sim 10^9$ yr ago (de Grijs *et al.* 2001, 2005).

Observations of clusters and integrated light properties can also provide more accurate means to measure the stellar initial mass function (IMF), and to address the long-standing question of whether the IMF differs in starburst environments. M82 has been the focus of many studies aimed at measuring the IMF, but owing to the difficulty of determining extinction corrections, has resulted in some conflicting scenarios. Some studies of the integrated mass-to-light ratio (*e.g.* O'Connell & Mangano 1978; Telesco *et al.* 1991; Satyapal *et al.* 1997) find a normal mass function, while others (*e.g.* Rieke *et al.* 1993; Förster Schreiber *et al.* 2003) find a deficiency of low mass stars. Modelling the assumed single-age population of a star cluster can be a more robust method than modelling integrated light from a whole region. Smith & Gallagher (2001) measured the dynamical mass of M82-F and showed that its visual mass-to-light ratio required a mass function deficient in low mass stars, and thus it is unlikely to become an old globular cluster. McCrady *et al.* (2003) determined dynamical masses for two SSCs on the western edge of the active

starburst region in M82, and found that one object appeared to be deficient in low mass stars. A re-analysis of M82-F by McCrady *et al.* (2005) based on *HST* images obtained with ACS (Advanced Camera for Surveys) and Keck/NIRSPEC spectra confirm that it has an abnormal mass function, and thus possibly a peculiar stellar mass function.

2.1.2 The superwind

A large-scale bipolar outflow or 'superwind', centred on regions A and C and extending along the galaxy minor-axis, is evident at many wavelengths (*e.g.* optical emission lines, IR dust emission, molecular CO, X-rays). A schematic diagram of the outflow is shown in Fig. 2.1 highlighting some of the main components. The Hα morphology exhibits a spectacular and complex distribution of loops and filaments extending many kpc out into the halo along the minor-axis (Sandage & Brucato 1979; Shopbell & Bland-Hawthorn 1998; Ohyama *et al.* 2002). McKeith *et al.* (1995) made an extensive kinematical study of the minor-axis flow with deep optical long-slit spectroscopy. They found line splitting in a number of optical hydrogen recombination lines and metal forbidden lines. Consistent with previous studies and the measured disc inclination, their data showed that the southern flow is on average blueshifted and the northern flow redshifted. Their velocity curves exhibit points of inflection at a height of $\sim$300 pc, which they interpret as the boundary of the wind 'energy injection zone', marking the point at which the wind becomes supersonic. They measure the base of the flow to have a radius of 300 pc at a height of only 100 pc, indicating that the flow probably breaks out of the plane at a location just interior to the molecular ring/bar, and opens out to a cone with $\sim$30° opening angle (see also Götz *et al.* 1990). At large radii, they find the wind tends to a constant velocity, and derive a de-projected outflow speed of $\sim$500–600 km s^{-1} for the Hα emitting gas. The outflowing gas is also expected to have entrained part of the rotation velocity of the disk (Greve 2004).

Shopbell & Bland-Hawthorn (1998) presented Fabry-Pérot Hα, [N II] and [O III] maps of the disc and superwind, covering the whole of the visible outflow region, and find a complex distribution of radial filaments and knots along the minor-axis, with a significantly different morphology in the north and south. A sharp edge on the south-eastern side and an abrupt reduction of flux at $\sim$500 pc radius is interpreted as a higher degree of collimation for the southern outflow, compared to a more chaotic flow in the northern lobe. Their line ratio maps show a region of low [N II]/Hα (log([N II]/Hα) = $-$0.6–0) along the

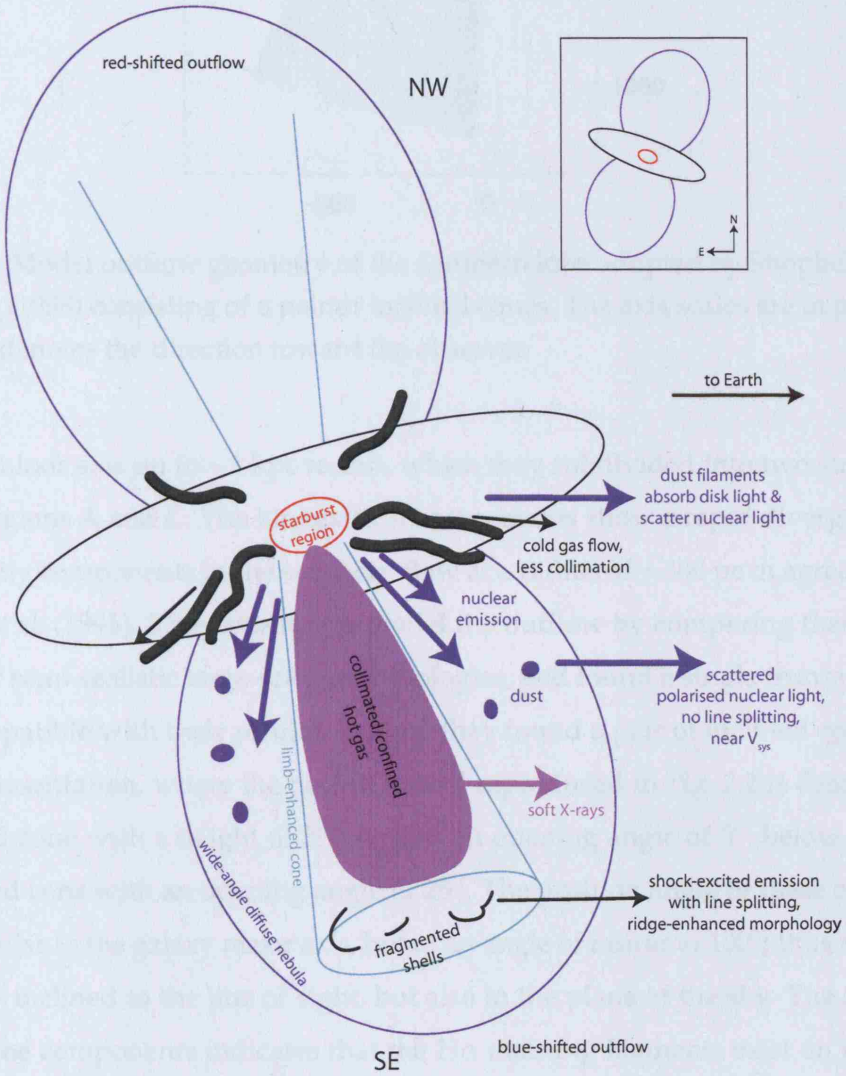

Figure 2.1: Schematic view of the M82 outflow viewed *side-on* summarising the main components of the outflow and illustrating the inclined aspect of the galaxy (reproduced from Ohyama *et al.* 2002). Inset is a view of the galaxy as seen from Earth.

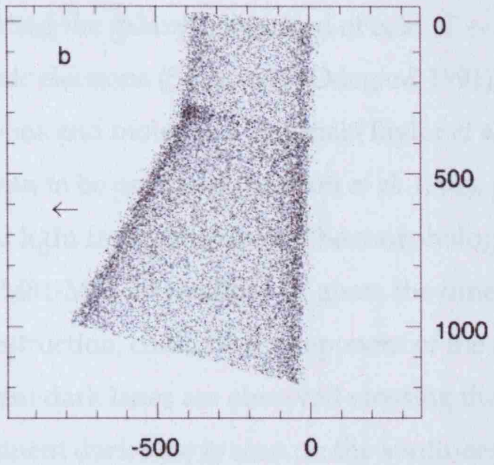

Figure 2.2: Model outflow geometry of the southern lobe adopted by Shopbell & Bland-Hawthorn (1998) consisting of a pair of inclined cones. The axis scales are in parsecs and the arrow denotes the direction toward the observer.

southern minor axis up to ~1 kpc radius, which they subdivided into two streams with bases at regions A and C. The kinematic measurements show a rapid divergence of the split velocity components in the southern flow at a radius of ~300 pc in agreement with McKeith *et al.* (1995). They attempt to model the outflow by comparing their data to a number of semi-realistic large-scale morphologies, and found a single truncated bubble is not compatible with their results. Instead they found a pair of inclined cones to be a better representation, where the best-fit model reproduced in Fig. 2.2 is described by a 5° inclined cone with a height of 350 pc and an opening angle of 5°, below which is a 15° inclined cone with an opening angle of 25°. The position angle of these cones is not perpendicular to the galaxy major axis, but at an angle of nearer to 100°; thus the outflow is not only inclined to the line of sight, but also in the plane of the sky. The strength of the split line components indicates that the Hα emitting filaments exist on the surface of the outflow cones at the interface between the wind and the ambient halo material. Shopbell & Bland-Hawthorn also present emission-line diagnostics indicating that the degree of ionization becomes harder at larger radii. This can be explained by either that the hot wind gas is transparent to UV photons from the starburst, leaving them to ionize the entrained disc and halo gas, or that shocks get more important at larger radii. By comparing their data to ionization models, they find a combination of photoionization and shocks is needed.

In their Fabry-Pérot data, Shopbell & Bland-Hawthorn also detect a smooth exponential

halo component surrounding the galaxy, comprised of cold ($T \sim$ 10–100 K) neutral H I gas (Yun *et al.* 1993), relativistic electrons (Seaquist & Odegard 1991), dust (Scarrott *et al.* 1991; Sofue *et al.* 1992), warm ions and molecular material (Taylor *et al.* 2001; Walter *et al.* 2002). The dust component is seen to be polarised (Scarrott *et al.* 1991), possibly indicating that it originates from scattered light from the galaxy. The morphology of the dust may reflect the consequences of the M81-M82 interaction, or, given the timescales of wind formation and dust creation and destruction, could be a component of the material entrained by the hot gas outflow. Prominent dark lanes are observed crossing the M82 disc and extending radially. The most prominent dark lane is seen on the south-eastern side of the disc and runs through part of the nuclear region (Ohyama *et al.* 2002). The dust lanes are thought to be situated above/below and in front of the disc (Ichikawa *et al.* 1995), and formed from dragged-out material from entrained molecular gas and dust (Ohyama *et al.* 2002). Recent hydrodynamic models (Suchkov *et al.* 1994, 1996) require a separate co-rotating halo component to be able to reproduce the observations, and find that the densest material near the base of the outflow serves to collimate the outflow at larger radii.

The superwind at other wavelengths

The Hα and X-ray morphology is very well correlated on scales as small as the respective resolution limits (Bregman *et al.* 1995; Strickland *et al.* 1997; Stevens & Hartwell 2003), and also exhibits very different morphologies in the north and south: the southern flow is brighter than the north at small radii, whereas the northern flow is brighter than the south at heights of >2 kpc. Stevens & Hartwell (2003) find that the northern outflow appears to have blown a hole in the H I gas distribution, which is now filled with X-ray emission, and that the ridge-like sharp-edged feature in the south-east of the wind may be caused by an interaction of the flow with an H I streamer. Strickland *et al.* (1997) model their X-ray data and show that the metallicity of the outflow is very low (0.05 $Z_{\odot}$), and spectra extracted at increasing heights indicate that the density decreases rapidly (10^{-1} to 10^{-3} cm^{-3}) but the temperature decreases slowly (expected since the cooling timescale of a 10^8 K gas is $\sim 10^9$ yrs, and the outflow timescale is $\sim 10^6$–10^7 yrs). The density and temperature distributions differ greatly from those predicted by simplistic models such as Chevalier & Clegg (1985), and detailed diagnostics of the southern wind reveal results which are incompatible with the basic assumptions of Chevalier & Clegg (1985), meaning that the observed X-ray emission cannot arise from a single phase expanding wind.

The Hα and UV morphologies are also well matched, as evidenced by observations from the *GALEX* satellite (Hoopes *et al.* 2005). These authors use UV/Hα flux ratios and the reported non-detection of [O VI] in the wind (Hoopes *et al.* 2003) as evidence to suggest that the most likely mechanism for producing such bright UV emission at large radii is by scattering of stellar continuum from the starburst by dust in the halo. This is consistent with the idea that cool, dusty material is entrained and ejected out into the halo by the hot outflowing wind.

CO measurements of the superwind by Taylor *et al.* (2001) and Walter *et al.* (2002) reveal the presence of large amounts of molecular material outside the central 1 kpc disc, distributed in an almost spherical halo out to distances of 2 kpc. They also detect a number of 'molecular streamers' extending out to 1.7 kpc, some of which are well correlated with the tidal H I features detected by Yun *et al.* (1993). They find that the halo rotates slower than the disc and has an outflow angle of $\sim$55°. Their estimated outflow velocities for the molecular material imply that a significant amount may escape the galactic potential.

Devine & Bally (1999) reported the discovery and identification of Hα emission from a structure located a projected distance of 11 kpc from the disc of M82, which they termed the 'cap'. In the same year, Lehnert *et al.* (1999) published *ROSAT*/PSPC and HRI X-ray observations of the same region, which they name the "ridge", and discuss the connection between the Hα and X-ray emission. It's position, directly above the brightest Hα emission associated with the superwind, implies a physical connection with M82, which was strengthened by the discovery of an X-ray 'bridge' connecting the main superwind to the cap (Stevens & Hartwell 2003). The study of such an object as this is important because if it is connected to the superwind outflow, it implies that winds driven by dwarf galaxies are able to reach high into the halo, and therefore likely to escape the gravitational potential of the galaxy. The cap has also been detected in both the far-UV (FUV) and near-UV (NUV) bands of *GALEX*, indicating the presence of dust within the structure, and has been found to have an abundance consistent with having been ejected from the starburst (Tsuru *et al.* 2006).

2.2 Space-based observations of M82

In this section we will describe the data-sets obtained using the *Hubble Space Telescope* (*HST*) and used to further our knowledge of the M82 starburst. The acquisition and reduction processes employed are detailed here, but the analysis is contained in Chapters 3 and 4.

The starburst clumps in M82, first identified by O'Connell & Mangano (1978) show evidence of structure on scales of 0.″1 (1.8 pc). Furthermore, the FWHM of an average star cluster is of the order ∼0.″3–0.″4. Ground-based observations, even with adaptive optics corrections, cannot reach this level of spatial resolution. We are fortunate therefore to have access to *HST* for very high spatial-resolution imaging and spectroscopic observations. The Space Telescope Imaging Spectrograph (STIS), Wide-Field and Planetary Camera 2 (WFPC2) and Advanced Camera for Surveys (ACS) instruments on-board *HST* have spatial resolutions on the order of 0.″05 pix^{-1} and are therefore ideal for such detailed observations of starbursts. An additional issue affecting ground-based observations, and is particularly prevalent in the starburst core of M82, is that of a rapidly varying, bright background. The seeing disc of even the best ground-based observation would cause severe background contamination of star-cluster sources, with a net effect of up to 40 per cent on the brightest sources in, for example, M82 region B (O'Connell 2001).

2.2.1 Spectroscopic data

In 2001, long-slit *HST*/STIS spectra at four positions in the center of M82 were obtained (GO 9117; P.I. O'Connell). One slit was centered on the brightest isolated cluster in region A, which we designate as M82-A1. Hereafter this slit will be referred to as 'slit A1'. Another slit sampled M82-F and L, while the two remaining pointings were centered on M82-B1-1 and M82-B2-1 within the post-starburst region (de Grijs *et al.* 2001). The latter of these additional pointings will be referred to as 'slit B2', since this study will be concerned with slits A1 and B2 only. In Fig. 2.3 we show the positions of these two slits superimposed on an archive *HST*/ACS WFC F656N image (see Section 2.2.2). The two slits (52 × 0.1 arcsec) pass close to the nucleus and just above and below the dust lane that perpendicularly bisects the disc of M82. Slit A1 intersects the cores of both regions A and C, and slit B2 passes through portions of regions D and E. The inset to this figure shows a section of region A, showing the position of slit A1 and the location of M82-A1 on an *HST*/ACS WFC F814W image.

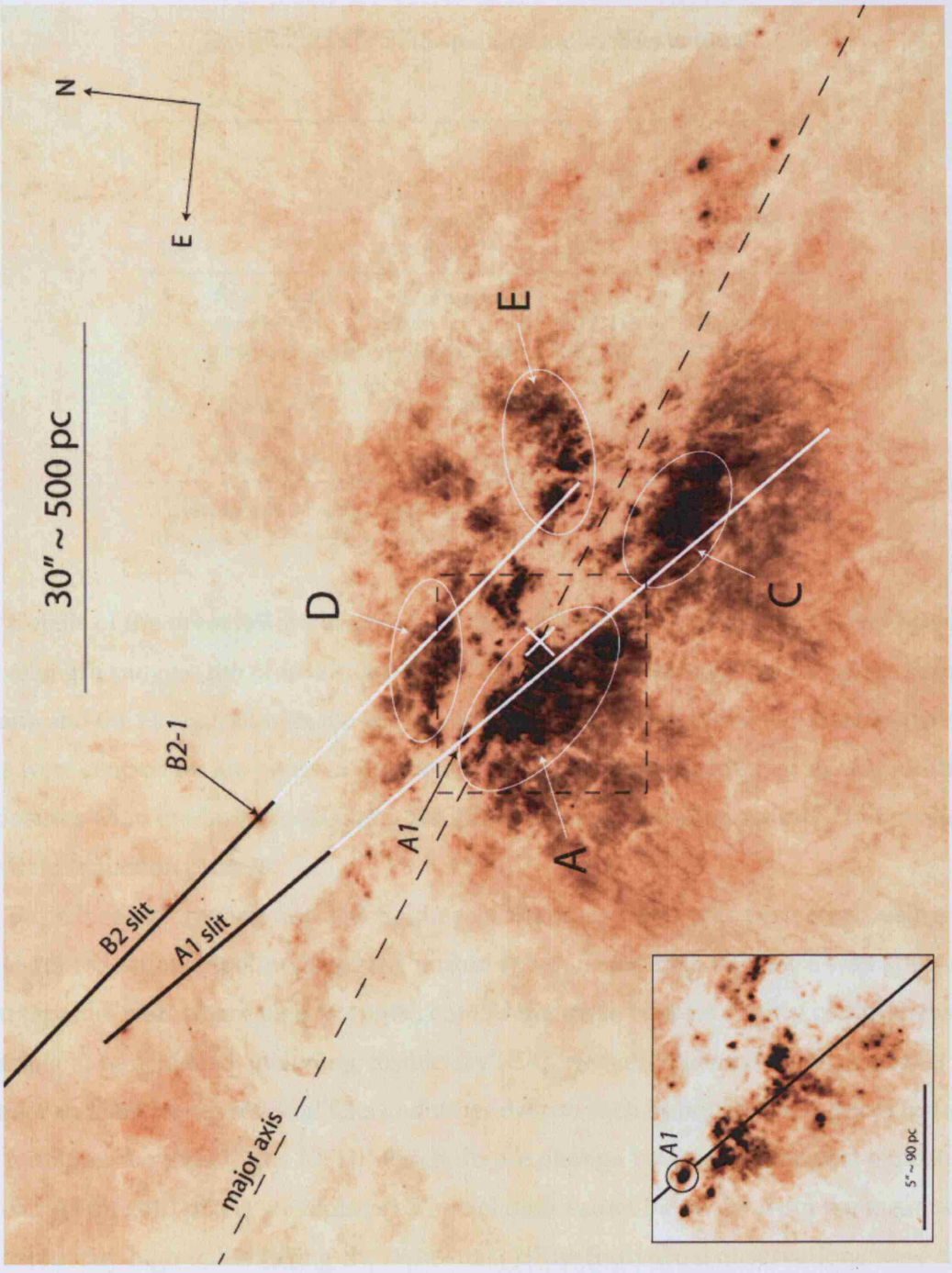

Figure 2.3: *HST*/ACS WFC F656N image of M82 with the two STIS slits and star clusters after which they are named (A1 and B2-1) marked. Also identified are some of the more prominent cluster-complexes (A, C, D and E). The dashed square around region A shows the outline of the area inset in the lower right, where the location of the STIS slit and M82-A1 are marked on an *HST*/ACS WFC F814W image. Portions of the 2D slit images corresponding to the white shaded parts of the slits are shown in Fig. 3.6, Section 3.3.1. The white cross marks the position of the 2.2 μm nucleus, and the long dashed line represents the galaxy major-axis.

Table 2.2: *HST*/STIS spectroscopic observations.

			Grating	
		Name	G430L	G750M
		λ range (Å) :	2900–5700	6295–6865
Slit		$\Delta\lambda$ (Å pix^{-1}) :	2.73	0.56
A	Ap=52″ × 0.″1	No. of exposures :	12	4
	PA=229°	Date :	27/11/2002	26/11/2002
	Offsets=multiple	Exposure time :	231.4 m	71.8 m
B2	Ap=52″ × 0.″1	No. of exposures :	3	2
	PA=235°	Date :	02/11/2002	02/11/2002
	Offsets=none	Exposure time :	52.2 m	39.1 m

A1: $\alpha = 09^h\,55^m\,53\overset{s}{.}42$; $\delta = +69°\,40'\,51\overset{''}{.}08$ (J2000)
B1-1: $\alpha = 09^h\,56^m\,03\overset{s}{.}34$; $\delta = +69°\,41'\,12\overset{''}{.}20$ (J2000)

Details of the observations are listed in Table 2.2. Spectra were taken in two different wavelength ranges: the blue continuum with the G430L grating (including the Balmer jump), and the Hα region with the G750M grating. Coordinates of the two clusters that the slits were centred on are given in the footnote to the table. In the case of slit A1, multiple exposures were made, stepped along the slit to improve the elimination of hot pixels in the data reduction process.

Basic bias subtracting and flat fielding of the image sets was performed using the CALSTIS reduction pipeline included within IRAF. Since each exposure was split into two separate read-outs called 'crsplits', combining these enables a fairly comprehensive cleaning to be achieved, including cosmic-ray (CR) rejection. However, this process is not perfect and still leaves residual CRs and other defects such as hot and cold pixels (caused by radiation damage to the CCD) which do not change between sequential exposures. To correct for cold pixels we replaced all pixel data values below 5σ from the mean with an arbitrarily high value (using the IMREP task). The individual observations were then shifted to correct for the spatial dither pattern used. We used the IRAF/STSDAS cosmic ray rejection (OCRREJ) task to combine all the images and eliminate the remaining cosmic rays and hot pixels (which now include all the cold pixels). Finally, we used the X2D task to provide rectified absolute flux and wavelength calibrated two-dimensional spectral images. Reduction of the additional slit positions (including slit B2) was performed by David Rosario (University of Virginia), but followed the same procedure as described

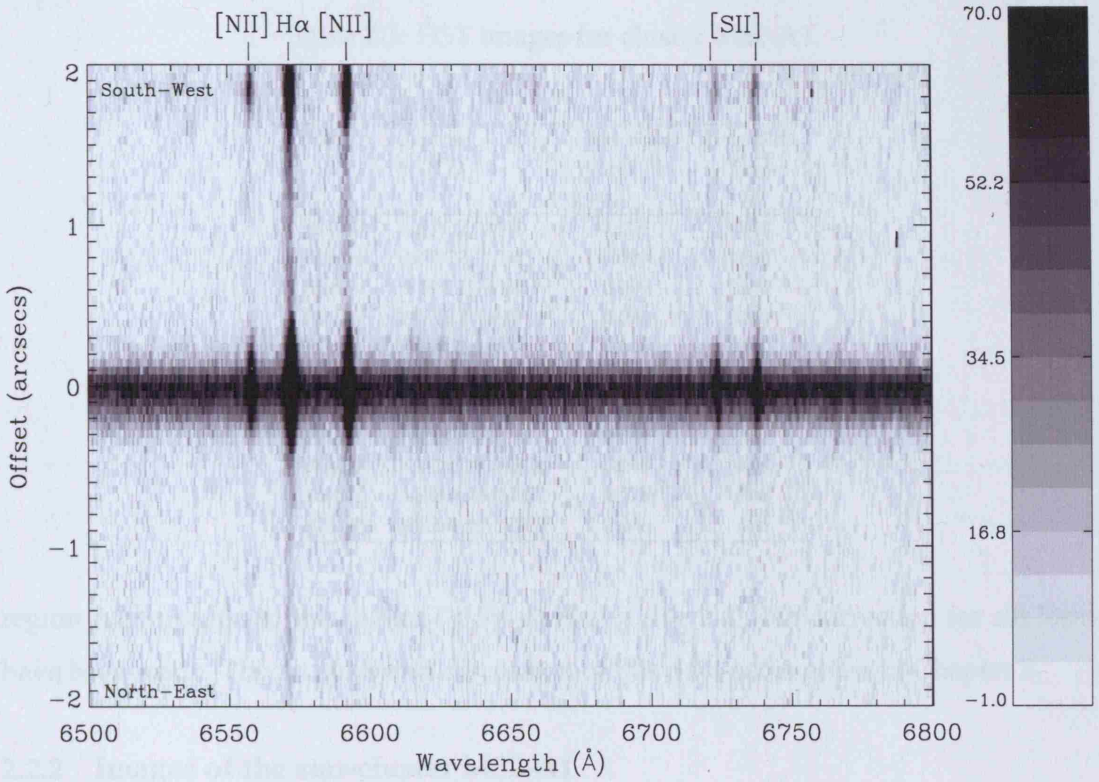

Figure 2.4: STIS G750M two-dimensional spectral image showing the cluster M82-A1 and its compact H II region over the wavelength range 6500–6800 Å. The y-scale is in pixels where 1 pixel = 0.″05 and a spatial extent of 4″ is shown. The nebular emission lines are marked and the surface brightness scale is in units of 10^{-16} erg cm^{-2} s^{-1} Å^{-1} arcsec^{-2}.

here.

In Fig. 2.4, a small portion of the reduced two-dimensional image for the G750M grating is shown. The cluster, M82-A1, is located at a y-axis offset of 0. It is clearly resolved and is surrounded by a compact H II region. From cuts across the STIS 2D spectra, we measure a FWHM of ∼6 pixels or 0.″3 for M82-A1, exceeding the slit width of 0.″1. The spectral resolution of the G430L and G750M gratings for an extended source is 2–3 pixels. We measure a resolution of 6.7 ± 0.6 Å from Gaussian fits to the unresolved nebular Hβ emission line originating in ionized gas along the slit. We will therefore assume that the actual spectral resolution is 2.5 pixels or 6.7 Å (G430L) and 1.4 Å (G750M grating).

To extract one-dimensional spectra, we used an extraction width of 14 pixels for M82-A1, to include all the cluster light. We performed a background subtraction using 10 pixel-wide regions centred at ±25 pixels from the centre of the cluster. These particular regions were chosen because they contain negligible emission from the ionized gas in

Table 2.3: HST images for cluster M82-A1.

Filter	Camera + CCD	Plate Scale ($''$ pix^{-1})	Exposure Time (s)
F439W	WFPC2/WF4	0.099	3300
F439W	WFPC2/WF4	0.099	4100
F555W	WFPC2/WF4	0.099	2500
F555W	WFPC2/WF4	0.099	3100
F547M	WFPC2/PC	0.045	100
F656N	WFPC2/PC	0.045	1000
F814W	WFPC2/WF4	0.099	140
F814W	ACS/WFC	0.049	120
F160W	NICMOS/NIC1	0.043	448
F190N	NICMOS/NIC2	0.076	384
F222M	NICMOS/NIC2	0.076	448

region A compared to the cluster ($< 5\%$ at Hα; *cf.* Fig 2.4). No correction for slit losses have been made. The analysis and discussion of this data-set is given in Chapter 3.

2.2.2 Images of the star-cluster M82-A1

This section describes *HST* archival images of cluster M82-A1 that were used for the purposes of performing photometry and size measurements. We obtained images taken with the WFPC2 (Wide , ACS and NICMOS cameras on-board *HST* for the central region of M82 from the *HST* archive; the details of these images are given in Table 2.3. The broad-band WFPC2 F439W, F555W and F814W images from the GO 7446 programme (PI O'Connell) are centred on the fossil starburst regions B1 and B2 (see de Grijs *et al.* 2001) and region A is on the WF4 CCD. We also obtained narrow-band images in the F656N and F547M filters which are part of the GO 6826 programme (PI Shopbell) on the superwind of M82. We used the F547M image for continuum subtraction of the F656N image. These data are discussed in more detail in Section 4.1, Chapter 4. The single ACS F814W image was obtained as part of the GO 9788 snapshot programme (PI Ho). The NICMOS images from the GO 7218 programme (PI Rieke) are described in Alonso-Herrero *et al.* (2003).

All images were reduced by the *HST* on-the-fly re-processing (OTFR) package before downloading. Cosmic rays were then removed using the Laplacian cosmic ray identification routine of van Dokkum (2001), LACOSMIC. The individual images were then checked for saturation and averaged.

Colour composite

The four WFPC2 CCDs (WF1–3 and PC) for each of the F439W, F555W, F814W and F656N images were mosaicked together into single fields using WMOSAIC. Continuum subtraction of the narrow-band F656N image was achieved using the off-band F547M image. The scaling factor required was determined by measuring the counts in a 35 pixel diameter aperture in both images, placed over part of the continuum emitting stellar disc.

The mosaicked images were then converted to TIFF format and loaded into the image manipulation software Adobe Photoshop. The three broad-band images, F439W, F555W, F814W, were assigned to the blue, green and red channels respectively, and the colour balance was adjusted to give a natural-looking representation. The F656N image was then imported as a new layer and by assigning a linked colour balance adjustment layer, the F656N image could be given a red hue, and the levels were tuned to accentuate the emission line wind. The final product was a balanced broad- and narrow-band composite with both continuum- and emission-line features.

2.3 Ground-based observations of M82 with WIYN

The Wisconsin, Indiana, Yale and NOAO (WIYN) 3.5m telescope on Kitt Peak, Arizona, U.S.A., is equipped with a number of instruments which are well suited to detailed observations of starburst regions. In this section we describe observations of M82 made with three of WIYN's instruments: the imaging camera, Mini-Mos; and two differently formatted IFUs, DensePak and SparsePak. The analysis of the data-sets is presented in Chapter 4.

2.3.1 Mini-Mos observations

The Mini-Mosaic Imager (Mini-Mos) is WIYN's primary imaging camera. Mounted at the Nasmyth port, it consists of two 4096 × 2048 CCDs separated by a small gap, and samples 9.6 × 9.6 arcsecs of the sky at $0\farcs14$ pixel^{-1}.

In December 2001, M82 was observed with Mini-Mos using the *R* broad-band filter and the Hα and [S II] narrow-band filters. Exposures were dithered so as to fill in the chip gap. Basic reduction (bias subtraction, flat fielding and exposure summation) was performed by Jay Gallagher (Univ. of Wisconsin) using the pipeline NOAO tasks included

in IRAF. The final steps of reduction were to combine the individual CCD images together then to mosaic the dithered offsets to create the final image; for this the MSCRED package in IRAF was used. First, the zero points of the world coordinate system (WCS) were set using the MSCZERO task with reference to a number of known bright stars in the fields. The backgrounds of each image were measured using a surface fit of order 2 in 4 separate sections. The division of the field into sections helped in minimising the effect of the contamination of the background by light from the galaxy (which extends almost to the edge of the field on two sides). The two CCD images for each exposure were combined using the pre-set offsets given with the package, then the task MSCIMAGE was used to map the WCS information of each frame onto a single grid. The intensity scales for each combined exposure were matched with MSCIMATCH using the background measurements, and the final mosaicking was performed using MSCSTACK. Cosmic rays were removed using LACOSMIC (van Dokkum 2001). This procedure was repeated for each of the three filters.

At this stage, we realised that we had an extensive set of images of M82 with qualities of both high spatial resolution (*HST*/WFPC2; see Section 2.2.2) and sensitivity over a large field (WIYN/Mini-Mos). Combining these two datasets could give, for the first time, an idea of how the large-scale emission line superwind is connected to the chaotic inner starburst core.

The first step in creating a colour composite was to subtract the continuum from the WIYN Hα and [S II] narrow-band images. This was achieved using the *R*-band image as a proximate off-band exposure. Unfortunately, in the mosaicking procedure, the stacked images for each filter are slightly different sizes, which made doing a subtraction within IRAF problematic (although not impossible). It was decided that since any colour composite was going to be made in Photoshop anyway, it would be easier to do the continuum subtraction then. The three filter images were loaded into Photoshop and aligned visually. The *R*-band image was subtracted from the Hα and [S II] filter images using the 'apply image' tool, where the scaling factors were based on exposure times and filter sensitivities, but the exact values came from a certain amount of trial and error. Two colour composites of the WIYN images were made to highlight different features: the first was made of the non continuum-subtracted *R* (blue), Hα (green) and [S II] (red) images, and was scaled to give a balanced colour for the stellar disc component. The second was made of just the continuum-subtracted narrow-band images, where Hα was assigned to

both the red and blue channels (to give a purple hue), and [S II] to the green. The [S II] emission lines are intrinsically fainter than Hα, and as such there was very little signal in the outer wind region. Thus the [S II] image was scaled to highlight the filamentary structure close to the disc and add to the general colour balance. The two WIYN colour composites were combined together in Photoshop to give an image showing both the disc and wind components at a high sensitivity.

Combining the WIYN and *HST* composites

The final *HST* and WIYN colour composites were merged together using a combination of Photoshop tools and techniques. Since the *HST* image was not as deep as the WIYN image, it contained much more black background that had to be removed in order for it to be successfully overlaid. This proved to be a very challenging task. Difficulties also arose in equalising the colour balance and contrast of the two composites so they could be blended together.

Firstly the images were aligned and scaled to a common orientation. Using a combination of brushing layer masks, the eraser tool and adjusting the colour channels, the *HST* images was gradually faded into the WIYN image using an iterative process. The aim was to merge the two in such a way that the wind plumes could be traced continuously from the outer regions into the starburst core. The technique of combining the high-resolution *HST* images of the inner part of M82, with the deep, sensitive, wide-angle WIYN images of the outer wind have allowed us to represent M82 over a large range in magnitudes and spatial scales. A detailed discussion of these images is given in Section 4.1.

The final image was released as a joint UCL/Univ. of Wisconsin press release on the 21st May 2004, and is shown in the frontispiece.

2.3.2 DensePak observations

DensePak (Barden *et al.* 1998) is a small fibre-fed integral field array attached to the Nasmyth focus of the WIYN telescope. It has 91 fibres, each with a diameter of 300 μm or 3″ on the sky; the fibre-to-fibre spacing is 400 μm making the overall dimensions of the array 30 $\times$ 45 arcsecs. Four additional fibres are offset by $\sim$60″ from the array centre that serve as dedicated sky fibres. Figure 2.5 shows the format of the DensePak fibre array on the sky, including the sky fibres. At the time of observation, there were 5 damaged

Table 2.4: DensePak observations of M82. Coordinates refer to the array centre, fibre 42.

Position	(J2000)		Exposure Time
	RA	Dec	(s)
1	$9^h\,55^m\,53\overset{s}{.}53$	$69°\,40'\,43\overset{''}{.}14$	4×1200
2	$9^h\,55^m\,48\overset{s}{.}56$	$69°\,40'\,32\overset{''}{.}20$	4×1200
3	$9^h\,56^m\,04\overset{s}{.}11$	$69°\,41'\,11\overset{''}{.}57$	4×1200

and unusable fibres in the main array (36, 40, 46, 59 and 93) making a usable total of 86. DensePak's fibre bundle is reformatted into a 'pseudo-slit' (see Section 1.4) to feed the WIYN bench-mounted echelle spectrograph. This spectrograph is part of the Hydra multi-object fibre positioner instrument, and uses a T2KC 2048 × 2048 CCD detector.

On 14th April 2001, four fields covering the stellar disc of M82 were observed with DensePak. Unfortunately, due to a telescope malfunction, the precise coordinates for the fourth position were not recorded, thus rendering this position unusable. This was a great shame since this field covered the gap in-between region A (position 1) and region B (position 3). The location of the three positions for which we have accurate coordinates are shown in Fig. 2.6. The 860 line mm^{-1} grating (blaze angle 30.9°) gave a wavelength range of 5820–6755 Å with a dispersion of 0.46 Å pix^{-1}. Details of the observations are given in Table 2.4. A number of bias frames, flat-fields and arc calibration exposures were also taken together with the science frames.

Data Reduction

Basic reduction was done using the CCDPROC task within the NOAO IRAF package. Once a master bias frame was created using the ZEROCOMBINE task, CCDPROC was used to fit the overscan region and subtract the bias for each object and flat-field frame. A master flat-field was created from the individual flat-fields using FLATCOMBINE. Instrument-specific reduction was then achieved using the HYDRA tasks, also within the NOAO package. The first step was to run APFIND on the master flat-field exposure to automatically detect the individual spectra on the CCD frame. The output of this task is an aperture identification table containing the trace of the dispersed light from each fibre, which can be applied to the science frames to extract out the individual spectra. The task DOHYDRA was then run to perform the flat-fielding and wavelength calibration. The datafile at this stage contained 90 reduced and wavelength calibrated spectra (one for each fibre in use, including the four

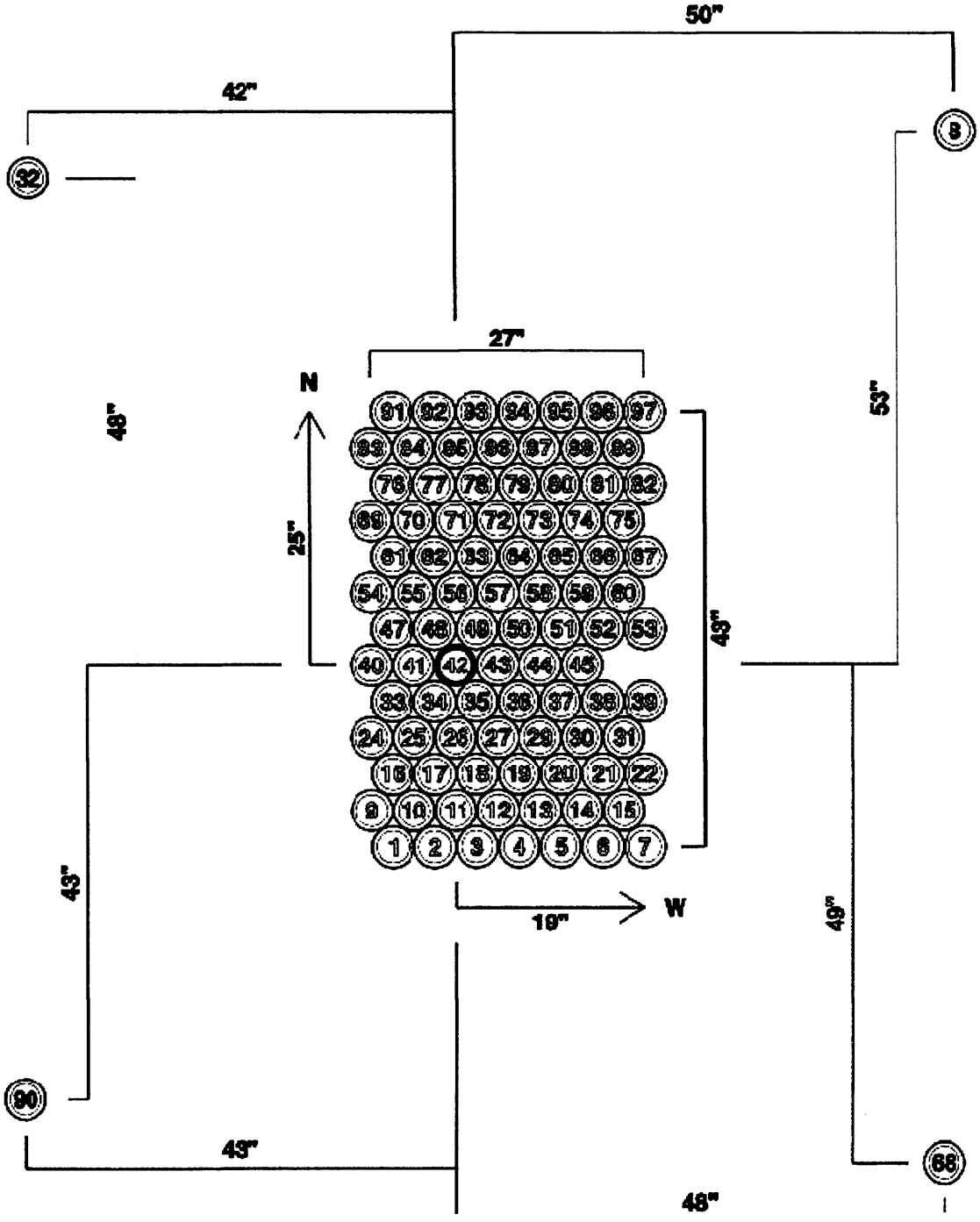

Figure 2.5: DensePak fibre array on-sky format (reproduced from Sawyer 1997). Fibre 42 is the field centre, and since installation fibres 36, 40, 46, 59 and 93 have failed.

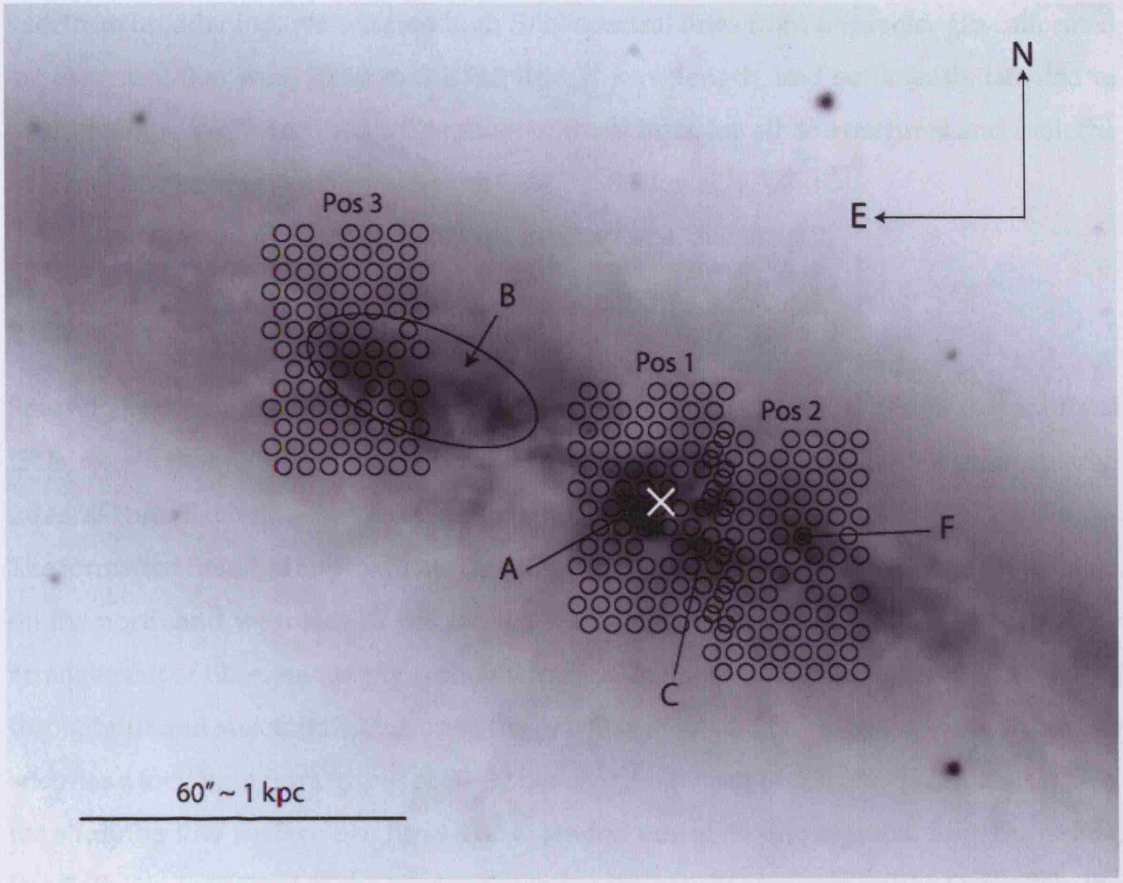

Figure 2.6: WIYN *R*-band image of M82 (inverted colours) with the positions of the DensePak fields overlaid. Some of the bright starburst clumps/clusters are marked, and the position of the 2.2 μm nucleus is shown with a white cross.

sky fibres).

Even with the sky fibres separated from the main array by 60″, extended emission from the galaxy contaminated, to varying degrees, each fibre in each of the positions. For Positions 1 and 2, sky fibre 8 was found to have minimal contamination, and for Position 3, fibre 32 was the least contaminated. Since the level of sky emission (particularly the molecular OH water vapour lines) was quite high, it was decided that subtracting a minimally contaminated sky spectrum was better than not subtracting it at all. We estimate that the Hα flux in all three positions is affected by <10 per cent. Cosmic-rays were cleaned from the data using LACOSMIC (van Dokkum 2001), before final combination of the individual frames using IMCOMBINE. The final datafiles now contained 86 (sky fibres removed) sky-subtracted spectra.

In order to determine an accurate measurement of the instrumental contribution to the

spectrum broadening, we selected high S/N spectral lines from a wavelength calibrated arc exposure that were close to the Hα line in wavelength, and sufficiently isolated to avoid blends. We then fitted a Gaussian to these lines for all 86 apertures and took the average. The instrumental broadening is 44.7 ± 3.1 km s^{-1}.

The data are analysed and discussed in Chapter 4, Section 4.2.

2.3.3 SparsePak observations

SparsePak (Bershady *et al.* 2004) is a "formatted field unit" similar in design to traditional IFUs, except that its 82 fibres are arranged in a sparsely packed grid, with a small, nearly-integral core. Each fibre has a diameter of 500 μm which corresponds to 4.″69 on the sky. The formatted field has approximate dimensions of 72×72 arcsecs; seven sky fibres located on the north and west side of the main array are separated by a distance of ∼25″. The arrangement of fibres on the sky is shown in Fig. 2.7. SparsePak was designed to maximise throughput and spectral resolution at the expense of spatial coverage/resolution, and as such has a total light throughput of 89–92 per cent longwards of 500 nm. This makes it ideal for studying low surface-brightness or extended emission line regions. Like DensePak, SparsePak is connected to the Hydra bench spectrograph; however unlike DensePak, the mapping order of fibers between telescope and spectrograph focal planes (pseudo-slit) was purposefully designed in a fairly randomised fashion in order to distribute sky fibres evenly along the slit, and to minimise the effects of spectrograph vignetting.

On the nights of 13–16th December 2004, I observed two fields in the northern wind outflow of M82 with SparsePak. Using the echelle 316 grating at order 8 with an angle of 63.25° gave a spectral coverage of 6450–6865Å. This meant we were able to cover the nebular lines of Hα, [N II]$\lambda\lambda$6548, 6583 and [S II]$\lambda\lambda$6716, 6731 with a dispersion of 0.20 Å pix^{-1} (R = 11 400). A number of bias frames, flat-fields and arc calibration exposures were taken together with the science frames. Since the M82 superwind is a faint emission line region, I also observed an offset sky field to enable accurate sky subtraction. Details of the SparsePak observations are given in Table 2.5.

Data Reduction

The data reduction procedure is almost identical to that for DensePak since the instruments are both mounted in the same Nasmyth port, use the same type of fibres, and feed the

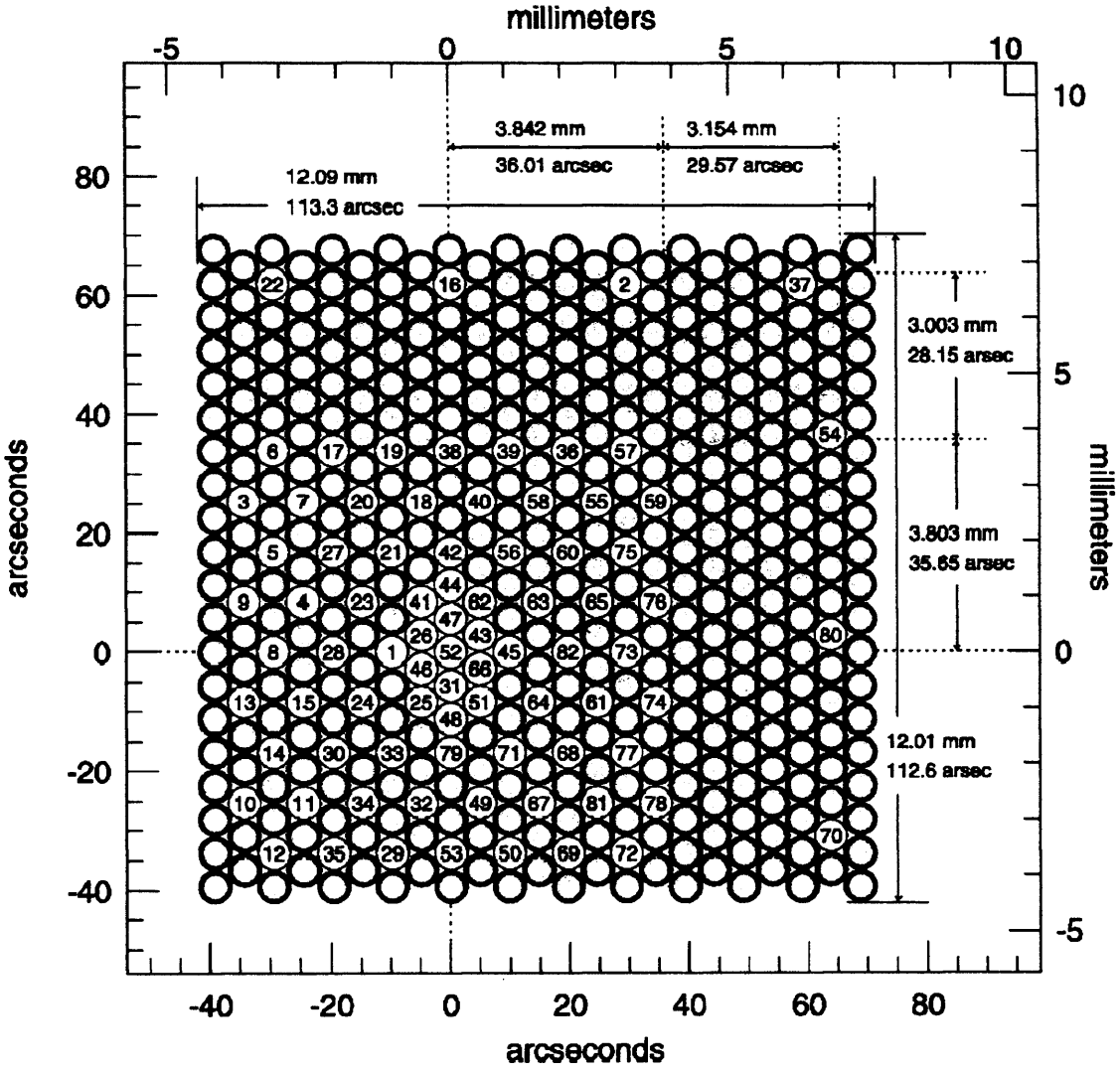

Figure 2.7: SparsePak on-sky fibre geometry (reproduced from Bershady *et al.* 2004). The fibre number refers to the order in which they are arranged in the pseudo-slit, and illustrates the random ordering on the sky.

Table 2.5: SparsePak observations of M82.

Position	(J2000)		Exposure Time
	RA	Dec	(s)
1	$9^h\,55^m\,49\overset{s}{.}4$	$69°\,43'\,26\overset{''}{.}7$	3×1800
2	$9^h\,55^m\,54\overset{s}{.}4$	$69°\,42'\,31\overset{''}{.}7$	3×1800
sky	$9^h\,57^m\,18\overset{s}{.}3$	$69°\,46'\,00\overset{''}{.}3$	1×1800

same spectrograph. The main difference however was sky-subtraction: for the fields covering the superwind flow, a straight scaled subtraction of the offset sky field accurately removed the sky emission from the spectra. Cosmic-rays were cleaned from the data again using LACOSMIC (van Dokkum 2001), and combination of the individual frames was done using IMCOMBINE. The final datafiles contained 82 reduced, wavelength-calibrated and sky-subtracted spectra.

Following the method described above for determining the instrumental contribution to the line widths, we fitted Gaussians to a number of isolated high S/N arc lines close to Hα in wavelength. We find the average instrumental resolution to be 30.9 ± 0.4 km s^{-1}.

The data are analysed and discussed in Chapter 4, Section 4.2.

CHAPTER 3

HST/STIS OPTICAL SPECTROSCOPY OF THE STARBURST CORE OF M82

In Section 2.2.1 of the previous chapter, we introduced a set of *HST*/STIS observations, including a description of the instrument set-up and the processes followed to reduce the data. We now present our analysis of this rich data-set in two main sections: part of this chapter concentrates on one bright star cluster in particular, and is based on the results from the published article: "HST/STIS optical spectroscopy of super star clusters in the starburst galaxy M82" (Smith L.J., Westmoquette M.S., Gallagher J.S., *et al.*, 2006, MNRAS, **370**, 513), which we hereafter refer to as SWG06. The remaining sections are concerned with the general interstellar environment within the starburst core, and provide a good context for the discussion focussing on the single star cluster.

3.1 The super star cluster M82-A1

In this section, we direct our attention on the brightest isolated star-cluster in region A of the M82 starburst core, which we have designated M82-A1. It is located on the eastern edge of this high surface-brightness clump, ~130 pc from the nucleus, and near to both the parallel and perpendicularly disc-intersecting dust-lanes.

3.1.1 M82-A1 imaging measurements

Photometry and radius measurements of M82-A1 are complicated by the varying background of emission and absorption by gas and dust in the starburst core. We tried various

Table 3.1: Derived parameters for cluster M82-A1 from *HST* images. The errors in the effective radius and magnitude measurements are ±30 mas and ±0.10 mag respectively.

Filter	FWHM (major axis) (mas)	Minor/Major Axis Ratio	$R_{\rm eff}$ (mas)	VEGAMAG Photometry (mag)
F439W	140	0.74	130	18.77
F439W	140	0.71	140	18.75
F555W	170	0.68	160	17.23
F555W	170	0.65	160	17.22
F547M	180	0.72	180	
F814W	220	0.66	210	14.77
F814W	210	0.70	210	14.91
F160W	200	0.79	200	
F190N	200	0.71	190	
F222M	160	0.79	160	
F656N	290	0.57	260	8.54×10^{-14} [a]

[a] Total Hα flux in units of erg cm^{-2} s^{-1}

approaches to subtracting the background and found that the most robust and simplest method was to use a flat plane. The level was calculated from an average of measurements, taken at four locations around the cluster M82-A1, that were deemed to contain "representative" background values.

To measure the size of M82-A1, we used the ISHAPE algorithm (Larsen 1999) together with the TINYTIM package (Krist 2004) to correct for the point-spread function (PSF) for the WFPC2 and NICMOS cameras. For the ACS F814W image, we used an empirical PSF generated from point sources in the field of 47 Tuc (M. Mora, private communication).

First, we determined the optimum fitting radius (the radius of the area around the specified coordinate to which the fit is made) for the profile modelling by examining fits to the F547M image using a standard Moffat function with a power index of 1.5. We found that a radius of 0.5 arcsec was optimal since this was sufficiently large to sample enough of the background level, but excluded light from other nearby sources. The *HST* images (*e.g.* Fig. 2.3) show that the projected cluster shape is quite elliptical. We therefore decided to allow the fit profile also to be elliptical, even though this introduces an additional source of error.

We experimented with the different profile types available in the ISHAPE package, and chose a Moffat function with a power index of 1.5 since this gave the lowest residuals in the overall fit. We also tried varying the power-law index of the Moffat profile but found that a value of 1.5 consistently gave the best fit. Elson *et al.* (1987) determined that profiles

of this type provide good fits to LMC star clusters while de Grijs *et al.* (2001) found similar results for the profiles of the brightest clusters in region B of M82.

Table 3.1 lists the FWHM of the major axis and the minor/major axis ratio, as determined by ISHAPE for each image. Also given are the effective (or half-light) radius, $R_{\rm eff}$, where the expression given below was used to convert the FWHM of an elliptical Moffat profile fit to a half-light radius (Larsen 2004).

$$R_{\rm eff,true}/R_{\rm eff,circ} \approx 0.5\left(1+\frac{w_y}{w_x}\right), \tag{3.1}$$

where $R_{\rm eff,true}$ and $R_{\rm eff,circ}$ are the effective radii of the true (elliptical) profile and the equivalent circular profile, and w_x and w_y are the FWHM of the major and minor axes of the elliptical profile, respectively. We find very consistent results for the WF4 and ACS F814W measurements given the different pixel scales and PSFs. To estimate appropriate errors, we fitted the F547M and F814W/ACS images with a number of different profile types. We find that, in terms of the residuals, King profiles with different concentration parameters also give acceptable fits. From the scatter in the resulting $R_{\rm eff}$ values, we find that the likely error in each measurement is $\pm$30 mas. Taking a straightforward mean of the radii measured in the continuum filters, we find $R_{\rm eff} = 170 \pm 30$ mas or 3.0 ± 0.5 pc for M82-A1. We derive a mean minor/major axis ratio of 0.72 ± 0.05 from the same images. For comparison, McCrady *et al.* (2003) have measured $R_{\rm eff}$ for several clusters (including M82-A1 which is MGG-a1 in their designation) from NICMOS NIC2 F160W images. From spherical King profile fits, they find $R_{\rm eff} = 119 \pm 14$ mas. This is smaller than our measurements, but can be explained by the fact that they did not take into account an ellipticity factor. It is apparent from Table 3.1 that the radius of M82-A1 decreases towards shorter wavelengths; this effect is discussed in the following subsection.

Measurements of the size and total flux of the compact H II region surrounding M82-A1, based on Hα emission measured in the F656N filter, are also given in Table 3.1. It is highly elliptical with a major axis FWHM value of 290 mas and an axis ratio of 0.57, giving a half-light radius $R_{\rm eff}$ of 260 ± 30 mas or 4.5 ± 0.5 pc. Thus the H II region is only 1.5 times larger than the cluster.

In Table 3.1, we list the magnitudes of M82-A1 for the broad-band filters in the VEGAMAG system (Holtzman *et al.* 1995). The photometry of M82-A1 was performed using the PHOT task within the NOAO DIGIPHOT package. It was decided that a 7 pixel radius aperture was the most appropriate, considering the non-circular projected shape of M82-

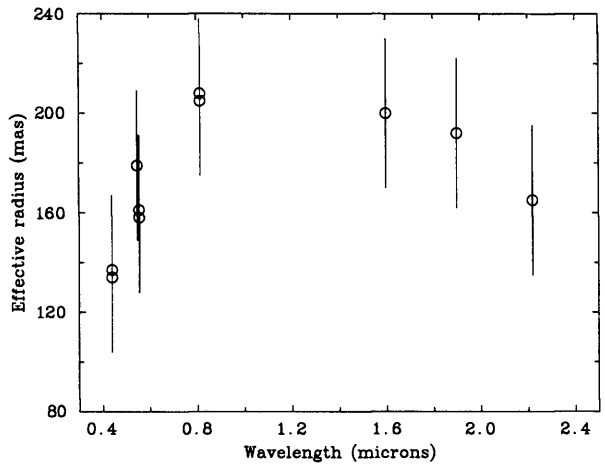

Figure 3.1: Measured effective radii (in mas) of M82-A1 plotted as a function of wavelength using the data in Table 3.1. The errors bars represent the measurement uncertainties of ±30 mas.

A1. The total counts measured in each aperture were corrected for CCD charge transfer effects using the formulation of Dolphin (2002). They were then converted to magnitudes using the zeropoints provided for the VEGAMAG system in the instrument handbooks. We estimate the measurements are accurate to ±0.10 mag because of the uncertainties in the varying background. This level of accuracy was verified by making independent measurements on each of the input image sets.

The change of radius with wavelength

Fig. 3.1 shows the variation of $R_{\rm eff}$ with wavelength as measured for each of the available filter images. The diffraction limit of the NICMOS images is close to the measured radius of A1, therefore we can exclude these points from the argument. Using just the optical broad-band size measurements we find that the radius is 30 per cent smaller at 4400 Å (F439W) than at 8140 Å (F814W).

McCrady *et al.* (2005) find that the radius of cluster M82-F decreases with *increasing* wavelength, and interpret this as being due to mass segregation, with the more centrally concentrated stars being the most massive cooler evolved stars which emit more light at shorter wavelengths. However, for M82-A1, we see the opposite effect with the radius deceasing towards blue wavelengths.

SWG06 discuss the possible reasons for the observed wavelength dependence of the measured radius, and find that from the output of the spectral synthesis code STARBURST99

Table 3.2: Absorption and emission line measurements for M82-A1. Velocities are in the heliocentric frame of reference.

Line	λ_{vac} (Å)	Velocity (km s^{-1})	FWHM (km s^{-1})	Equivalent Width (Å)	Comments
G430L spectrum					
[O II]	3728.48	448		-2.9 ± 0.6	blended doublet
H8 abs	3890.15	171		3.2 ± 0.5	blended with He I?
Ca II K	3934.78	205		3.8 ± 0.6	Interstellar
Ca II H	3969.59	415			Interstellar; blended with Hϵ
Hϵ abs	3971.19	294		3.9 ± 0.7	blended with Ca II H
Hδ abs	4102.89	335		3.0 ± 0.7	
Hγ em	4341.68	332			
Hγ abs	4341.68	327		2.0 ± 0.9	
Hβ em	4862.68	298		-1.8 ± 0.2	
[O III]	4960.30	343		-1.0 ± 0.1	
[O III]	5008.24	319		-1.8 ± 0.2	
G750M spectrum					
[N II]	6549.85	322	93	-4.8 ± 0.2	
Hα	6564.61	319	95	-27.6 ± 0.3	
[N II]	6585.28	318	96	-15.5 ± 0.2	
[S II]	6718.29	319	77	-2.3 ± 0.2	
[S II]	6732.67	322	84	-3.1 ± 0.2	

(SB99; Leitherer *et al.* 1999) for the young age of this cluster (see below), most of the light should originate from stars with approximately the same mass. Therefore, if the cluster is mass segregated (with the more massive stars located near the centre) it would show up as only a very shallow gradient in radius with wavelength. They also discuss whether the surrounding H II region could affect the cluster size measurements, and find that the presence of dust may be a contributing factor. However, in order to explain the wavelength dependence, the dust would have to be centrally concentrated. In this scenario, the cluster would get dimmer and smaller with decreasing wavelength due to increased obscuration at shorter wavelengths.

3.1.2 Cluster M82-A1 results

In Figs. 3.2 and 3.3, we show the flux-calibrated spectra of M82-A1 for the G430L and G750M gratings. The major line identifications, heliocentric velocities, FWHMs (for the G750M spectrum only) and equivalent widths are presented in Table 3.2 for both the absorption and emission features. The equivalent widths were measured by defining sections of continuum on either side of each spectral line and the errors represent 1σ

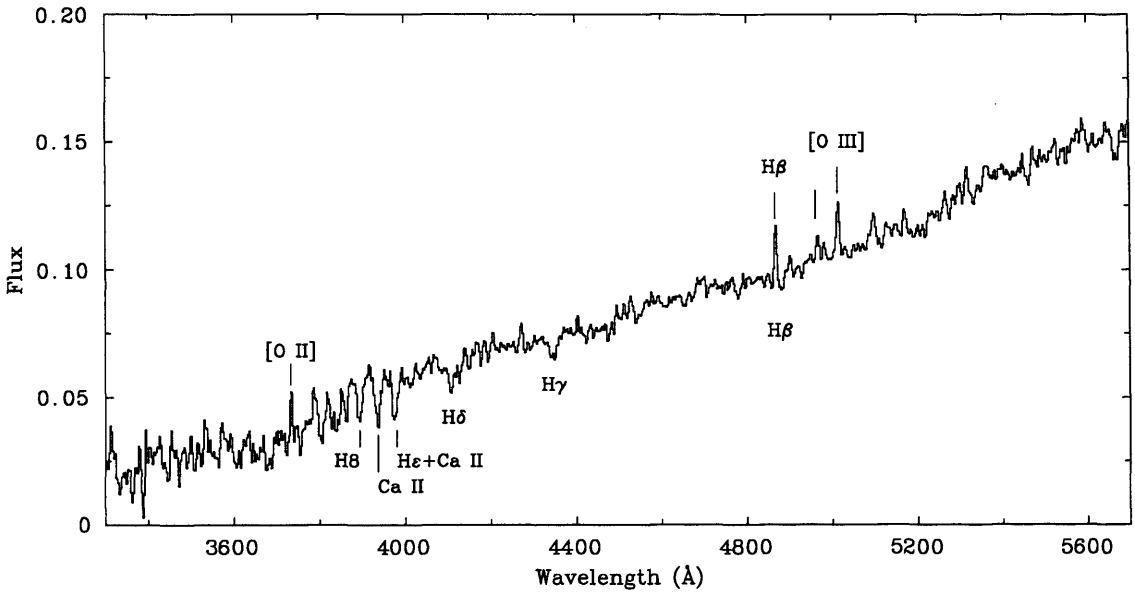

Figure 3.2: G430L spectrum of the cluster M82-A1 and its H II region smoothed by 2 Å. The nebular emission and cluster absorption lines are marked above and below the spectrum respectively. The flux is in units of 10^{-15} erg s^{-1} cm^{-2} Å^{-1}.

uncertainties based on the error in the continuum level.

The G430L spectrum clearly exhibits Balmer absorption lines from the cluster, and a weak Balmer jump at 3650 Å, indicating a young age. Strong interstellar Ca II absorption lines are also present. No stellar absorption lines are detected in the G750M spectrum. The mean heliocentric radial velocity of the cluster as measured from the Balmer absorption lines is 319 ± 22 km s^{-1}. The velocity of the resolved interstellar Ca II K line is $+205$ km s^{-1}, and is very close to the systemic velocity of M82 of $+200$ km s^{-1} (Achtermann & Lacy 1995). This indicates that the cold interstellar gas located near the nucleus of M82 is at rest.

A number of emission lines arising from the compact H II region surrounding M82-A1 are apparent in the STIS spectra. We detect nebular emission lines of Hα, Hβ, Hγ, [O II]$\lambda\lambda$3726, 3729, [O III]$\lambda\lambda$4959, 5007, [N II]$\lambda\lambda$6548, 6583 and [S II]$\lambda\lambda$6717, 6731. The low [S II]/Hα flux ratio of 0.21 is consistent with photoionization rather than shock heating. In Fig. 3.3, the red member of the [S II] doublet is the strongest of the two lines, indicating that the H II region has a high density. We derive the electron density and oxygen abundance below.

The comparatively high resolution of the G750M spectrum allows us to measure accurate velocities and FWHMs for the H II region, as given in Table 3.2. We find a

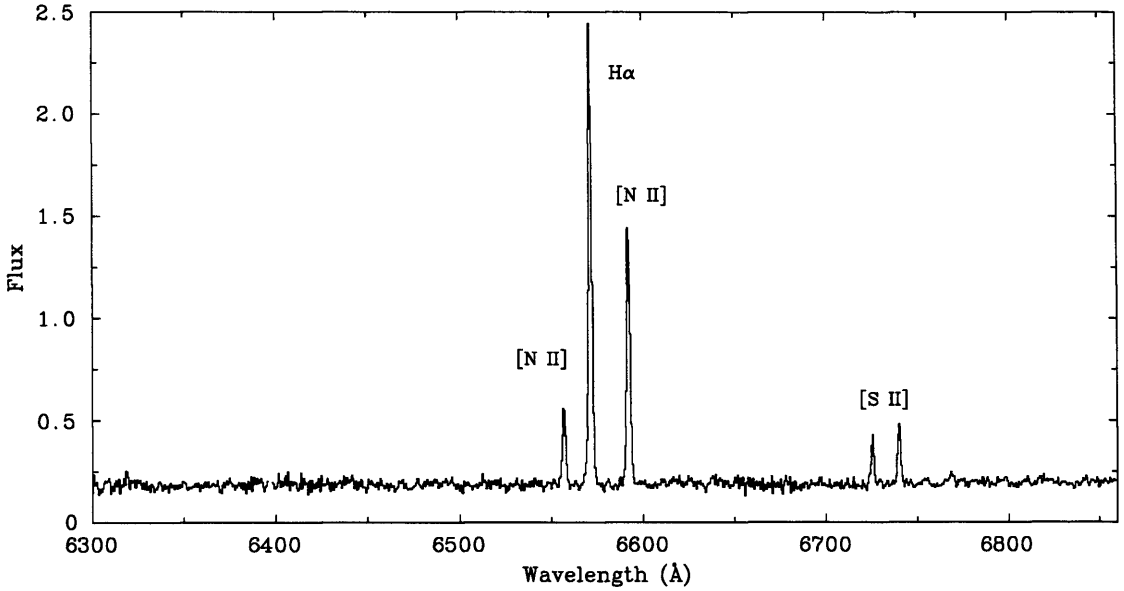

Figure 3.3: STIS G750M spectrum of the cluster M82-A1 and its H II region. The nebular emission lines from the surrounding H II region are marked. The flux is in units of 10^{-15} erg s^{-1} cm^{-2} Å^{-1}.

mean heliocentric velocity for the Hα, [N II] and [S II] nebular lines of 320 ± 2 km s^{-1}, in excellent agreement with the measured value of the cluster radial velocity. The lines have an observed FWHM of 89 ± 8 km s^{-1} and are clearly resolved since the measured resolution is 63 km s^{-1} (1.4 Å; see Section 2.2.1); correcting the observed FWHM for the instrumental contribution gives an intrinsic mean FWHM of 62 ± 11 km s^{-1}. The maximum expansion velocity for the H II region is therefore $\sim$30 km s^{-1}.

Parameters of M82-A1

The starburst core of M82 suffers from a high and non-uniform extinction. For example, Satyapal *et al.* (1995) find values for the visual extinction, A_V, ranging from 2–12 mag from near-IR nebular line ratios, assuming a foreground screen model. As can be seen from Figs. 2.3 and 2.4 (previous chapter), the STIS slit crosses some areas of complete obscuration at optical wavelengths. The cluster M82-A1 sits close to the conspicuous dust lane that bisects the galactic disc; to the east of this cluster (or to negative offsets in Fig. 2.4), we detect little emission due to the very high extinction. The orientation of the slits in relation to the dust lane and its presence in relation to region A and M82-A1 is discussed more fully in Section 3.3 where the data for the whole slit length is analysed.

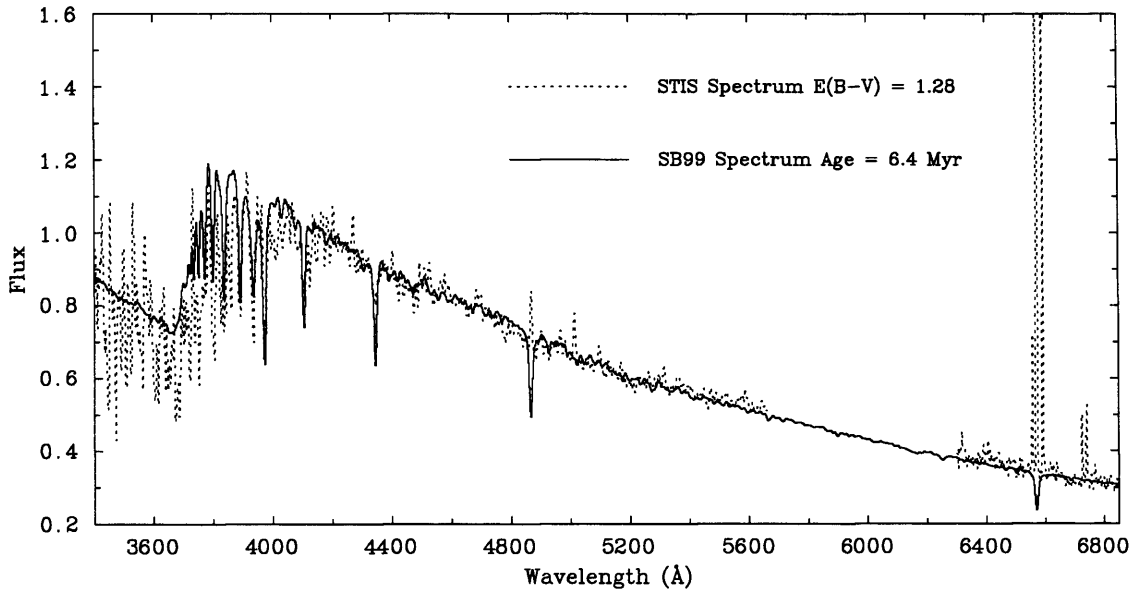

Figure 3.4: Comparison of the de-reddened [$E(B-V) = 1.28$] STIS spectrum of M82-A1 with a synthetic Starburst99 (SB99) spectrum for an age of 6.4 Myr. For this combination of age and reddening, the depth of the Balmer jump and the overall SED are well-fitted. The flux is in units of 10^{-14} erg s^{-1} cm^{-2} Å^{-1}.

Ages and reddening for clusters less than 10 Myr old are usually determined from spectroscopy using the UV wavelength region because here the spectral energy distribution (SED) is largely independent of age, but the easily identifiable stellar wind features are sensitive age indicators (*e.g.* Tremonti *et al.* 2001; Chandar *et al.* 2004). However, given sufficient spectral resolution, the blue optical region (in particular the continuum shape and strong absorption lines in the Balmer jump region between 3500–4100 Å) can provide a comparable handle on age and reddening. For example, Gallagher & Smith (1999) successfully derived the age of cluster M82-F by comparing the observed spectrum in the region of the Balmer jump with theoretical model cluster spectra.

SWG06 use *v*5.0 of SB99 (Leitherer *et al.* 1999; González-Delgado *et al.* 2005) which includes a new synthetic high resolution (0.3 Å) spectral library from 3000–7000 Å containing non-LTE models for OB stars (Martins *et al.* 2005) to fit the combined G430L and G750M spectra. The observed combined spectrum was first dereddened using a foreground dust screen and a Galactic reddening law, then normalised to each generated synthetic spectrum. A weighted χ^2 statistic was used to judge the quality of the fit. A good match was found for a relatively narrow age range of 5–7 Myr and $E(B-V) = 1.5$–1.2 mag,

where instantaneous burst models of solar metallicity, a Kroupa (2001) IMF, lower and upper masses of 0.1 and 100 $M_{\odot}$, and the enhanced mass loss Geneva tracks were used.

In Fig. 3.4 we show the SB99 fit for the best fitting SB99 model, at an age of 6.4 Myr and $E(B-V) = 1.28$ mag. The overall fit to the continuum is good, and it can be seen that the upper members of the Balmer series are also fairly well-fitted (*e.g.* H8 λ3890 which has minimal nebular line contamination). Residual inaccuracies in the model fits and their reasons are discussed in SWG06.

Two independent indicators for reddening and age were employed to determine if they are consistent with those found from the spectral analysis. First, we use the nebular H I emission lines to measure the interstellar extinction by comparing the observed Hα/Hβ and Hγ/Hβ ratios with the intrinsic case B values of Hummer & Storey (1987). The stellar absorption effects were corrected for by directly subtracting the reddened synthetic SB99 spectrum from the observed STIS spectrum using the reddening values determined for the best-fit age range. We find $E(B-V) = 1.38 \pm 0.15$ mag, in good agreement with dereddening the cluster energy distribution. This method of directly subtracting the synthetic spectrum to recover the intrinsic nebular line fluxes has the advantage that we can recover the Hγ emission line and obtain a more accurate measurement for the Hβ line flux. We also compare the observed $(B-V)$ and $(V-I)$ colours of M82-A1 with the predicted colours from SB99 for ages of 6 and 7 Myr and find $E(B-V) = 1.54 \pm 0.26$ mag in reasonable agreement with the above. For the reddening towards M82-A1, we adopt the mean value given by the cluster SED and the nebular lines of $E(B-V) = 1.35 \pm 0.15$ mag.

Our independent age indicator is the strength of the observed equivalent width of the nebular Hα emission (Table 3.2) when compared with the predicted values from SB99. The observed equivalent width of 32 ± 2 Å (corrected for stellar absorption) gives an age of 6.7 Myr. This is an upper limit since it assumes that all the ionizing photons produced by the cluster go into ionizing the surrounding gas and the recombination emission produced is fully accounted for in our observations. If a fraction of the ionizing photons escape then the equivalent width decreases and the age is underestimated. Since this value is consistent with the age determined from the Balmer jump, it suggests that few ionizing photons are escaping from the H II region. We therefore conclude that the age of M82-A1 is 6.4 ± 0.5 Myr.

Using the above values, we can derive the absolute V-band magnitude using the

Table 3.3: Summary of derived parameters for cluster M82-A1 and its H II region.

Parameter	Value
Cluster	
Radial velocity, v_r (km s^{-1})	$+320 \pm 20$
M_{F555W} (mag)	17.23 ± 0.10
Half-light radius, R_{eff} (pc)	3.0 ± 0.5
$E(B-V)$ (mag)	1.35 ± 0.15
M_V (mag)	-14.84 ± 0.38
$\log L_V/L_\odot$	7.87 ± 0.15
Age (Myr)	6.4 ± 0.4
Mass, M ($M_\odot$)	$6.6 \pm^{0.3}_{0.2} \times 10^5$ [a] $1.3 \pm^{0.5}_{0.4} \times 10^6$ [b]
Photon luminosity in Lyman continuum, Q_0 (s^{-1})	$7.5 \pm 3.0 \times 10^{50}$
H II Region	
Half-light radius R_{eff} (pc)	4.5 ± 0.5
Electron density (cm^{-3}), n_e	$1800 \pm^{340}_{280}$
$12 + \log(O/H)$	~ 8.8 [c]
Ionization parameter, $\log \mathscr{U}$	-2.24 ± 0.18

[a] using a Kroupa (2001) IMF
[b] using a Salpeter IMF
[c] solar metallicity is $12 + \log(O/H) \sim 8.66$ (Asplund *et al.* 2004)

distance modulus:

$$m - M = 5\log(D) - 5 + A_V, \tag{3.2}$$

where m is the apparent magnitude, M is the absolute magnitude, D is the distance to the source in parsecs, and A_V is the visual extinction in magnitudes; and the luminosity, L:

$$\log\left(\frac{L}{L_\odot}\right) = 0.4\,(M_{V,\odot} - M_V), \tag{3.3}$$

where $M_{V,\odot}$ is the absolute V-band magnitude of the Sun. We find $M_V = -14.84 \pm 0.38$ and $\log L_V/L_\odot = 7.87 \pm 0.15$. We can then use this information to get an estimate of the cluster mass by comparing our values to the luminosity-to-mass ratio tabulated by SB99 for the derived age of cluster. A mass derived in this way is very dependent on the form of the IMF since it can only be determined by assuming *a priori* a particular mass-to-light ratio. For a Kroupa and Salpeter IMF (and a lower mass limit of 0.1 $M_\odot$), we derive masses of $6.6^{+0.3}_{-0.2} \times 10^5$ and $1.3^{+0.5}_{-0.4} \times 10^6$ $M_\odot$, respectively. The derived parameters of M82-A1 are given in Table 3.3.

Parameters of the M82-A1 H II region

We now turn our attention to the properties of the H II region that surrounds the cluster M82-A1. We have already established that it is compact with a half-light radius of 4.5 ± 0.5 pc (Section 3.1.1). From Gaussian fits to the [S II] emission line profiles, we derive an electron density $n_e = 1800^{+340}_{-280}$ cm^{-3}, assuming a standard electron temperature value of $T_e = 10^4$ K. This can be converted into a pressure by assuming the ideal gas law

$$P = nk_BT \quad \text{cm}^{-3}\,\text{K}, \tag{3.4}$$

where for a fully ionized nebula, the density, n, can be approximated by n_e, and the temperature to T_e; k_B is the Boltzmann constant. The H II region surrounding M82-A1 can therefore be classified as a high pressure ($P/k = 2 \times 10^7$ cm^{-3} K), compact H II region. We are also able to derive n_e for the diffuse gas along the STIS slit in region A and find a mean value of ~1200 cm^{-3}, suggesting that the ionized gas in region A is also at high pressure. O'Connell & Mangano (1978) derived a similar value of n_e = 1800 cm^{-3} for regions A and C from the [S II] ratio. For a more detailed discussion of the properties of the gas surrounding M82-A1 and in the rest of the M82 starburst core, see Section 3.3.

Our n_e measurements are far higher than those of Förster Schreiber *et al.* (2001) who measured n_e in the starburst core using observations obtained with the Short Wavelength Spectrograph (SWS) onboard the *Infrared Space Observatory* (*ISO*). The SWS aperture covers an area of 14 × 20 arcsecs and they find that the line ratios of the fine structure lines of [S III], [Ne III] and [Ar III] all lie at the low density limit; they adopt n_e = 300 cm^{-3}. This large difference in density between the STIS and *ISO* measurements may be due to sampling different environments, since the IR observations probe deeper into the starburst, and possibly into a region where the gas is less compressed.

In SWG06 we obtained approximate oxygen abundances for the H II region using empirical techniques that rely on the relative strengths of strong optical emission lines. These techniques are calibrated by observations that include temperature sensitive line ratios so that they may be used in cases where temperature sensitive lines are not observed, such as here. Two methods developed recently by independent groups were used: Kewley & Dopita (2002) give the [N II]/[O II] ratio calibration and Pettini & Pagel (2004) use the ratios of [N II]λ6583/Hα ($N2$) and [O III]λ5007/Hβ to [N II]λ6583/Hα ($O3N2$) to derive abundance. The latter method is advantageous as it is insensitive to reddening. The average oxygen abundance was found to be between 1.2–2 solar, but with uncertainties

consistent with solar values. We also compared their derived oxygen abundances with Förster Schreiber *et al.* (2001), who measure slightly super-solar abundances for Ne, Ar and 0.25 solar abundance for S, and with Origlia *et al.* (2004) who measure red supergiant stars in the nuclear region of M82 and find evidence for a solar oxygen abundance.

The ionized mass of the H II region was derived from the observed total Hα flux listed in Table 3.1. Using the adopted value for $E(B-V)$, a distance of 3.6 Mpc, $T_e = 10^4$ K, and $n_e = 1800$ cm^{-3}, we find an ionized mass of >5000 M$_\odot$ using the standard equation from Pottasch (1980):

$$M = 11.06 \frac{F_{H\beta} D^2 T_4^{0.85}}{n_e}, \tag{3.5}$$

where M is the mass in units of $M_\odot$, $F_{H\beta}$ is the dereddened Hβ flux, D is the distance in kpc and T_4 is the temperature in units of 10^4 K. This value is a lower limit because the close agreement between the ages derived from the cluster spectrum and the equivalent width of nebular Hα strongly suggests that the H II region is radiation-bounded (*i.e.* there may be more mass outside the ionized envelope that cannot be detected).

3.2 Discussion

The combination of high spatial resolution *HST* optical spectra and images have allowed us to derive numerous parameters for the young massive cluster M82-A1 and its H II region in the starburst core of M82.

3.2.1 M82-A1 and the evolution of the M82 starburst

The age and location of the M82-A1 can now be discussed in terms of the star-formation history of the central burst. In SWG06 we put forward the argument that M82-A1 is spatially and kinematically associated with the ionized gas in the starburst core. Also, we point out that the epoch of the cluster's birth is consistent with recent star-formation history determined by Förster Schreiber *et al.* (2003). These authors conclude that M82 has undergone two short bursts of star-formation in the recent past occurring at 8–15 and 4–6 Myr ago, meaning that A1 falls into the second event. SWG06 also comment that since region A has a high surface density of young clusters (Melo *et al.* 2005), and that the bright base of the superwind appears to be centred on regions A (and C; see Chapter 4), this

indicates that the star clusters within this clump must be of similar age and all correspond to an intense star-formation burst ~6 Myr ago.

Förster Schreiber *et al.* (2001) use ground- and space-based IR observations of the M82 starburst to measure the ionization parameter throughout the central regions as given by

$$\mathscr{U} = \frac{Q_0}{4\pi\, R^2\, n_e\, c}, \tag{3.6}$$

where Q_0 represents the photon luminosity in the Lyman continuum, R is the nebula radius. They find $\log \mathscr{U} \approx -2.3$ for scales ranging from a few tens to 500 pc. This uniformity suggests that a similar star-formation efficiency and evolutionary stage exists in the starburst regions. Using our measurements of M82-A1 and its surrounding gas, we find $\log \mathscr{U} = -2.24 \pm 0.18$ which is in excellent agreement with Förster Schreiber *et al.* (2001), and extends the uniformity down to scales of only a few parsecs. SWG06 conclude from this that the starburst is self-adjusting in the sence that the number of ionizing photons per atom is constant from scales of a few parsecs up to ~500 pc.

3.2.2 The M82-A1 H II region

SWG06 discuss in depth the compact H II region associated with M82-A1 in context with recent studies such as Förster Schreiber *et al.* (2001). Here we will summarise the main points only. The H II region is clearly compact and measurements of the density and turbulence (from the velocity dispersion) of the gas immediately surrounding M82-A1 indicate that is immersed in an unusually high-pressure environment (see also Sections 3.3.3 and 3.4.3). They find for the H II region $P/k = 1\text{–}2 \times 10^7$ cm^{-3} K, and for the surrounding gas $P_{\rm turb}/k = 3 \times 10^8$ cm^{-3} K. Furthermore, measurements of the size of radio SNR in the core of M82 (Muxlow *et al.* 1994; Pedlar *et al.* 1999) show that they are unusually compact, meaning that, together with our H II region measurements, this suggests that the densities and pressures are the dominant drivers of the H II region evolution and that pressure in the starburst core is a major factor influencing the starburst evolution.

An attempt to model the evolution of the H II region is given in SWG06 assuming the standard formula for pressure-driven bubbles from Weaver *et al.* (1977):

$$R = \left(\frac{125}{154\pi}\right)^{1/5} \left(\frac{L_{\rm mech}}{\rho_0}\right)^{1/5} t^{3/5}, \tag{3.7}$$

where R is the shell radius, $L_{\rm mech}$ is the cluster-wind mechanical luminosity, ρ_0 is the ambient mass density, and t is the age. Using the derived values of cluster age (6.4 Myr),

gas density (1000 cm^{-3}) and a cluster mechanical luminosity estimated from SB99 ($L_{mech} \approx 2.5 \times 10^{40}$ erg s^{-1}), they find that the projected radius of the H II region should be ~100–150 pc. This is clearly in excess of the 4.5 pc measured. They then consider the evolution of the H II region in a high ambient interstellar pressure. The growth of the bubble stalls when the internal pressure equals the ambient pressure. The internal pressure, P, is also given by Weaver *et al.* (1977):

$$P = \frac{7}{(3850\pi)^{2/5}} \left(\frac{125}{154\pi}\right)^{4/15} \left(\frac{L_{mech}}{\rho_0}\right)^{2/3} \frac{\rho_0}{R^{4/3}}. \tag{3.8}$$

Using our derived values, this gives an internal pressure P/k of ~6–13 $\times$ 10^9 cm^{-3} K, which is roughly equivalent to our estimate of the ambient interstellar pressure. While this is only a rough comparison, it illustrates that a high ambient pressure is sufficient to explain the non-standard evolution of M82-A1's H II region, and possibly the uniformity of the ionization parameter over such a large scale range.

In SWG06, we extend our discussion to the evolution of the cluster wind and the implications on the formation of the galactic wind. We comment that it is hard to understand how the observed galaxy-wide superwind is generated if the environment around M82-A1 is typical of the central starburst core, and is such that is stifles the development of individual cluster winds. The only conclusion we could make is that A1 and its immediate environment are *not* typical of the wind-producing regions in the starburst core.

3.3 The interstellar environment in the nucleus of M82

Now we have explored the properties of one bright SSC in the core of the M82 starburst, we can divert our attention to the broader environment, and how different regions relate to each other in the nuclear starburst. We aim to address questions such as: what is the typical environment in a powerful starburst, and is M82-A1 and its H II region representative of the whole starburst? What implications does the finding of a high-density H II region around M82-A1 have for other such clusters, the flow of their winds, and production of the galaxy-wide superwind?

The data on which this section is based was introduced in Section 2.2.1 of the previous chapter. Here we make use of both slits crossing the central regions of M82 (see Fig. 3.5), and discuss the results derived.

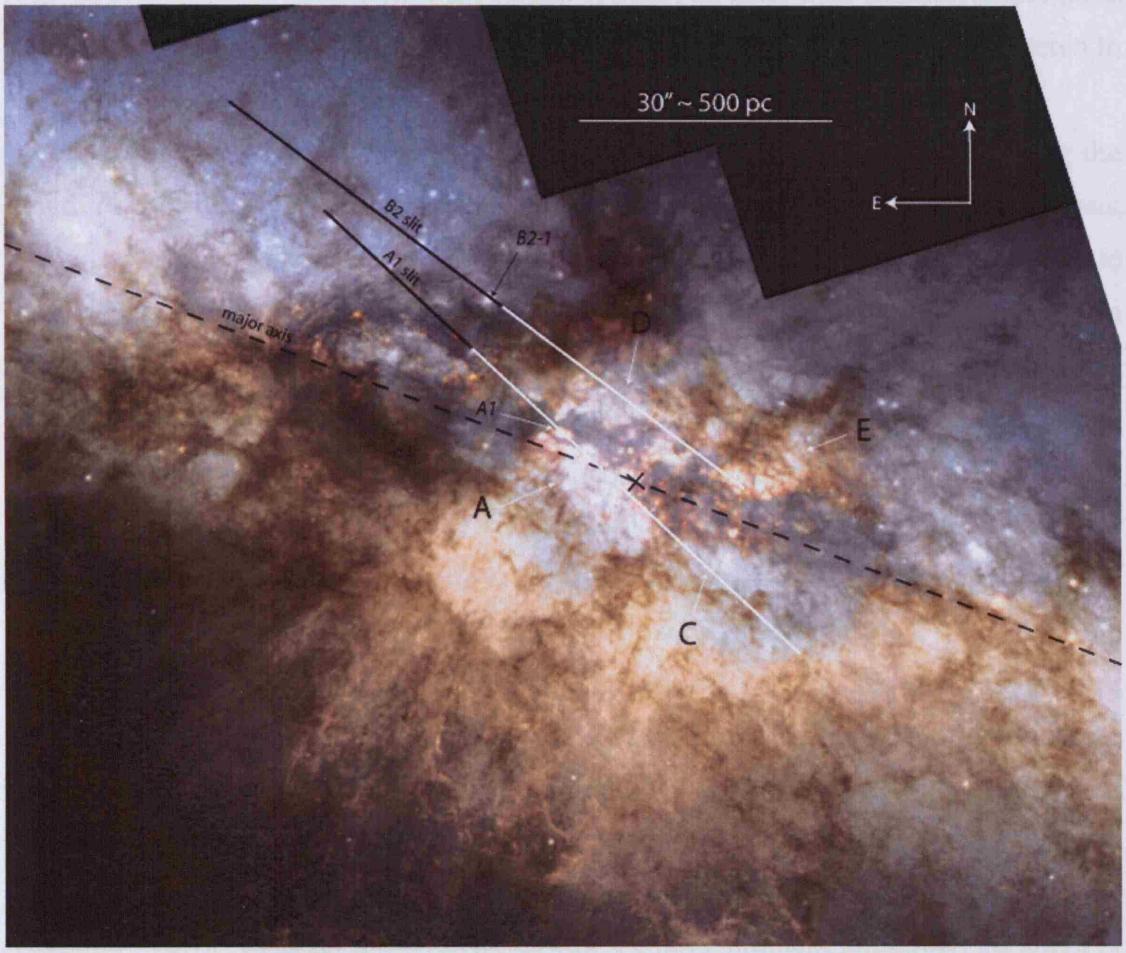

Figure 3.5: *HST*/WFPC2 broad-band colour composite (F814W: red, F555W: green, F439W: blue) of M82 (courtesy: NASA/ESA, R. de Grijs) with the two STIS slits and some of the more prominent cluster-complexes (A, C, D and E) marked; adapted from Fig. 2.3 (Chapter 2). Portions of the 2D slit images corresponding to the white shaded parts of the slits are shown in Fig. 3.6, Section 3.3.1. The cross marks the position of the 2.2 μm nucleus, and the long dashed line represents the galaxy major-axis. This broad-band composite highlights both the stellar continuum emission and the prominent dust absorption lanes across the starburst.

3.3.1 Description of the two-dimentional spectra

Fig. 3.6 shows the Hα and [N II] spectral region of the G750M 2-dimentional (2D) spectral images from slits A1 and B2. Both 2D slit images are able to share the same x-axis (which is given in arcseconds offset from the position of M82-A1) since their position angles (PAs) are sufficiently similar (Fig. 3.5). The spatial extent of the slit images is also restricted to show only the nuclear regions where emission is actually detected.

Fig. 3.6 clearly shows how the emission line profiles vary continuously along the length of the slit. It would be ideal to track these variations on a pixel-to-pixel basis, but in order to make accurate measurements of the gas conditions, the spectra need to have a sufficiently high signal-to-noise (S/N) ratio. We therefore summed the spectra using multiple-pixel apertures. To measure the kinematics of the gas, observations of a strong emission line (*e.g.* Hα) are all that is required, but to derive gas properties requiring information from additional, fainter lines, a higher S/N was needed. To satisfy these two criteria, we extracted two sets of spectra from each of the 2D images: a high S/N set for each slit was made by stepping along in 20 pixel intervals ($\equiv$1.″0), extracting apertures of width equal to this interval (hereafter referred to as set A20), and resulted in spectra from slit A1 with an average S/N of 10 in Hβ (G430L grating) and 20 in Hα (G750M grating; measured by dividing the line flux by the line flux error as measured by DIPSO ELF fits to the lines). In order to maximise spatial-resolution for the kinematics measurements whilst maintaining sufficient S/N for accurate line fitting, we decreased the extraction widths to 10 pixels ($\equiv$0.″5) separated by intervals of 10 pixels to create the second data-sets (hereafter referred to as set A10). No background subtraction was attempted for either of the slit A1 or B2 data-sets due to the bright and variable nature of the diffuse emission in the starburst core.

Fig. 3.7 shows four representative spectra from regions A, C, D and E illustrating the variation between these clumps. The position along the slit that each spectrum was extracted from is marked by numbered arrows on Fig. 3.6, referring to the spectrum number shown in each plot title.

3.3.2 Line profile fitting

The S/N and spectral resolution of the 10 pixel wide spectra are high enough to resolve multiple Gaussian components in Hα in many regions along the slit. In general, a bright,

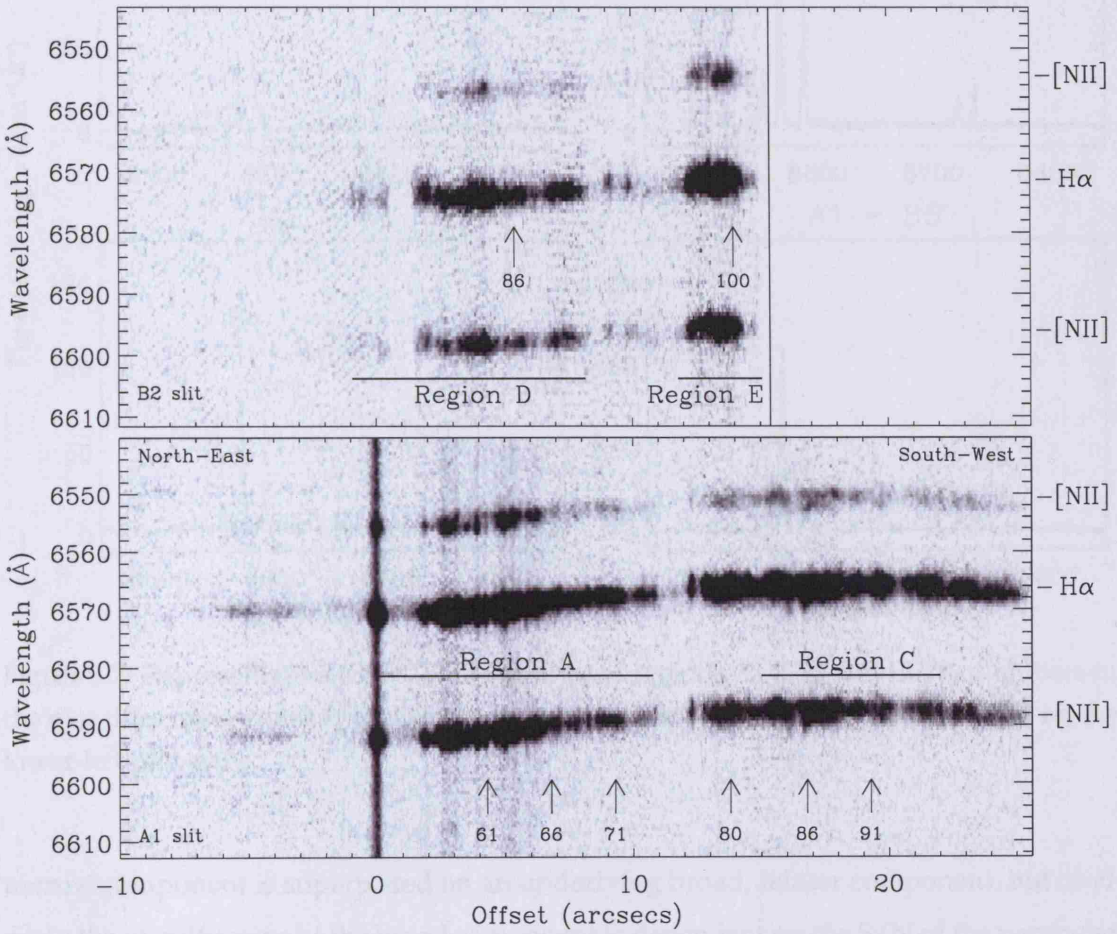

Figure 3.6: STIS G750M 2D spectral images showing the Hα and [N II] emission lines over the portion of the slits covering the nuclear regions (equivalent to the white shaded parts of the slits shown in Fig. 2.3). The lower plot shows the image from the A1 slit, and the upper plot shows the B2 slit. In both cases, the x-scale is in arcseconds offset from M82-A1 and the brightness scale is in units of 10^{-16} erg cm^{-2} s^{-1} Å^{-1} arcsec^{-2}. The emission lines are identified, and the slit orientation is marked. On the lower plot, arrows show the position of the spectra shown in Fig. 3.7 and the Hα profiles shown in Fig. 3.8 (numbers correspond to the plot titles).

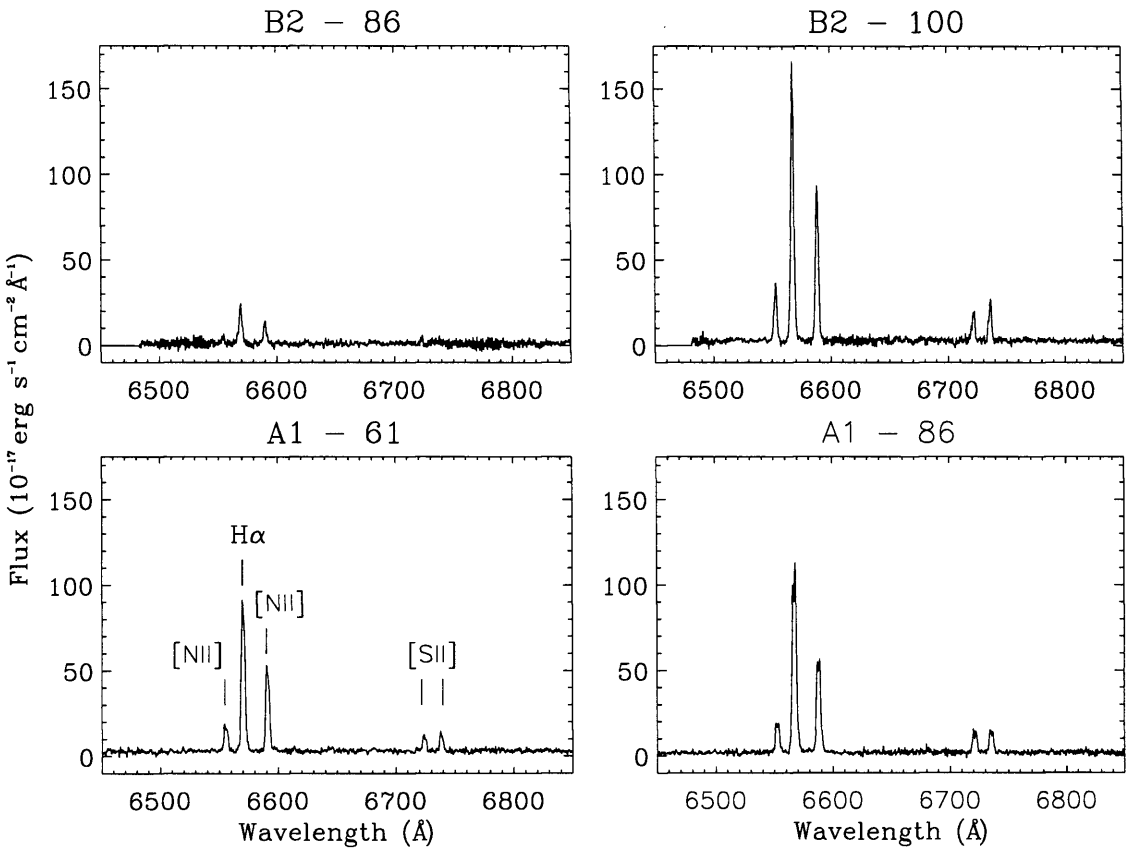

Figure 3.7: Representative STIS G750M spectra of regions A, C, D and E. The numbers in the plot titles correspond to the arrows in Fig. 3.6. The emission lines are identified on the lower-left plot only.

narrow component is superposed on an underlying broad, fainter component, but obviously the identification of the broad component is dependent on the S/N of the particular spectrum. The component profiles are best approximated by a Gaussian function since the line broadening mechanism is dominated by Doppler effects caused by the gas temperature or turbulent state. In the optical, natural broadening is of the order ~few m s^{-1}, and collisional (pressure) broadening is assumed to be negligible due to the very low gas densities.

Examples of Hα line profiles from different parts of regions A, C, D and E are shown in Fig. 3.8 together with the Gaussian profiles needed to model the integrated shapes (see below). Again, the position along the slit that each Hα profile has been extracted from is marked by numbered arrows on Fig. 3.6. These were chosen to represent a range in the variety of line shapes seen: bright, narrow emission lines with underlying broad components; double-peaked lines with no detectable underlying broad emission; and

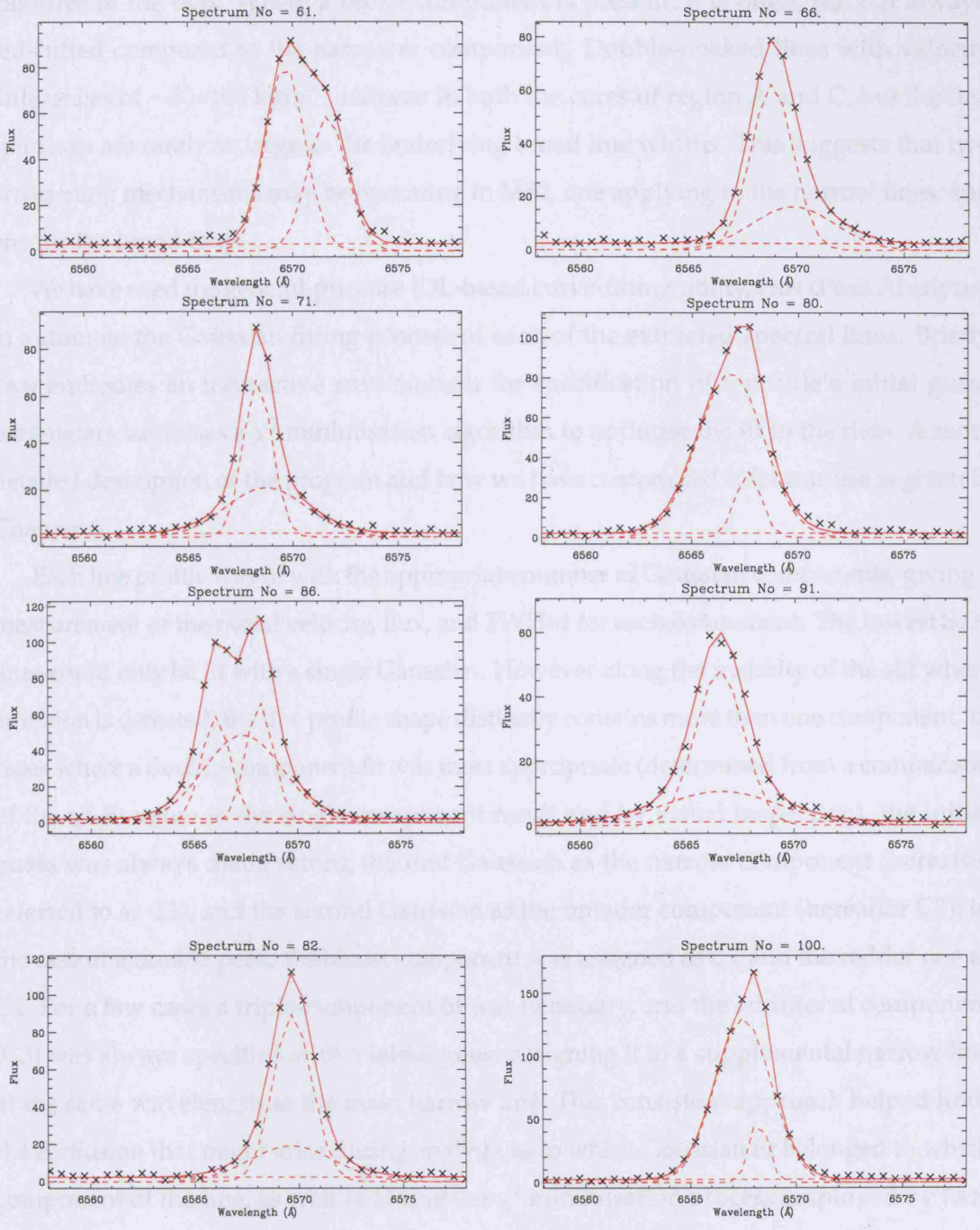

Figure 3.8: Example Hα line profiles for slit A1 (upper six) and slit B2 (lower two): arrows on Fig. 3.6 indicate where the spectra are located along the slits (numbers correspond to plot titles). This sample was chosen to represent a range in line profile shapes including broad, underlying features and second narrow peaks. The observed data are plotted with un-joined crosses; the flat continuum and individual Gaussian profiles are plotted as dashed red lines with y-offsets relative to the zero level, and the summed model profile is plotted with a solid red line. The flux is in units of 10^{-17} erg s^{-1} cm^{-2} Å^{-1}.

mixtures of the two. Where a broad component is present, it is often, but not always, redshifted compared to the narrower component. Double-peaked lines with velocity differences of ~50–100 km s^{-1} are seen in both the cores of region A and C, but the line splittings are rarely as large as the underlying broad line widths. This suggests that two broadening mechanisms may be operating in M82, one applying to the narrow lines, and one for the broad lines.

We have used the general-purpose IDL-based curve-fitting utility, PAN (Peak ANalysis), to automate the Gaussian fitting process of each of the extracted spectral lines. Briefly, PAN embodies an interactive environment for specification of a profile's initial guess parameters, and uses a χ^2 minimisation algorithm to optimise the fit to the data. A more detailed description of the program and how we have customised it for our use is given in Chapter 6.

Each line profile was fit with the appropriate number of Gaussian components, giving a measurement of the radial velocity, flux, and FWHM for each component. The lowest S/N lines could only be fit with a single Gaussian. However along the majority of the slit where emission is detected, the line profile shape distinctly contains more than one component. In cases where a double-component fit was most appropriate (determined from a comparison of the χ^2 fit value to the single component result and by visual inspection), the initial guess was always made setting the first Gaussian as the narrow component (hereafter referred to as C1), and the second Gaussian as the broader component (hereafter C2); in the case of a double peak, the bluest component was assigned as C1 and the redder one as C2. For a few cases a triple-component fit was necessary, and the additional component (C3) was always specified with a initial guess assigning it to a supplemental narrow line at the same wavelength as the main narrow line. This consistent approach helped limit the confusion that might arise during analysis as to which Gaussian fit belonged to which component of the line, as well as aiding the χ^2 minimisation process employed by PAN. This assignment convention means that wherever an underlying broad component exists, we always refer to it as C2.

3.3.3 Results

There have been a number of previous studies aimed at measuring the characteristics of the gaseous component in the disc and wind of M82 (*e.g.* Götz *et al.* 1990; Heckman *et al.* 1990; McKeith *et al.* 1993, 1995; Shopbell & Bland-Hawthorn 1998). From these studies,

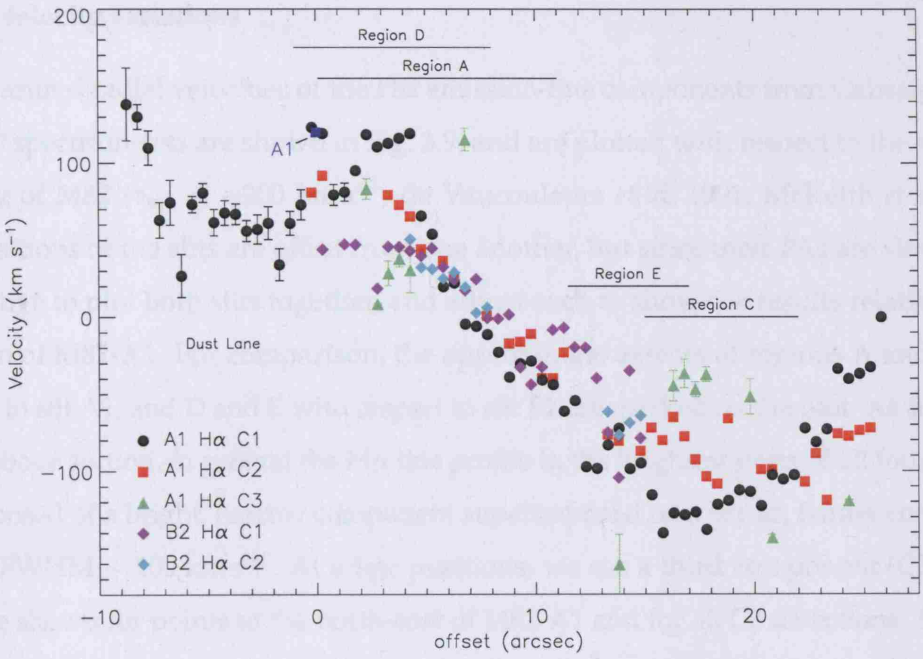

Figure 3.9: Heliocentric Hα radial velocities measured from the A10 spectrum sets, in units of km s^{-1} with respect to the systemic velocity of M82 ($v_{\rm sys} = +200$ km s^{-1}); error bars are not shown because they are approximately the same size as the symbols used. The x-axis scale corresponding to both slits is measured in arcseconds offset from the position of M82-A1. The projected distance along the slit to the nucleus is $\sim 5''$. The approximate extent of regions A and C that coincide with slit A1, and regions D and E that coincide with slit B2 are marked. C1 refers to the bright, narrow component, C2 to the broad component, and C3 to the longer wavelength component when the line is resolved into two narrow components.

it is apparent that the wind outflow, as defined by two well-separated ($\sim$300 km s^{-1}) velocity components, is observed at distances greater than 1 kpc from the nucleus along the minor axis (see also Chapter 4). The disc of M82 is inclined at an angle of 81.5° (Lynds & Sandage 1963) such that the near side of the disc is projected on to the north-west side of the nucleus and the nuclear regions, including clumps A, C, D and E, are observed from underneath through the southern side (although this has been disputed in the past; Wills *et al.* 2000). We therefore directly view the roots of the wind near regions A and C. The two STIS slits are inside the 300 pc wind injection zone (Shopbell & Bland-Hawthorn 1998) where disc material is being entrained into the flow, and likely sample much of the inter-cluster material within the main starburst clumps.

Radial velocity variations

The measured radial velocities of the Hα emission-line components from Gaussian fits to the A10 spectrum-sets are shown in Fig. 3.9, and are plotted with respect to the systemic velocity of M82 ($v_{\rm sys}$ = +200 km s^{-1}; de Vaucouleurs *et al.* 1991; McKeith *et al.* 1993). The positions of the slits are offset from one another, but since their PAs are similar it is instructive to plot both slits together, and adjust each to show the results relative to the position of M82-A1. For comparison, the approximate extents of regions A and C with respect to slit A1, and D and E with respect to slit B2 are marked on the plot. As described in the above section, in general the Hα line profile in the brightest parts of all four regions is composed of a bright, narrow component superimposed on a broad, fainter component with a FWHM $\sim$ 100 km s^{-1}. At a few positions, we see a third component (C3). Error bars are shown for points to the north-east of M82-A1 and for all C3 detections. For most of the other points, the error bars are smaller than the size of the plotting symbol.

The brightest component, C1, is expected to trace the velocity of the densest (*i.e.* bulk of the) ionized gas in M82. From Fig. 3.9, the slit A1 velocity curve for C1 reaches a maximum velocity of $\approx$+100 km s^{-1} at an offset of $\sim$+2″, flattens out between −2″ to −7″ coincident with the conspicuous dust-lane bisecting the galaxy disc (see Fig. 2.3; also O'Connell *et al.* 1995), then begins to rise again beyond −7″. The velocity of M82-A1 (Section 3.1.2), together with two points either side of it, are redshifted by $\sim$40 km s^{-1} from the general trend. On the opposite side, the rotation curve shown by C1 reaches a maximum blueshifted velocity of $\approx$−130 km s^{-1} then begins to decrease again beyond +20″. At these offsets, however, the A2 slit is farthest from the major-axis and begins to sample the inner regions of the wind – we return to this point below. We measure a C1 Hα velocity gradient for the region nearest to the nucleus of 12 km s^{-1} arcsec^{-1}, in excellent agreement with the measurements of McKeith *et al.* (1993) and Shopbell & Bland-Hawthorn (1998) of 11 km s^{-1} arcsec^{-1}. The radial velocities of the C1 gas in slit B2 follow the same velocity trend as the gas sampled along slit A1, but with a shallower gradient of 7 km s^{-1} arcsec^{-1}. We discuss what these measurements tell us about the rotation curve in Section 3.4.2.

The broad underlying component, C2, largely follows the C1 velocity curve although there are some deviations. In the core of region C, C2 is redshifted by up to 60 km s^{-1} compared to C1. Here we detect a third component (C3), which is redshifted by a further

30–40 km s^{-1}, and may represent the front side of an expanding structure and possibly the roots of the wind flow. Further along the slit, to the south-west of region C, C2 becomes blueshifted by ~40 km s^{-1}, and there are two detections of a 40–80 km s^{-1} blueshifted third component. Again, these could be signatures of expanding structures and/or ordered flows. An unusual situation occurs at ~+4″ offset (right in the core of region A), where C1 is redshifted compared to its expected velocity, and it is C2 that instead conforms to the trend. Here we also detect a third component, blueshifted by ~80 km s^{-1} compared to C1, which might explain the unexpected velocities if they are both two halves of an expanding shell where the faintest component is the nearest (implying an expansion velocity of $v_{\rm exp} \approx 40$ km s^{-1}). This position is coincident with the western edge of shell 2, identified by Wills *et al.* (2002) from H I absorption measurements. They measure an expansion velocity $v_{\rm exp} = 34$ km s^{-1} for this shell, in very good agreement with what we find in Hα. In slit B2, we can only detect C2 in the brightest parts of regions D and E, and find that their velocities are similar in all cases to that of C1, except for in the core of region E where there is evidence of a 20–40 km s^{-1} offset.

FWHM variations

Fig. 3.10 shows the FWHM of the individual Hα line components for both slits, corrected for instrumental broadening (1.4 Å; Section 2.2.1, but not thermal broadening). The large scatter in FWHM values across the two slits can be partly explained by a contribution from multiple unresolved kinematic components. We have attempted to show this by highlighting profiles in both slits that only required a single Gaussian to fit with circled symbols: the FWHMs of circled points are on average broader than the narrow component (C1) of a multiple-Gaussian fit. This is particularly obvious in the −9″ to 0″ region of slit A1 where a second component cannot be fit at all due to the low S/N of the extracted spectra. It is very unlikely that these differences in width reflect real changes, so we conclude that multiple components are present everywhere, but the S/N is not sufficient in all cases to permit a more accurate fit to be made. This argument is strengthened by the observation that in every spectrum extracted from either slit where the Hα line has a high enough S/N, we see evidence of a C2- or C3-type component.

To measure the following averages, we ignore all single-Gaussian-only fits, as these are assumed to be biassed by unresolved components. For slit A1, we find an average FWHM of ~60 ± 40 km s^{-1} for C1 (whereas the average width of single-Gaussian-only

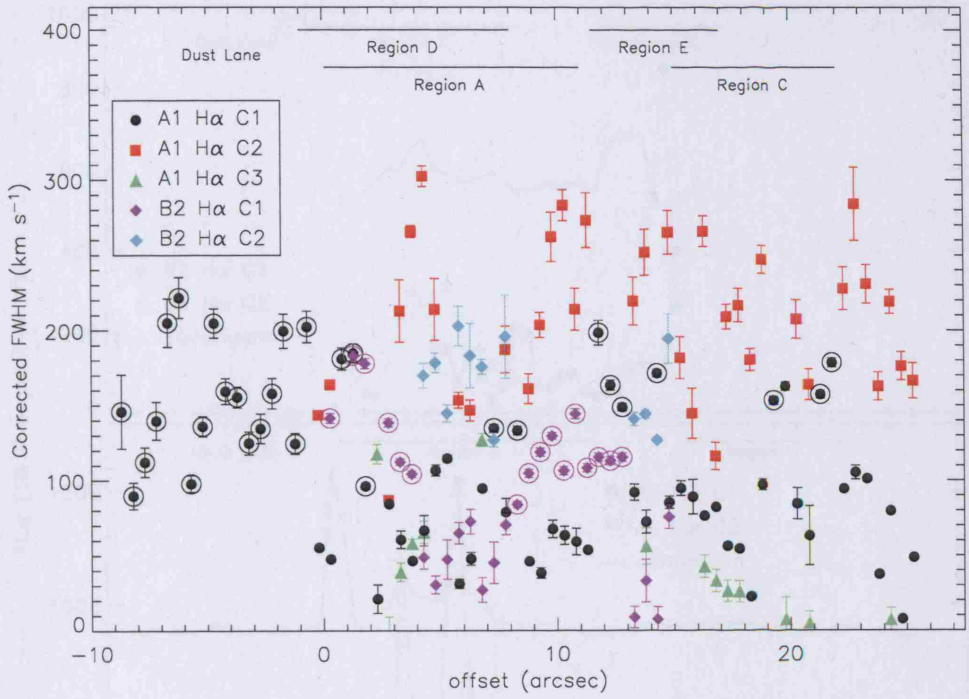

Figure 3.10: Hα FWHMs measured from the A10 spectrum sets. The units are in km s^{-1} corrected for instrumental broadening, and the x-axis scale is measured in arcseconds offset from the position of M82-A1. Circled points are those where no more than one component was required to fit to the line.

fits is $\sim$160 $\pm$ 40 km s^{-1}). For C2, we find an average FWHM of $\sim$210 $\pm$ 60 km s^{-1}, but in a few cases the width of C2 approaches 300 km s^{-1}. Where detected, the mean FWHM of C3 is $\sim$50 km s^{-1}, which is consistent with the mean line width of C1. In general, the FWHM of the gas in slit B2 is narrower: in region D the width of C1 is as low as 20–30 km s^{-1}, with a corresponding C2 FWHM of 150–200 km s^{-1}. In parts of region D and the area between regions D and E, only one component can be fit (shown by circled symbols), with a width of $\sim$100–140 km s^{-1}. The line widths in region E are similar to region D, and in both regions C2 is never $>$200 km s^{-1}.

Flux variations

Fig. 3.11 shows the distribution of the integrated Hα line-flux in C1 and C2 along the section of the slits highlighted in white in Fig. 2.3. Also plotted are the continuum flux levels (measured in the range 6620–6700 Å) for each slit, multiplied and offset for ease of comparison (factors are listed in the figure caption). The relative continuum flux levels

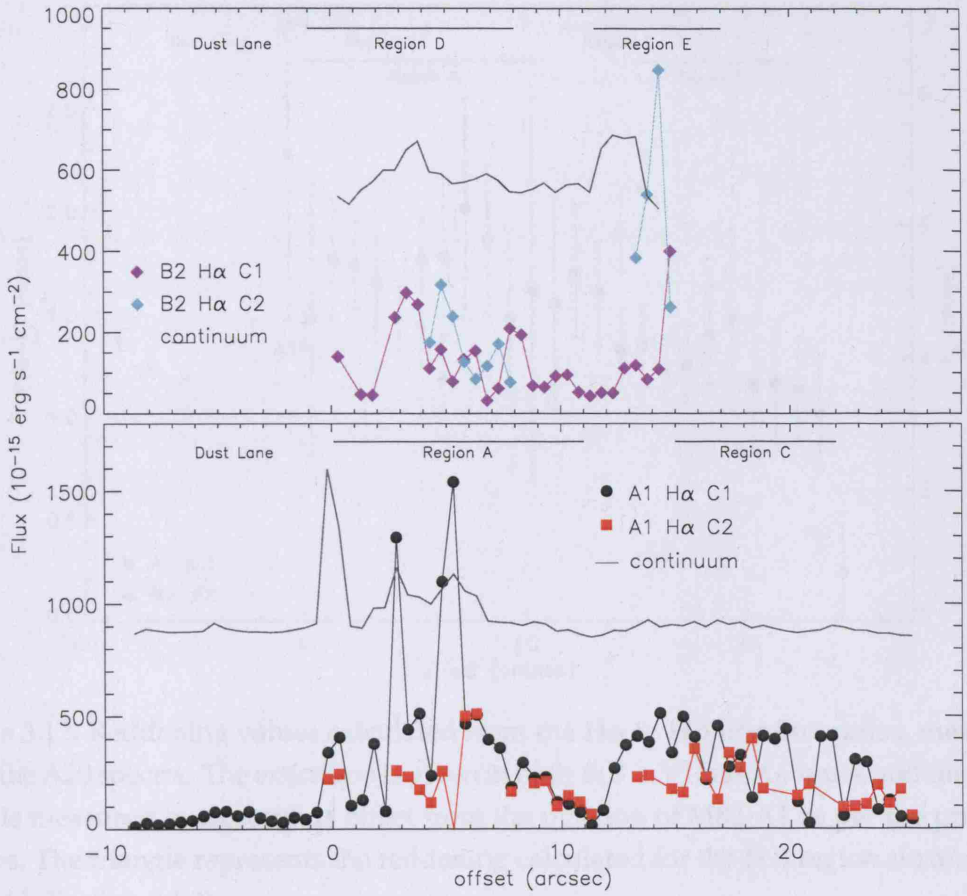

Figure 3.11: Hα flux for C1 and C2 measured from the A10 spectrum sets for slit A1 (lower) and B2 (upper). The solid lines show the continuum level (in 10^{-15} erg^{-1} s^{-1} cm^{-2}, multiplied by 30 and offset by 800 for slit A1 and by 500 for slit B2) measured in the range 6620–6670 Å.

are consistent with the *HST* F814W image, and clearly show the bright clumps (A, C, D and E). These regions can also be seen in both the flux levels of C1 and C2. In region A, the two peaks in C1 correspond well to peaks in the continuum brightness, but at the location of M82-A1 (offset = 0″), the Hα intensity does not peak so strongly. This could be due to a spatial sampling effect if the continuum and Hα intensities are offset by less than one spatial resolution element, but if the levels shown are correct, it would suggest that the ionizing flux emerging from the core of region A is higher than at M82-A1, possibly indicating that the age of region A is even younger than that of M82-A1 (6.4 Myr; Section 3.1.2).

The flux in C2 relative to C1 indicates the importance of the C2 emitting gas. C2 is less than or equal to half the intensity of C1 in the north-eastern half of region A and most

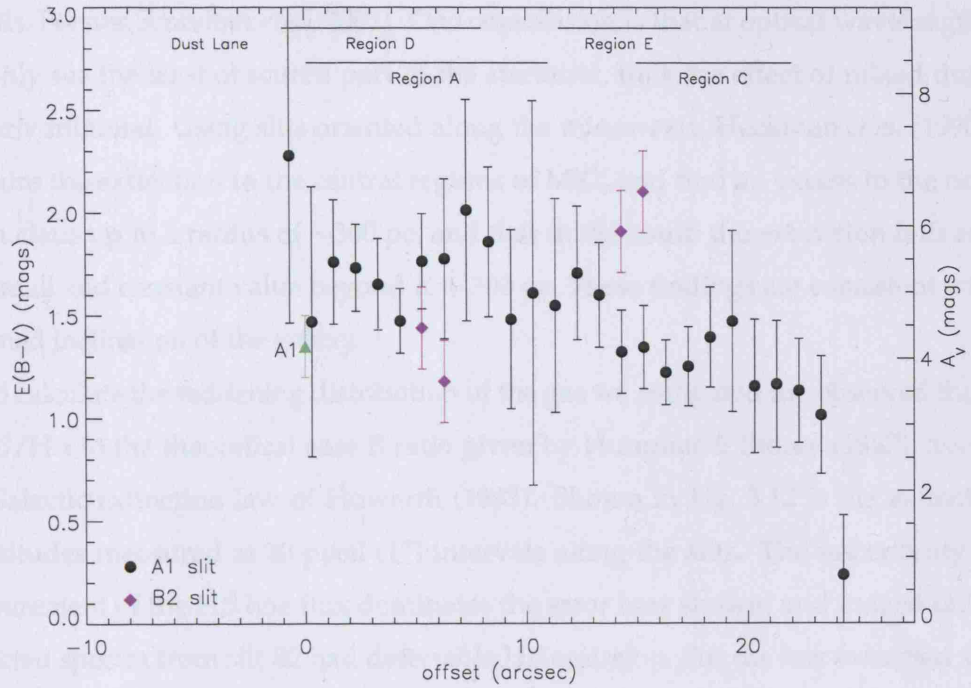

Figure 3.12: Reddening values calculated from the Hα to Hβ line flux ratios, measured from the A20 spectra. The extinction is given in both $E(B-V)$ and A_V units, and the x-axis scale is measured in arcseconds offset from the position of M82-A1 as per the previous figures. The triangle represents the reddening calculated for the H II region surrounding M82-A1 (Section 3.1.2).

of region C. C2 has an equal intensity to C1 in the south-western half of region A and in region D (but here the peak is spatially offset by 2″). In region E, C2 peaks at twice the brightness of C1 (but again is spatially offset by ∼2″). A close examination of the line profiles at this position show that C2 has likely been misidentified, and should really be assigned to C3. However, the flux peaks are real, and are definitely offset from the continuum peak.

Interstellar extinction

The starburst core of M82 suffers from a high and non-uniform extinction. For example, several studies have found values for the visual extinction, A_V, of 2–12 mags from near-IR nebular line ratios (assuming a foreground screen model; Satyapal *et al.* 1995; Förster Schreiber *et al.* 2001). In this analysis we adopt a foreground screen model for simplicity, although we realise that this is likely to be unrealistic considering the level of dust present in the M82 disc (values of $A_V \approx 20$–40 mags have been derived using mixed gas and dust

models; Förster Schreiber *et al.* 2001). One consolation is that at optical wavelengths, we can only see the least obscured part of the starburst, thus the effect of mixed dust will be fairly minimal. Using slits oriented along the minor-axis, Heckman *et al.* (1990) also measure the extinction in the central regions of M82, and find an excess to the north of the nucleus up to a radius of ~300 pc, and that in the south the extinction falls rapidly to a small and constant value beyond $R \approx 300$ pc. These findings are consistent with the assumed inclination of the galaxy.

To calculate the reddening distribution of the gas we compared the observed flux ratio of Hβ/Hα to the theoretical case B ratio given by Hummer & Storey (1987), assuming the Galactic extinction law of Howarth (1983). Shown in Fig. 3.12 is the extinction in magnitudes measured at 20 pixel (1″) intervals along the slits. The uncertainty in the measurement of the Hβ line flux dominates the error bars shown, and indeed only four extracted spectra from slit B2 had detectable Hβ emission. For the few extracted spectra from slit A1 where we detect Hγ, we also derived A_V from the Hγ/Hβ ratio. The results were consistent with the extinction values obtained using the Hα/Hβ ratio, although the errors were large.

The average extinction in region A is $A_V = 5.5$ mags, which falls to an average of 4 mags in region C, and the data are consistent with a further decrease past region C towards the south-west. The extinction towards M82-A1 (Section 3.1.2) is less than that towards the majority of region A, perhaps explaining why this cluster stands out so clearly in optical images. We can only measure the reddening for one point to the north-east of M82-A1, and although the errors are large, it is consistent with being at a much higher value than the surroundings. This coincides with the beginning of a region of complete obscuration at optical wavelengths, extending towards the north-east of the starburst core (the dust-lane). Extinction measurements of the diffuse gas in this region (−10″ to −2″) are therefore made impossible due to the very low S/N or absence of the Hβ lines.

The extinction in slit B2 could only be measured for four points representing the brightest emission in the cores of regions D and E. In region D we find $A_V \approx 4$ mags, and is lower than that in region A. In region E, however, the extinction appears to be much higher at $A_V \approx 6$–6.5 mags.

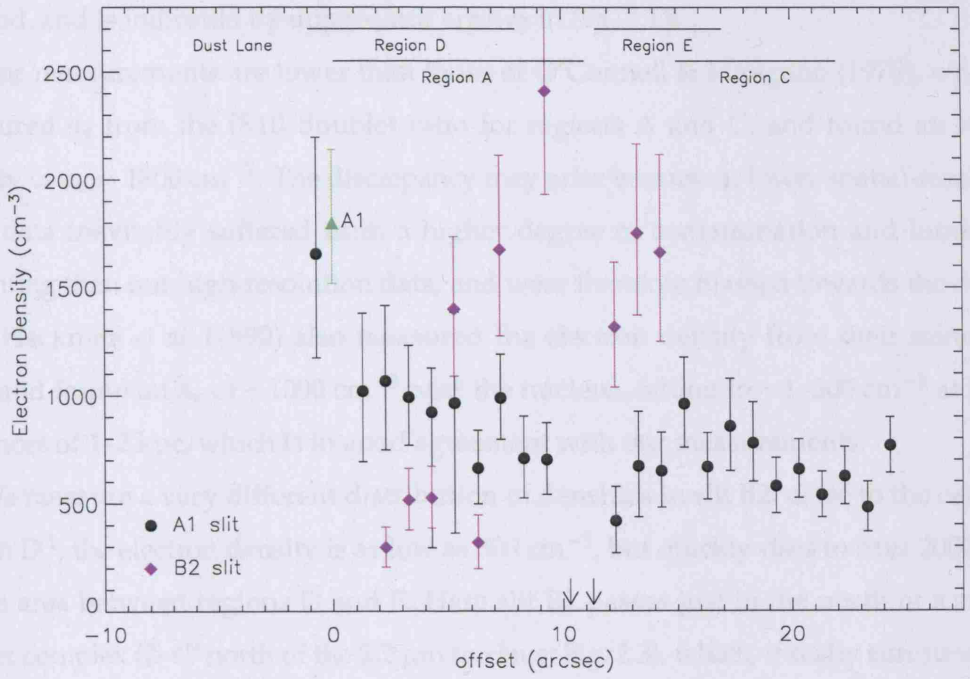

Figure 3.13: Electron density derived from the [S II]λ6717/λ6731 flux ratio, measured from the A20 spectrum sets. The triangle represents the electron density of the H II region surrounding M82-A1 (Section 3.1.2), and the arrows represent measurements which fell below the low density limit for the [S II] method.

Electron density

We have measured the [S II]λ6717/λ6731 line ratio by fitting Gaussian profiles to the emission lines in each of the A20 spectra for both slits. The distribution of derived electron densities, n_e, (assuming an electron temperature, $T_e = 10^4$ K) is plotted in Fig. 3.13.

In slit A1, we find the electron density to be highest around M82-A1 ($n_e = 1800^{+340}_{-280}$ cm^{-3}; Section 3.1.2). [S II] emission is not detected at all in spectra extracted from the north-east of M82-A1 (negative offsets), so in an attempt to derive an approximate average density for this region, we extracted a 60 pixel wide spectrum. However, even summing over this many pixels did not yield a [S II] detection, and therefore no density could be derived. From M82-A1, the density falls rapidly to ~1000 cm^{-3} in the centre of region A and to 600–800 cm^{-3} in region C. Our observations provide constraints on the steepness of the density gradient from region A to A1: an enhancement of $n_e \sim 1000$ cm^{-3} takes place over a projected distance of only 2.″5 (45 pc). In the area located between the two cluster complexes A and C, n_e falls below the low-density limit (<100 cm^{-3}) for the [S II] ratio

method, and is indicated by upper-limit arrows in Fig. 3.13.

Our measurements are lower than those of O'Connell & Mangano (1978), who also measured n_e from the [S II] doublet ratio for regions A and C, and found an *average* density of $n_e = 1800$ cm^{-3}. The discrepancy may arise because at lower spatial-resolution, their data inevitably suffered from a higher degree of contamination and luminosity weighting than our high-resolution data, and were therefore biassed towards the densest gas. Heckman *et al.* (1990) also measured the electron density from their minor-axis slits, and found an n_e of ~1000 cm^{-3} near the nucleus, falling to ~1–300 cm^{-3} at lateral distances of 1–2 kpc, which is in good agreement with our measurements.

We measure a very different distribution of densities in slit B2: close to the centre of region D[1], the electron density is as low as 300 cm^{-3}, but quickly rises to over 2000 cm^{-3} in the area between regions D and E. Here slit B2 passes just to the north of a smaller cluster complex (2–4″ north of the 2.2 μm nucleus; Fig. 2.3), which, if really surrounded by gas at this density, would be a very stifled region indeed. In region E, the electron density is also high with values of ~1300–1700 cm^{-3}, similar to that measured near M82-A1.

Emission measure

In Section 3.2.2 we discussed the surprising uniformity of the starburst over a large scale range by comparing our calculation of the ionization parameter of the M82-A1 H II region to the results of the IR study by Förster Schreiber *et al.* (2001). We now use the observed Hα fluxes to derive an estimate of the scale-length of the emitting region to compare to and extend this discussion.

First, we must deredden the observed fluxes using the following relations. The extinction at V can be related to the colour excess, $E(B-V)$ (given in Fig. 3.12), by the ratio of total to selective extinction, R_V:

$$\frac{A(V)}{E(B-V)} = R_V. \tag{3.9}$$

The extinction at a particular wavelength is related to the extinction at V by a reddening parameterisation (*e.g.* Seaton 1979; Howarth 1983; Cardelli *et al.* 1989). The relation of $A(\mathrm{H}\alpha)$ to $A(V)$ given by Cardelli *et al.* (1989) is $A(\mathrm{H}\alpha)/A(V) = 0.817$. Combining these formulae together, the extinction at Hα can be related to $E(B-V)$ as

$$A(\mathrm{H}\alpha) = 2.53\, E(B-V), \tag{3.10}$$

[1]Note: slit B2 is not aligned with the major axis of region D and misses most of the eastern extent.

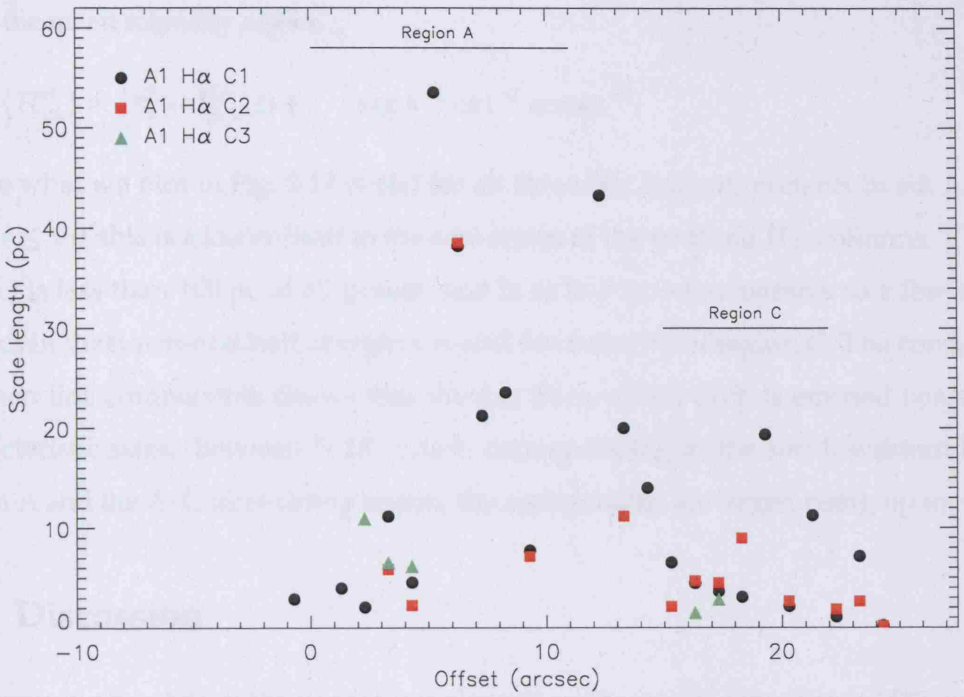

Figure 3.14: The characteristic scale-length of the emitting regions along slit A1 for all three Hα line components, as calculated from the gas emission-measure.

where the canonical value of $R_V = 3.1$ is assumed. Since the extinction at a particular wavelength, $A(\lambda)$, is defined as

$$A(\lambda) = 2.5 \log \left(\frac{F_\lambda^{int}}{F_\lambda^{obs}} \right), \tag{3.11}$$

the extinction-corrected Hα flux, $F_{\mathrm{H}\alpha}^{int}$, can be derived from the observed Hα flux, $F_{\mathrm{H}\alpha}^{obs}$, by

$$F_{\mathrm{H}\alpha}^{int} = \exp[1.012\, E(B-V)]\; F_{\mathrm{H}\alpha}^{obs}. \tag{3.12}$$

Now, a characteristic scale-length can be derived from the emission-measure, which is defined by:

$$F_{\mathrm{H}\alpha}^{int} = \int n_e^2\, \alpha_{\mathrm{eff}}^{\mathrm{H}\alpha}\, \frac{h\nu(\mathrm{H}\alpha)}{4\pi D^2}\, \epsilon\, dV, \tag{3.13}$$

where $\alpha_{\mathrm{eff}}^{\mathrm{H}\alpha}$ is the case B recombination coefficient for Hα (8.64×10^{-14} cm^3 s^{-1}; Osterbrock 1989), $h\nu$(Hα) is the energy of an Hα photon, D is the distance to the source, and ϵ is the gas volume filling factor. To remove the distance dependence, and to re-arrange in terms of a scale-length, dV can be substituted with $dA\, d\ell$, where $dA = A/4\pi D^2 \equiv$ angular area on the sky (or 0.1×1 arcsec in this case). Integrating over the whole emitting volume

gives the mean intensity of Hα,

$$\langle F^{int}_{\mathrm{H}\alpha} \rangle = \langle n_{\mathrm{e}}^2 \rangle \, \alpha^{\mathrm{H}\alpha}_{\mathrm{eff}} \, \langle \epsilon \rangle \, \ell \qquad \mathrm{erg\,s^{-1}\,cm^{-2}\,arcsec^{-2}}. \tag{3.14}$$

Hence what we plot in Fig. 3.14 is $\ell(\epsilon)$ for all three Hα line components in slit A1, and since $\epsilon \leq 1.0$, this is a lower-limit to the size-scales of the emitting H II columns.

$\ell(\epsilon)$ is less than 100 pc at all points, and is as low as ~few parsecs to a few tens of parsecs in the north-east half of region A and the majority of region C. The consistency between line components shows that the gas from which each is emitted has similar characteristic sizes. Between 5–15″ offset, corresponding to the south-western half of region A and the A–C inter-clump region, the scale-lengths are larger, rising up to ~50 pc.

3.4 Discussion

By measuring the state of the ionized gas along two slits crossing the disc of M82, we have been able to quantify part of the environment in which the starburst exists. This is the first time that such detailed, high spatial-resolution optical observations have been presented for M82.

3.4.1 The state of the ionized ISM

Lord *et al.* (1996) developed a model of the ISM in the central 700 pc of M82 from far-IR spectroscopic observations (see also Förster Schreiber *et al.* 2001). They proposed that the observed forbidden-line emission can be explained as originating in multiple H II regions and PDRs (photo-dissociation regions) mixed uniformly with the ionizing stars and clusters. Modelling the observed line ratios, line strengths, and emission morphology, they found that the clouds have a characteristic size, $r_{\mathrm{cl}} \sim 0.4$–1 pc (with a molecular core and extended ionized envelope), density, $n_{\mathrm{e}} \sim 10^4$ cm^{-3}, and mass, $M_{\mathrm{cl}} \sim 200$–3000 M$_\odot$, and are highly pressured ($P/k \sim 3 \times 10^6$ cm^{-3} K). These states are maintained by a hot (10^6 K), diffuse surrounding medium of equal pressure, supported by the influence of a large number of SN shocks. The continuous nature of the shocks results from the high estimated SN rate in the centre of M82 (~0.1 yr^{-1}; Muxlow *et al.* 1994; Pedlar *et al.* 1999). Since this model was developed, we now know that the hot, diffuse medium in M82 has a characteristic temperature nearer 10^7 K (Stevens *et al.* 2003), meaning that the density at $T \sim 100$ K would have to be $n_{\mathrm{e}} \sim 10^5$ cm^{-3} to achieve near pressure equilibrium. In their

model, Lord *et al.* found the average separation of the clouds to be of the order of their size (1–4 pc), and in order to maintain the observed ionization levels, the separation of the ionizing sources (the clusters) must be on the order of 3–7 pc. Despite the disparities in assumed and measured temperatures quoted above, these figures agree very well with the findings of Melo *et al.* (2005), who catalogued the star cluster content of the central starburst clumps and found >80 visually identifiable clusters in region A alone, with an average separation of <10 pc. This model is also supported by high-resolution CO observations that corroborate the typical cloud size adopted through area and volume filling-factor arguments, and give evidence that the clouds are partly disrupted and dissociated (Mao *et al.* 2000; Weiß *et al.* 2001). By modelling the observed forbidden-line profiles, Lord *et al.* argued that the clouds are clustered in two 'hot-spots' of size 125 × 125 pc located at $\sim\pm15''$ either side of the nucleus. These either represent a cross-section through the molecular torus, or a concentration of molecular gas just exterior to the ionized gas torus that is found to surround the nucleus at $\pm6''$ (Larkin *et al.* 1994; Shen & Lo 1995; Achtermann & Lacy 1995; Weiß *et al.* 2001), and is thought to result from the presence of an inner Lindblad resonance (ILR) and bar feature (Telesco *et al.* 1991; Wills *et al.* 2000; Greve *et al.* 2002*a*). Fig. 3.15 shows contours of integrated CO (J=1→0) line intensity from Weiß *et al.* (2001) overlaid on the *HST* broad-band colour-composite of Fig. 3.5, clearly showing how the peak of the CO emission corresponds to the location of the dust clouds either side of the nucleus and the proposed position of the two PDR hot-spots. This is the first time that observations of the ISM conditions in M82 have been of sufficient resolution to probe down to the smallest size-scales of the Lord *et al.* model. We shall now discuss how our findings relate to this model and what that implies for the M82 starburst.

Already in Section 3.2.1, we considered how our measurement of the ionization parameter for the H II region surrounding M82-A1 extends the uniformity of the ISM conditions, as determined by Förster Schreiber *et al.* (2001), down to parsec-scales. To augment this argument, we can use our results from calculating the emission-measure of the gas along slit A1 to see how the characteristic sizes of the emitting regions varies, and how this relates to the ionization parameter measurements of Section 3.2.1. From Fig. 3.14 we see that the scale-size of the emitting regions (a lower-limit, once volume filling factors of <1 are considered) remains below ∼50 pc ($3''$) throughout regions A and C, but the smallest sizes (∼few parsecs) are found in or near the dense cores of the clumps, whereas the largest sizes are found in the inter-clump region. The uniformity of the starburst

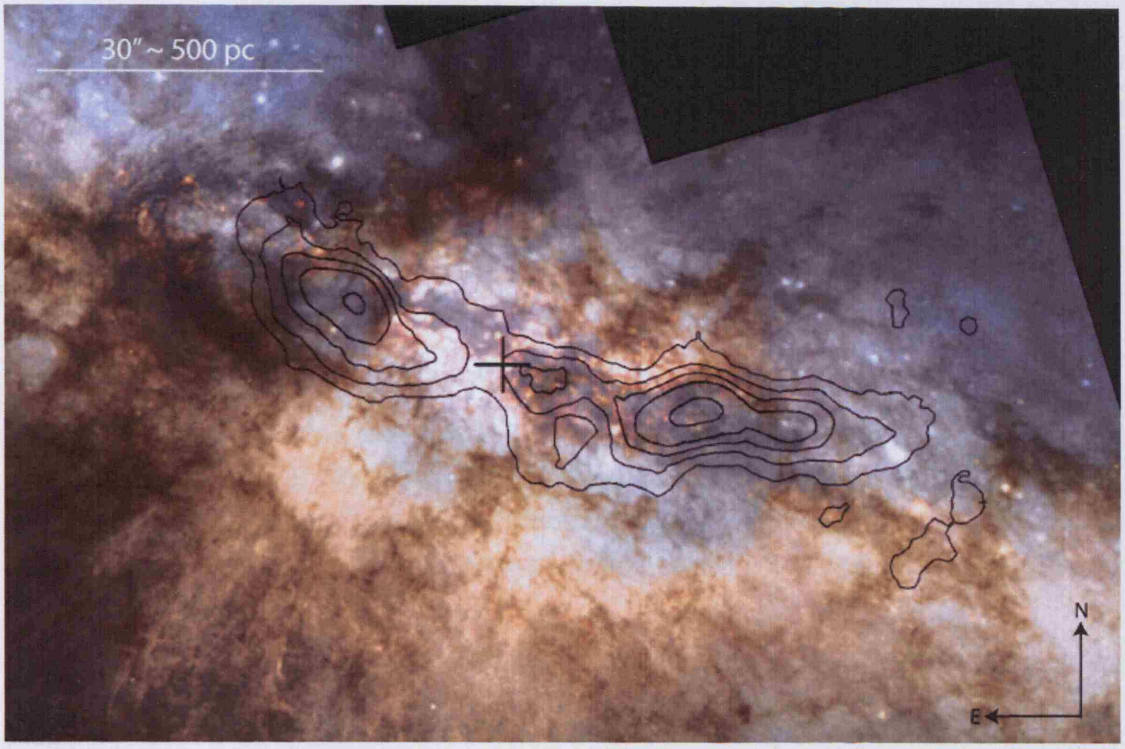

Figure 3.15: Contours of integrated $C^{18}O(J=1\rightarrow0)$ line intensity (Weiß *et al.* 2001) overlaid on an *HST* broad-band colour-composite (blue: F439W, green: F555W, red: F814W; credit NASA/ESA R. de Grijs). The CO peaks trace the molecular/dust torus surrounding the stellar bar on either side of the nucleus. The cross marks the position of the 2.2 μm nucleus.

conditions must therefore stem from the fact that the scale of the emitting regions remains very small, as suggested by the Lord *et al.* model. However, within this overall uniformity, the small-scale variations imply that the most compact clouds are found in the clump cores where the star-formation is most intense.

Diagnostic flux ratios derived from the most commonly observed nebular lines can give a further indication of the ionization parameter and the mean level of ionization within the M82 starburst. The ratios of [S II]λ6717+λ6731/Hα and [N II]λ6548+λ6583/Hα are primarily tracers of the ionization parameter of the gas (Dopita *et al.* 2000, 2006, Chapter 1), and are shown in Fig. 3.16 as a function of position along slit A1. We find that the [S II]/Hα ratio changes very slowly across regions A and C, from ~-1.8 dex at M82-A1, to ~-1 dex to the south-west of region C. For [N II]/Hα, we were able to measure the ratio independently for both C1 and C2 in many places, but find no significant difference between the two (except for perhaps in the inter-clump region where C2 is consistently higher than C1 for seven consecutive points). Again, the ratio stays roughly constant across

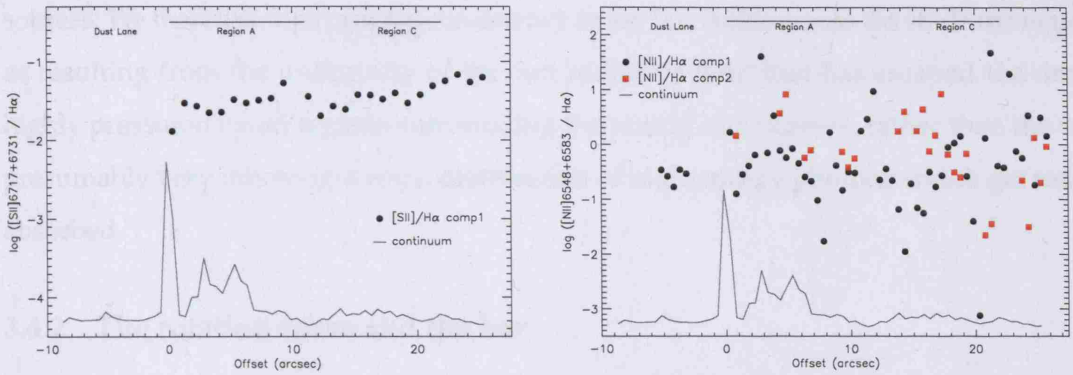

Figure 3.16: Plots showing the variation in the flux ratio of [S II]λ6717+λ6731/Hα (*left*) and [N II]λ6548+λ6583/Hα (*right*) with position on the A1 slit. The S/N of the Hα and [NII] lines are high enough for the excitation of the two line components to be shown separately. For comparison, the continuum flux level is plotted as a solid line (arbitrary scale) on both plots.

regions A and C at an average of -0.2 ± 0.5 dex. As a comparison, Shopbell & Bland-Hawthorn (1998) measure equally high [N II]/Hα ratios (-0.5 to -0.2 dex) in the inner collimated zone for their low velocity component. Having access to the bluer nebular lines of [O III] and Hβ means that we can use their ratio as an indicator of the mean temperature ($T_{\rm eff}$) of the ionizing sources, but our ability to measure this ratio, like that of measuring the extinction, is limited by the S/N of the Hβ line. Where this line is detected, we find the flux ratio to remain constant within the uncertainties at $\log([\mathrm{O\,III}]/\mathrm{H}\beta) \approx -0.5$ over both regions A and C. Rigby & Rieke (2004) discuss the effectiveness of certain optical and IR nebular line ratios, including [O III]/Hβ, at tracing the mean temperature of the ionization source by comparing the consistency of the indicators between themselves and to models. They suggest that finding low ratios (implying a low mean $T_{\rm eff}$) in starburst galaxies (*e.g.* Thornley *et al.* 2000) is likely to result from the fact that the ultracompact H II region phase is prolonged by the high densities and pressures in starburst ISMs. Massive stars (or indeed clusters) may therefore spend a large proportion of their lifetimes embedded within the dense, highly-extincted ($A_V \lesssim 50$; Hanson *et al.* 2002) regions, and will remain undetectable, even through re-processed nebular optical or IR emission. This situation agrees very well with what we know about the environment in M82, particularly for M82-A1. It therefore may not come as a surprise that none of the line ratios show evidence for having a non-photoionized contribution (*e.g.* from shocks; *c.f.* Kewley *et al.* 2001), since we are not seeing any gas emission from deep within the clouds, near the powerful ionizing

sources. We therefore interpret the consistency in the line ratios across the starburst regions as resulting from the uniformity of the soft radiation field that has escaped the dense, highly pressured cloud regions surrounding the young star clusters, rather than the true, presumably very inhomogeneous, distribution of high-energy photons which get totally absorbed.

3.4.2 The rotation curve and the bar

The high spectral- and spatial-resolution of our observations has been used to track the kinematics of the Hα line components across the two slits in unprecedented detail. We now use these measurements to provide constraints on the orbital parameters of the ionized gas, and the location of the individual starburst clumps within the galaxy.

As we have already mentioned, M82 has been found to host a stellar bar which may have formed during its encounter with M81 (Telesco *et al.* 1991; Wills *et al.* 2000). In a bar, the elliptical orbits forming the major-axis are called x_1-orbits (or cuspy orbits; Contopoulos & Mertzanides 1977). However Bureau & Athanassoula (1999, hereafter BA99) show the existence of many families of periodic orbits associated with a bar, including numerous types with a lower velocity-amplidude that can occupy the x_1-orbit region (*e.g.* 2:1 resonant orbits). If an inner Lindblad resonance (ILR) is present, a set of unique perpendicular orbits, the so-called x_2-orbits, are induced along the minor axis (Athanassoula 1992*a*). Fig. 3.17 (left panel) shows a simulation of what a bar with an ILR might look like (Athanassoula & Bureau 1999, hereafter AB99). The bar acts to channel gas from its far ends towards the centre by forming shocks at the intersection of the x_1- and x_2-orbits that allow the gas time to lose angular momentum. This results in the accumulation of material near and inside the x_2-orbits and the formation of dust lanes along the leading x_1-orbits as the gas makes its way towards the nucleus (Athanassoula 1992*b*; BA99; AB99). AB99 perform extensive hydrodynamical simulations of bars, concentrating specifically on the gaseous component. The gas is found to follow stream-lines that correspond to the x_1- and x_2-orbits qualitatively, but detailed inspection shows that there are differences arising from the fact that in reality the gas stream-lines only loosely resemble the stellar orbit families.

Wills *et al.* (2000) developed a model of the M82 bar system by comparing the predictions of their analytical model to neutral (H I, CO) and ionized ([Ne II]12.8 μm) gas position-velocity (p-v) diagrams derived from their own work and the literature. They

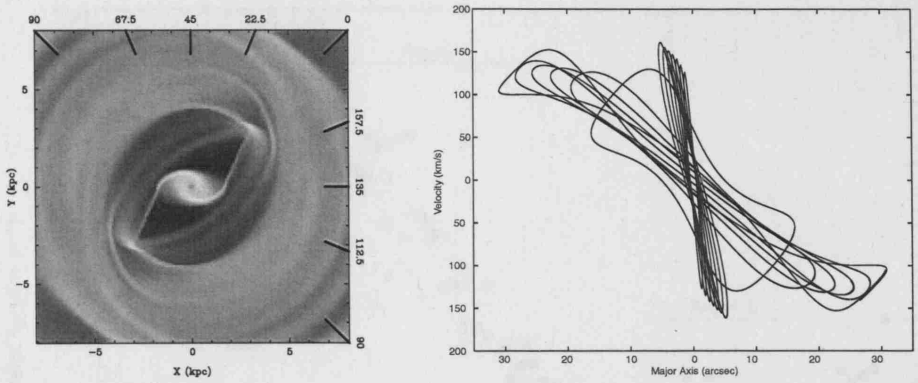

Figure 3.17: *Left:* face-on logarithmic gas surface density of the bar simulation of AB99 with an inner Lindblad resonance (ILR); *right:* the best-fitting model for the case of M82 from Wills *et al.* (2000) projected onto a p-v diagram, showing the cusped (peanut-shaped) x_1-orbits extending to $\pm 25''$ along the major-axis, and the x_2-orbits in the central $10''$.

found that the ionized gas is dominated by a faster rotating component that they identify with x_2-type orbits, thus corresponding to the ionized ring identified by Achtermann & Lacy (1995), whilst the neutral and molecular gas appears more consistent with the slower rotating cusped x_1-type orbits. They found the best-fitting bar model to have a peak radial velocity projected onto the sky of 140 km s^{-1}, an angular velocity of 217 km s^{-1} arcsec^{-1}, a total length of 1 kpc, a core radius of 25 pc, and an inclination of 80°. This results in an orbital revolution time of the x_2-orbit stars of ~2 Myr. The inclination they assumed, however, was opposite to the generally accepted value where the disc is tipped back from the line-of-sight and the southern side is closest (see Chapter 2; McKeith *et al.* 1995; Ohyama *et al.* 2002). The model is shown in the right-hand panel of Fig. 3.17, projected onto a p-v diagram.

In Greve *et al.* (2002*a*), K. Wills and her collaborators used the near-IR Ca II λ8542 stellar photospheric absorption lines of McKeith *et al.* (1993) to compare their bar model directly to stellar velocities rather than the previously used gas measurements. McKeith *et al.* themselves discuss the rotation of M82 using a variety of emission lines and stellar absorption lines, and found that the central velocity gradient increases with wavelength because of the high extinction towards the core. The use of IR lines by Greve *et al.* meant that the effects of the strong and variable extinction were reduced. By making this comparison, Greve *et al.* were able to estimate that the mass of the stars following x_2-orbits to be ~15 per cent of the total mass of the bar.

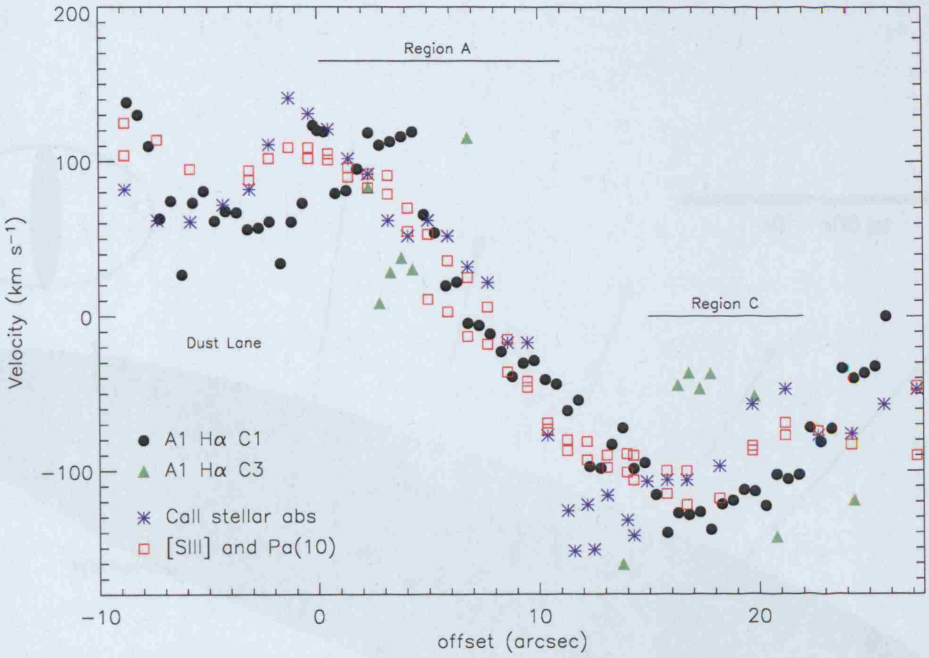

Figure 3.18: Hα C1 and C3 radial velocities for slit A1 plotted together with the near-IR stellar absorption line Ca II λ8542 and the [S III]λ9069 and Pa(10) λ9014 emission lines from McKeith *et al.* (1993). Offsets are measured relative to the position of M82-A1.

We can also compare the data from McKeith *et al.* to our observations to determine if we detect evidence for any of the orbit families. We plot their observed Ca II stellar absorption, and [S III]λ9069 and Pa(10) nebular emission line velocities together with our Hα C1 and C3 velocities in Fig. 3.18. The x_2-orbits, as traced by the stellar Ca II measurements, can clearly be seen departing from the gas velocities at offsets of $\sim$+13″ and $\sim$0″, where there is clear evidence that M82-A1 is indeed located at the end of one such orbit. The close match in other parts of the plot between the two data-sets indicates that the Hα gas follows the stellar rotation closely, although the rapidly varying extinction introduces inevitable complications, and that the inflection points at $\sim$0 and $\sim$+17″ simply represent the intersection between the x_2- and x_1-like orbits, where the gas is expected to shock and begin its journey towards the nucleus. Region C is clearly not associated with the x_2-like orbits, implying that it may be located within the molecular ring of material beyond the bar.

Bearing in mind that the Wills *et al.* bar model assumed the opposite inclination to that which is generally accepted, we can now re-assess how the bar might be oriented with respect to the line-of-sight, and to the individual clumps. Recall that the Lord *et al.* ISM

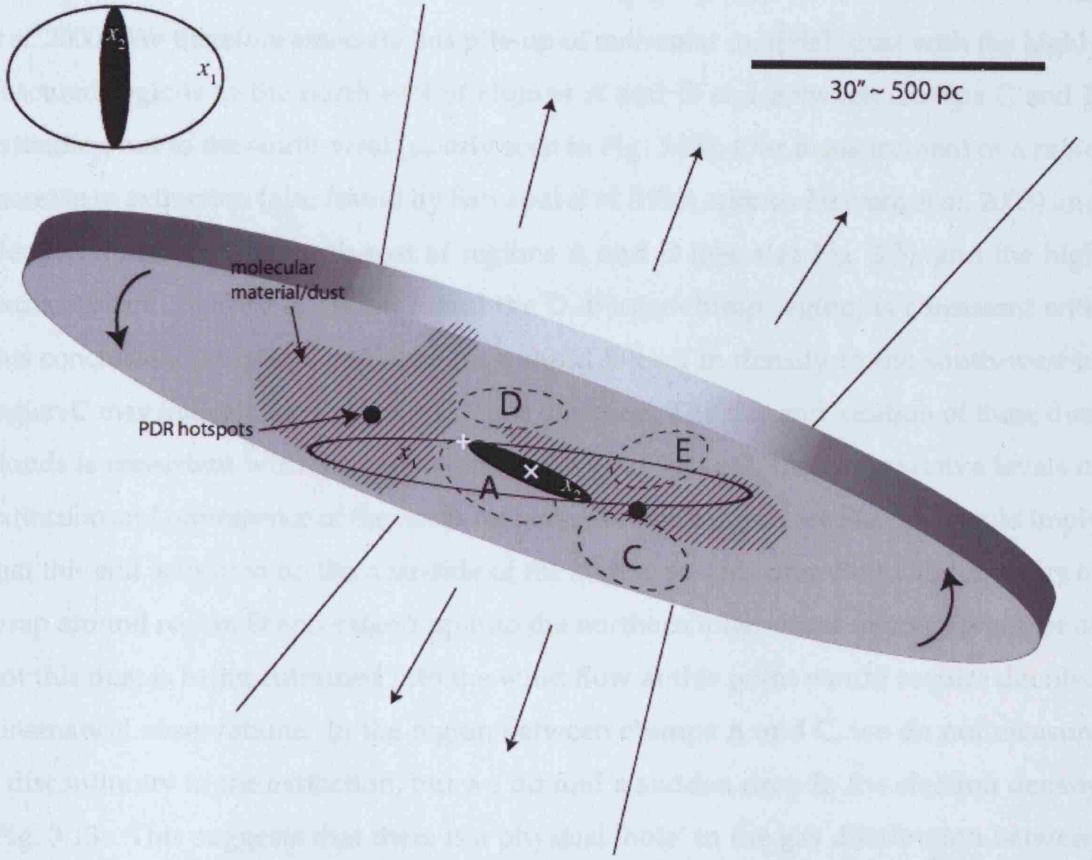

Figure 3.19: Our proposed orientation of the M82 bar and disc, with respect to the main starburst clumps (labelled A, C, D and E) within the inner 2 kpc of the galaxy. The disc is inclined 80° to the line-of-sight and at a PA of 70°. The bar x_1- and x_2-orbits are shown with an outlined and filled ellipse, respectively, and are also reproduced in plan-view in the upper-left. The major-axis of the bar extends along the x_1-orbits and is ~1 kpc in length. At the ends of the bar, molecular material and dust pile-up (hatched regions) and correspond the location of the PDR hot-spots in the Lord *et al.* (1996) ISM model. The cluster M82-A1 (shown as a white plus-sign) is located at the end of an x_2-orbit with the maximum redshift observed. Clump C shows the highest blueshift indicating that it is located at the opposite end of the bar, whereas regions D and E must be located either behind or in front of the nucleus (shown as a white cross) due to the shallower velocity gradient observed between the two. The wind outflow cones are indicated above and below the disc. For comparison, it may be helpful to refer back to Figs 2.3 and 3.5.

model predicted a concentration of molecular clouds (PDR regions) at either end of the bar, and that the interaction of x_1- and x_2-orbits causes the build-up of dust along the leading x_1-orbits (a phenomenon sometimes termed 'spraying'; Athanassoula 1992*b*; Wills *et al.* 2000). We therefore associate this pile-up of molecular material/dust with the highly obscured regions to the north-east of clumps A and D and between clumps C and E extending out to the south-west (clearly seen in Fig. 3.15). Our measurement of a rapid increase in extinction (also found by Satyapal *et al.* 1995; Alonso-Herrero *et al.* 2003) and electron density to the north-east of regions A and D (see also Fig. 3.5), and the high extinction and density in region E and the D–E inter-clump region, is consistent with this conclusion. Marginal evidence for a rapid fall-off in density to the south-west of region C may indicate the torus edge in this direction. The size and location of these dust clouds is consistent with the predicted bar length (~1 kpc); the comparative levels of extinction and prominence of the north-eastern dust cloud (again see Fig. 3.5) would imply that this end is located on the near-side of the starburst. This dust cloud also appears to wrap around region D and extend up into the northern inner-wind region – whether or not this dust is being entrained into the wind flow at this point would require detailed kinematical observations. In the region between clumps A and C, we do not measure a discontinuity in the extinction, but we do find a sudden drop in the electron density (Fig. 3.13). This suggests that there is a physical 'hole' in the gas distribution between these two clumps and that the two regions are physically distinct, rather than the decrease in surface-brightness being due to an obscuring dust-lane (see also O'Connell & Mangano 1978; O'Connell *et al.* 1995). The remaining gas in this 'void' must still be kinematically associated with the two clumps (confirming the suggestion of O'Connell & Mangano 1978) since there is no velocity discontinuity here. We can therefore now associate region C, located to the south of the bar region, as being outside the x_2-orbit region, and part of (or a result of star-formation within) the molecular torus surrounding the bar.

The fact that M82-A1 appears to be located at one end of the x_2-orbits places a strong constraint on the orientation of the bar within M82, and indicates that region A may have formed as a result of intense star-formation in the intersection between the x_1- and x_2-orbit families. The shallower velocity gradient between regions D and E indicate that they are located at a larger radius than that of regions A and C, but the distinction between these two regions is less clear than that between clumps A and C. Comparing Fig. 2.3 to Fig. 3.5 shows that there is a great deal of extended emission and variable extinction in

this inter-clump region, and the confused and variable velocities in this region indicate that we are seeing glimpses of star clusters through holes in a foreground dust screen. Fig. 3.19 shows a schematic of our proposed spatial configuration of the starburst clumps and dust lanes in relation to the orientation of the bar orbits. This model implies that the eastern side of the bar is more distant, and that it extends from behind the dense dust cloud to the east of region A to just past region E. This orientation also implies that the eastern side of the inner x_2-orbits, where M82-A1 is located, is nearest.

3.4.3 Implications for the production of the galactic wind

In this section, we will use our observations together with the discussion given in the previous two sections to consider what implications our findings may have on how the superwind is produced in the starburst core. We will first consider how our spatially-resolved measurements of the gas density may affect the individual cluster winds, then go on to discuss possible explanations for the width of the observed line profiles, and finally how the dynamics of the broad component may indicate that we are seeing the roots of the large-scale galactic superwind.

Densities and pressures

In Section 3.2.2, we explored how the unusually high density of the gas surrounding M82-A1 has stifled the growth of its H II region, and comment how it is hard to understand the development of the superwind if this cluster is representative of the entire starburst. We are now in a better position to know what the representative conditions are, and how these might vary over the face of the starburst. It is clear from high-resolution *HST* images of the galactic wind (see Chapter 4) that the outflow *is* being driven directly from the central clumps (region A in particular), but our measured densities of the gas within these cluster complexes are still very high (500–900 cm^{-3}, or $P/k \approx 0.5\text{–}1.0\times10^7$ cm^{-3} K; Section 3.3.3) compared to standard Galactic ISM values. However, they are less than half of that found near M82-A1, so if this kind of steep gradient continues towards the outer regions of the starburst (as measured by Heckman *et al.* 1990), it becomes easier to envisage how the high pressures in the clump cores manage to equalise with their surroundings through expelling gas along the density gradient out into the halo. This also highlights the difference between a relatively isolated cluster such as M82-A1 and

the densely-packed clusters in the clump cores where cluster wind–wind interactions are likely to be much more important.

Line broadening mechanisms

Fig. 3.10 shows that the widths of all but a few line components are > 30 km s^{-1}, but are systematically narrower in regions D and E (even including those that could only be fit with a single component), possibly indicating a more quiescent gas state. The sound speed of a gas can be calculated using the following argument: the adiabatic equation of state is

$$a^2 = \frac{5}{3}\frac{P}{\rho}, \tag{3.15}$$

where a is the sound speed, P is the pressure, and ρ is the density. For a perfect gas

$$P = \frac{\rho k T}{\mu m}, \tag{3.16}$$

where k is the Boltzmann constant, T is the gas temperature, μ is the mean atomic weight, and m is the mass of a hydrogen atom. Substituting these two, we can define the adiabatic sound speed, a, as

$$a = \sqrt{\frac{5}{3}\frac{kT}{\mu m}}. \tag{3.17}$$

Therefore, for a gas of $T \sim 10^4$ K (typical H II region), $a \sim 10$ km s^{-1}, for an X-ray emitting gas of $T \sim 10^7$ K, $a \sim 500$ km s^{-1}, and for $T \sim 10^2$ K (typical H I cloud), $a \sim 1$ km s^{-1}. These values refer to line width in terms of σ, where FWHM = 2.355σ. We will now explore the possible explanations for the observed widths of the narrow (C1) and broad (C2) lines in turn, but also refer the reader to Section 7.4.2 of Chapter 7 where we make similar arguments for the explanation of line broadening in the dwarf starburst galaxy NGC 1569.

Supersonic line widths have been observed in many intense star-formation sites both within our own Galaxy (30 Dor: Chu & Kennicutt 1994; Melnick *et al.* 1999), in nearby galaxies (NGC 604: Yang *et al.* 1996; NGC 2363: Roy *et al.* 1992; González-Delgado *et al.* 1994) and in more distant dwarf galaxies (Izotov *et al.* 1996; Homeier & Gallagher 1999; Marlowe *et al.* 1995; Mendez & Esteban 1997; Sidoli *et al.* 2006). In these studies, the following explanations have been proposed for the broadening of the brightest component (what we refer to as C1): gravitational broadening through virial motions of ionized gas clouds (Melnick 1977; Terlevich & Melnick 1981); or multiple unresolved kinematical components along the line-of-sight. A number of other possibilities also proposed, such

as dust or electron scattering (Roy *et al.* 1992), can be immediately disregarded on physical grounds.

The fact that we rarely measure FWHMs $< 30\ \mathrm{km\,s^{-1}}$ across both slits may indicate a global origin for the observed widths. A clear lower-limit to the width of C1 observed in some studies of similar environments (Muñoz-Tuñón *et al.* 1996; Yang *et al.* 1996, Chapters 7 and 8) supports this explanation. In Chapter 7 we propose that the ambient ISM turbulence resulting from the stirring effects of wide-scale, intense star-formation provides a base level of broadening in NGC 1569, but cannot discount a contribution from gravitationally induced virial motions to the line-widths. However, either of these globally determined values cannot account for the large local variations in line-width (30–100 $\mathrm{km\,s^{-1}}$) we observe across the slits. The bright background, variable extinction, and the small size-scale of the emitting regions in the core of M82 (Section 3.3.3), lend support to the fact that an inevitable contribution must result from including multiple, superimposed, small-scale kinematical components along every sight-line. We already alluded to this effect in Section 3.3.3, where we invoked the unresolved nature of the line profile to explain the increased width of the profiles where only a single-Gaussian was required for a satisfactory fit.

A ubiquitous broad underlying component (FWHM $\sim$ 150–250 $\mathrm{km\,s^{-1}}$) is observed in both slits where the Hα line is of sufficient S/N. Like the phenomenon of the supersonic narrow component, broad underlying profiles have also been observed in many intense star-formation sites (see in particular Melnick *et al.* 1999), but to our knowledge have never been studied in detail in the central regions of M82. Observations of the broad component in other systems are less well constrained, particularly for more distant galaxies, so the proposed explanations cited in the literature are more varied. These include: rotational effects, direct observations of stellar/cluster winds (González-Delgado *et al.* 1994); the effects of SN remnants (SNRs; Roy *et al.* 1992; Izotov *et al.* 1996); large-scale superbubble expansion and/or blow-out (Roy *et al.* 1992; Marlowe *et al.* 1995; Tenorio-Tagle *et al.* 1997); multiple unresolved expanding shells (Homeier & Gallagher 1999); champagne flows (Yorke *et al.* 1984; Tenorio-Tagle *et al.* 2000; Melnick *et al.* 1999); or ablation of gas from molecular clumps resulting from the impact of stellar/cluster winds (Melnick *et al.* 1999).

Only one of these proposed explanations, the effects of galactic rotation, is not due to the effects of massive stars, and may be discounted by considering the following: the maximum radial velocity relative to the systemic velocity of M82, $v_{\mathrm{rad}}^{\mathrm{max}}$, is of the order

100 km s^{-1}. If this were purely caused by rotation, then the line width would be $\sim 2 \times v_{\rm rad}^{\rm max}$ or $\sim$200 km s^{-1}. However, we see line widths of up to 300 km s^{-1}, thus proving that the broad line component cannot result from simple rotation. In reality, the $v_{\rm rad}$ observed is due to large-scale orbital motion, not local gas rotation, and rotational broadening is likely close to negligible.

In Chapter 7 we present a detailed discussion of how the remaining explanations relate to spatially-resolved observations of the broad line component in the central regions of NGC 1569. Following our observation of a clear correlation between the width of C2 (the broad component) and the emission intensity of C1 in NGC 1569 (Section 7.3, Chapter 7), we envision a situation whereby the energetics and dynamics of the brightest clumps are driven by an interaction with the high-energy ionizing photons and fast-flowing wind from the surrounding star clusters, and that all the observed emission originates from a thin interface layer at the clump surfaces. As the gas clouds are impacted by hot, fast, cluster winds, thermal evaporation and/or mechanical ablation of gas from their surfaces produces a highly turbulent velocity field that is strongest where the impact occurs (*i.e.* near the cloud surfaces, where in NGC 1569 we observe the broadest lines), but pervades the whole region as the gas becomes entrained into the flow. Since our observations of M82 are of a similar environment, we will begin with the premise that this explanation also applies here, and explore how this relates to what we have already discussed in the previous sections.

In the following we must take full consideration of the fact that the starburst in M82 is a much larger-scale entity than that found in NGC 1569. Only a handful of SSCs dominate the energetics in NGC 1569, whereas in M82 literally hundreds of SSCs are packed into cluster complexes with separations on the order of their radii (Melo *et al.* 2005). Lord *et al.* (1996) propose that these star clusters are well mixed with molecular matter in the form of clouds of characteristic sizes, $r_{\rm cl} \lesssim 1$ pc (see above), thus providing copious sites from which gas can be evaporated and/or ablated. This high density of ionizing sources and ionized regions explains why we do not see a correlation between the emission intensity and line width for M82, since even with the resolution of STIS, the individual sources/clouds are still unresolved. Thus, the fact that multiple PDR regions are predicted from far-IR spectroscopy, together with the observed close packing of the individual sources, the uniformity of the starburst conditions throughout the central regions, and the identification of a ubiquitous broad-line component, all point towards

gas evaporation/ablation by cluster winds causing a highly turbulent velocity field being the root cause of the observed broad line widths in M82, and possibly even the superwind itself.

Dynamics of the broad line component

We can now turn our attention to whether, by observing this broad, underlying component to the Hα line, we are indirectly detecting the roots of the superwind flow. In our proposed hypothesis, C2 represents gas that has been stripped off the surface of gas clouds embedded in the starburst, so in principle the radial velocity offset between this component and the brighter (hence presumably denser) C1 gas can be used to trace the flow of the hot superwind into which it is being entrained.

Slit A1 passes through the very core of region A, and even though here we see some of the broadest line widths (up to 300 km s^{-1}), we do not see any velocity offset between the components, indicating that at this point there is still no preferred outflow direction. In region C, the slit passes through the southern side of this clump, rather than its core. Already at this radius, some evidence of an ordered wind flow is detected in the kinematical studies of McKeith *et al.* (1995) and Shopbell & Bland-Hawthorn (1998). These authors find that within 200 pc south of the nucleus the Hα components are separated by $\sim$50 km s^{-1}. However, this is still within the chaotic zone of the outflow (see Chapter 4, and the discussion of Fig. 4.4), and certainly well within the energy injection zone, where it is thought the wind flow is still subsonic but rapidly accelerating (Shopbell & Bland-Hawthorn 1998). In this region we find that C2 is redshifted with respect to C1 by $\sim$40 km s^{-1} and we also detect an $\sim$80 km s^{-1} redshifted C3 profile. These values are consistent with the aforementioned studies, and indicate that here we are beginning to see an ordered flow with a preferred direction, and that C2 may be tracing the wind roots.

The region beyond clump C is interesting in a number of ways: here the C1 velocities rapidly decrease back to $v_{\rm sys}$, departing from the major-axis velocity measurements of McKeith *et al.* (1993), and the offset between C1 and C2 reverses direction, becoming blueshifted by $\sim$40 km s^{-1} relative to C1. This far end of the slit is coincident with lateral ionized streamers pointing towards the south-west (see Fig. 4.4 or Fig. 2.3), indicating that this region may be part of a distinct flow, separate to the main collimated stream. If clump C is located within the molecular torus surrounding the bar, then this region may be less influenced by the bar's collimating effects, explaining the lateral flow.

3.5 Summary

The use of high spatial resolution *HST* optical images and STIS spectra have enabled us to fill in a few more pieces of the large and complex jigsaw puzzle of M82. The data-set has allowed us to derive the properties of one bright, isolated cluster, and to probe the ionized gas environment across the nuclear starburst in unprecedented detail.

3.5.1 M82-A1

- We have designated the star cluster in Region A on which one of the STIS pointings was centred M82-A1. From extracting a spectrum of the cluster, we measure a mean heliocentric radial velocity of $+320 \pm 20$ km s^{-1}, and associate it kinematically and spatially with the starburst core.

- By comparing our observations to the predictions of the evolutionary synthesis code SB99 (Leitherer *et al.* 1999), we find a reddening of $E(B-V) = 1.35 \pm 0.15$ mag and an age of 6.4 ± 0.5 Myr. Comparison with star-formation history models (Förster Schreiber *et al.* 2003) suggest that the formation of M82-A1 is associated with the most recent burst wich took place ≈4–6 Myr ago.

- Archive *HST* images were used to measure the radius and photometry of M82-A1. We find that the cluster is elliptical with a mean effective radius of 3.0 ± 0.5 pc and a minor/major axis ratio of 0.72 ± 0.05. From comparing our photometry measurements to those predicted by SB99 for our derived cluster age, we find M82-A1 to have a mass of 0.7–1.3 $\times$ 10^6 $M_\odot$, depending on the IMF parameterisation used.

- The *HST* images were also used to measure the radius of the H II region surrounding this cluster. We find an effective radius of 4.5 ± 0.5 pc, and and a high ellipticity (minor/major axis ratio = 0.57), indicating that the H II region is unusually compact for its age. Measurement of the H II region spectrum shows it has a high electron density, $n_e = 1800 \pm 300$ cm^3, or a thermal pressure of P/k = 1–2 $\times$ 10^7 cm^{-3} K. Density and velocity dispersion measurements of gas in the immediate vicinity of the cluster show it to be surrounded by an unusually high-pressure medium, which may have caused the bubble to stall or follow a different wind solution to the standard supersonic adiabatic one.

3.5.2 The interstellar environment in M82

The second half of this study has concentrated on mapping the ionized gas properties in the starburst core using two STIS slit pointings. One slit passes through the core of region A, and the southern edge of region C, whilst the other slit passes through part of region D and ends within region E.

- By performing a comparison of our radial velocity measurements to previous observations and models, we confirm the presence of a stellar bar with an inner Lindblad resonance (ILR), resulting in a set of unique family of x_2-orbits perpendicular to the bar major-axis. The radial velocity of M82-A1 is consistent with being on an x_2-orbit at one end of the perpendicular ellipse, implying that region A may have formed as a result of intense star-formation at the intersection of the x_1- and x_2-orbits (as predicted by models; Athanassoula 1992*a*).

- Since the interaction of x_1-orbits with the perpendicular x_2-orbits is predicted to lead to a build-up of gas and dust along the leading x_1-orbits (AB99), we conclude that the prominent dust clouds to the north-east of regions A and D, and between regions C and E extending towards the south-west, must have been formed in this way.

- By comparing CO observations to an *HST* broad-band colour composite of M82, we identify that the peak of the molecular emission corresponds to the molecular torus surrounding the ionized ring detected (Achtermann & Lacy 1995; Weiß *et al.* 2001), the proposed positions of the PDR (photo-dissociation region) hotspots from Lord *et al.* (1996), and the prominent dust clouds located on either side of the nucleus. Since region C is clearly not associated with the x_2-orbits, we assume it to be located within this molecular torus.

- Our data are consistent with a physical distinction between clumps A and C, but that the gas in the inter-clump region must still be kinematically associated with the surrounding gas since there is no discontinuity in the radial velocity curve.

- A shallower velocity gradient between regions D and E lead us to believe that they are located at a larger radius to clumps A and C, but the strong, patchy foreground extinction indicates that we see these cluster complexes through gaps in a foreground dust screen.

- By measuring the [S II] doublet ratio along the slits, we find the gas densities (pressures) in the individual clumps to be high (500–900 cm^{-3}; $P/k \approx 0.5$–1.0×10^7 cm^{-3} K), but significantly lower than that measured for the gas immediately surrounding M82-A1. The observed density gradients attest to the highly variable conditions in the starburst core, however the measured values make it no easier to understand how the cluster winds escape this stifled environment to form the large-scale superwind.

- We extend the uniformity of the ISM conditions found by Förster Schreiber *et al.* (2001) down to parsec-scales by deriving the emitting scale-sizes and by measuring the ionization parameter sensitive line-ratios of [S II]/Hα and [N II]/Hα. We find the size-scale of the emitting regions to be always less than $50/\epsilon$ pc (where ϵ is the filling-factor) along slit A1, and that the smallest regions (few pc) are in or near the dense cores of clumps A and C, implying that the most compact clouds are found where the star-formation is most intense. This is the first time that the smallest scales predicted by the Lord *et al.* (1996) ISM model have been probed, and our results confirm the prediction of a uniform environment throughout the starburst, and the well-mixed nature of the embedded ionizing sources and ionized gas.

- The reason for the uniformity in the nebular line ratios may arise from the fact that the high densities and pressures that we measure in the starburst prolong the ultracompact H II region phase (Rigby & Rieke 2004), meaning that we never observe the highest energy photons as they are completely absorbed near the cluster. What we do observe is likely to be the relatively homogeneous soft radiation field that has escaped these dense regions.

- Our line-profile analysis has shown that the widths of all but a few line components are >30 $km\,s^{-1}$. We have explored the possible mechanisms for producing the observed broad-line widths in both the narrow component (C1) and the broad component (C2). The most likely explanation for broadening of C1 is a combination of gravitationally induced virial effects and the stirring of the ISM through the intense star-formation activity. A base level of turbulent broadening ($\sim$30 $km\,s^{-1}$) exists over the whole starburst region, whilst the scatter to broader widths (up to 100 $km\,s^{-1}$) is likely to result from the presence of multiple unresolved kinematical components (*e.g.* expanding shells) along the line-of-sight. A contribution from

unresolved components is inevitable due to the presence of large numbers of densely packed, highly dynamically active SSCs.

- A ubiquitous broad component (150–250 $\mathrm{km\,s^{-1}}$) is seen in all nebular lines with a high enough S/N. Drawing on our detailed study of the relation between the narrow and broad lines in Chapter 7, we conclude that turbulent mixing or thermal evaporation/gas ablation from the surface of dense clouds by the action of stellar winds and SN from the surrounding SSCs, is the most likely cause of the broad line widths.

- Since, in this model the broad component represents turbulent gas stripped from the surface of gas clouds, we can therefore use it to track the hot superwind as the cooler material becomes entrained into the wind flow. We find no velocity offset between C1 and C2 in region A, implying that here in the clump core the wind has yet to possess a preferred outflow direction. Where the slit passes through the southern edge of region C, we begin to see an ordered flow: C2 has a consistent redshifted offset, and a further redshifted narrow component (C3) can be identified.

- Beyond clump C, the offset between the C1 and C2 velocities is reversed, and C1 departs from the radial velocity pattern measured along the major-axis. Since these measurements are coincident with a number of lateral south-west pointing streamers, this has lead us to believe that this region may not be associated with the main collimated flow. If clump C is located within the molecular torus surrounding the bar, then this region may be less influenced by the bar's collimating effects, explaining the lateral flow.

CHAPTER 4

THE M82 SUPERWIND

M82 is unique in the local Universe in having a large-scale, optically bright, bipolar superwind that appears highly structured at every wavelength. However, the tenuous, multi-phase nature of the wind makes it very difficult to observe in any quantitative way. In this chapter we first focus on characterising the detailed optical morphology of the wind using new, deep, high-resolution narrow-band images. In the second half, we use two sets of IFU observations to examine the disc and inner-wind, and parts of the outer-wind, to try and further understand the superwind phenomenon.

4.1 Morphology of the wind outflow

In Sections 2.2.2 and 2.3.1 of Chapter 2, we introduced images of M82 taken by the *HST* and WIYN telescopes, and in Section 2.3.1 we explained how we took advantage of the range in spatial-resolution, sensitivity and field-of-view between the two sets of images to produce a colour-composite showing the full extent and depth of the M82 superwind. In this section, we will first describe the detailed morphology of the outflow as seen in these new composite images, beginning with the large-scale, and moving to progressively smaller scales, secondly how the optical morphology compares to that seen in other wavebands, and thirdly discuss possible explanations/theories of how the flow is as we observe it.

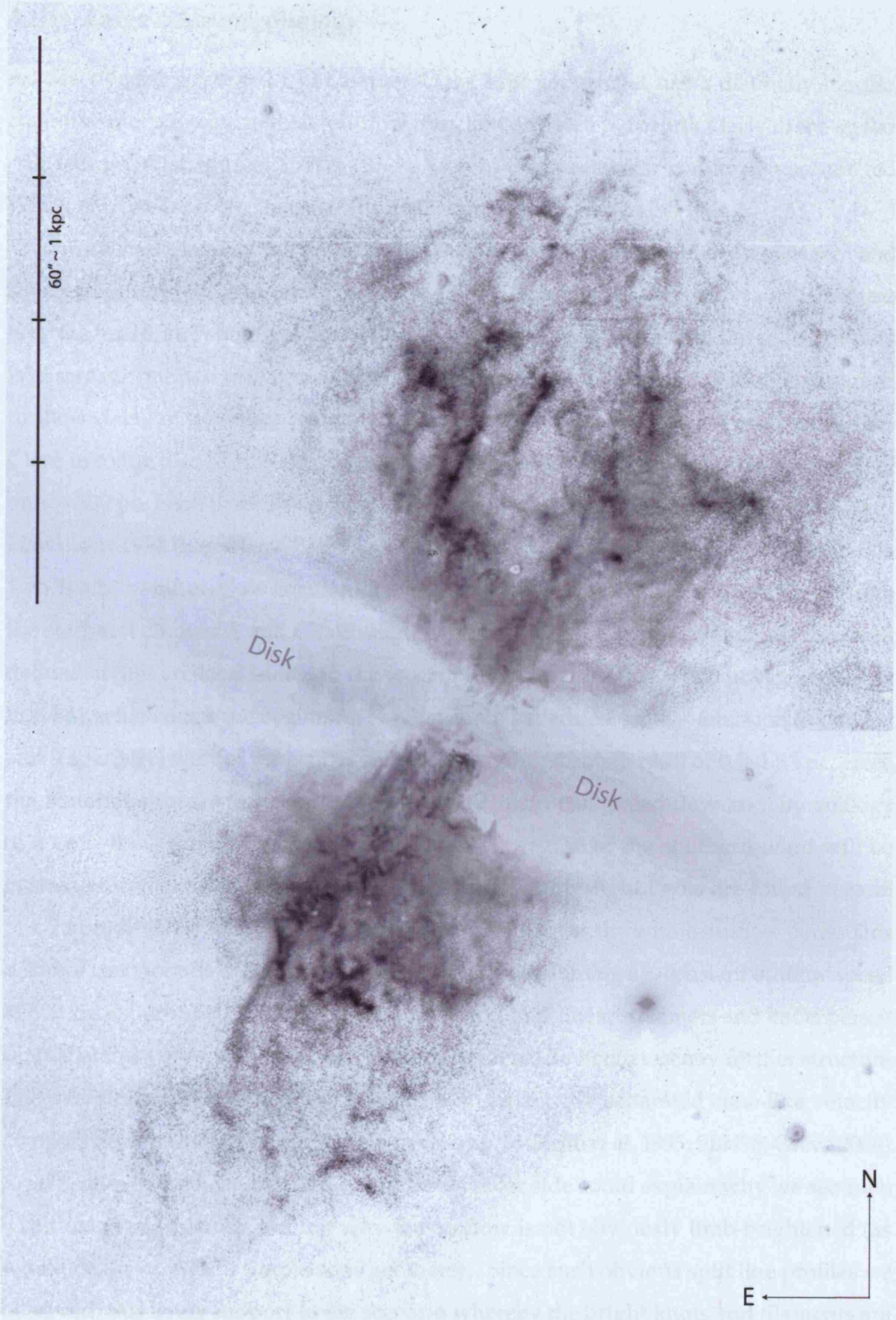

Figure 4.1: Continuum subtracted Hα image of the M82 superwind taken with the WIYN telescope (grey-scale inverted). The stellar disc is almost totally removed, so is labelled on both sides.

4.1.1 Large-scale morphology

As described in Section 2.1 of Chapter 2, the M82 superwind has a distinctly bipolar, cone-like morphology, with an outflow direction oriented perpendicularly to the stellar disc (seen almost edge-on). This can be seen in the spectacular continuum-subtracted WIYN narrow-band Hα image of the M82 superwind is shown in Fig. 4.1.

Only a brief glance at the image shows that the distribution of gas in the northern and southern plumes is significantly different. In the following paragraphs, we will examine how the broad morphologies of the two plumes differ, beginning with the southern flow. Whilst reading this, it may be helpful to refer also to Figs 4.2–4.4, which, although designed to show detail of the inner-wind, may also be of use in understanding our description. Close in to the disc ($R < 500$ pc), the southern flow looks almost jet like with a width of only $\sim$500 pc. Here it seems well collimated within angles of 25–30° [Shopbell & Bland-Hawthorn 1998 (hereafter SBH98) quote 25°] and the flow is parallel to the minor axis. Two 'walls' of the outflow are identifiable as brighter emission directly downstream from the starburst clumps A and C (although that is not very clear on this image). Two well defined arches are located just to the west of the inner flow at $R \approx 500$ pc (identified on Fig. 4.4), which mark the beginning of what could be termed 'frothy' emission to the east and (especially) west of the central column extending through radii of 0.5–1.5 kpc. Here, the material appears to have escaped from the main collimated flow and, by analogy to a river flow, formed a 'backwater'. The inner region of the southern wind will be examined in more detail in Section 4.1.2. A number of bright knots are found at radii of $\sim$2 kpc, which is followed by a sharp drop in flux over the whole outflow cone. This distance corresponds to a dynamical age of $\sim$3 Myr (assuming a $\sim$constant outflow speed of 600 km s^{-1} or $\approx$ 600 pc Myr^{-1}; SBH98). Beyond this, linear streamers and knots persist up to distances of more than 4 kpc, at which point we do not detect any further structure. The overall morphology betrays nothing of the distinctly separated cone-like velocity components found through spectral observations (McKeith *et al.* 1995; SBH98; Greve 2004). A projection of the near side of the cone onto the far side could explain why we see such a confusion of structure, but not why the outflow is not obviously limb-brightened (as would be the case for a simple cone geometry). Since such obvious split line profiles *are* observed, this lends support to the scenario whereby the bright knots and filaments are located at an interaction interface between the wind and halo material.

The inner part of the northern wind is obscured by the disc due to its inclination with respect to our line-of-sight (up to 0!8; SBH98). Beyond this, we find the northern plume opens with a much larger angle (roughly 55°) than the corresponding southern flow and consists of many more bright linear features. In Fig. 4.1, this plume does appear limb-brightened, with the two edges being defined by large linear streamers extending to the north-east and the north-west of the disc. The western streamer is almost parallel to the minor axis, implying that the flow direction in the north is angled away from the minor-axis by 5–10° (*i.e.* PA = 160–165°). An overall drop in flux, similar to that seen in the south, is observed at ~2.5 kpc radius, but a large array of faint knots and filaments (mostly located on the eastern side) are observed extending to heights of ~4 kpc. Even though the detailed morphologies of the northern and southern flows are very different, we can see that their extent and brightness are approximately equal, indicating comparable levels of energy input. In neither plume do we observe preferential emission along the outflow axis, contradicting a volume-brightened scenario.

4.1.2 The link between the large- and small-scale

The combination of the WIYN and *HST* datasets has enabled, for the first time, the link between the large- and small-scale wind structure to be made, and by combining both the broad- and narrow-band imaging, we have produced two figures that highlight the inner-wind in different ways. Fig. 4.2 is a mosaic of the broad-band composite and the Hα narrow-band images from *HST* only. Now that the contribution of continuum light is included, the stellar disc can be seen running from upper-left to lower-right, but the Hα contribution reveals the spectacular detail of the inner-wind. Fig. 4.3 shows a portion of the WIYN and *HST* mosaic (shown in the frontispiece) focussing on the nuclear regions and inner-wind zone. This again shows the disc running from upper-left to lower-right, but shows the inner-wind captured by *HST* in context with the continuing outflow. The advantage of combining broad- and narrow-band imaging is that the link between the stellar disc, starburst clumps, dust lanes and filaments, and the emission-line wind can be examined together.

The southern inner-wind is remarkably structured, and shows detail down to the resolution limit of the image. In general, the linear features and arcs are arranged such that they point directly back to regions A and C, indicating that the outflow must be driven from these clumps. The features closely resemble plumes of smoke originating

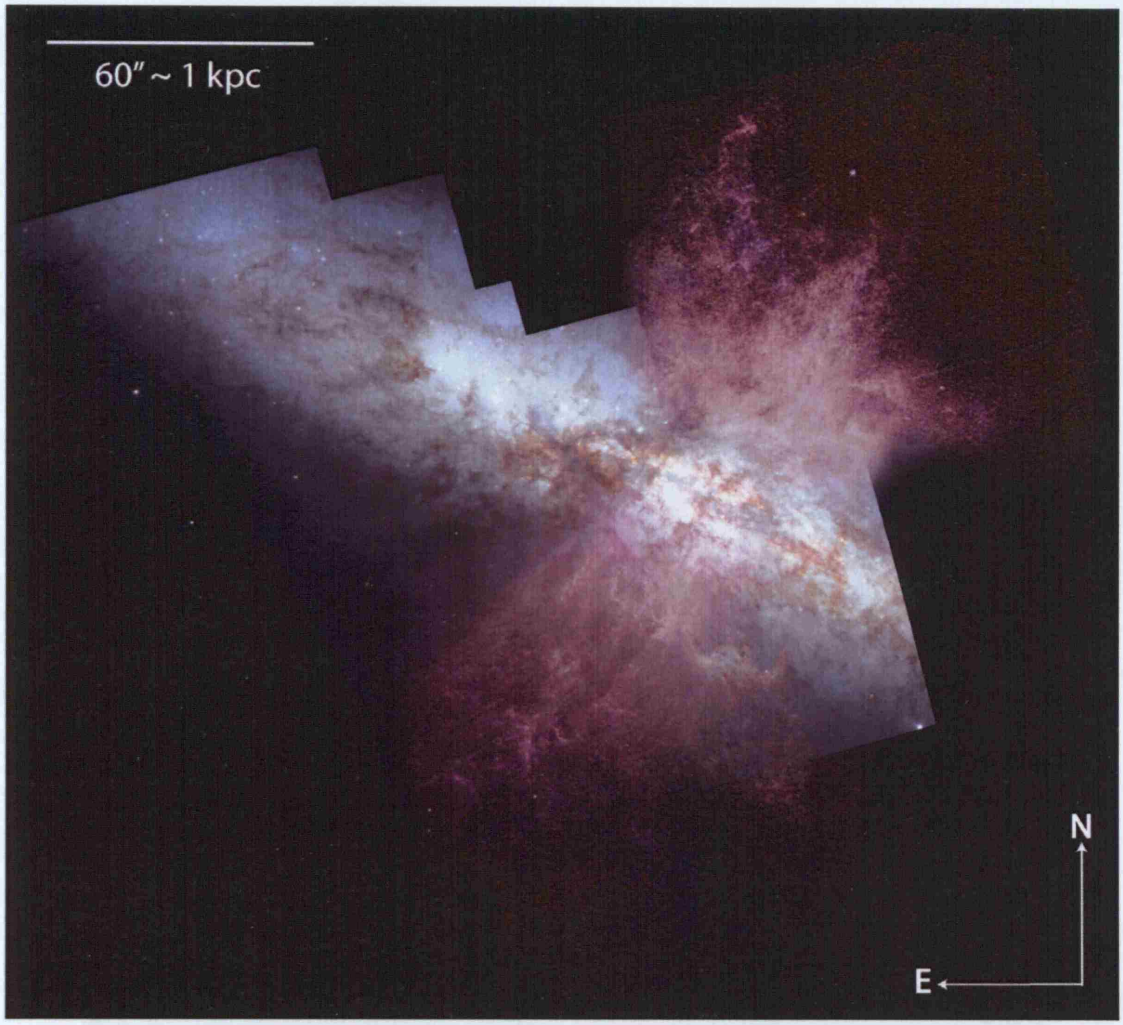

Figure 4.2: *HST* broad-band (blue: F439W, green: F555W, red: F814W; credit NASA/ESA R. de Grijs) and narrow-band (F656N) composite image showing part of the disc and inner-wind.

from individual chimneys lined up in the starburst core (an analogy also made by Wills *et al.* 1999, when describing radio data of the northern flow). At the end of the smoke plumes are loops or arcs resembling remnants of bubbles that have blown out from the disc. In this way, formations in the wind can be traced directly back to the clump or sub-clump from which they were produced. The thickness of the wind base can now be more accurately measured, and is found to be ~400 pc, or slightly narrower than the combined lateral extent of the two clumps A and C. The eastern side of the flow has a very linear boundary, indicating that a tight collimation has occurred on this side, and a 'search-light' formation can be seen extending along this boundary into the outer wind, which may

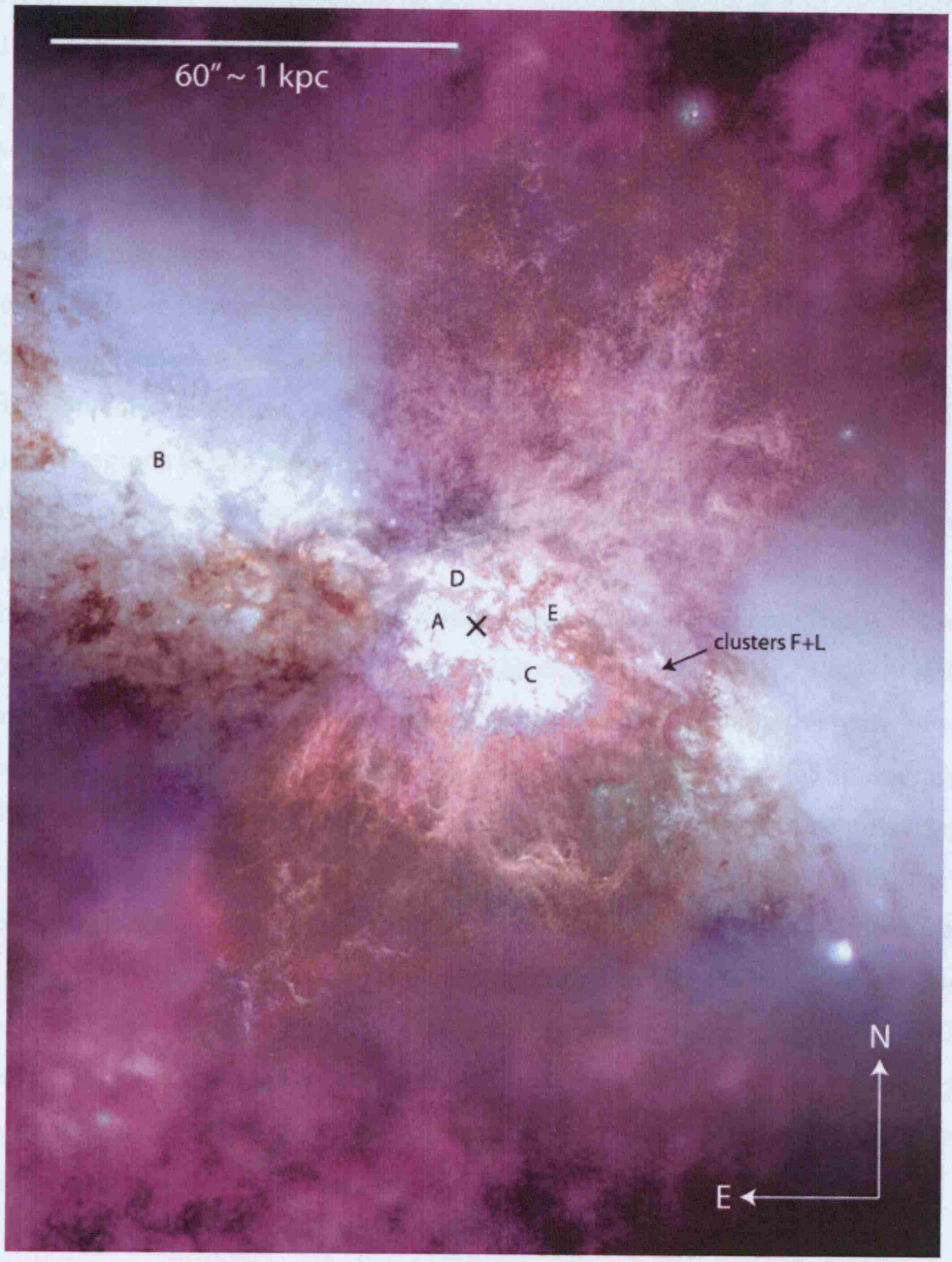

Figure 4.3: WIYN and *HST* composite image showing the inner-wind. The prominent starburst clumps and star clusters F and L are labelled (O'Connell & Mangano 1978), and the location of the 2.2 μm nucleus (Lester *et al.* 1990) is marked with a cross.

result from scattered light escaping the nuclear starburst along an unobscured line-of-sight. An abrupt decrease in flux occurs at $R \approx 500$ pc (corresponding to a dynamical age of <1 Myr). The wind must therefore be highly temporally variable and/or sensitive to density fluctuations in the halo, thereby meaning that its structure and flow characteristics must depend strongly on the prevailing conditions in the starburst.

As we mentioned above, the inner part of the northern flow is expected to be partially obscured by the disc to projected radii of $\sim$0.'8, due to the inclination of the system. Thus it is not as clear as in the south which part of the starburst is currently driving the northern outflow. The inner-flow appears smoother than in the south, and intricate structure is not so evident, presumably because of the obscuration. The outflow base also appears wider than the southern equivalent, measuring $\sim$1 kpc in width at the base. A cloud of emission surrounds regions D and E and extends around to the south-west, up to clusters F and L. Three spurs in the northern flow emerge at the transition between the *HST* and WIYN coverage at a radius of $R \approx 700$ pc.

To the north of region B, a large grey-blue coloured area stands out. This is not seen in the narrow-band images, and must therefore be continuum emission, possibly stellar in origin, suggesting the presence of a reflection nebula located above the plane of region B. Region B contains a population of older stars and star clusters (at an average age of 10^9 yr; de Grijs *et al.* 2003) and would therefore not be expected to be powering any current outflows. However, the eastern large-scale streamer mentioned in the previous section, forming part of the outer northern wind, contains a number of linear features (at $R = 2$–3 kpc) that point directly back to region B. If these structures were formed by starburst activity in region B, then they would have been ejected in the last 5–10 Myr, assuming the outflow speed quoted above. This would imply that *(a)* there is on-going star-formation in region B, or *(b)* the outflow speed is incorrect, or *(c)* these streamers were ejected by a different part of the starburst.

Classifying the small-scale structure of the wind

Fig. 4.4 shows a schematic representation of the southern inner-wind morphology, overlaid on an *HST*/WFPC2 F656N mosaic. The flow can be divided into a number of zones based on prominent feature sets. The southern half of the nuclear starburst consists of two large star-cluster complexes, regions A and C. Directly below these is a chaotic zone consisting of uncollimated gas knots extending for $\sim$100 pc, labelled as zone 1 on the figure. Zone

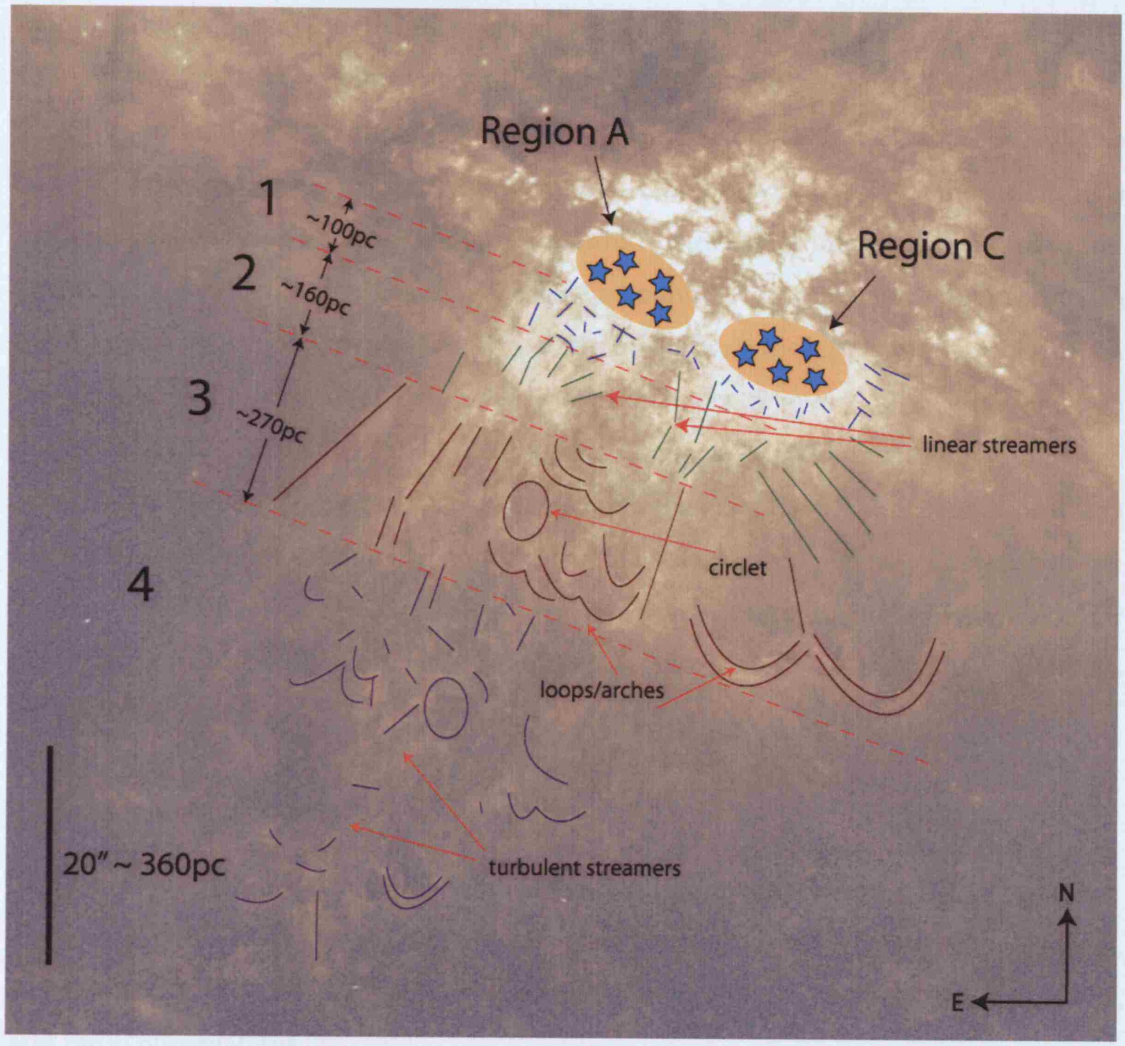

Figure 4.4: Structural guide to the southern inner-wind. The background image is an *HST*/WFPC2 F656N ($\approx$ Hα) mosaic.

2 extends for another ~160 pc and contains mostly linear streamers, and is where the inner-wind seems most collimated. In zone 3, larger structures are seen consisting of circlets, streamers, loops and two large arches in the west. These are the same arches as discussed in Section 4.1.1. Within zone 3, the velocity of the split line components (front and back of the wind cone) rapidly diverges (McKeith *et al.* 1995; SBH98), indicating the outer extent of the energy injection zone and the point at which the wind flow is thought to become supersonic. South-west of these arches is where the region of what we termed 'frothy' gas is found. At the boundary of this zone, 530 pc from the nucleus, the average brightness drops by $\sim\frac{2}{3}$. Beyond this region, in zone 4, the wind again becomes turbulent and ragged edges of loops and arches persist out to the edge of the WFPC2 field-of-view

marking the transition into the outer-wind.

At lower resolution, what looked like two 'walls' in the southern outflow are now shown to be two distinct streams, emanating from regions A and C respectively. The current main flow seems to be driven by region A, below which most of the structure is evident. In the region between the two columns, a number of linear features are found (spanning zones 2 and 3) which may indicate a boundary or interaction region between the two flows (see Section 4.1.4). South of region C, the wind appears to extend much more towards the west, with a series of linear streamers in zone 2 followed by the two prominent arches located in zone 3. These arches are most likely remnants of wind-blown bubbles that have ruptured and been entrained into the wind flow. The expansion towards the west infers that the collimation mechanism is not as effective here, compared to the eastern side. An explanation for this would be if region C was located within the molecular torus (Section 3.4.2, Chapter 3; Shen & Lo 1995; Weiß *et al.* 2001), therefore less subject to its collimating effects.

4.1.3 Comparison to other wavebands

M82 has been the subject of a great many observing campaigns over the full range of the electro-magnetic spectrum. We will now compare our new high-resolution optical images, and the results of our morphological analysis, to infra-red (IR), ultra-violet (UV), X-ray, and radio observations.

Dust emission

Fig. 4.5 compares the distribution of IR dust and PAH (poly-cyclic aromatic hydrocarbon) emission as observed with *Spitzer*/IRAC to the WIYN broad- and narrow-band image of the disc and superwind and the UV flux distribution as observed by *GALEX*. IRAC's shorter wavebands highlight the stellar disc component extending north-east to south-west, but in the longer wavebands (here in red) considerable PAH emission is seen tracing the distribution of dust in the M82 halo through the re-processing of UV radiation from the central starburst to these longer wavelengths. Dust is detected out to distances of 4–5 kpc, similar to the extent of Hα emission seen in the WIYN image. However, the large-scale morphology of the dust is very unlike the bipolar distribution of optically emitting gas. The dust distribution seems remarkably uniform and forms an almost spherical halo with

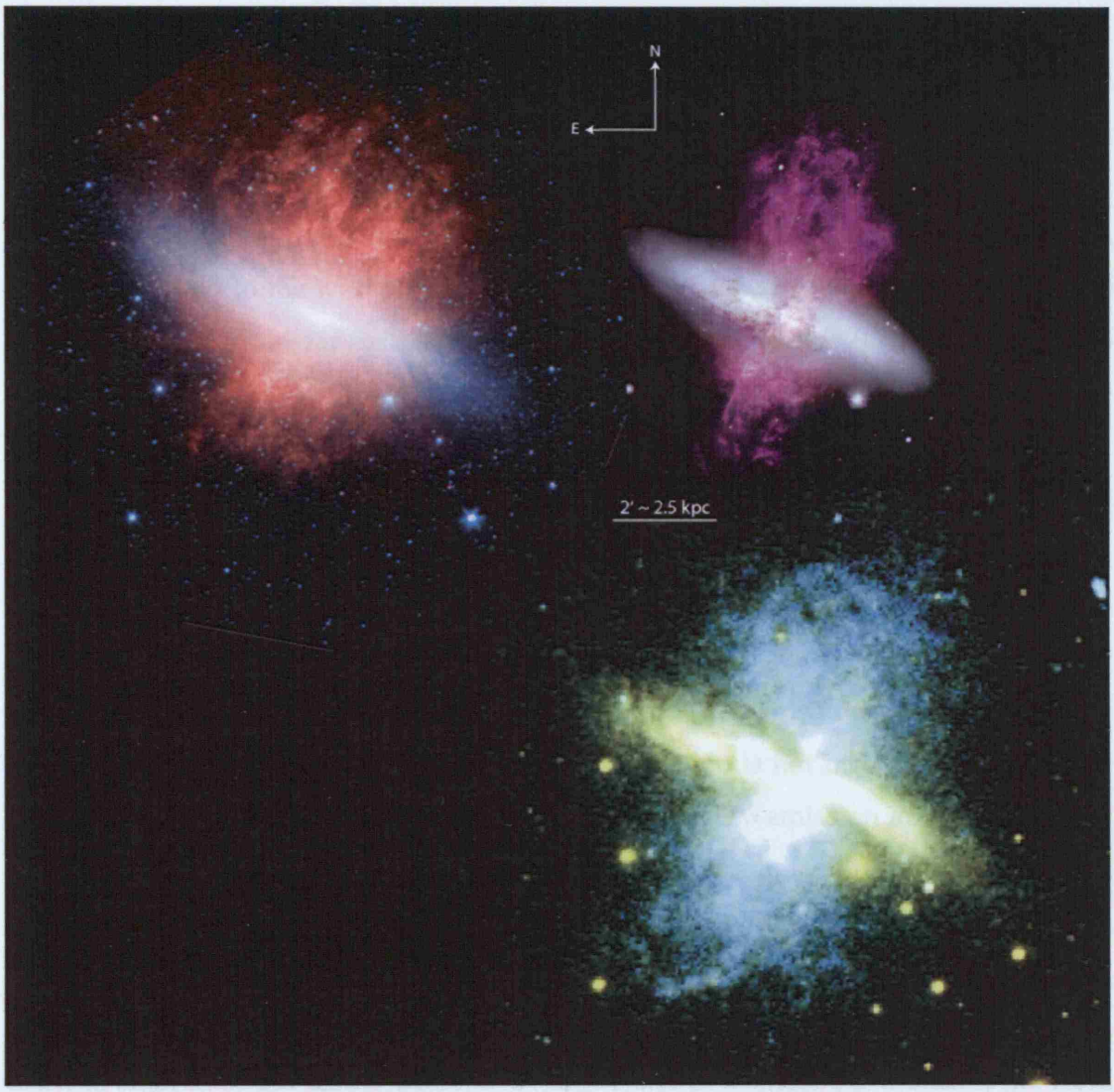

Figure 4.5: Comparison of *upper-left: Spitzer*/IRAC (blue: 3.6 μm, green: 4.5 μm, red: 5.8–8.0 μm; credit: NASA/JPL-Caltech/C. Engelbracht, *upper right:* WIYN optical and *lower-right: GALEX* UV (near-UV red, far-UV blue; Hoopes *et al.* 2005) images shown at same orientation and spatial scales.

little evidence of a collimated outflow structure. Despite this initial impression however, a surprising number of smaller-scale features can be identified in both the IR and optical images. Most of the larger morphological features mentioned in Section 4.1.2 are present in both images, including the sharply defined linear streamer in the southern flow, and many of the arcs, loops and knots in both the northern and southern wind. Furthermore, a number of the disc-obscuring dust lanes obvious in the optical broad-band images (particularly Fig. 4.2) are also present in the *Spitzer* composite. The cavity in the northern flow is present in the IR image, but the two streams surrounding it in the optical image are not as well defined in the IR. The outer northern outflow contains a number of streamers that curve round to the west with increasing radius – a shape that is mimicked by the faintest material in the far eastern half of this hemisphere. We shall see in Fig. 4.7 how these curved streamers follow the distribution of a large H I streamer extending out to heights of >8 kpc.

A preliminary analysis of the *GALEX* UV images was given in Hoopes *et al.* (2005), including a brief discussion of the possible origins of the UV emission from the wind. They find from measuring the UV/Hα flux ratios of contiguous areas across their field-of-view that the majority of the UV emission likely results from scattered light from the central starburst by dust in the halo/wind (note that they also find that a significant contribution from photoionization and shock ionization is not inconsistent with their measured ratios). Since a significant proportion of the UV emission in the outer-wind traces the dust component, we can directly compare this image to the IR and optical counterparts, with the caveat that we cannot be sure exactly to what extent scattering and ionization contribute to the observed flux. In the colour stretch chosen by Hoopes *et al.* (2005), the disc and inner wind emission is completely saturated, but this was chosen in order to emphasise the fainter emission at large radii. In the north, evidence of the wind can be seen out to distances almost equal to that of the Hα (4–5 kpc). Certain large-scale features correlate well with the *Spitzer* image, including the general diffuse wide-angle distribution of emission and a large arc on the eastern side. FUV (blue) emission is stronger on this eastern side and the outflow direction is consistent with being offset from the minor axis by 5–10°. The shape of the southern plume is more distinct, and the emission intensity is significantly more pronounced in the inner regions on this side. The wind is observed out to radii of 5–6 kpc and appears to flow parallel to the minor-axis, in agreement with the optical data. There are a number of explanations as to why the IR

and UV morphologies are different here in the southern plume. The IR emission results from the re-processing of UV radiation from the starburst core by dust particles, so the enhancement of UV radiation may result from an increased efficiency of the UV scattering relative to the absorption and re-emission mechanisms in this area. Alternatively, shock ionization may play an increased role in the UV emission budget, since an enhancement of photoionization at these radii is unlikely due to the large distance from the central starburst (>3 kpc). The inclination of the system may also play a part, since the northern plume will be strongly attenuated by the obscuring disk.

The only measurement of the dust kinematics comes indirectly from scattered light measurements of McKeith *et al.* (1995). They measure the velocity of the Ca II triplet stellar absorption lines along a slit oriented along the minor-axis of M82, which they think originate from radiation from late-type stars in the core, scattered by dust in the halo. They find that the Ca II radial velocities, out to distances of ~1.5 kpc in both the northern and southern winds, are at or near the systemic velocity, which indicates that the dust component responsible for the scattering is not entrained into the wind outflow.

X-ray emission

We compare the qualitative distribution of X-ray gas, as measured by *Chandra*/ACIS observations, with both the WIYN continuum-subtracted Hα (to show the large-scale) and *HST*/WFPC2 F656N image (showing the nuclear regions) in Fig. 4.6. Although commented on many times before, the correlation between the Hα and X-ray emission is striking, particularly in the inner-wind zones (see inset). The distinction of the two outflow streams in the southern flow, centred on regions A and C, is easily discerned in X-rays. The highly collimated eastern side of the southern flow is mirrored in X-rays, and the two large arcs in the western side at $R \sim 500$ pc also have X-ray counterparts. It is interesting to note that an increase in X-ray flux is observed over region B in the east (clearly seen in the inset), and an equal increase takes place at the location of the possible reflection nebula to the north of this region. This interesting discovery deserves further investigation in the future. A number of the larger-scale features in the outer-wind also correlate well, including the larger opening angle and offset flow direction in the north.

Deep X-ray observations of M82 taken with the *XMM-Newton* observatory were presented by Stevens & Hartwell (2003). Although *XMM-Newton* does not have as high spatial resolution as *Chandra*, its large light-collecting area allows it to probe to fainter

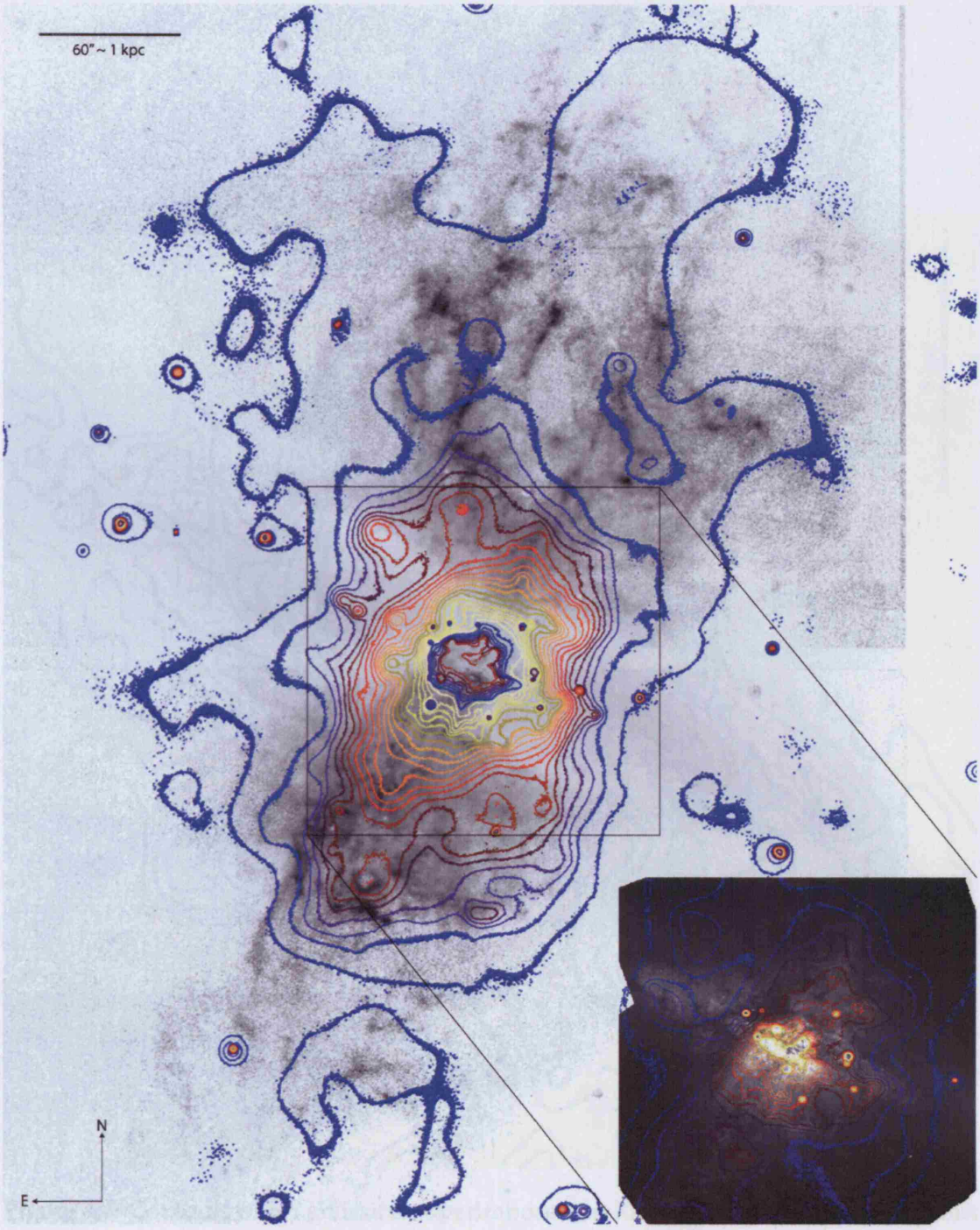

Figure 4.6: Continuum subtracted WIYN Hα image (inverted greyscale) overlaid with contours of a *Chandra* X-ray map (credit: NASA/*Chandra* X-ray Centre). The energy of the X-rays are represented with a colour scale, here blue is low, red is intermediate and yellow is high energy (the colour scale was allowed to wrap around in the centre to extend the sensitivity depth). Inset, the mosaicked *HST*/WFPC2 F656N image is shown (greyscale) with overlaid contours from the X-ray observations but with a more sensitive colour scaling. The correspondence between Hα and X-ray emission is clear, both at large and small-scales.

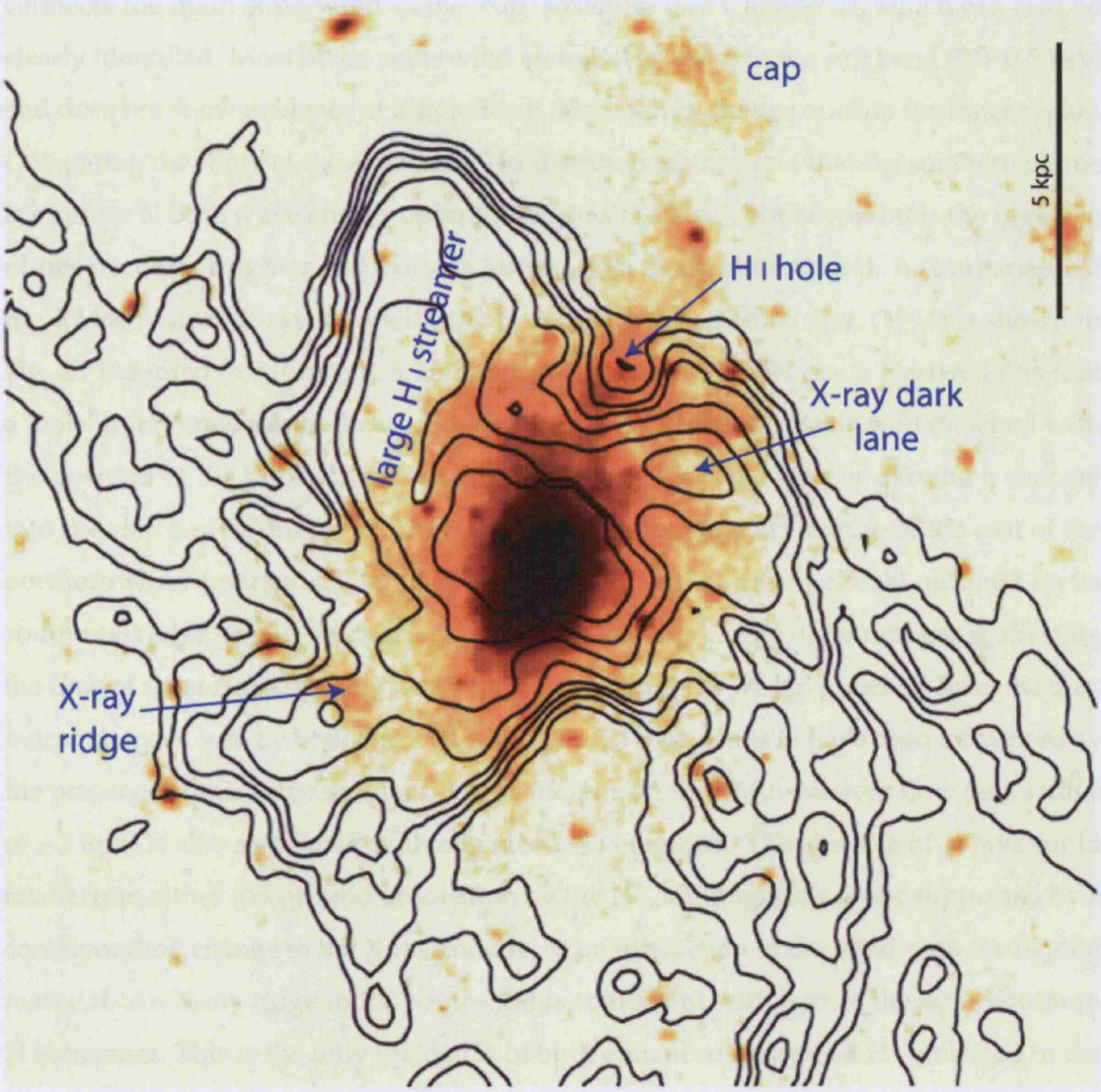

Figure 4.7: Contours of H I emission superimposed on *XMM-Newton* EPIC observations (0.2–10 keV; greyscale) of M82 (adapted from Stevens & Hartwell 2003). A number of large-scale X-ray and H I features are labelled.

magnitudes. A comparison of the data to both Hα and H I observations was given in their paper, but it is pertinent at this point in our analysis to give a brief summary of their findings. Their observations reveal that X-ray emission extends to greater distances in the north ($\sim$13.5 kpc) than in the south ($\sim$7.5 kpc), and a continuous stream of X-ray gas connects the main superwind to the 'cap' structure (see Chapter 2), which can also be clearly identified. Most of the superwind emission is found in the soft band (0.2–0.5 keV) and does not show evidence of a significant temperature change outside the inner-region. Comparing the X-ray to the equivalent Hα distribution, they find that the southern plume is brighter at both wavelengths up to 1.2 arcmins (1200 pc), but beyond this the northern plume becomes brighter and extends further than the southern wind. A comparison of the *XMM-Newton* X-ray data with the H I observations of Yun *et al.* (1994) is shown in Fig. 4.7 (adapted from Stevens & Hartwell 2003). From this, Stevens & Hartwell find that a 'hole' in H I emission in the north-west (indicated on the figure) is well matched with the position of the northern plume, indicating that the wind may be carving a channel into the cold neutral material. They also find that the large H I feature to the east of the northern wind (marked as 'large H I streamer' on the figure) is clearly outlined on its south-west edge by X-rays, possibly indicating that this clump of neutral gas is affecting the flow of wind material. This is a likely situation since, as we have already seen, the dust morphology as seen by both the *Spitzer* and *GALEX* also seems to have been influenced by the presence of this large streamer. The 'dark lane' in the north-western flow (at a radius of $\sim$3 kpc) is also associated with enhanced H I emission. The absence of X-rays could result from either foreground absorption by the H I, although this is not supported by a corresponding change in the X-ray colours, or an interaction of the wind with the neutral material. An X-ray ridge in the south-east is coincident with part of the large southern H I streamer. This is the only incidence of both enhanced X-ray and H I emission in the same place. Unfortunately, no dynamical information is available for the X-ray wind at large radii, so a comparison of the location of the X-rays and H I in velocity space cannot be made.

In light of our detailed Hα morphological analysis of Sections 4.1.1 and 4.1.2, we see that the southern X-ray ridge lies to the east of the clearly delineated eastern extent of the southern Hα wind. This is a surprise, considering the assumed tight collimation mechanism needed to create such a clear boundary in Hα, since it is unclear how wind-blown gas knots could exist at the position of the X-ray ridge.

Radio emission

Observations at longer wavelengths are the only ones that can penetrate the high levels of attenuation to study the northern inner-wind, and the radio domain is the only one that can give high enough resolution (<1″) to study the morphology in any detail. Fig. 4.8 shows the 5 GHz radio map from Wills *et al.* (1999) overlaid on the *HST*/ACS F656N image, where the four arrows mark the possible chimneys in the northern flow identified by these authors (also seen at 1.4 GHz). The chimneys appear as narrow vents $\lesssim$15 pc in width, and broaden as they extend out of the plane to the north. It is interesting that only chimney 4 has a corresponding radio structure in the south, and has been identified with the brightest, most compact SNR in M82, which may be located in a very high pressure environment that has inhibited its expansion (Wills *et al.* 1999; Pedlar *et al.* 1999). Wills *et al.* comment that the location of regions A and C are "in good agreement with the location of the chimneys" they identify, but by comparing their positions to the Hα image, we find very little evidence for a clear connection. We caution that a significant amount of confusion will arise from high and variable levels optical obscuration on the northern side of the disc therefore hesitate to confirm their findings.

Summary of observations

We will now summarise the important points from the above morphological analysis.

- In the south, the inner-flow ($R \lesssim 500$ pc) is well collimated within angles of 25–30° and emanates distinctly from regions A and C, with a width at the base of $\sim$400 pc. The flow is remarkably structured, exhibiting features that can be traced back to individual starburst clumps. An abrupt decrease in flux occurs at $R \approx 500$ pc corresponding to a dynamical age of <1 Myr.

- A significant and sudden drop in Hα flux is observed at $R \approx 2$ kpc and $R \approx 2.5$ kpc in the southern and northern winds, respectively. At a constant outflow speed of 500 pc Myr^{-1}, this corresponds to a dynamical age of $\sim$5 Myr, and is consistent with the age of the most recent burst of star-formation in the starburst core (4–6 Myr; Förster Schreiber *et al.* 2003). The wind downstream of this intensity drop must therefore have been produced by the remains of the preceding burst (8–15 Myr; Förster Schreiber *et al.* 2003).

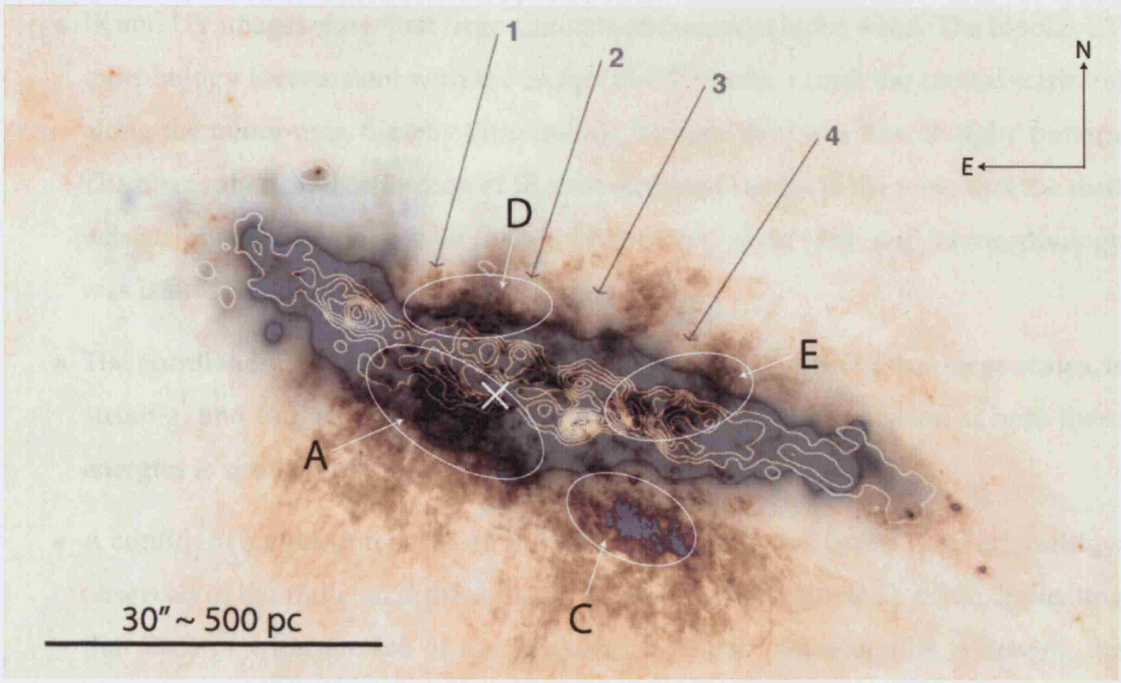

Figure 4.8: Superposition of the 5 GHz VLA image with contours of the unsharp masked version of the same image shown in semi-transparent inverted greyscale (Wills *et al.* 1999), overlaid on the *HST*/ACS F656N image. The four arrows mark the positions of the holes in the radio emission, interpreted as being chimneys in the flow by Wills *et al.*. The main starburst clumps are marked and labelled and the 2.2 μm nucleus is shown with a cross.

- All evidence suggests that at small radii, the southern outflow is brighter and more collimated than the northern plume, but at larger radii ($R \gtrsim 1.75$ kpc) the situation is reversed and the northern wind becomes brighter, has a larger opening angle ($\approx 55°$) and extends much further (up to ~13 kpc in X-rays, corresponding to a dynamical age of 25 Myr, assuming a constant outflow speed).
- The southern outflow is ~parallel to the minor axis, whereas the northern outflow is angled by 5–10° towards north.
- Large-scale H I features seem to be correlated with X-ray wind morphology, indicating that the flow is affected by the presence of cold neutral gas in the halo.
- The difference between the northern and southern outflow morphologies could be due to the influence of the tidally disrupted neutral gas distribution, intrinsically different densities in the haloes, or the propagation of the starburst towards the southern half of the disc.

- IR and UV images show that large amounts of dust exist in the wind. The bipolar UV morphology is consistent with the escape of UV photons from the central starburst along the minor-axis, thereby illuminating the halo dust in a 'search-light' pattern. The near spherical distribution of IR dust emission supports the view that the dust was stripped from the disc by the tidal interaction with M81, and its morphology was later shaped by the wind flow.
- The correlation between X-ray and Hα emission, at both small and large scales, is striking, and indicates that the mechanism for producing emission at both these energies is similar and occurs at the same place.
- A confident connection between the individual chimneys in the northern outflow observed in the radio, and the optical Hα morphology cannot be made, indicating that little of what we see of the starburst at shorter wavelengths is driving the northern outflow.
- Structure is seen down to the resolution limit of every observation, indicating that we are limited by sensitivity and spatial resolution at *all* wavelengths.

4.1.4 Comparison to superwind models

The superwind models described in the Introduction (Chapter 1) have been compared to, and in some cases designed specifically for, the M82 super-galactic wind. The first application of such a theory to the case of M82 was by Chevalier & Clegg (1985), who compared their predictions to the best known observations at the time to derive some basic morphological and kinematical properties of the outflow. Since that ground-breaking publication, there have been a number of further attempts to compare or tailor superwind models to the M82 wind, including Tomisaka & Ikeuchi (1988), Suchkov *et al.* (1996) and a series of papers expanding on the idea first proposed by Tenorio-Tagle *et al.* (2003) (Silich *et al.* 2004; Tenorio-Tagle *et al.* 2005, 2006). In light of our detailed morphological analysis of the superwind, we can re-evaluate these models and their predictions regarding M82.

Beginning with the simplest model (Chevalier & Clegg 1985), we now compare their assumption of a single smooth energy injection zone (the starburst), which in their model, results in an adiabatic, freely expanding, spherically symmetric wind, to our results. This form of model predicts an Hα outflow geometry resembling a smooth cone (hence limb-brightened in appearance) with an opening angle, assuming the appropriate disc scale

height, of ~80–90°. The hot (X-ray emitting) wind would flow down the centre of this cone, and out into the halo, resulting in a strong prediction of the relative locations of Hα and X-ray emission. A wide, limb-brightened, smooth outflow cone is not consistent with our optical emission line images (see also SBH98). On the contrary, we find highly detailed structure at every scale, with filaments, loops and arches distributed throughout the flow. Furthermore, the X-ray morphology is seen to correlate well with that of the Hα emission, ruling out the prediction of a collimated X-ray wind surrounded by Hα "walls". A detailed discussion of models which can predict the coincidence of X-ray and Hα emission is given in the Introduction.

Suchkov *et al.* (1996) developed a superwind model that treated the effect of mass-loading for the first time, after it was realised that the gas mass needed to produce the observed level of X-ray emission is larger than that thought to be ejected by SNe alone. A detailed comparison of this model to the M82 case is given in their paper, so here we only summarise their main points. They consider two sets of models, both with an inner collimating cone (with height 1.5 kpc) and an outer halo cone. The first set comprises a 'fan-like wind' with an outer opening angle of 60° (similar to what we find for the northern plume) and two different sizes of wind base ($r_{\rm base}$ = 500 and 150 pc). The second model results in a 'jet-like wind' (their terminology) with an opening angle of 22° and $r_{\rm base}$ = 160 pc. They find both models to satisfy the X-ray constraints on pressure and temperature profiles, and that the outflow must be strongly collimated over the central 1.5 kpc, but become less collimated in the outer halo. Their results lead them to conclude that the mass-loading rate must be a factor of 2–5 times larger than the mass deposition rate expected from SNe, and that all the mass-loading must be confined to a thin layer within the central starburst. These results have far-reaching consequences, but in light of more recent, higher resolution imaging in both optical and X-ray wavebands, we see that their adopted initial conditions would benefit from a little adjustment. From our above analysis, we find that the wind base is at least 400 pc wide, and that any increase in opening angle occurs at a radius of <500 pc (SBH98). Furthermore, we have found that the morphology of the northern and southern plumes are significantly different, and both have opening angles $\gg$22°.

By far the most hopeful models proposed to date to explain the observed detailed structure of the inner superwind are the models of Tenorio-Tagle *et al.* (2003, hereafter TSM03). As described in the Introduction, these models were the first to assume that

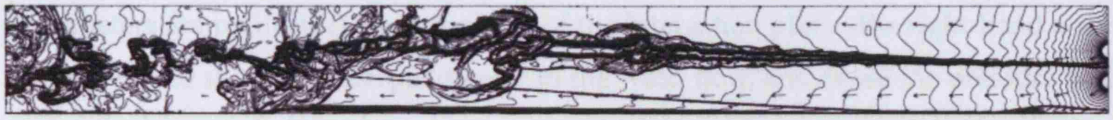

Figure 4.9: Cross-sectional cut showing isodensity contours and the velocity field (arrows) of a developing superwind resulting from the interaction between two SSCs separated by 30 pc and situated on a common plane, reproduced from Tenorio-Tagle *et al.* (2003). The metallicity of the flow is set at $Z = 10\ Z_{\odot}$, and the evolutionary time for this cut is 1.4×10^6 yr. The size of the plot is 100 pc $\times$ 1 kpc.

energy deposition into the wind does not arise from a single star-forming clump spanning tens of parsecs, but from multiple discrete sources (super-star clusters; SSCs) distributed throughout the starburst region. As we have seen in Chapter 3, and made obvious in the preceding sections, the central starburst in M82 is by no means composed of smoothly distributed star-formation, but of many hundreds of SSCs arranged in irregular clumps or complexes injecting energy at a very localised scale (Wills *et al.* 1999; Melo *et al.* 2005).

As TSM03 point out, once a channel has been carved in the ISM and the superwind has developed, major differences will arise from the assumption of a single or a multiple source of energy. For example, a freely expanding wind will experience strong radiative cooling, resulting in the prediction of X-ray emission restricted to only a few times the size of the SB nucleus (not observed), Hα emission from the lateral walls of the disrupted supershell (therefore strongly limb-brightened; also not observed), and the wind base being very wide (several kpc; much larger than extent of starburst). It is therefore essential for the success of any superwind model applied to M82 for multiple sources to be considered. Furthermore, since we have seen that the small-scale inner-wind filaments emanate distinctly from individual starburst clumps, it makes perfect sense to try to model these structures as caused by interactions from the individual energy sources, rather than simply instabilities in a large-scale blown-out supershell structure. Fig. 4.9 shows a reproduction of a two-dimentional superwind model from TSM03, illustrating how the structure of the superwind can form through interactions of the winds from individual clusters (see TSM03 for a more detailed description of this figure).

The interaction of neighbouring supersonic winds, as modelled by TSM03, causes the immediate formation of reverse shocks accompanied by a high pressure region directly behind them. These shocks propagate initially in a spherically symmetric fashion (the

star clusters are point-like), so at the base of the interaction plane (the right-hand edge of Fig. 4.9), the shocks are perpendicular to the wind flow, and cause the pressure and temperature to reach their highest values. The high densities promote radiative cooling and a loss of temperature behind the shocks. This leads to a condensation of gas, and the build-up of narrow, dense, cold filaments. These dense structures are then entrained into the wind flow and dragged out away from the interaction plane. Effects such as Kelvin-Helmholtz instabilities will act to "broaden, twist and generally shape" the filaments as they flow out of the central starburst region. The enhanced densities of these structures will lead them to be susceptible to photoionization from the intense UV field from the central starburst, and due to their shape and enhanced cross-section, shock interactions with the fast-flowing wind will cause emission of soft X-rays.

TSM03 consider two models, one involving three clusters irregularly spaced by 30 and 60 pc, and one following the interaction of just two clusters, 30 pc apart (as shown in Fig. 4.9). In both these scenarios, the clusters are located on a single flat plane. Whilst these models are rather small-scale compared to the extent of M82 starburst, we can nonetheless make some general comparisons to the results of our morphological analysis. We have already mentioned that in zones 2 and 3 (see Fig. 4.4), we see coherent linear features in the southern wind flow extending out to ~200 pc. We also identify a turbulent, chaotic region (zone 4), most likely resulting from flow instabilities, extending from ~500–1000 pc in radius. These observations match well with the TSM03 predictions. The temperature distributions predicted are consistent with the location of the Hα emitting and X-ray emitting gas, *i.e.* 10^4–10^5 K gas is found along the perpendicular filaments resulting from the cluster wind interactions, and 10^7–10^8 K gas is found near the end of the flow (or computational grid), where instabilities have acted to break up the coherent structures. The first chaotic region (zone 1) found close to the starburst core is, however, difficult to reconcile with these models. We have measured the base of the southern outflow to be 400 pc, and in the inner-wind coherent structure is observed out to distances of ~500 pc from the central starburst. Furthermore, the wind driven from regions A and C must be older than the clusters found within these clumps (~4–6 Myr; Förster Schreiber *et al.* 2003; Chapter 3). Therefore, since TSM03 track the evolution of the wind only up to a t_{max} of 1.4×10^6 yr, and they consider the interaction of two or three clusters over a (relatively small) 100 pc $\times$ 1 kpc grid, we cannot expect the models to accurately predict every feature observed.

Obviously, the intensity of star-formation and energy ejected from each SSC is affected by their individual age, size, mass, mass function and metallicity. Moreover, the total number of SSCs, their compactness, their distribution within a starburst, and the ambient density of the intra- and inter-cluster medium (*i.e.* the ISM), will all have an impact on the development of a superwind at the small to medium scales. Clearly, models predicting superwind evolution over a larger grid for more clusters for a longer time period are required to explore the full parameter space for this promising theory, and should ideally take into account the third dimension. Predictions including the amount of matter entrained into the flow, the flow speed, and emission line fluxes, ratios and widths would also be very useful for comparing to observations.

4.2 Integral field spectroscopy of the wind

In this chapter, we have so far examined the M82 superwind morphology in detail using high-resolution images. We will now attempt to quantify a little of what we have found from this analysis by discussing results of observations taken with the WIYN DensePak and SparsePak IFUs of the wind roots and parts of the outer northern outflow. These instruments, the observations, and the steps followed to reduce the data-sets, are described in Chapter 2, Sections 2.3.2 and 2.3.3. The advantage of performing spatially resolved spectroscopy on M82 is that we can combine both morphological information (including what we have learnt in the first half of this chapter) with dynamical data and more precise measurements of the line intensities to get a better understanding of the wind formation and evolution mechanisms. Instead of having a one-dimensional long-slit or two-dinemsional image, we now have simultaneous access to the third dimension, and can easily relate changes in spectral properties to spatial locations.

4.2.1 DensePak observations of the wind roots

Fig. 4.10 shows a reconstructed image of the three combined DensePak fields in the line-free continuum region 6645–6660 Å, overlaid on a WIYN *R*-band image of the nuclear regions. The inset shows the position of the DensePak fields on the *HST*+WIYN narrow-band composite presented in Section 4.1.2, for comparison to the Hα emission from the wind. Position 1 was centred on region A of the starburst, and is also coincident with parts of the two STIS slits discussed in Chapter 2, Section 2.2.1. Position 2 samples the region

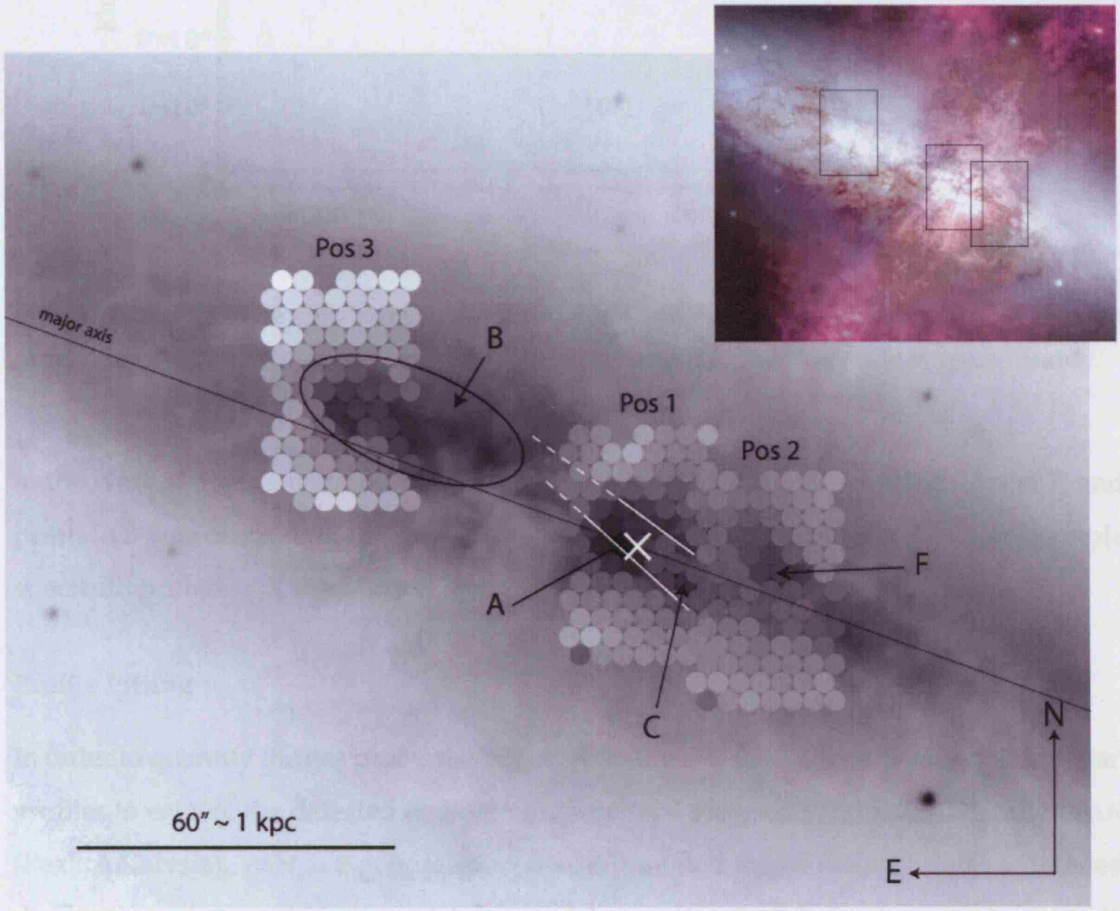

Figure 4.10: WIYN *R*-band image of M82 (inverted greyscale) overlaid with DensePak continuum flux maps (also inverted) for all three pointings. Some of the bright starburst clumps/clusters are marked, and the position of the 2.2 μm nucleus is shown with a white cross. The galaxy major axis (PA = 70°) is indicated by a solid line. The position of the two STIS slits discussed in Chapter 2 are shown as dashed lines (the solid sections are where Hα radial velocities could be measured). The inset shows a section of the *HST*+WIYN composite presented in Section 4.1.2 covering the same area as that shown in the main image, and includes narrow-band emission from the wind outflow. The outlines of the DensePak fields are shown for comparison.

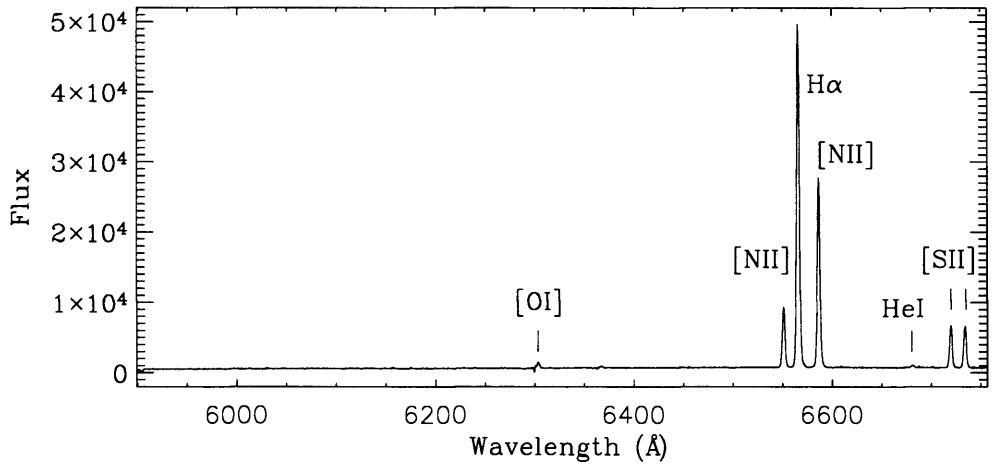

Figure 4.11: Example spectrum from fibre 35 in position 1 showing the full wavelength range observed. The detected emission lines are labelled; the flux scale is uncalibrated.

to the west of the main starburst nucleus, including the area surrounding Cluster F, and position 3 was centred on the fossil starburst contained within region B. A full example spectrum from one of the fibres is shown in Fig. 4.11.

Profile Fitting

In order to quantify the gas properties observed in the IFU fields, we fitted model Gaussian profiles to each of the detected emission lines using a program written in IDL called PAN (Peak ANalysis). PAN is a general-purpose, automated curve-fitting utility; a detailed description of the program, and how we have customised it for our use is given in Chapter 6.

Examples of the Hα and [N II]λ6583 line profiles from fibres covering the nuclear starburst regions are shown in Fig. 4.12, together with the Gaussian fits needed to model the integrated shapes. These are shown to illustrate the high quality of the spectra and to show the variety of integrated shapes observed.

Hα is detected in every fibre for all three positions; in many of the fibres centred on the starburst nucleus, the S/N of the emission lines is very high (>500 for Hα at the centre of position 1). This fact, coupled with the high resolution of the spectra (45 km s^{-1}; Section 2.3.2), have allowed us to quantify the line profile shapes to a high degree of accuracy. In general, the emission lines are composed of a bright, narrow component (hereafter referred to as C1), a broad, fainter, underlying component (C2), and in some

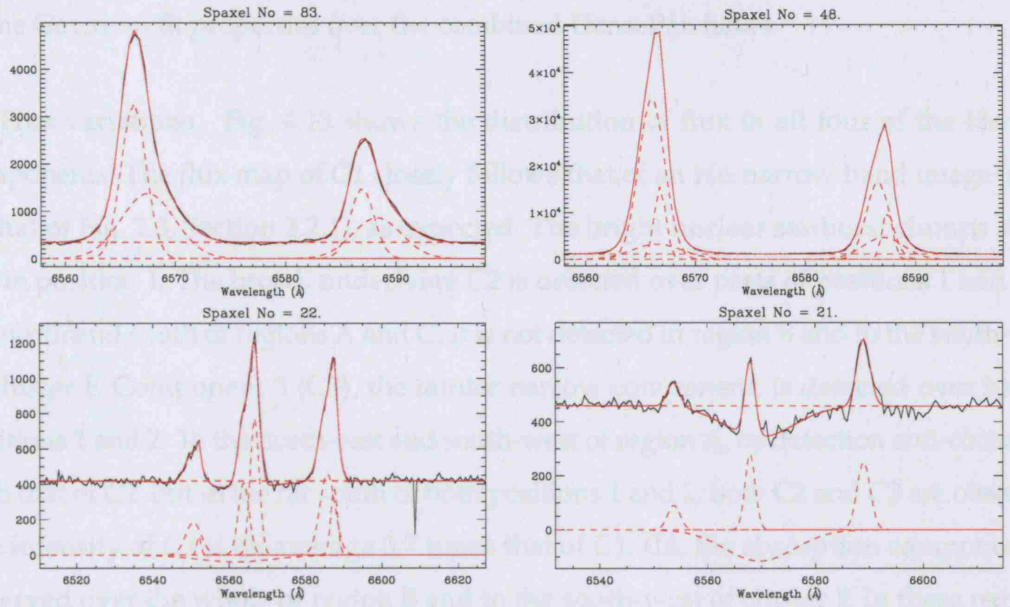

Figure 4.12: Example Hα and [N II]λ6583 line profiles from the inner-wind north of position 1 *(upper-left)*, just to the east of region A *(upper-right)*, to the south-west of cluster F *(lower-left)*, and south of the centre of region B *(lower-right)*. This sample was chosen to represent a range in line profile shapes including broad, underlying emission features, second narrow peaks, and absorption profiles. The observed data are plotted as a solid black line, and the summed model fit is plotted as a solid red line. The flat continuum and individual Gaussian profiles are plotted as red dashed lines relative to the y-axis zero level. The units are in an arbitrary intensity scale.

cases (Hα only) a stellar absorption component (C4). In the wind region, double peaked narrow components are seen. Where this is the case, the brighter of the two is assigned to C1 and the fainter to C3, regardless of their wavelength relationship. This consistent approach helped limit the confusion that might arise during analysis as to which Gaussian fit belonged to which component of the line. The appropriate number of components to fit to each line was determined by a combination of the χ^2 fit value and visual inspection of the data. The result is a measurement of the continuum level, and the radial velocity, flux, and FWHM for each Gaussian component.

Results

To display the results in a meaningful way, it was first necessary to combine the data-sets for all three fields so that they could be shown together at the same scale. The visualisation tool, DAISY (described in detail in Chapter 6), was then used to plot the spatial variation

of the Gaussian fit properties over the combined DensePak fields.

Flux variations Fig. 4.13 shows the distribution of flux in all four of the Hα line components. The flux map of C1 closely follows that of an Hα narrow-band image (such as that of Fig. 2.3, Section 2.2.1), as expected. The bright nuclear starburst clumps stand out in position 1. The broad, underlying C2 is detected over parts of positions 1 and 2, to the north and south of regions A and C. It is not detected in region B and to the south-west of cluster F. Component 3 (C3), the fainter narrow component, is detected over half of positions 1 and 2. To the north-east and south-west of region A, its detection anti-correlates with that of C2, but in the far south of both positions 1 and 2, both C2 and C3 are observed. The intensity of C3 is on average 0.7 times that of C1. C4, the absorption component, is observed over the whole of region B and to the south-west of cluster F. In these regions, an absorption component is expected since these are the older parts of the starburst and hence contain a large fraction of A-type stars which absorb Hα in their atmospheres (de Grijs *et al.* 2001; Förster Schreiber *et al.* 2003). The Hα flux absorbed is at a maximum in the core of region B. Example line profiles from spaxels in region B and to the south-west of cluster F are given in Fig. 4.12, clearly illustrating the presence of broad Hα absorption.

FWHM variations The Gaussian full-width half-maximum (FWHM; corrected for instrumental broadening) is shown in Fig. 4.14. The FWHM of C1 is approximately 70–100 km s^{-1}, but increases up to 150–180 km s^{-1} in the far south-west of position 2, towards the east of position 1, and in the south of position 3. These areas of broader C1 lines are coincident with faint absorption, which causes difficulties in fitting the model profiles. Since here the S/N of the Hα emission is also low, a confident fit, including the absorption is made impossible, and results in artificially elevated C1 FWHMs. In the core of region B (upper half of position 3), the C1 line width decreases down to the resolution limit of the spectra. The broad underlying component, C2, is found in all the nuclear starburst regions. In clumps A and C (south of the nucleus), this component exhibits widths of >200 km s^{-1}, but to the north, in regions D and E, the width is narrower. In some cases this has caused the line to be assigned to C3 (*e.g.* the four orange spaxels just to the north-east of the nucleus, covering region D). These measurements confirm what we found from our STIS long-slit observations, where line widths north of the nucleus were found to be generally narrower than in the south. The broadest C2 widths are found in the farthest spaxels

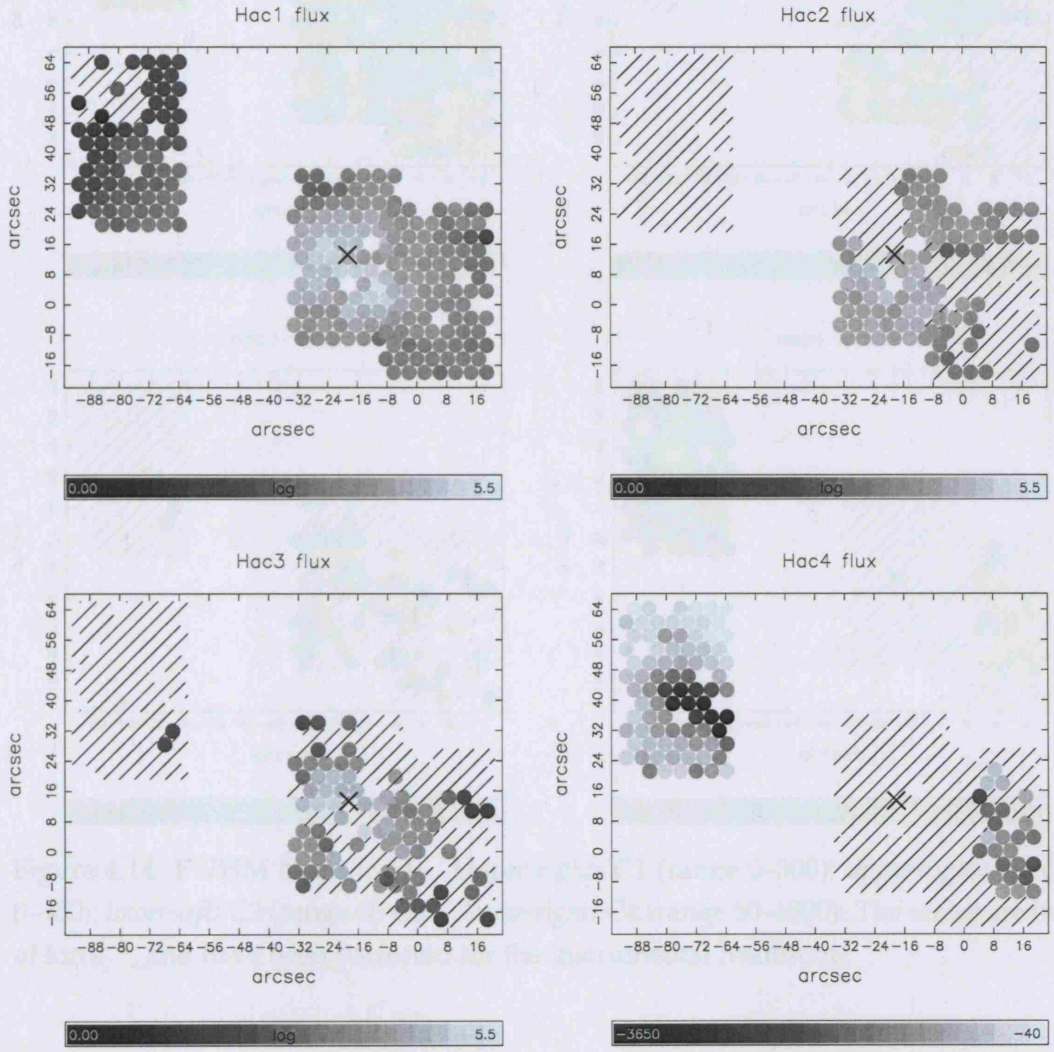

Figure 4.13: Flux maps in Hα for all three fields. *Upper-left:* C1 in log scale (range 0–5.5); *upper-right:* C2 in log scale (range 0–5.5); *lower-left:* C3 in log scale (range 0–5.5); *lower-right:* C4 in linear scale (range −3650 to −40). The flux scale is in arbitrary units. The position of the 2.2 μm nucleus is denoted with a cross on each map. The axis scales are in arcsecs, and the origin indicates the field-centre of position 2.

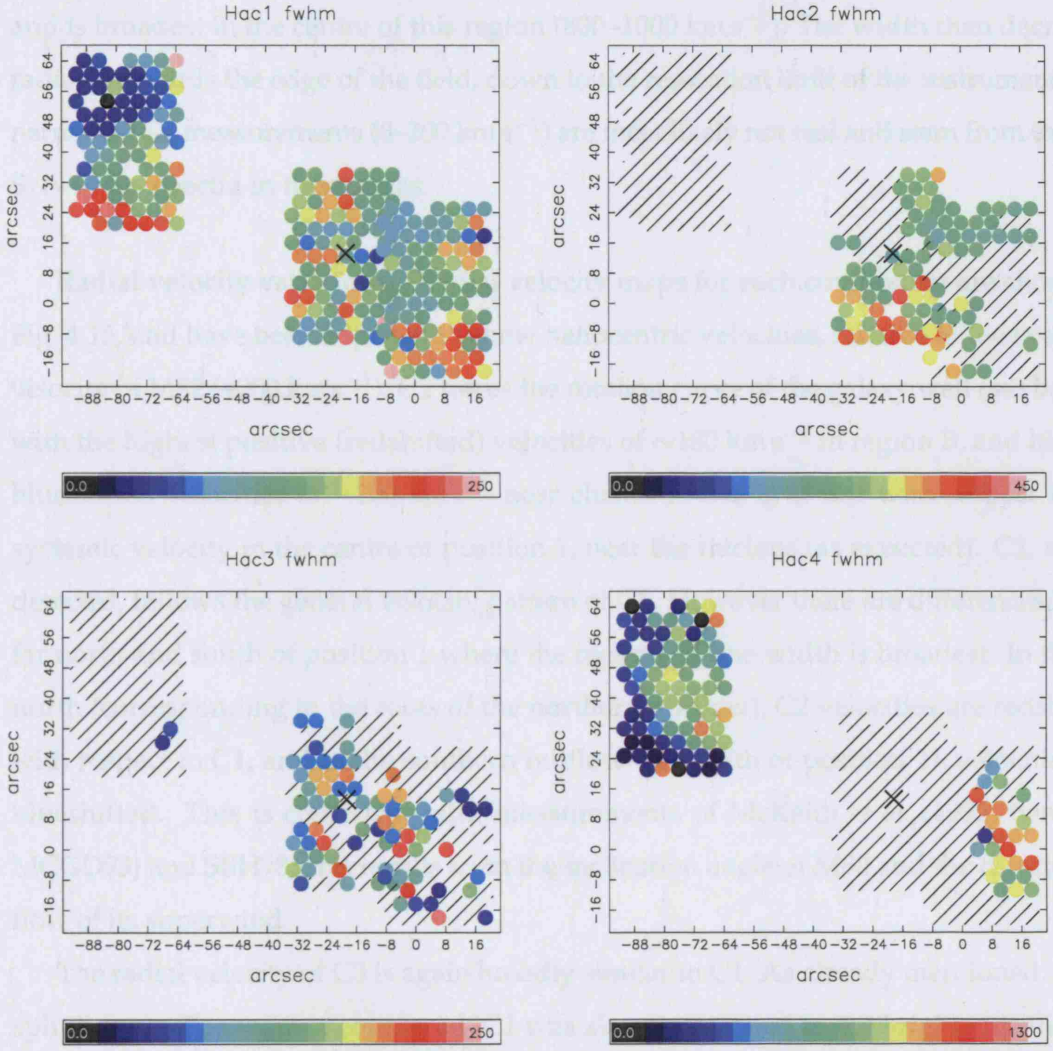

Figure 4.14: FWHM maps in Hα. *Upper-right:* C1 (range 0–300); *upper-right:* C2 (range 0–450); *lower-left:* C3 (range 50–300); *lower-right:* C4 (range 50–1500). The scales are in units of km s^{-1}, and have been corrected for the instrumental resolution.

from the starburst nucleus (at radii of 400–500 pc), reaching up to 400–450 km s^{-1} in the lower half of position 1, and are coincident with the point of inflection in the wind outflow velocities and the hypothesised energy injection zone of the southern outflow (McKeith *et al.* 1995; SBH98), where it is thought the wind flow becomes supersonic.

C3 exhibits line widths that are the same or less than that of C1. The FWHM map is fairly noisy, but it appears that the broadest C3 lines are coincident with regions A and C. The absorption component, C4, is broadest in the region to the south-west of cluster F. Here its width is $\sim$1500 km s^{-1}, however the associated uncertainties are fairly high ($\approx \pm$100 km s^{-1}). C4 is detected over the whole of position 3 (covering region B),

and is broadest in the centre of this region (800–1000 km s^{-1}). The width then decreases radially towards the edge of the field, down to the resolution limit of the instrument. The narrowest C4 measurements (0–200 km s^{-1}) are most likely not real and stem from the low S/N of the spectra in those areas.

Radial velocity variations Radial velocity maps for each component are shown in Fig. 4.15, and have been adjusted to show heliocentric velocities, relative to the systemic velocity of M82 (+200 km s^{-1}). C1 traces the rotation curve of the galaxy well (see below), with the highest positive (redshifted) velocities of ∼180 km s^{-1} in region B, and highest blueshifted velocities of −200 km s^{-1} near cluster F. Gas is at rest with respect to the systemic velocity in the centre of position 1, near the nucleus (as expected). C2, where detected, follows the general velocity pattern of C1. However there are differences in the far north and south of position 1 where the measured line width is broadest. In the far north (corresponding to the roots of the northern outflow), C2 velocities are redshifted with respect to C1, and in the southern outflow (far south of position 1), velocities are blueshifted. This is consistent with measurements of McKeith *et al.* (1993, hereafter MCGD93) and SBH98, and results from the inclination angle of M82 and the direction of flow of its superwind.

The radial velocity of C3 is again broadly similar to C1. As already mentioned, when split line profiles were encountered, C1 was always assigned to the brighter of the two components. In the southern outflow region, we see a brighter blueshifted component (C1) and a fainter redshifted component (C2). This is again consistent with the inclination and outflow direction of the M82 wind whereby the southern cone is angled towards us. The absorption component (C4) follows the galactic rotation pattern of C1, but is exaggerated in comparison. The most positive (redshifted) velocities are seen over the whole of position 3 (region B), and have values of ∼300 km s^{-1}. The most negative velocities are seen to the south-west of cluster F at ∼−350 km s^{-1}. These extremes are more than 100 km s^{-1} larger than in C1.

Taking full advantage of the spatially resolved nature of our observations, we have extracted line velocities for each component from spaxels located ±5″ away from the galaxy major-axis (PA = 70°; Telesco *et al.* 1991) in order to produce a rotation curve. Fig. 4.16 shows the position-velocity diagram for all four line components, relative to the position of the galaxy nucleus. We will now compare this diagram to our optical *HST* STIS

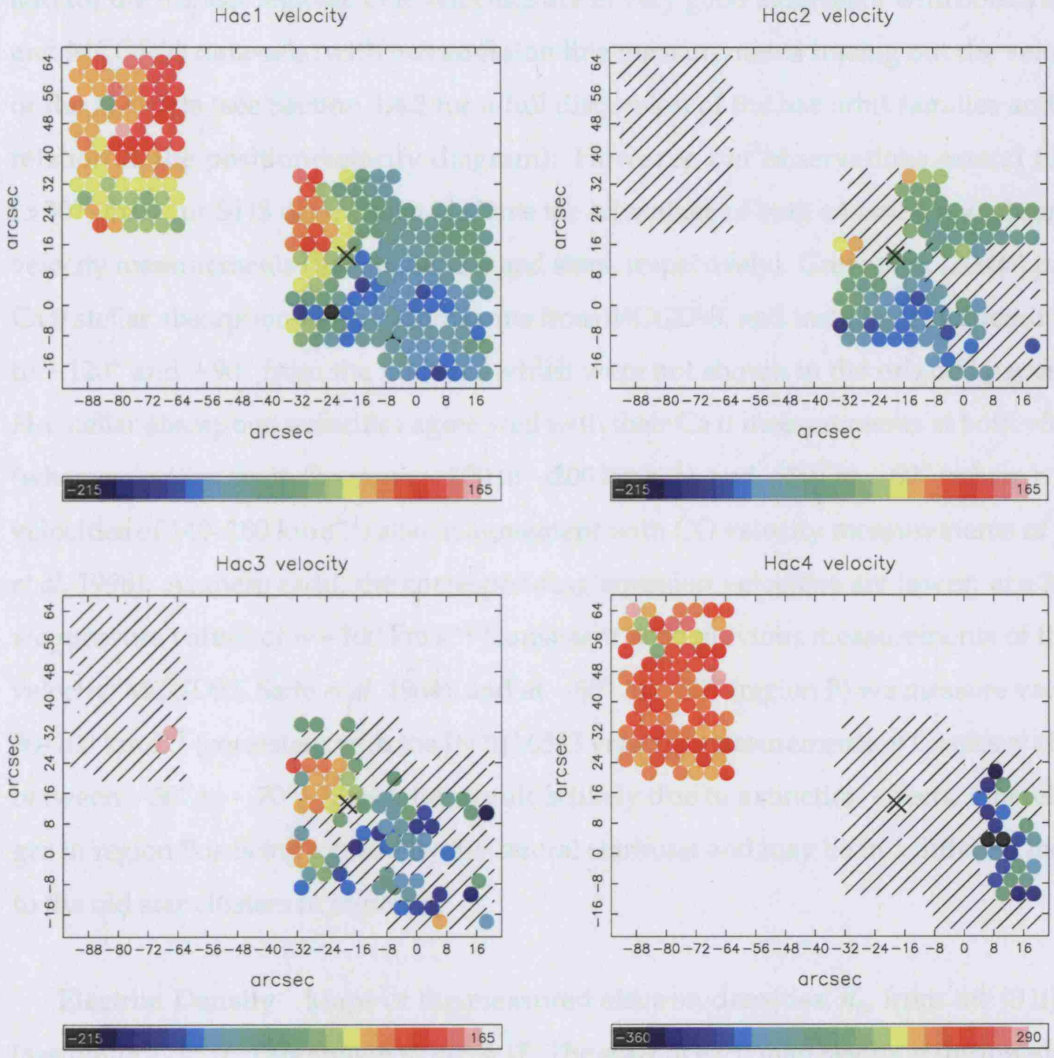

Figure 4.15: Radial velocity maps in Hα. *Upper-right:* C1 (range −205 to 180); *upper-right:* C2 (range −205 to 180); *lower-left:* C3 (range −205 to 230); *lower-right:* C4 (range −350 to 300). The scales are in units of heliocentric km s^{-1} and have been adjusted to be relative to the systemic velocity of M82 (+200 km s^{-1}).

data presented in Section 3.3.3, and the near-IR data given by MCGD93 and discussed in Greve *et al.* (2002*a*).

Since the spatial-resolution of the DensePak data is much coarser than the long-slit measurements of both our STIS data and those given by MCGD93, there is little we can add for the nuclear regions. Our velocities are in very good agreement with both the STIS and MCGD93 data-sets, with our emission line measurements tracing out the velocities of the x_1-orbits (see Section 3.4.2 for a full discussion of the bar orbit families and their relation to the position-velocity diagram). However, our observations extend further (>30″) than our STIS data, where we have the advantage of both emission and absorption velocity measurements (tracing the gas and stars, respectively). Greve *et al.* (2002*a*) present Ca II stellar absorption line measurements from MCGD93, and include data extending out to −120″ and +90″ from the nucleus, which were not shown in the original paper. Our Hα stellar absorption velocities agree well with their Ca II measurements at both +30–40″ (where velocities are in the range −100 to −200 km s^{-1}), and −50″ to −80″ (where we find velocities of 140–180 km s^{-1}; also in agreement with CO velocity measurements of Sofue *et al.* 1998). At these radii, the corresponding emission velocities are lower: at +30–40″ we measure values of $\sim$−100 km s^{-1} (consistent with previous measurements of the gas velocity; MCGD93, Saito *et al.* 1984), and at −80″ to −50″ (region B) we measure values of 50–100 km s^{-1} (consistent with the [N II]λ6583 velocity measurements of Castles *et al.* 1991, between −50″ to −70″). This latter result is likely due to extinction effects, whereby the gas in region B is being ionized by the central starburst and may be in a different location to the old star clusters in region B.

Electron Density Maps of the measured electron densities, n_e, from the [S II] ratio (assuming $T_e = 10^4$) are shown in Fig. 4.17. The scale of each map begins at the low-density limit for this indicator ($\sim$100 cm^{-3}; Osterbrock 1989). The S/N of the [S II] lines is such that we can only identify a maximum of two components in any one spaxel. In places where we identify three components in Hα, the second component of [S II] will in most cases be equivalent to Hα C3. In C1 (left-hand panel) we see that the highest densities (up to 900 cm^{-3}) are found in the vicinity of region A. The majority of spaxels in position 2 have densities close to or at the low-density limit; however in region B, a significant number of spaxels show evidence for densities reaching 500–600 cm^{-3}. The right-hand panel shows densities derived from C2 of the [S II] lines. Here we see values rising to

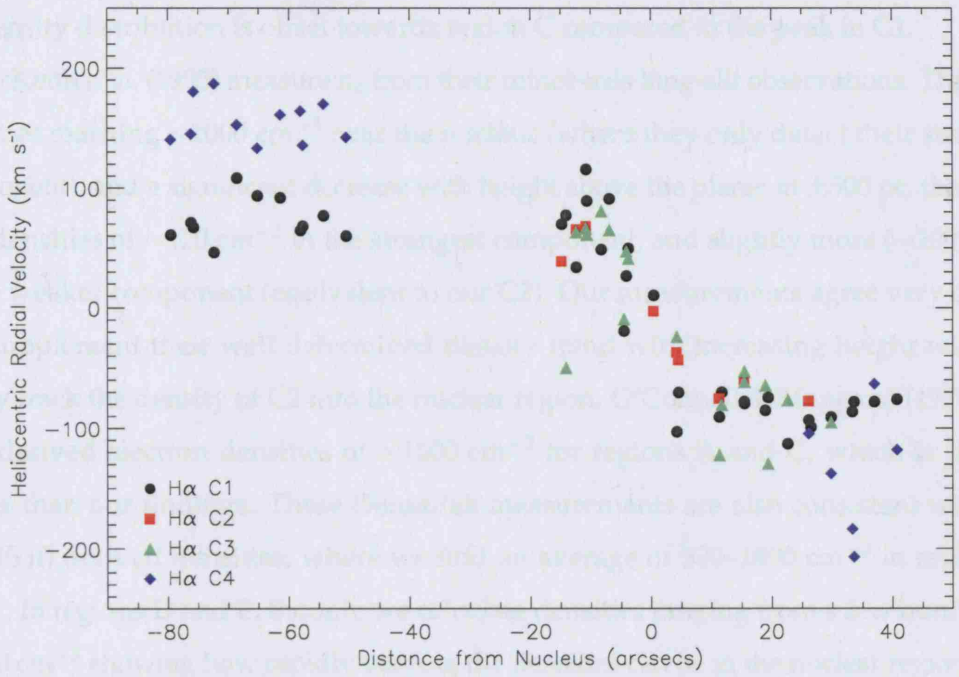

Figure 4.16: The position-velocity diagram extracted from spaxels located $\pm 5''$ from the major-axis, where the velocities are shown with respect to $v_{\rm sys}$. Error bars are not shown since they are approximately the same size as the symbols, except for C4, where the uncertainties lie in the range $\pm$30–50 km s^{-1}.

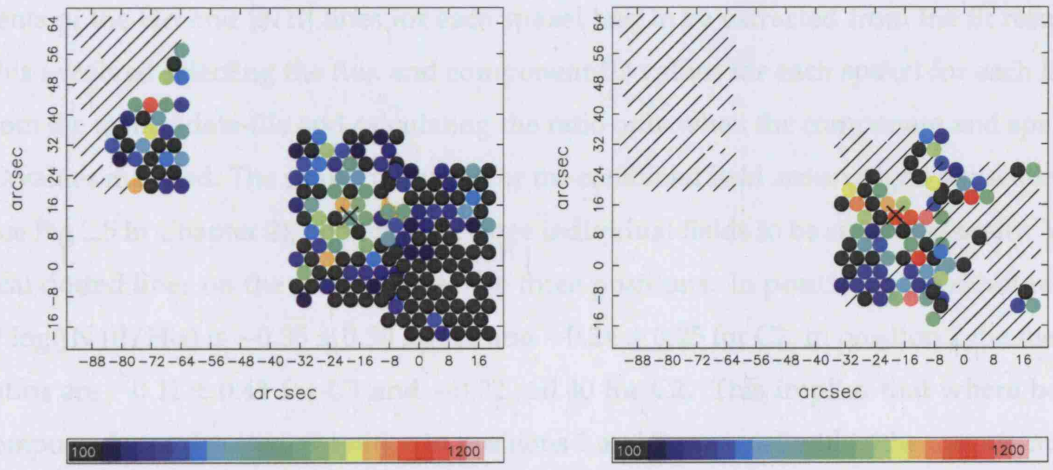

Figure 4.17: Map of the derived $n_{\rm e}$ for *left:* C1 (range 100–1200) and *right:* C2 (range 100–1200) for the three DensePak fields. Units are in cm^{-3}, and uncertainties lie in the range $\pm$500 for the highest densities to $\pm$50 for the lowest.

$\gtrsim$1000 cm^{-3} in the spaxels covering regions A and C, but it is interesting that the peak of the density distribution is offset towards region C compared to the peak in C1.

McKeith *et al.* (1995) measure n_e from their minor-axis long-slit observations. They find densities reaching $\sim$1000 cm^{-3} near the nucleus (where they only detect their strongest component), and a significant decrease with height above the plane: at $\pm$500 pc, they measure densities of $\sim$120 cm^{-3} in the strongest component, and slightly more ($\sim$200 cm^{-3}) in the weaker component (equivalent to our C2). Our measurements agree very closely, and supplement their well determined density trend with increasing height with our ability track the density of C2 into the nuclear region. O'Connell & Mangano (1978) find [S II] derived electron densities of $\sim$1800 cm^{-3} for regions A and C, which is slightly higher than our findings. These DensePak measurements are also consistent with our STIS [S II] derived densities, where we find an average of 500–1000 cm^{-3} in regions A and C. In regions D and E, though, we calculate densities ranging from a few hundred to >2000 cm^{-3} showing how rapidly varying the densities can be in the nuclear regions. It is not unsurprising then that we do not see the highest densities since these are found in small knots which cannot be resolved with DensePak, and the densities measured become diluted by the surrounding, more diffuse gas.

Excitation ratios Fig. 4.18 shows the ratio of [N II]λ6583/Hα for both C1 and C2 plotted against spaxel number. In order to plot these values, the corresponding components of the Hα and [N II] lines for each spaxel had to be extracted from the fit results. This involved selecting the flux and component ID values for each spaxel for each line from the results data-file and calculating the ratio only when the component and spaxel ID values matched. The spaxel numbers for the combined field are arranged sequentially (see Fig 2.5 in Chapter 2), allowing the three individual fields to be separated easily. Vertical dotted lines on the plot separate the three positions. In position 1 the mean ratio of log([N II]/Hα) is -0.35 ± 0.30 for C1 and -0.24 ± 0.25 for C2; in position 2 the mean ratios are -0.11 ± 0.41 for C1 and -0.32 ± 0.40 for C2. This implies that where both components are detected, the ratios in positions 1 and 2 are equal within the uncertainties. In position 2, there is more of a scatter towards higher ratios in C1 and lower ratios in C2. In position 3, a trend in ratio with spaxel number is seen, where higher ratios are found at greater spaxel numbers.

The spatial distribution of these values is mapped in Fig. 4.19. The change in flux

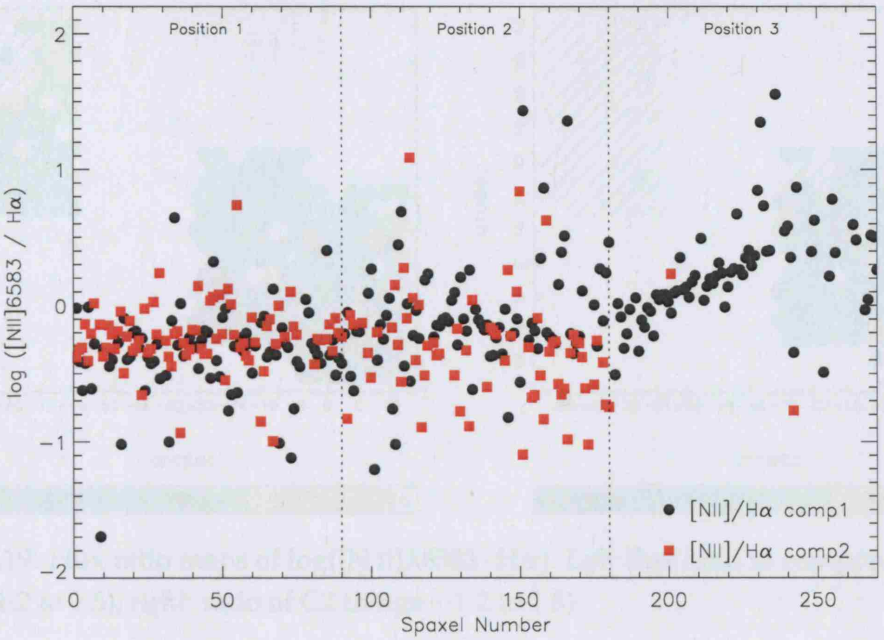

Figure 4.18: Plot of the flux ratio [N II]λ6583/Hα for all three fields. The flux ratio in C1 is shown with black circles, and of C2 with red squares. The three positions are divided by spaxel number (see Fig. 2.5 for the spatial format of the fibre numbers) and shown by vertical dotted lines.

ratios in position 3 is now clearly seen as a gradient from the south to the centre-north of the field. A close inspection of the spectra, their corresponding fits, and the maps plotted in the preceding figures, reveals that the spaxels exhibiting log([N II]/Hα) > 0 have an Hα absorption component. Since flux from the emission components C1 and C2 is being absorbed by C4, but no flux is absorbed from either of the [N II] components, the flux ratio is overestimated, but a correction cannot be made since it is not known in what ratio C1 and C2 should be corrected (*i.e.* how much is being absorbed from each component). We therefore disregard these points in the following analysis. In the north-west of position 2, log([N II]/Hα) decreases down to ~ -1 in C2, explaining the downward scatter in the plot mentioned above. This location coincides with the western part of the inner northern outflow.

The distribution of [S II]$\lambda\lambda$6717, 6713/Hα is very similar to that of [N II]/Hα, and of course suffers from the same Hα absorption effects, so is not shown here. We find in position 1 the mean ratio of log([S II]/Hα) is -0.55 ± 0.33 for C1 and -0.48 ± 0.33 for C2; in position 2 the mean ratios are -0.14 ± 0.39 for C1 and -0.40 ± 0.33 for C2.

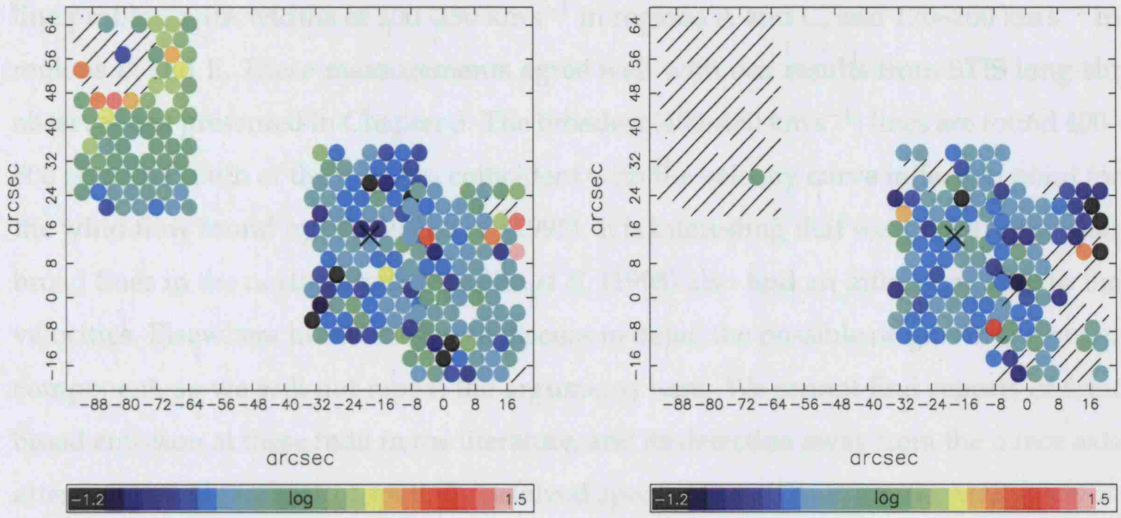

Figure 4.19: Flux ratio maps of log([N II]λ6583/Hα). *Left:* flux ratio in component 1 (C1; range -1.2 to 1.5); *right:* ratio of C2 (range -1.2 to 1.5).

O'Connell & Mangano (1978) find a log([N II]/Hα) ratio for the nuclear regions (including clumps A, C and E) of -0.28 from long-slit data. SBH98 find uniform and low values of log([N II]/Hα) in the inner 1 kpc of the M82 outflow ranging from -0.5 to -0.2. Both these results are consistent with our measurements. The line ratio maps of SBH98 also show very high values further out in the disc, in the same place as we find exaggerated values due to Hα absorption. Since SBH98 also made [O III] measurements, they were able to plot their flux ratios on nebular diagnostic graphs, and were able to determine that the inner superwind region lies distinctly in the cool H II region regime. The lack of [O III] flux rules out shocks as being significant contributors to the ionization balance. At heights of 1 kpc or more, SBH98 find increasing values of [N II]/Hα which they attribute to a dilution of the radiation field in the outer-wind together with a possible increasing influence of shocks.

Summary and Discussion

We have observed three regions of the M82 disc with the DensePak integral field unit, covering the nuclear starburst and the fossil starburst region to the north-east. We detect Hα in every spaxel; in some places we can identify three emission components, and in parts of the disc which do not have current starburst activity, we also detect an absorption component. In the nuclear regions, we find a broad, underlying component to the emission

line profiles, with widths of 200–250 km s^{-1} in regions A and C, and 170–200 km s^{-1} in regions D and E. These measurements agree well with our results from STIS long-slit observations presented in Chapter 3. The broadest (400–450 km s^{-1}) lines are found 400–500 pc to the south of the nucleus, coincident with the velocity curve inflection point for the wind flow found by McKeith *et al.* (1995). It is interesting that we do not see similar broad lines in the north, where McKeith *et al.* (1995) also find an inflection point in the velocities. Elsewhere in this thesis we discuss in detail the possible origins of the broad component, so we will not repeat the arguments here. We cannot find reports of faint broad emission at these radii in the literature, and its detection away from the minor axis attests to the advantages of spatially resolved spectroscopy. For example, McKeith *et al.* (1995) place their long-slit parallel to the minor axis, thus missing this region. SBH98 make use of Fabry-Perot observations which have very good spatial resolution, but only make an attempt to fit the brightest component of the emission lines across their field-of-view, so do not discuss line-width variations.

The Hα absorption component is detected only where the older stellar populations are found within the disc. The depth and breadth of the absorption feature peaks in the centre of region B, but the broadest absorption is found south-west of cluster F, where its FWHM reaches >1000 km s^{-1}. The emission and absorption profiles have been used to trace the velocity of the stars and gas over the section of the disc covered by our observations. Our measurements agree well with the literature for regions previously observed. We have been able to extend determinations of the gas velocity to larger radii in the north-east and find a velocity offset between the gas and stars of $\sim$80 km s^{-1}, but attribute it to simple extinction effects.

We find the highest electron densities in the nuclear regions, but remarkably, find the highest densities in C2 rather than C1. This is strange since we can explain not measuring the highest densities found by O'Connell & Mangano (1978) and with our STIS data in C1, by spatial dilution caused by our coarse spatial sampling, but measuring densities as high as $\sim$1000 cm^{-3} in C2 is surprising. These densities do not reflect those of the superwind itself, but of photoionized 10^4 K gas making up the filaments and other structure described in Section 4.1 that is entrained into the flow. We were also able to measure the flux ratios of [N II]/Hα and [S II]/Hα and find uniform and low values over the whole of the nuclear regions in good agreement with our STIS measurements. This indicates that the excitation and ionization field strength is constant over the whole starburst and that photoionization

is the dominant ionization mechanism. The only region which does not conform to this homogeneous distribution is the north-west of position 2 coincident with part of the northern wind flow, where a particularly low ratio is found in C2.

4.2.2 SparsePak observations of the northern wind plume

Two fields covering part of the northern wind plume in M82 were observed with the 'formatted field unit' SparsePak. The data and the reduction process was described in Chapter 2. Overlapping positions parallel to the minor-axis were chosen to cover one side of the outflow cone, at radii large enough to avoid obscuration by the disc due to its inclination. Fig. 4.20 shows the SparsePak positions overlaid on part of the continuum subtracted Hα image from Fig. 4.1. The positions cover the bright large-scale linear streamers and knots that were discussed in Section 4.1.1. We will now describe and discuss the properties of the emission lines observed over the two fields, and compare what we find to previously published data.

Results

The emission line profiles were fit in a similar manner to the DensePak data described above (Section 4.2.1). The S/N of the data varies widely over the two fields but Hα is detected in all but 28 of the 150 available spaxels. In general, the line profile exhibits a single or double peaked structure, and the number of Gaussians fit to each line was determined using a combination of the χ^2 fit value and visual inspection of the data. With a poorer S/N than the DensePak data, more emphasis was given to a visual determination. Where two components existed, the second (C2) was always assigned to the redder of the two, regardless of the relative brightness. This is contrary to the assignment convention used in the DensePak data presented in the previous section, but was adopted to aid interpretation in this different environment. Where only one component could be identified, its assignment to C1 or C2 was only decided after knowledge of its position in velocity space was known. Hence, many single component fits were re-assigned after the initial analysis work was begun.

In a similar fashion to the DensePak data, we map the profile fit results for the combined fields with plots made using the visualisation tool DAISY.

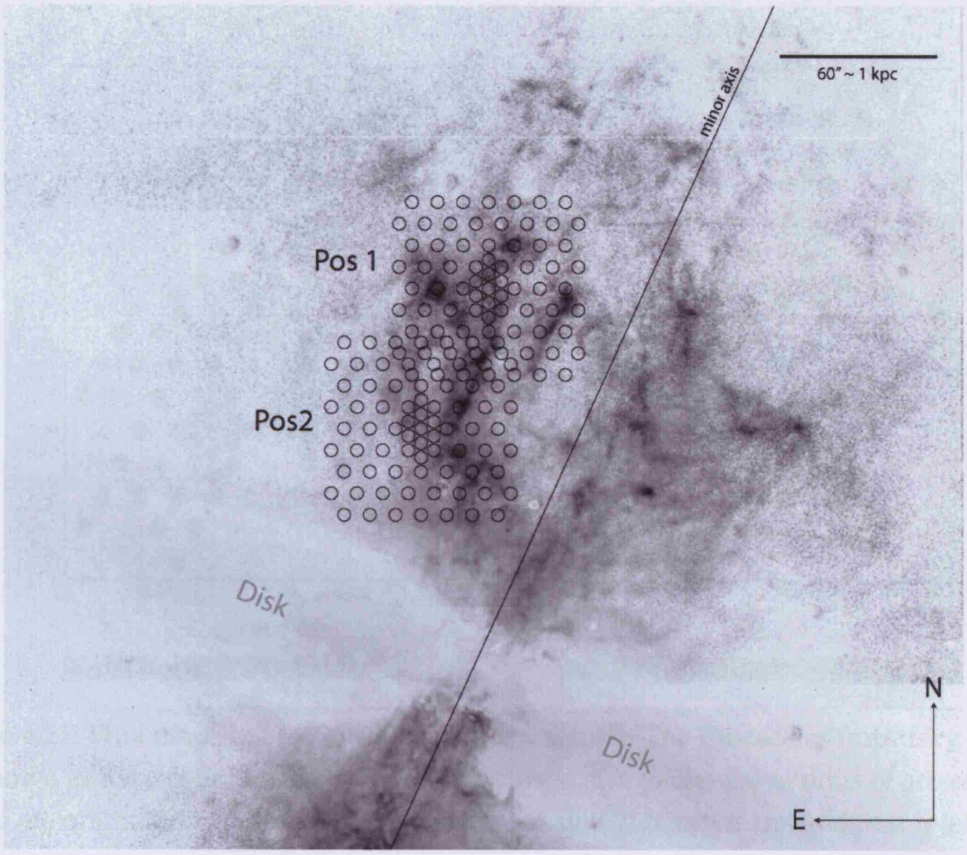

Figure 4.20: Continuum subtracted WIYN Hα image of M82's northern outflow with footprints of the two Sparsepak pointings shown. The disc runs diagonally along the bottom of the image, and is labelled. A solid line marks the minor axis (PA $\approx$ 155°).

Flux variation The flux distribution in both components of Hα is shown in Fig. 4.21. Two components are detected in a strip parallel to the large-scale linear feature seen in the Hα image (Fig. 4.20), and extending along almost the full length of the combined fields ($\sim$2 kpc). According to our C1/C2 assignment convention, more spaxels contain lines belonging to C2 than C1. The brightness of C2 is on average less than that of C1. This makes sense in context with the inclined outflow cone geometry discussed in Section 2.1, since because C2 was always assigned to the redder of the two components, it must be moving away from the average velocity of the cone, and therefore represents the far side of the outflow.

FWHM variation Fig. 4.22 shows the variation of FWHM over the two fields. The FWHM of C1 varies from 50 km s^{-1} to as much as 200–300 km s^{-1} in a few spaxels. However, due to the low S/N of the spectra, the uncertainties associated with the FWHM

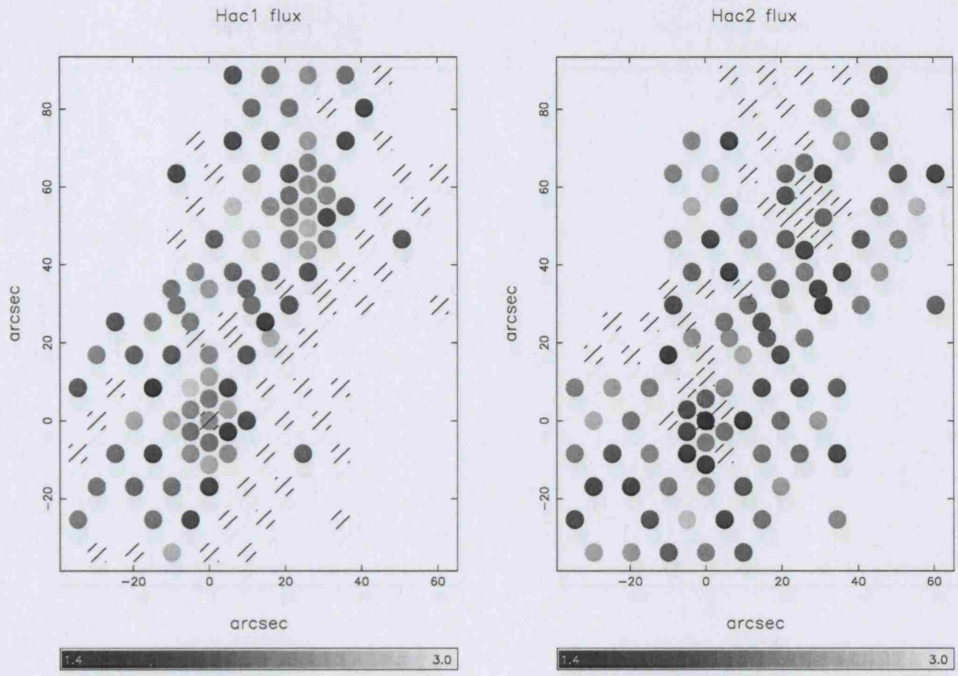

Figure 4.21: Flux maps in Hα for both fields combined. The flux scales (arbitrary units) are shown in the colour bars below each maps; the x and y-axes are in units of arcseconds, where the origin indicates the field-centre for position 2. North is up, and east is left.

measurements are quite large ($\pm$50–100 km s^{-1}), and not much emphasis should be put on these broader results. The FWHM of C2 covers the same range as C1; nowhere do we detect the kind of broad, underlying component as seen in the DensePak fields that cover the central starburst regions.

The FWHMs are represented in a graph form in Fig. 4.23 (in a similar fashion to Fig. 4.18 for DensePak) to better illustrate their relative distribution. On this two-dimentional representation, it is clear that few spaxels contain emission with widths $\lesssim$50 km s^{-1}, and that most are in the range 50–200 km s^{-1}. By looking at the points surrounded by circles (C1) and squares (C2), representing lines that could only be fit with a single Gaussian, we find that the broader lines (>150 km s^{-1}) are predominantly those where only one component was required to fit the observed line. It is likely that in these cases a second component is present, but due to the low S/N, cannot be confidently identified, thus biassing the fit widths to unrealistically large values. There are, of course, true single component lines present with FWHMs of $\sim$100 km s^{-1} (evident at the higher spaxel numbers in each position).

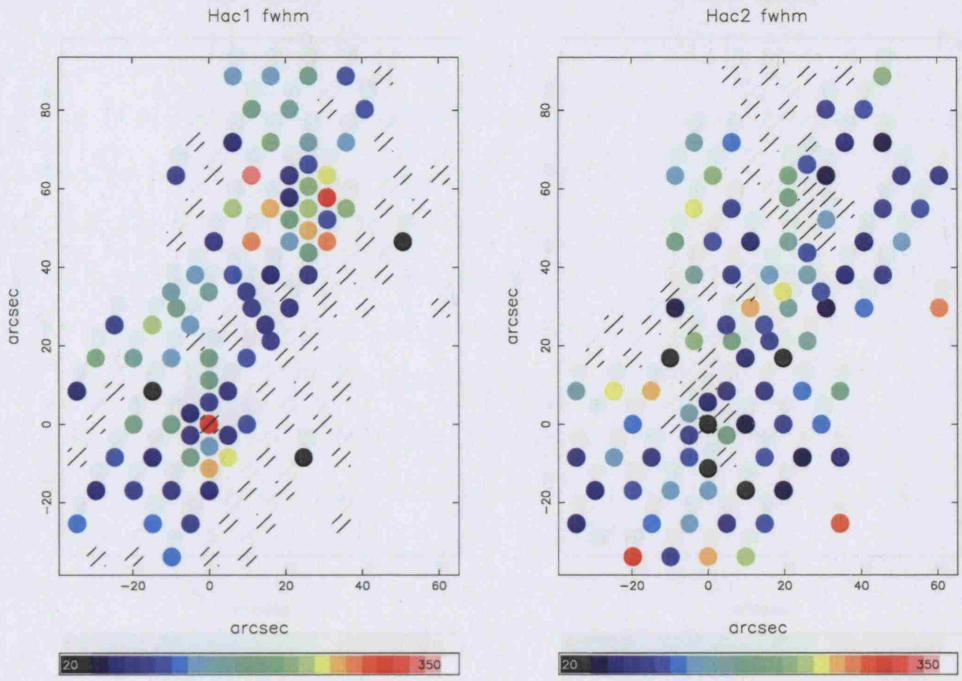

Figure 4.22: Maps of Hα FWHM for the two components. Units are in km s^{-1}, corrected for instrumental broadening. The colour range is 20–350 km s^{-1} for both maps.

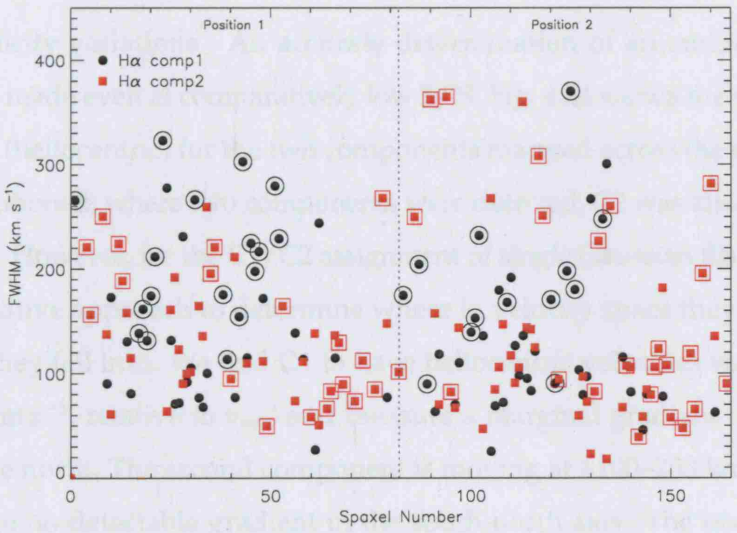

Figure 4.23: Plot of the FWHMs of C1 (black filled circles) and C2 (red filled squares) against spaxel number (see Fig. 2.7 for a plot of the spatial format of the fibre numbers). Points surrounded by open circles and squares represent C1 and C2 lines, respectively, that only required a single Gaussian to fit the line. The division between positions 1 and 2 is shown with a vertical dotted line. The units of FWHM are in km s^{-1}, corrected for instrumental broadening.

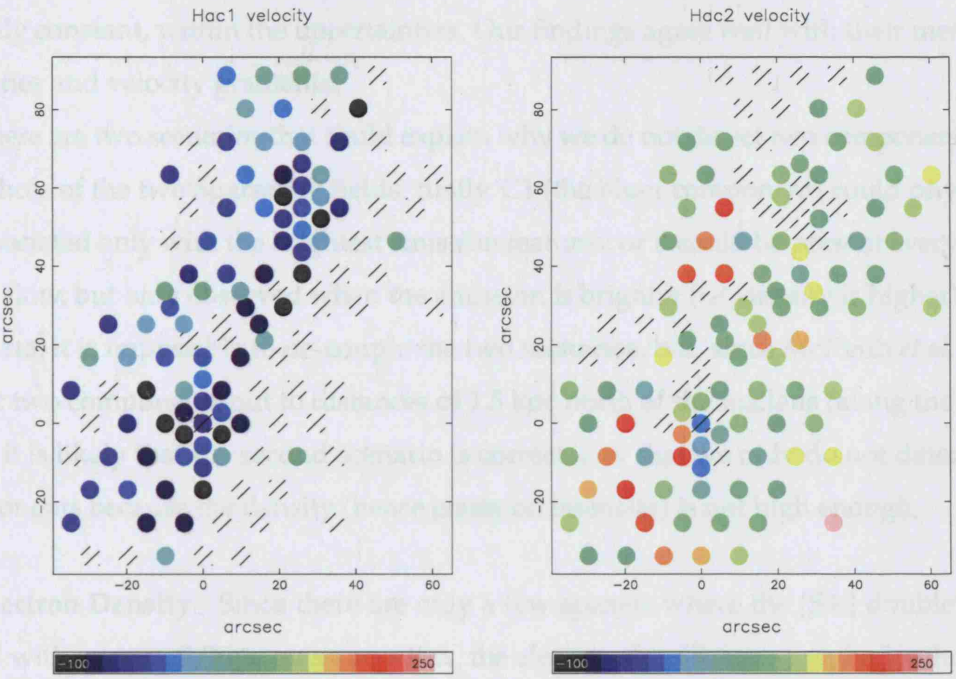

Figure 4.24: Maps of the radial velocity of Hα for the two components. Units are in heliocentric km s^{-1}, relative to $v_{\rm sys}$ (+200 km s^{-1}). The same scale (-100 to +250 km s^{-1}) is used for both maps.

Radial velocity variations An accurate determination of an emission line radial velocity can be made even at comparatively low S/N. Fig. 4.24 shows the variation in Hα radial velocity (heliocentric) for the two components mapped across the observed fields. As already mentioned, where two components were detected, C2 was always assigned to the redder one. However, for the C1/C2 assignment of single Gaussian fits, we used these plots in an iterative approach to determine where in velocity space they lay, and hence which group they fell into. We find C1 to have heliocentric velocities varying between -100 to +20 km s^{-1}, relative to $v_{\rm sys}$, and measure a marginal gradient towards redder velocities in the north. The second component is moving at +100–200 km s^{-1} relative to $v_{\rm sys}$, but we see no detectable gradient in the south-north axis. The resulting velocity separation between the two components is ∼200–300 km s^{-1}. McKeith *et al.* (1995) trace the radial velocity of the wind out to radii further out than our positions, and find at distances along the minor axis (which is parallel to our observations, but offset ∼1 kpc to the west) corresponding to the radii of our observations (note: they assumed 1″ = 15 pc, whereas we assume a distance giving 1″ = 17.5 pc), the velocities of C1 and C2 become

roughly constant, within the uncertainties. Our findings agree well with their measured velocities and velocity gradients.

There are two scenarios that could explain why we do not detect two components over the whole of the two SparsePak fields: firstly, C1 (the bluer component) could physically be associated only with the brightest emission features; or it could be present everywhere in the flow, but only observed when the emission is brighter (*i.e.* density is higher). With this data, it is impossible to de-couple the two scenarios, but, since McKeith *et al.* (1995) detect two components out to distances of 1.5 kpc north of the nucleus (along the minor axis), it is likely that the second scenario is correct, and that we only do not detect both components because the density (hence emission intensity) is not high enough.

Electron Density Since there are only a few spaxels where the [S II] doublet is detected with enough S/N to measure a flux, the electron densities are graphed rather than mapped. Fig. 4.25 shows the variation of electron density with spaxel number in a similar manner to Fig. 4.23. The spatial distribution of the spaxels with measurable densities closely follows that of the Hα bright filaments seen in Fig. 4.20. The majority of these spaxels exhibit densities at or below the low density limit ($\sim$100 cm^{-3}; Osterbrock 1989), however there are a small number of spaxels with derived densities of a few $\times$ 10^3 cm^{-3}. Since the S/N of the [S II] lines is quite low and the flux determinations are fairly uncertain, it is difficult to know how much emphasis to put on these results, but if true, shows that the bright knots of emission making up the linear features seen in the Hα image are at a significant density.

Discussion and summary

We have observed a section of the northern wind plume in M82 with SparsePak, covering one side of the outflow cone and a number of optically bright linear filaments. After 120 and 90 mins of integration (position 1 and 2 respectively), we only achieved a maximum S/N of 90 in Hα, which has restricted our analysis somewhat.

Two Hα line components are detected in a strip extending the vertical distance of our combined fields. The FWHM of both components is $\sim$50–150 km s^{-1}, but the measurement uncertainties are high. The presence of a faint, unresolved second component is thought to bias many of the widths of single Gaussian fits to unrealistically high values (>150 km s^{-1}). The radial velocity of C1 across our fields varies between $-$100 to +30 km s^{-1}, and for C2

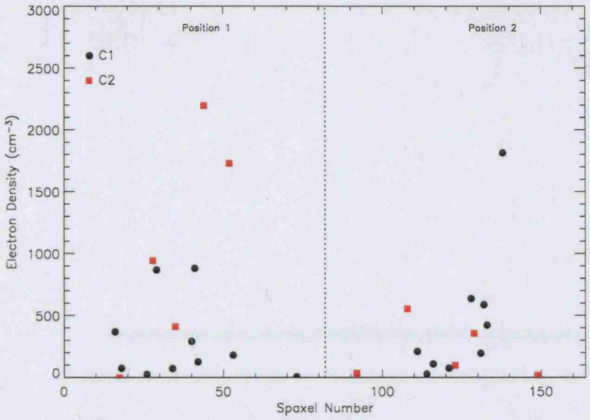

Figure 4.25: Plot of the electron density derived from the ratio of [S II]λ6717/λ6731 for position 1 (left) and position 2 (right); a dotted line divides the two fields. Where a second component is detected, its density is shown in red squares. Units are in cm^{-3}.

between +100–200 km s^{-1}. This results in a separation of the components of between 150–200 km s^{-1}, in good agreement with McKeith *et al.* (1995) even though our observations cover an area 0.5–1.5 kpc to the east of the galaxy minor axis (through which their slit passed). It is interesting to find that velocities at this part of the outflow are similar to that at the centre of the outflow axis. A simple cone geometry would infer that the velocity separation of the two walls get smaller towards the edge, with the observational consequence of a closure of the velocity ellipse. This would imply that either the outflow geometry is not cone-like, or that the cone opening angle is larger than that measured in Section 4.1.1 using Hα data, and is sufficiently large for an east-west velocity gradient not to be observed.

Although we have concluded that the reason for not detecting both Hα line components over the whole field is that it is only over the denser filaments that the emission is bright enough for both components to be observed, it is interesting that we see both in the south-east of position 2 where in the Hα image, the emission is almost undetectable.

CHAPTER 5

INTRODUCTION TO NCG 1569

This chapter contains an introduction to the dwarf galaxy NGC 1569, and a summary of previously published work. We focus on its star-cluster population and their interaction with the existing ISM, and the resulting galaxy-wide gas outflow. In Sections 5.2 and 5.3, we describe the observations acquired to further study this interaction, and the procedures followed to reduce these data.

5.1 The starburst in NCG 1569

NGC 1569 is classified as a post-starburst, dwarf ($M_{\rm HI} \approx 1 \times 10^8\ M_\odot$; Stil & Israel 2002; Mühle *et al.* 2005) irregular (Irp+ III-IV) galaxy, and at a distance of 2.2 ± 0.6 Mpc (Israel 1988), is the closest example of a starburst and an excellent analogue to high-redshift starburst galaxies. The total B magnitude of NGC 1569, $M_B = -17$ mag (Israel 1988), and a remarkably homogeneous metallicity of 0.25 $Z_\odot$ (Devost *et al.* 1997; Kobulnicky & Skillman 1997) makes this galaxy similar to the Small Magellanic Cloud. The basic properties are summarised in Table 5.1.

NGC 1569 has attracted considerable attention because observations at a variety of wavelengths show that it has recently undergone a galaxy-wide burst of star formation that ended 5–10 Myr ago (Greggio *et al.* 1998). During this event the galaxy witnessed at least 10^4 supernova explosions, and the formation of many star clusters, including the two well-known super-star clusters (SSCs) A and B (Arp & Sandage 1985). The result of the energy input into the ISM can clearly be seen: NGC 1569 has a highly chaotic and turbulent ISM, exhibiting structure on a range of scales (Hunter *et al.* 1993; Heckman

Table 5.1: Basic observed and derived properties of NGC 1569

Parameter	Value	Reference
Designations	NGC 1569, Arp 210, UGC 3056, VII Zw 16	1
Coordinates (J2000)	$4^h30^m49'$, $64°50'53''$	1
Distance (Mpc)	2.2	2
Position angle	110–120° (major axis)	1, 7
Inclination	63°	3
B magnitude (mag)	−17	2
Systemic velocity ($km\,s^{-1}$)	−80	1, 3, this work
Galactic extinction (mag)	$A_V = 1.64$	8
Total H I extent	$9.'0 \times 5.'5$ (5.2 × 3.2 kpc)	1
H I mass ($M_\odot$)	$7\text{–}10 \times 10^7$	1, 3
Metallicity ($Z_\odot$)	0.25	4, 5
Star formation rate ($M_\odot\ yr^{-1}$)	0.5–3	6
	4–20 $M_\odot\ yr^{-1}\ kpc^{-2}$	6

(1) Mühle *et al.* (2005); (2) Israel (1988); (3) Stil & Israel (2002); (4) Devost *et al.* (1997); (5) Kobulnicky & Skillman (1997); (6) Greggio *et al.* (1998); (7) Heckman *et al.* (1995); (8) Relaño *et al.* (2006)

et al. 1995; Anders *et al.* 2004), and an impressive bipolar outflow extending over many kpc. X-ray observations show that the wind is metal-enriched and emanates from the full extent of the Hα emitting disc (Martin *et al.* 2002), but only from ∼0.6 times the extent of the H I disc (Waller 1991; Stil & Israel 2002; Martin *et al.* 2002, their fig. 7). Stil & Israel (1998) find a possible H I bridge between NGC 1569 and a nearby, previously undetected, H I cloud. This is confirmed by Mühle *et al.* (2005), who also find an H I stream extending from the south-east to the south-west, and attribute the most likely cause of the starburst event to an interaction with this cloud. The presence of numerous H II regions reveals that there is still substantial ongoing star-formation in the disc (Waller 1991). Fig. 5.1 shows an *HST*/WFPC2 colour composite of NGC 1569 illustrating the chaotic complexity of the ionized gas distribution across the galactic disc. Marked on it are the positions of three of the most studied central star clusters and the most prominent H II region complex 2 (Waller 1991).

The star-cluster population of NGC 1569 has been studied extensively using *HST* observations. Hunter *et al.* (2000) identify and catalogue a total of 48 compact but resolved clusters using WFPC2 imaging. Anders *et al.* (2004) use the same data but different criteria to find 179 clusters, with the majority being formed in an intense starburst event which began ∼25 Myr ago. Of the cluster population, only the most luminous clusters, A, B and No. 30 (nomenclature from Hunter *et al.* 2000) have been studied in any detail. These three SSCs alone provide a significant fraction (20–25 per cent) of the total optical and

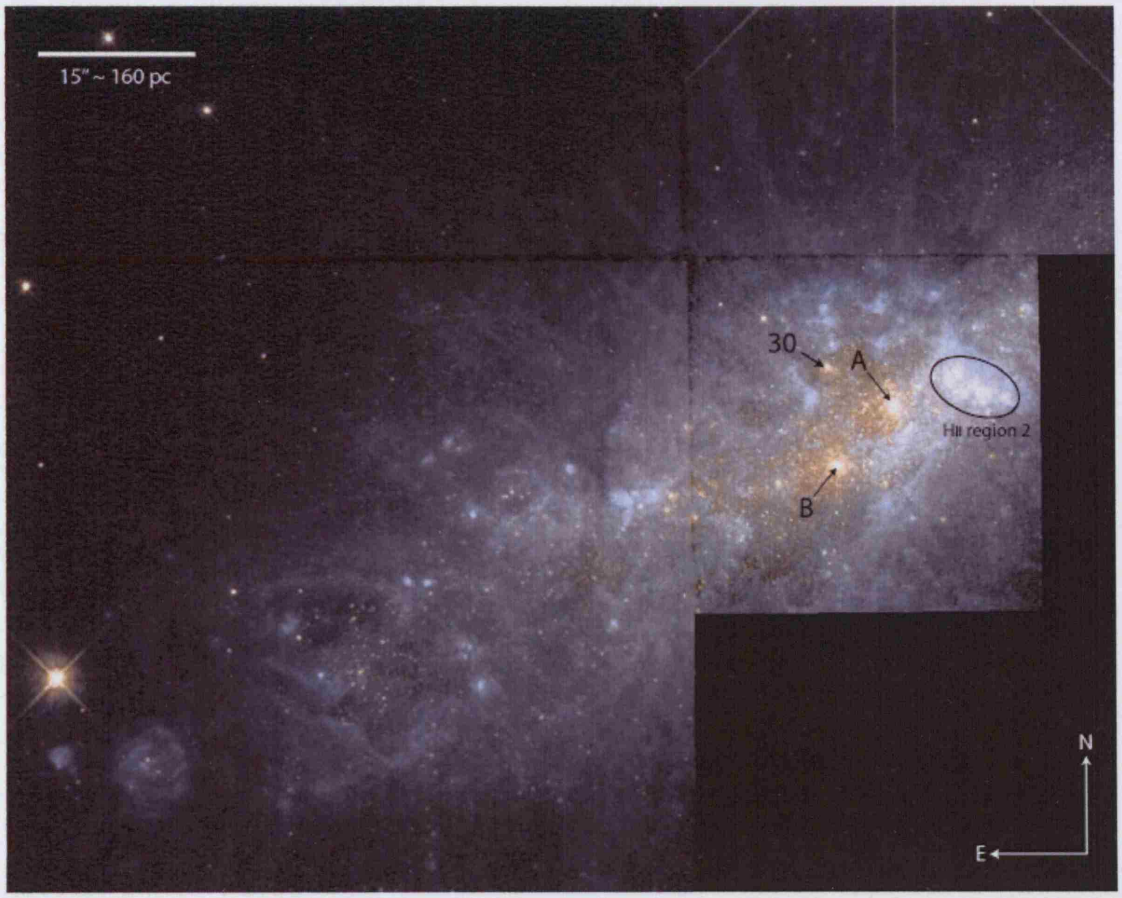

Figure 5.1: *HST*/WFPC2 colour composite of NGC 1569 with broad-band emission represented in yellow and Hα emission in blue. The SSCs A and B are marked, together with the prominent H II region complex 2 (Credit: NASA/ESA, L. Lesurf).

near-infrared light in the central region of NGC 1569 (Origlia *et al.* 2001). Cluster A has actually been resolved into two clusters (de Marchi *et al.* 1997), and has an integrated age of ~7 Myr, with a probable small age difference between the two components (Hunter *et al.* 2000; Maoz *et al.* 2001; Origlia *et al.* 2001). Clusters B and 30 are older with ages of 10–20 and ~30 Myr respectively (Hunter *et al.* 2000; Origlia *et al.* 2001).

The most conspicuous currently active star-forming region is located 90 pc to the west of cluster A and corresponds to the brightest H II region in NGC 1569 (No. 2; Waller 1991; see Fig. 5.1), and the peak of the thermal radio emission (Lisenfeld *et al.* 2004), the dust emission (Lisenfeld *et al.* 2002) and the sub-mm/FIR emission (Galliano *et al.* 2003). This region is also at the eastern edge of a large CO cloud complex (Taylor *et al.* 1999). Hunter *et al.* (2000) identify three clusters in this area; numbers 6, 7 and 10. Cluster 10, one of the main subjects of this study, is the third visually brightest cluster after A and B, but

has not been studied in any detail thus far. Greve *et al.* (2002*a*) identify a number of radio supernovae (SNe) and supernova remnants (SNRs) distributed throughout the NGC 1569 disc using MERLIN and VLA 1.4 GHz and 5 GHz observations. M-1 is a strong thermal source coincident with the location of the large H II complex No. 2, and is surrounded by the tentative 1.4 GHz detections M-b, M-c and M-d. To the north of cluster 10 are the sources VLA-16 and M-3 (25 and 50 pc distant, respectively), both of which are likely SNRs. The source VLA-8, ~30 pc from SSC A, is found to have a non-thermal spectrum leading Greve *et al.* (2002*a*) to believe that this is an extended (~20 pc) SNR. Further to the east, the thermal source M-4 is coincident with H II region 5 (Waller 1991), and M-5 is found to have a mixed thermal and non-thermal spectrum. Tokura *et al.* (2006) detected a number of mid-IR sources in NGC 1569 with the Subaru telescope, the most prominent of which (MIR1) is coincident with H II region 2 (and the radio source M-1). They also find continuum emission associated with a point immediately to the south of H II region 2 (MIR2; interpreted as a very embedded star-formation site), and a diffuse region of [S IV]10.5μ line emission (MIR3) coincident with the semi-circular gas cloud surrounding Cluster 10. Another [S IV] source (MIR5) is found to coincide with the radio source M-4.

As we have already seen, stellar wind and supernova-driven outflows powered by the collective injection of kinetic energy and momentum from massive stars in starbursts can drastically affect the structure and subsequent evolution of dwarf galaxies. Understanding the feedback effects between massive stars, star clusters and the ISM is fundamental to the study of galaxy evolution. In NGC 1569, Hα images show a chaotic, complex, ionized structure with filaments, bubbles and loops (Hunter *et al.* 1993; Tomita *et al.* 1994; Fig. 5.1); the neutral ISM is also highly turbulent (Stil & Israel 2002). Martin (1998) composed a kinematical and morphological catalogue of expanding supershells around dwarf galaxies, including NGC 1569. Using seven long-slit pointings across the face of the galaxy, she finds a number large-scale shell structures corresponding to velocity ellipses in her Hα data. Fig. 5.2 summarises the positions of the Martin (1998) slits and the large-scale shells identified. Her data indicate significant differences in the shell kinematics from the north to the south, and from east to west. The southern flow was found to be composed of three main expanding shells (F, G, and A), where the largest line-splitting was found in shell A, corresponding to an expansion velocity, $v_{\rm exp} \sim 70$–100 km s^{-1} between a height of 140–460 pc. This shell is outlined on the western side by a prominent Hα arm. In general, she finds the redshifted component of the split-line profile to be stronger in the south, and

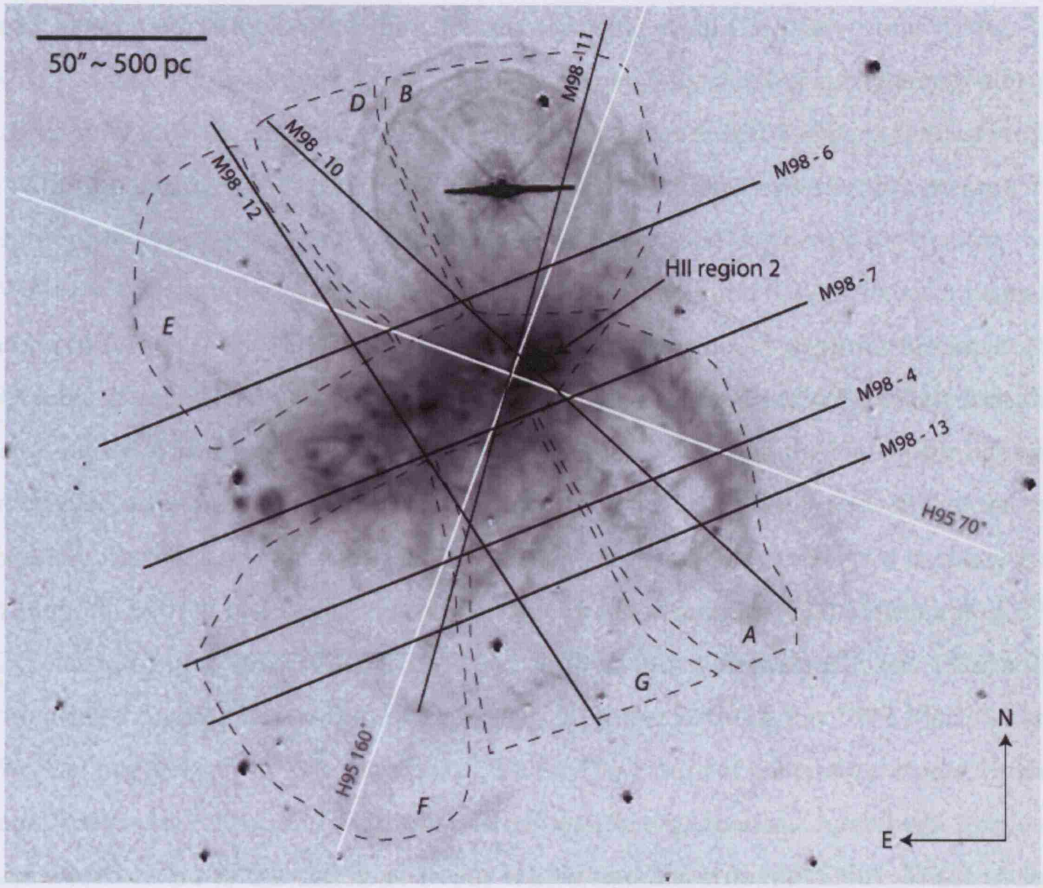

Figure 5.2: Continuum subtracted Hα image of NGC 1569 (from Martin 1998) with the long-slit positions of Heckman *et al.* (1995, white; which intersect at the position of SSC A) and Martin (1998, black) overlaid. Also shown are the positions of the large-scale expanding shells identified by Martin (1998, dashed lines).

weaker in the north (indicating an inclined outflow aspect), but this becomes confused in shells F and G. The northern flow is found to be composed of three large-scale shells (E, D and B) where the measured $v_{\rm exp}$ in shell B is 80 km s^{-1}. Shell C, also identified by Tomita *et al.* (1994) in their long-slit observations, represents the central cavity in NGC 1569 centred on SSCs A and B, and measures $\sim$20″ in diameter with a $v_{\rm exp}$ of $\sim$40 km s^{-1}.

Heckman *et al.* (1995) presented the first spatially resolved X-ray images of NGC 1569, together with deep Hα long-slit spectroscopy of the disc and filament system (slit positions also shown in Fig. 5.2). They find a general (but not precise) correspondence between the X-ray and Hα morphology (a more detailed study was made by Martin *et al.* 2002, using high spatial resolution Chandra data). Most pertinent to this study, however, is their Hα findings. They observe Hα line profiles which are "distinctly non-Gaussian", exhibiting

broad, asymmetric wings which they decompose using multi-Gaussian profile fitting. This decomposition allowed them to detect two kinematically distinct subsystems: a bright and centrally located 'quiescent system' (covering an area of 650 × 650 pc, centred on SSC A) with line widths of FWHM = 30–90 $\mathrm{km\,s^{-1}}$ and radial velocities within 30 $\mathrm{km\,s^{-1}}$ of their adopted v_{sys} (-68 $\mathrm{km\,s^{-1}}$), and a fainter and extended 'high-velocity system' with FWHMs $\leq$ 150 $\mathrm{km\,s^{-1}}$ and velocities up to 200 $\mathrm{km\,s^{-1}}$ relative to v_{sys}. This confirms the finding of Tomita *et al.* (1994) who also report two similar velocity systems. Heckman *et al.* (1995) detect a number of velocity ellipse/expanding shell features in their data including shell A and B of Martin (1998). At the location of SSC A, they find the Hα profile has weak but very broad wings (30–50 Å at full-width zero-intensity), making up ~30% of the total Hα flux within this region. Broad emission line wings have been detected in many giant H II regions both in nearby galaxies (30 Dor: Chu & Kennicutt 1994; Melnick *et al.* 1999; NGC 604: Yang *et al.* 1996; NGC 2363: Roy *et al.* 1992; González-Delgado *et al.* 1994) and in more distant dwarf galaxies (Izotov *et al.* 1996; Homeier & Gallagher 1999; Marlowe *et al.* 1995; Mendez & Esteban 1997; Sidoli *et al.* 2006). The nature of the energy source for these broad lines is not clear, and a number of contesting explanations have been proposed, all of which relate to the action of stellar winds and supernovae (SNe). These include the direct observations of stellar/cluster winds; the effects of SN remnants; large-scale superbubble expansion and/or blow-out (Tenorio-Tagle *et al.* 1997); multiple unresolved expanding shells; champagne flows (Yorke *et al.* 1984; Tenorio-Tagle *et al.* 2000; Melnick *et al.* 1999) [1]; or the ablation of gas from molecular clumps resulting from the impact of stellar/cluster winds (Melnick *et al.* 1999). The available observations are often conflicting, possibly indicating that some mechanisms may operate to a different degree in each case.

Heckman *et al.* (1995) also measure the ratios of [O I]λ6300/Hα, [S II]/Hα and [N II]/Hα and find strong radial gradients in their values. They find the ratios in all three indicators to be high in the outer filaments, indicating either an increase in the importance of shocks, or simply that the ionizing radiation from the central starburst is diluted with distance (hence the radiation field softens). Measuring the electron density from the [S II] doublet gives densities of ~200 ± 100 $\mathrm{cm^{-3}}$ in the central 15″ and < 100 $\mathrm{cm^{-3}}$ (low density limit)

[1] Champagne flows occur when the ionization front from a star embedded in a molecular cloud overruns the cloud edge, causing a large pressure gradient and strong isothermal shocks and resulting in the expulsion of ionized cloud matter (Yorke *et al.* 1984). This phenomenon can only produce motions on the order of the sound-speed of the medium, which for Hα-emitting gas is ~10 $\mathrm{km\,s^{-1}}$.

for the outer gas.

HST images illustrate the complexity of the small-scale ISM in NGC 1569 very well. Buckalew & Kobulnicky (2006) use *HST*/WFPC2 narrow-band imaging to examine the detailed small-scale structure of the ISM and the underlying ionizing emission mechanisms. They use the ratios of [S II]/Hα and [O III]/Hβ and the theoretical "maximum starburst line" from Kewley *et al.* (2001) to determine a threshold between photoionized and non-photoionized (shock excited) emission (see also Calzetti *et al.* 2004). Identifying pixels in this way, they find structures of non-photoioinized points across the face of the whole galaxy. The most important correlation they find between the non-photoionized points and individual sources is at the largest H II complex (no. 2) to the west of SSC A (see Fig. 5.1). Here a ring of non-photoionized points encompasses the Hα emission at a radius of ~3.5–4″ (~40 pc). As we have already noted, this interesting region contains the strong thermal radio source M-1, together with strong mid-IR continuum and [S IV]10.5μm line emission (Tokura *et al.* 2006), extended X-ray emission (Martin *et al.* 2002), WR stars (Buckalew *et al.* 2000) and star clusters (including clusters 6, 7 and 10). They also find "walls" or arcs of non-photoionized points near SSCs A and B, indicating interaction between their respective cluster winds and the surrounding ISM. Another is located west of SSC A between it and cluster 10, indicating a possible wind-wind interaction between these two clusters.

The distribution of He II λ4686 emission in NGC 1569 was reported by Buckalew *et al.* (2000). Where the location of the non-photoionized points (indicating shocks) corresponds to He II emission, they suggest the shock velocity is ~120 km s^{-1}, since this is the velocity where He II emission peaks (Garnett *et al.* 1991). In a starburst environment, shock-excited emission dominates when the level of photoionization from very young stars starts to decline, but the energy input from stellar winds and SNe (which drive the shocks) is constant. This corresponds to the period 6–40 Myr (Leitherer *et al.* 1999) and is consistent with the post-starburst classification and the typical ages of star clusters in NGC 1569 (González-Delgado *et al.* 1997; Anders *et al.* 2004). Pockets of star-formation still persist in smaller areas of the galaxy providing the continued photoionized component.

As we have seen, morphological and kinematical evidence for shells and outflows in NGC 1569 have been presented by numerous studies combining optical narrow-band imaging and long-slit spectroscopy. However, these studies have concentrated mainly on the large-scale features of the outflow – there exists a paucity of data of sufficient

quality and resolution to compare directly to high-resolution superwind models such as those of Stevens & Hartwell (2003) or Tenorio-Tagle *et al.* (2003). To probe the roots of the wind outflow, it is necessary to investigate the interaction of the individual winds from clusters with their environments on high angular-scales. Good spectral resolution and spatial coverage are, however, equally important for determining properties such as gas dynamics and excitation mechanisms. Integral Field Spectroscopy (IFS) is ideally suited to these type of observations, and modern, large format IFUs such as those found on 8m-class telescopes provide the best opportunity to date to fulfill these demanding requirements. Historically, it has been very difficult to manage the data products from such instruments, but in recent years the infrastructure to deal with the reduction, analysis and visualisation of IFS data has improved dramatically.

To this end we have obtained Gemini-North GMOS/IFU observations of the cluster wind–ISM interaction zone in the central region of NGC 1569. These observations focus on the small-scale and are of high enough spatial resolution to study the wind–ISM interaction processes in detail. We have also obtained WIYN SparsePak observations of the outer wind zones with the aim of linking up what we see in the central regions to that in the outer regions. The following two sections describe the data acquisition methods and reduction procedures followed, and the results are presented and analysed in Chapters 7 and 8.

5.2 Gemini GMOS/IFU observations of NGC 1569

5.2.1 Observations

In November 2004 queue-mode observations using the Gemini-North Multi-Object Spectrograph (GMOS) Integral Field Unit (IFU; Allington-Smith *et al.* 2002) were obtained covering four regions near the centre of NGC 1569 (programme I.D.: GN-2004B-Q-33, PI: L.J. Smith), with 0.5–0.8 arcsec seeing. A nearby bright star was used to provide guiding and tip-tilt corrections using the GMOS on-instrument wave front sensor (OIWFS).

Depending on the combination of spatial and spectral coverage required, the GMOS IFU can be operated in one- or two-slit modes. For our purposes, we opted for the one-slit mode giving a field-of-view of 5×3.5 arcsec (which corresponds to approx. 50×35 pc at the distance of NGC 1569) sampled by 500 hexagonal contiguous fibres of $0\farcs2$ diameter. An additional block of 250 fibres (covering 2.5×1.7 arcsec) are offset by $1'$ from the

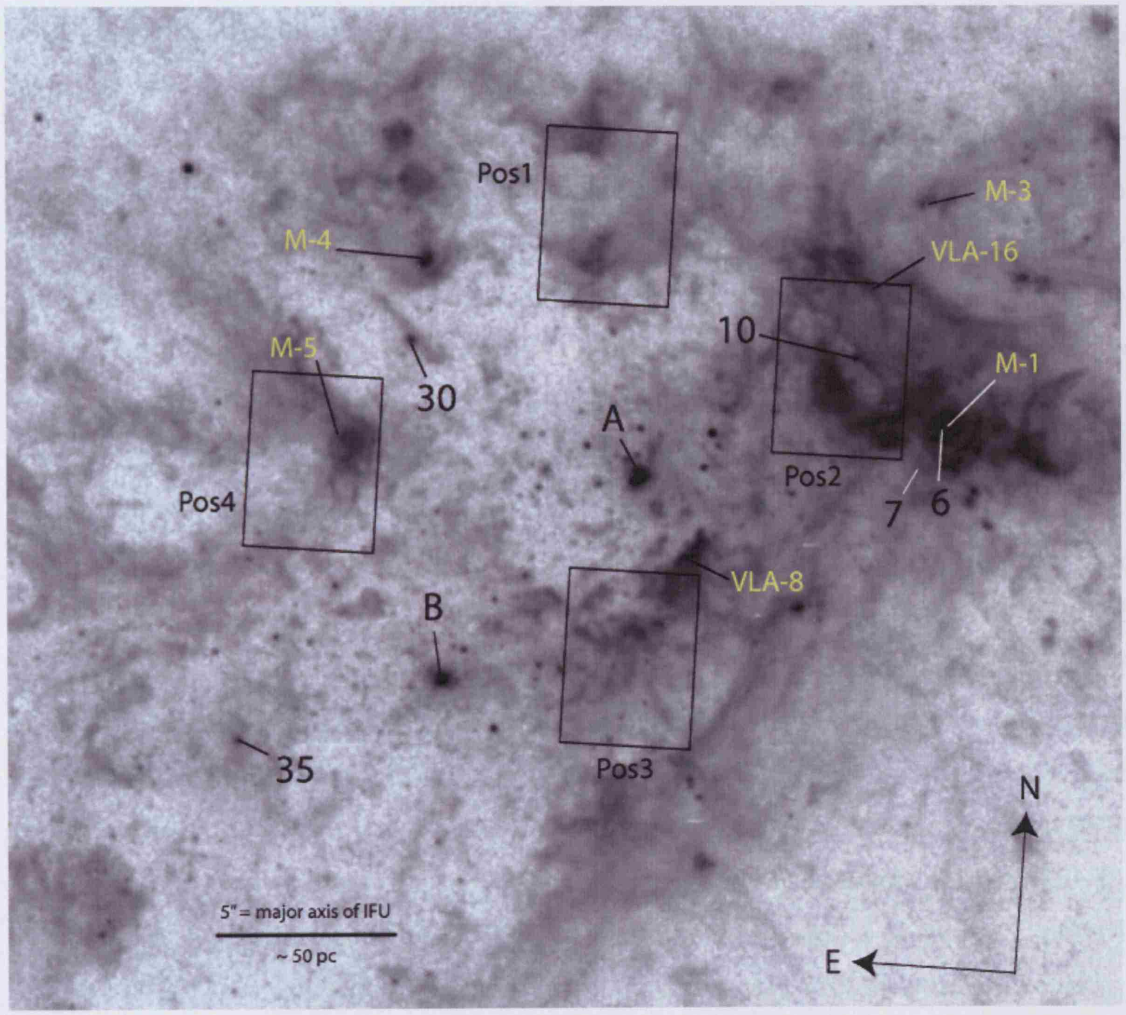

Figure 5.3: *HST*/WFPC2 F656N image of the nucleus of NGC 1569 showing the positions of the four IFU fields. A number of the most prominent star clusters (Hunter *et al.* 2000) and radio continuum sources (Greve *et al.* 2002*a*) have been labelled in black and white, respectively.

object field providing a dedicated sky view. We took four exposures at each position with integration times between 940 and 1680 s each. Table 5.2 lists the coordinates and exposure times for each position, and Fig. 5.3 shows the positions of the four fields on an *HST*/WFPC2 image (GO 6423, P.I. D. Hunter; see Table 5.4) .

Using the R831 grating to give a spectral coverage of 4740–6860 Å and a dispersion of 0.34 Å pix^{-1}, we were able to cover the important nebular diagnostic lines of Hα, Hβ, [O III]$\lambda\lambda$4959, 5007, [N II]$\lambda\lambda$6548, 6583 and [S II]$\lambda\lambda$6716, 6731.

The GMOS spectrograph is fed by optical fibres from the IFU which reformats the arrangement of the spectra for imaging by the detector. This is composed of three 2048×4068 CCD chips separated by small gaps. In order to remove the pixel-to-pixel sensitivity differences, and enable the wavelength and flux calibration of the data, a number of bias frames, flat-fields, twilight flats, arc calibration frames, and observations of the photometric standard star G191-B2B were taken contemporaneously with the science fields.

Position 1 was chosen to intercept the (possibly) high velocity outflow emanating from the central regions of the galaxy. Position 2 is coincident with Cluster 10 (Hunter *et al.* 2000) and covers some of the Hα gas on the easternmost part of the ionized complex centred on H II region 2 of Waller (1991). Cluster 10 is located on the easternmost part of the ionized complex centred on H II region 2 of Waller (1991) and is ideal for the study of the cluster-ISM interaction. Just off the south-west edge of the IFU field are two tentative 1.44 MHz detections M-c and M-d of Greve *et al.* (2002*a*). To the north of the field, ∼25 pc from Cluster 10, is VLA-16, a non-thermal radio source also reported by Greve *et al.* (2002*a*) who consider it may be an extended low surface brightness supernova remnant (SNR). Position 3 was placed to the south of SSC A, and covers a number of compact ionized knots. VLA-8, a non-thermal radio source which Greve *et al.* (2002*a*) attribute to being low surface brightness SNR, is located at the very top of the field-of-view. IFU Position 4 was chosen to focus on an ionized knot to the east of SSC A, north of SSC B, and south of Cluster 30. We suspected this region might show signs of the interaction of winds from

Table 5.2: Gemini GMOS observations

Pos. No.	Date	Coordinates (J2000)		Exp Time (s)
1	7/10/04	$04^h30^m48\overset{s}{.}38$	$64°51'06\overset{''}{.}5$	1600 × 4
2	7/11/04	$04^h30^m47\overset{s}{.}27$	$64°51'03\overset{''}{.}2$	1680 × 4
3	7/10/04	$04^h30^m48\overset{s}{.}04$	$64°50'54\overset{''}{.}8$	940 × 4
4	8/11/04	$04^h30^m49\overset{s}{.}58$	$64°50'58\overset{''}{.}9$	1680 × 4

these three star clusters. This knot also contains the non-thermal radio source M-5 (Greve *et al.* 2002*a*). In Fig. 5.3, we show the position of the IFU field on an archive HST F656N image obtained with the Wide Field Planetary Camera 2 (WFPC2). The IFU fields and features referred to are all marked on Fig. 5.3.

5.2.2 Data reduction

Because of the complexity of the data products from IFU instruments, a considerable amount of time was invested in learning and developing reduction and analysis tools to enable us to extract the most information we could from this extensive dataset.

The field-to-slit mapping for the GMOS IFU reformats the layout of the fibres on the sky to one long row containing five blocks of 100 object fibres interspersed by five blocks of 50 sky fibres. In this way, all 750 spectra can be recorded on the detector at the same time.

Basic reduction was performed using the Gemini pipeline reduction package (implemented in IRAF). There are a number of tasks within this package that are designed to perform specific functions, and each contain switches to allow them to be applied at different stages of the reduction procedure. The first stage was to run the GFREDUCE task on the flat-fields, twilight flats and arc calibration exposures in order to prepare the raw files for reduction, and subtract the overscan level and bias frames. GFEXTRACT traces and extracts the spectrum of each fibre (using a ± 2.5 pixel aperture in the spatial direction), and by running this on the flat-field image, produces a reliable trace of the position of each spectrum on the CCD. We then ran GFRESPONSE on the GFREDUCE'd twilight flats to create a throughput correction function for each fibre (an essential step to correct differences in fibre-to-fibre transmission). The final step before reducing the science data was to extract the 750 arc calibration spectra from the arc lamp exposures (using GFREDUCE) and establish a wavelength calibration solution using GSWAVELENGTH.

Running GFREDUCE on the science observations using the spectrum trace created from the flat-field, the throughput correction determined from the twilight flat, and the wavelength calibration from the arc exposures, creates a data file containing 750 reduced spectra, each one pixel in width and ordered by the position they were recorded on the CCD (which we will call the 'fibre order'). After extraction of the spectra, the x and y spatial unit is now termed 'spaxel' to differentiate from 'pixel' which refers to the position of the spectrum on the CCD.

Cosmic-rays were cleaned from the data at this stage with the Laplacian cosmic-ray identification routine LACOSMIC (van Dokkum 2001). Fits to the flux of the [O I]λ5577 telluric emission line, assumed to remain stable in intensity for each observation set, for each of the 750 object spectra, showed a significant ($\sim$10 per cent) dip from the centre to the edges when plotted against fibre order. We decided that a second throughput correction was needed to remove this variation. This correction was measured by fitting a fourth order polynomial to the intensity curve, inverting the profile, normalising it to unity, then dividing this into the data using the IRAF task IMARITH.

Fits to the FWHM of the [O I]λ5577 line also showed unexpected flux variations with fibre order. We found that the groups of 50 sky fibres at either end of the CCD showed elevated widths compared to the central groups. Thus we decided to extract only sky fibres in the central blocks (*i.e.* fibres 200–250, 350–400 and 500–550). After extracting and averaging these fibres for each science frame, the resulting spectrum was subtracted using IMARITH. Because of diffuse emission extending past the 1 arcmin separation of the object and sky fields surrounding NGC 1569, there is the possibility that nebular emission could contaminate the sky spectra. To check the level of such contamination, we compared the flux of the Hα line in representative spectra with and without sky subtraction. The difference in the flux for each case was 1–2 per cent and therefore deemed insignificant.

5.2.3 Flux calibration

As part of the calibration dataset, the flux standard star G191-B2B (Oke 1990) was observed using the same instrument set-up as described above. Reduction of these data followed the same procedure as described above for the science frames, except that we used the throughput response file and wavelength solution determined from the reduction of one of the science fields. In order to obtain the optimum S/N spectrum for the standard star, we summed all object spaxels across the field of view using GFAPSUM to create one averaged spectrum of the standard star. The sensitivity function was computed using the GSSTANDARD task (which includes a second-order extinction correction relevant to the Gemini-N Observatory), and the flux calibration for each science frame was performed by the GSCALIBRATE task.

Final combination of the individual exposures for each position was done using IMCOMBINE. The resulting data file was then formed of 750 reduced, sky-subtracted and flux-calibrated spectra, one corresponding to each spaxel in the field-of-view (including

Table 5.3: Differential atmospheric refraction corrections (Hβ to Hα). 1 spaxel has a diameter of 0.″18.

Position	Spaxel Shift
1	1.50 east, 2.50 north
2	0.39 west, 2.98 north[†]
3	0.50 west, 2.50 north
4	1.15 west, 2.75 north

[†] measured using the centroid fitting routine described in the text.

the sky field). Removal of the sky fibres from the data files was achieved using the E3D Visualisation Tool (Sánchez 2004), the development of which was a primary goal of the European Commission's Euro3D Research Training Network. Each science file now only contained the 500 object spectra. The resolution of this final dataset varies between FWHM = 74 ± 5 km s^{-1} at the blue end (with an average S/N of 4.6 in the continuum), to 59 ± 2 km s^{-1} at the red end (with an average S/N of 14.5). The resolutions were measured by fitting a number of arc lines from a wavelength calibrated arc exposure (see also Chapter 6).

5.2.4 Differential atmospheric refraction (DAR) correction

When observing the spectrum of an object, its light is refracted by the Earth's atmosphere by varying amounts at different wavelengths. This effect, termed Differential Atmospheric Refraction (DAR), is therefore a function of wavelength (horizontal) and airmass (vertical). An advantage of IFS over traditional long-slit methods is that it is possible to determine and correct the effects of DAR using an *a posteriori* procedure (*e.g.* Arribas *et al.* 1999). In order to correct our data for DAR, we first had to convert each dataset to standard cube format. This involves changing the way in which the data are stored, from one spectrum (wavelength vs. flux) per spaxel (spatial coordinate) to a 2-D image of flux for each wavelength point. For the DAR correction procedure, it is required that the data are sampled evenly in x and y, and since the format of the GMOS fibres is hexagonal we had to apply an interpolation routine to resample the data into contiguous squares with an equivalent 'diameter'. A diameter of 0.″18 gave the closest match to the *number* of original spaxels when interpolating from hexagons to squares.

Measurement of the DAR shift can be achieved easily and automatically if there is an unresolved point source in the field-of-view: for position 2, this was Cluster 10 (see Fig. 5.3). With the data in cube format (2 spatial axes and one of wavelength) and using

Table 5.4: HST archive images of NGC 1569.

Filter	Camera/CCD	Plate Scale ($''$ pix^{-1})	Exposure Time (s)	Programme I.D.	P.I.
F330W	ACS/HRC	0.026	220 × 3	9300	H. Ford
F439W	WFPC2/PC	0.045	700 × 16	6111	C. Leitherer
F555W	ACS/HRC	0.026	130 × 3	9300	H. Ford
F656N	WFPC2/PC	0.045	800 × 2	6423	D. Hunter
F814W	ACS/HRC	0.026	130 × 3	9300	H. Ford

scripts provided by L. Christensen (ESO), the spatial shifts were traced by cutting the cubes into a series of monochromatic images, and fitting a two-dimensional Gaussian function to the unresolved star cluster to determine the centroid position. A polynomial of third order was used to fit this trace (with wavelength) through the datacubes, giving the relative shifts in Right Ascension (RA) and Declination (Dec) for each slice with respect to the first (reference) wavelength. The measured offsets were then used to shift each wavelength slice by the required amount, and were then combined back into a datacube with the original grid sampling using a modified version of the IRAF STSDAS DRIZZLE task (originally written as an implementation of the image combination method known as variable-pixel linear reconstruction; Fruchter & Hook 2002). The result is a datacube where every flux at each point in the object corresponds to the same position in the image for each wavelength point.

Unfortunately none of the other fields contain a suitable unresolved source, and we had to employ a method of visual inspection to determine the DAR shift. The E3D Visualisation Tool enables a spatial intensity map of a specific wavelength range for each IFU field to be plotted. After selecting two maps of the field isolating the Hβ and Hα emission lines respectively, we measured the offset in position of a representative bright gas knot between these two known wavelengths. Assuming that these measurements represent the wavelength extrema (a reasonable approximation for our set-up), we normalised the curve output from the automatic DAR tracking algorithm for position 2 to our measured values for positions 1, 3 and 4 in order to get the DAR corrections. The calculated offsets from Hβ to Hα for each field are given in Table 5.3.

The final stage was to crop the edges of each field in order to remove spaxels only containing flux for part of the wavelength range. This is an inevitable side-effect of performing a DAR correction.

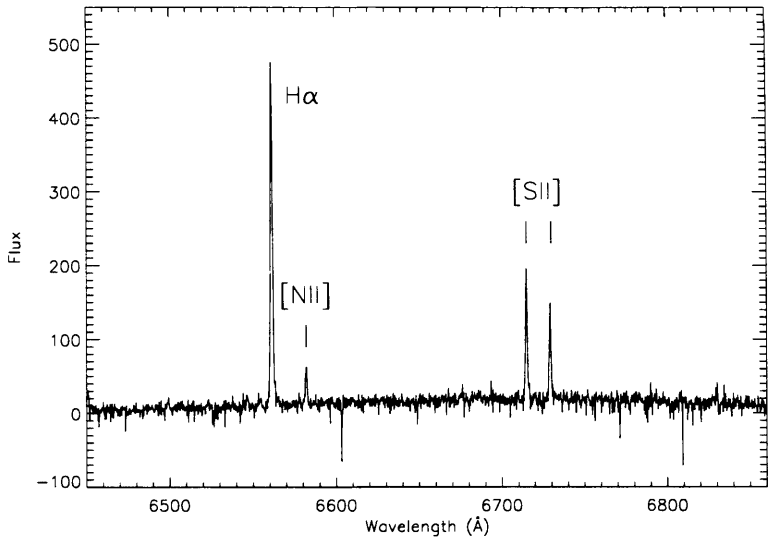

Figure 5.4: Example high S/N SparsePak spectrum from a spaxel covering part of the Hα disc showing the full wavelength range recorded. The observed nebular emission lines are labelled; the flux scale is in arbitrary units.

5.2.5 *HST* images

To supplement our studies, we obtained *HST* ACS/HRC and WFPC2 broad- and narrow-band images of the central regions of NGC 1569 from the *HST* archive. These images are listed in Table 5.4 and were calibrated using the "on-the-fly" pipeline system. Dithered images were first registered using their WCS (World Coordinate System) information, then combined using the IRAF IMCOMBINE routine in order to remove cosmic-rays.

5.3 SparsePak observations of NGC 1569

The SparsePak instrument, mounted on the WIYN 3.5 m telescope on Kitt Peak, Arizona, U.S.A., has already been described in Chapter 2, Section 2.3.3. During the same run that we observed M82 (Section 2.3.3), we also obtained observations of NGC 1569. The instrument set-up was therefore identical for the two datasets. Here we only summarise the important details.

SparsePak fields covering the outer regions of the NGC 1569 outflow were obtained on the nights of 13–16th December 2004. The spectrograph set-up gave us a dispersion of 0.20 Å pix^{-1}, and a spectral coverage of 6450–6865 Å, meaning we could observe the nebular lines of Hα, [N II]λλ6548, 6583 and [S II]λλ6716, 6731. Calibration exposures were

Table 5.5: SparsePak observations of NGC 1569.

Position	RA (J2000)	Dec (J2000)	Exposure Time (s)	Sky fibres used for subtraction
1	$4^h31^m01\overset{s}{.}0$	$64°51'25\overset{''}{.}0$	8×1800	16,22
2	$4^h30^m48\overset{s}{.}5$	$64°51'37\overset{''}{.}0$	9×1800	2,37,54,80
3	$4^h30^m52\overset{s}{.}0$	$64°49'18\overset{''}{.}0$	8×1800	70,80
4	$4^h30^m42\overset{s}{.}0$	$64°50'15\overset{''}{.}0$	8×1800	2,37,54,80

taken together with the science frames. Details of the observations are given in Table 5.5.

The data reduction procedure is described in Section 2.3.3, and differs only with respect to the sky subtraction method. Since SparsePak is formatted with seven sky fibres located on the north and west side of the main array, separated by only $\sim 25''$, many of which fell on regions of strong galactic emission and were therefore unusable. By a combination of visual inspection of both the finding charts and the sky fibre spectra themselves, we determined which fibres to use for the sky subtraction process. Once we had done this, the respective sky spectra for each position were created by averaging the individual uncontaminated sky fibre spectra. A list of which fibres were used for each position is given in Table 5.5. An example high S/N spectrum is shown in Fig. 5.4 for a fibre covering part of the bright Hα disc.

CHAPTER 6

EMISSION-LINE FITTING AND VISUALISATION

6.1 Emission line fitting

The spectral resolution and S/N of the spectra presented thus far have been high enough for multiple line components to be resolved in the bright nebular emission lines detected. The decomposition of these individual components by modelling the overall line profile is a difficult business: as with any equation fitting process, the more individual components added to the model, the less unique the fit becomes.

The basis of model fitting is to derive the point at which a chosen model function best represents the data. The parameters of the function (which in the simplest case is a straight line) are then 'minimised' to the smallest possible values with respect to the data points. These are then the 'best-fitting' results.

The first choice when attempting to model any observed data is that of which function applies, and for that, knowledge of the physics behind the process being observed is necessary. Spectral lines in the ideal case are single, infinitely narrow peaks. However, in reality they are affected by three types of broadening processes. Natural broadening is the result of quantum mechanical uncertainty in a particle's energy (and is of the order $\sim$few m s^{-1} in the optical wavelength range); collisional (pressure) broadening is due to the physical interaction of atoms with one another, and is therefore directly proportional to the gas density; and Doppler broadening is due to the temperature or turbulence of the gas. Here, the random movements or vibrations of the atoms causes some to emit

slightly blueshifted emission and others slightly redshifted, and is always a convolution of the thermal motions (dependent on temperature) and micro-turbulent components. Natural and collisional broadening are approximated by a Lorentzian function, whereas the Doppler width is described by a Gaussian profile due to being derived from the Maxwellian velocity distribution. In the ionized ISM of galaxies, collisional processes are assumed to be negligible due to the very low gas densities, therefore the dominant broadening mechanism is the Doppler effect. The Gaussian function is given by:

$$\phi(\lambda) = \frac{A}{\sigma\sqrt{2\pi}} \exp\left[\frac{-(\lambda - \lambda_0)^2}{2\sigma^2}\right] \tag{6.1}$$

where A is the area under the curve, λ_0 is the centre of distribution, and σ is the standard deviation of the distribution. The full-width at half-maximum (FWHM) is given by FWHM $= 2\sqrt{2\ln 2}\,\sigma \simeq 2.355\sigma$.

One additional broadening mechanism is introduced by the intrinsic resolution of the spectrograph being used to detect the lines, and is proportional to the detector plate scale and the dispersion of the grating. Usually, a spectrograph is designed with an intrinsic shape as close to Gaussian as possible.

Since fitting model profiles to spectral lines is a common procedure, there are many programmes/routines available for this task. However, with the volume of data produced by a modern IFU, it becomes very important to automate the fitting procedure, and for this there are very few available software packages. For example, in Chapter 5 we introduced data taken by the Gemini/GMOS IFU containing 500 spectra, each containing up to eight emission lines. Assuming each line can be fit by two components, this makes a total of 8000 individual components which must be modelled. The fitting must be done in a way that minimises the error that an automated procedure can introduce. Furthermore, particularly in the case of fitting multiple line components, the user must be able to see the fit result for each case to check that the routine is performing properly, and to adjust the parameters if necessary. With these criteria, we sought a package that would allow user interactivity, has a stable fitting engine, and methods for plotting and recording the fit results.

6.1.1 Peak ANalysis (PAN)

We adopted an IDL-based, general-purpose curve-fitting package, called PAN (Peak ANalysis; Dimeo 2005). It was written with the aim of allowing the user to visually interact

with the program through the use of IDL's sophisticated 'widget-based' toolkits, and uses a least-squares minimisation algorithm to obtain the best-fit. The primary features that caused us to favour this program over any other was its ability to read in multiple spectra at once in an array format, and its method of determining the initial guess parameters of a model profile (see below).

Minimisation is achieved using the Levenberg-Marquardt least-squares technique for iteratively searching for a best-fit. The implementation used in PAN is the MPFIT.PRO function (Markwardt 2006) which allows a user-supplied function to be fit to a data array containing both measurements and their associated error. PAN is essentially a graphical user interface (GUI) wrapper to this function. A library of functions is available including linear, Gaussian and Lorentzian profiles, but an option for defining new functions via a 'user-function' dialogue is also included. For any fit, a set of initial guess parameters must be given (*i.e.* for a Gaussian: amplitude/flux, position/central wavelength and width) which forms the starting point for the minimisation routine. Within PAN, these initial guesses are specified by 'drawing' a model profile onto the data using the mouse. The advantage of this method is that the starting points are defined more quickly and easily than numerically entering the initial guesses (although numerical entry is offered), and is consistent with its graphical, interactive approach. Options are available for limiting the wavelength range used in fitting, constraining the fit parameters (*e.g.* upper and lower bounds or fixing the values), and selecting which individual spectra from the whole set should be fit. A postscript output option is also available for producing high-quality reproductions of the model and data plots.

Originally written to analyse data from neutron-scattering experiments, the program has required some modification to suit our needs. Minor changes to the plot style have been made, and we have had to add modules to convert our FITS format data into a format that PAN can read, and a module for creating the associated error arrays. The format in which PAN records the fit results and χ^2 values have also been modified to something that can easily be read by an external plotting package (*e.g.* see Section 6.1.3).

From experience, to achieve accurate results over multiple data-sets, it was found that a consistent approach to fitting was necessary. For each line measured, the wavelength range to be included in the fit had to be specified. These values are listed in Table 6.1, and are common to fits to all data-sets presented in this thesis.

We also constrained the FWHM in every case to be greater than the measured instru-

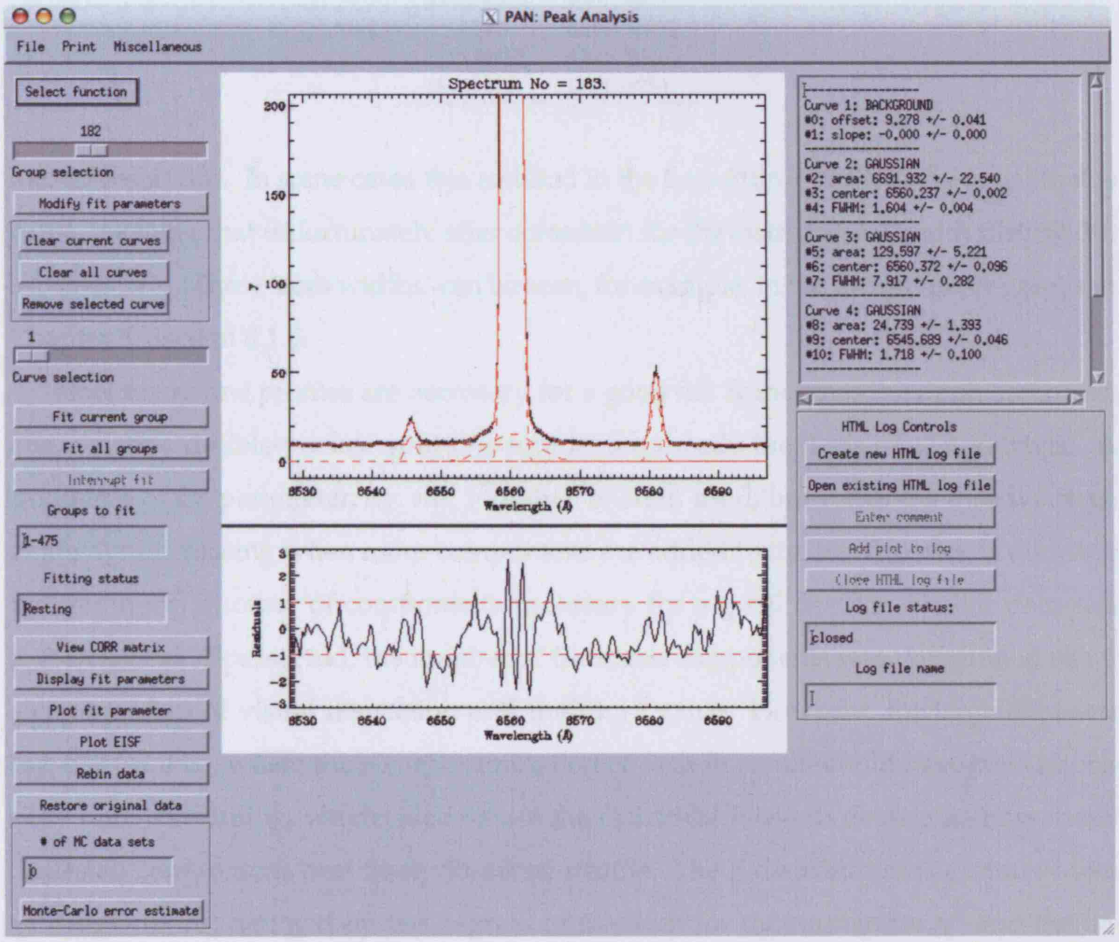

Figure 6.1: A screen-shot of the main PAN interface window showing a multiple-Gaussian fit to the Hα and [N II] lines in an example spectrum. The data is represented by a solid black line, the individual Gaussian components as dashed red lines, and the summed model profile as a solid red line. The (model − data) residuals are shown below the main plot, and the fit parameters are listed in a box to the right of the window. In the top-left a slider shows the spectrum number currently shown, and allows the user to step through the spectrum array.

Table 6.1: Wavelength limits used in fitting each line

Spectral Line	Wavelength (Å)
Hβ	4840 – 4880
[O III]λ5007	4940 – 5020
[O I]λ6300	6250 – 6308
[N II]λ6583	6570 – 6595
Hα	6550 – 6575
[S II]λ6717	6700 – 6724
[S II]λ6731	6720 – 6750

mental resolution. In some cases this resulted in the best-fitting width being equal to this value, meaning that unfortunately after correction for the instrumental width their width becomes zero. These 'zero widths' can be seen, for example, in the line property graphs in Chapter 8, Section 8.1.5.

How many line profiles are necessary for a good fit? Sometimes the decision is obvious, *e.g.* for a double-peaked split line profile, but mostly the decision is non-trivial. A 'goodness of fit' parameter, *e.g.* the χ^2 value, is often used, but it has the disadvantage of always decreasing when more components are added to the fit. The trick is deciding the minimum number of components necessary for a good fit. For smaller data-sets (*e.g.* DensePak/SparsePak), the number of Gaussian components was determined using a combination of visual inspection and the fit χ^2 value. However, for large data-sets (*e.g.* GMOS IFU), where the visual examination of each fit result would have been impossibly time-consuming, we decided to use the statistical F-test to determine how many Gaussian components best fit an observed profile. The F-distribution is a ratio of two χ^2 distributions, denoted by the degrees of freedom for the numerator χ^2 and the denominator χ^2. For statistically comparing the quality of two fits, this function allows one to calculate the significance of a variance (χ^2) increase that is associated with a given confidence level, for a given number of degrees of freedom. The test will output the minimal increase of the χ^2 ratio that would be required at the given confidence limit for deciding that the two fits are different. If the χ^2 ratio is higher than this critical value, the fits are considered statistically distinguishable. The output files for single and multiple Gaussian models were passed through a script which applied the F-test to extract the results for the most suitable case for each spectral line.

We also applied a number of physical tests to further improve the accuracy of the results. Firstly, for a fit to be accepted, the measured FWHM had to be greater than the

associated error on the FWHM result, and secondly the FWHM had to be smaller than 15Å (to guard against fitting continuum or spurious features). We also applied some additional filtering in order to ensure the first Gaussian component always corresponds to our definition of the first component (*i.e.* if flux(C1) < flux(C3) AND fwhm(C1) < fwhm(C3) then swap C3 with C1). This only applied when the line contained more than two components and was sufficiently well resolved to reliably fit them all.

In the cases where a visual inspection was made, the residual plot was helpful in determining whether a further component was necessary. A missing component would often show up as a consistent asymmetric profile in the residuals when stepping though the spectra. The residuals, r_i, are calculated by PAN using the following formula:

$$r_i = \frac{y_i^{fit} - y_i^{data}}{\sigma_i} \tag{6.2}$$

where σ_i are the uncertainties on y_i^{data}.

Fig. 6.2 shows a number of example Hα line profiles showing single, double and triple Gaussian component fits using PAN. Three are from the Gemini/GMOS IFU data presented in Chapter 5 and one is from the DensePak data of M82 presented in Chapter 4.

6.1.2 How well can we fit each component?

The χ^2 minimisation algorithm used by PAN is very sensitive to the uncertainties associated with the input spectra. Because of this, we paid special attention to creating accurate Poissonian error arrays from the raw un-calibrated spectra, which we then associated with the fully reduced spectra for the purposes of fitting. We made a number of tests comparing the results of Gaussian fits to high and low S/N arc lines made with PAN with those output by other line fitting routines (such as the well-established ELF within the STARLINK DIPSO program). Shown in Figs 6.3 and 6.4 are comparisons of the errors estimated by both routines for single Gaussian fits to a selection of high and low S/N arc lines spread over the wavelength range observed by the Gemini/GMOS instrument (Chapter 5). Despite differences in the minimisation techniques employed, results and uncertainties quoted are very similar, and the results quoted by PAN are in fact more consistent over the full wavelength range. We are therefore confident with the quality of results derived by PAN.

The errors that PAN quotes on its fit results are derived simply from the formal errors on the χ^2 minimisation. Unfortunately, when an accurate associated error array is not

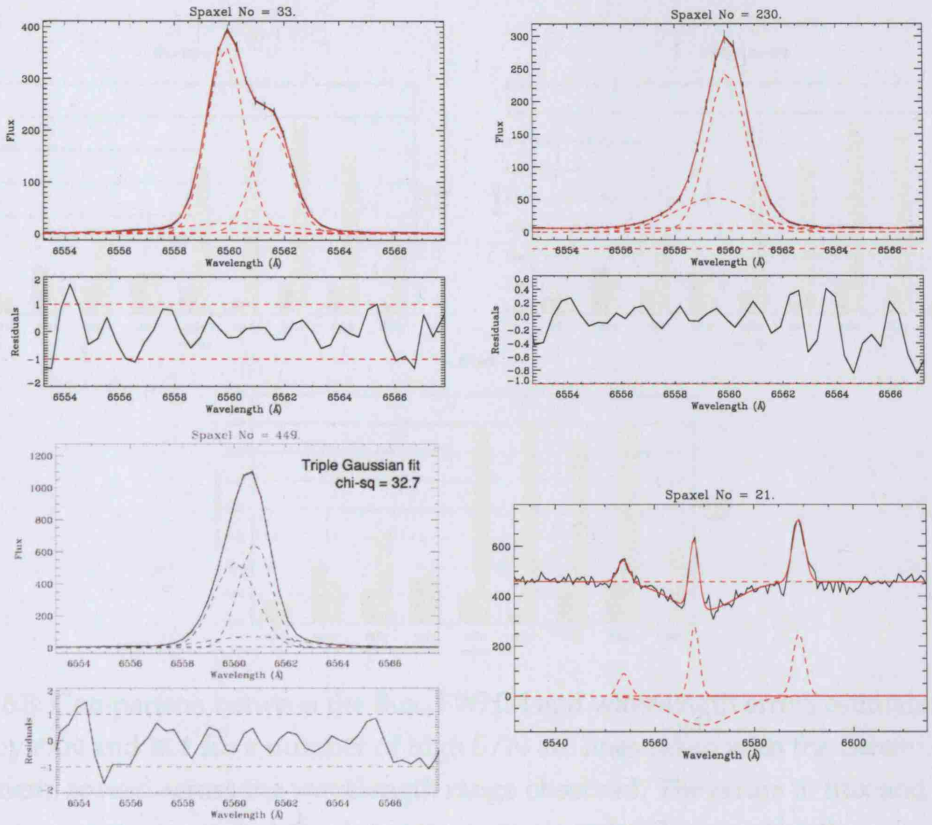

Figure 6.2: Upper two plots and lower-left are fit examples from three different Gemini/GMOS IFU positions in NGC 1569 showing split line profiles and underlying broad components. The lower-right plot is from a DensePak position in the M82 disk showing fits to the [N II] and Hα lines in emission and the Hα line in absorption. The residual plot is not shown since the associated error array for this data-set was not well determined.

given (*i.e.* the associated errors are simply estimated from the reduced data), or a variable number of multiple Gaussian components are used, we found the errors on the fit results to be an under-estimate of their true values. For results quoted in the various chapters of this document where either of these conditions apply, realistic errors have been estimated through visual inspection of the fit quality taking into account noise in the continuum (*i.e.* S/N of line) and the number of fitted components. In general, we find for the Hα line flux, the percentage error varies between 0.5–10 per cent for the first component fit (for high–low S/N lines), 8–15 per cent for a second component and 10–80 per cent for a third. The addition of multiple Gaussian components always increases uncertainties; we estimate that where we can fit a third component, the errors in the flux of the first two components increase by 5–10 per cent. For our GMOS IFU data, we find that the

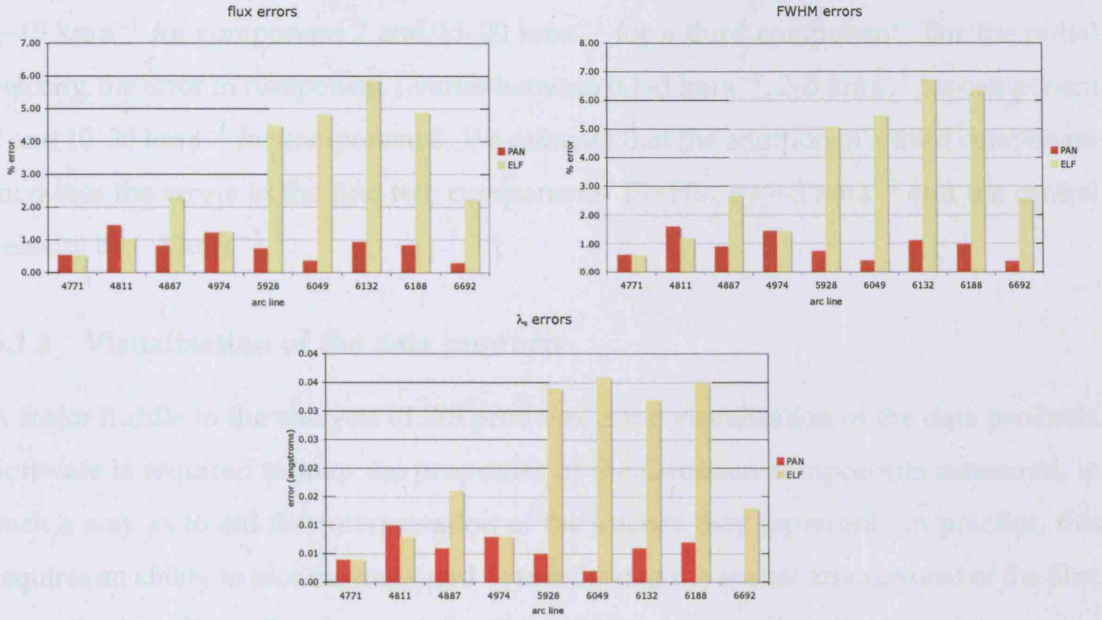

Figure 6.3: Comparison between the flux, FWHM and wavelength errors estimated by fits made by PAN and ELF for a number of high S/N arc lines taken with the *Gemini*/GMOS instrument, spread across the wavelength range observed. The errors in flux and FWHM are given as percentages, but absolute errors are given for the wavelengths.

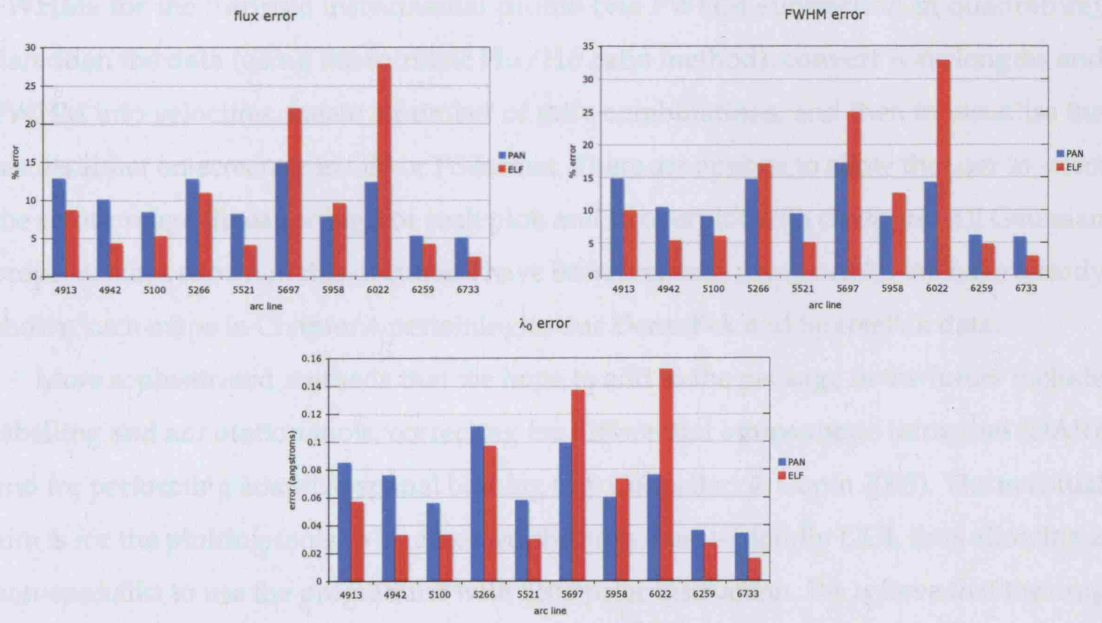

Figure 6.4: As for Fig. 6.3 but for low S/N arc lines.

FWHM errors vary between 0.25–2 $\mathrm{km\,s^{-1}}$ for high–low S/N of component 1 respectively, 4–15 $\mathrm{km\,s^{-1}}$ for component 2 and 15–20 $\mathrm{km\,s^{-1}}$ for a third component. For the radial velocity, the error in component 1 varies between 0.1–3 $\mathrm{km\,s^{-1}}$, 2–5 $\mathrm{km\,s^{-1}}$ for component 2 and 10–30 $\mathrm{km\,s^{-1}}$ for component 3. We estimate that the addition of a third component increases the errors in the first two components' FWHM by $\sim$5 $\mathrm{km\,s^{-1}}$ and the central velocity by $\sim$3 $\mathrm{km\,s^{-1}}$.

6.1.3 Visualisation of the data products

A major hurdle in the analysis of IFS products is the visualisation of the data products. Software is required to map the properties of the Gaussian components measured, in such a way as to aid the interpretation of the science they represent. In practice, this requires an ability to plot the measured data following the spatial arrangement of the fibre array (*i.e.* two-dimentional mapping). The software also need methods of determining the plot ranges and colour tables, calculating the ratios of properties (*e.g.* for determining reddening), and overplotting multiple maps in a sensible way. To this end, Katrina Exter (STScI) and I have developed a PERL/PGPLOT based plotting and analysis package to enable the mapping of Gaussian properties measured from our data-sets.

The program, with the *provisional* name DAISY, allows the user to correct the measured FWHMs for the intrinsic instrumental profile (via FWHM subtraction in quadrature), deredden the data (using the intrinsic Hα/Hβ ratio method), convert wavelengths and FWHM into velocities, create a number of ratio combinations, and then to visualise the results either on-screen or in GIF or PS format. There are options to allow the user to select the colour range (linear or log) for each plot, and to overplot with contours. All Gaussian property maps shown in this document have been prepared using DAISY. We have already shown such maps in Chapter 4 pertaining to our DensePak and SparsePak data.

More sophisticated methods that we hope to add to the package in the future include labelling and annotation tools, correcting for differential atmospheric refraction (DAR), and for performing adaptive spatial binning (*e.g.* Cappellari & Copin 2003). The eventual aim is for the plotting tools to be accessed through a user-friendly GUI, thus allowing a non-specialist to use the programme with little prior instruction. We believe that the only way current and future large-format IFUs will be accepted by a non instrument-specialist astronomical audience, is by developing useful, user-friendly analysis tools and help to dispel some of the misgivings people have with such instruments.

CHAPTER 7

MAPPING THE ROOTS OF THE GALACTIC WIND IN NGC 1569 – I. A YOUNG SUPER-STAR CLUSTER AND ITS ENVIRONMENT

In Chapter 5 we gave a comprehensive introduction to the dwarf-starburst galaxy NGC 1569 and described how the latest starburst episode has resulted in a large-scale galactic wind formed from a number of discrete supershell structures. In the following two chapters, we analyse the observations also described in Chapter 5, with the aim of understanding how and where the galactic wind in NGC 1569 is produced, driven, accelerated, interacts and evolves to be what we observe.

In this first chapter we present a detailed analysis of one of the four Gemini/GMOS IFU positions (position 2), which covers a young star cluster and its immediate surroundings within the largest H II region complex in the galaxy. In Chapter 8 we present the analysis of the other three IFU positions covering the central outflow region, and discuss our findings for this IFU position in context with the whole central region.

After data-reduction, flux-calibration and DAR correction (Chapter 5), the data were in row-stacked spectra (RSS) format, meaning that we could simply analyse each spectrum and relate its spatial location back to the array using the position table. Fig. 7.1 shows IFU position 2 overlaid on an *HST* WFPC2 F656N image of the surrounding region. We can use the spectral information to derive an IFU image to compare directly with

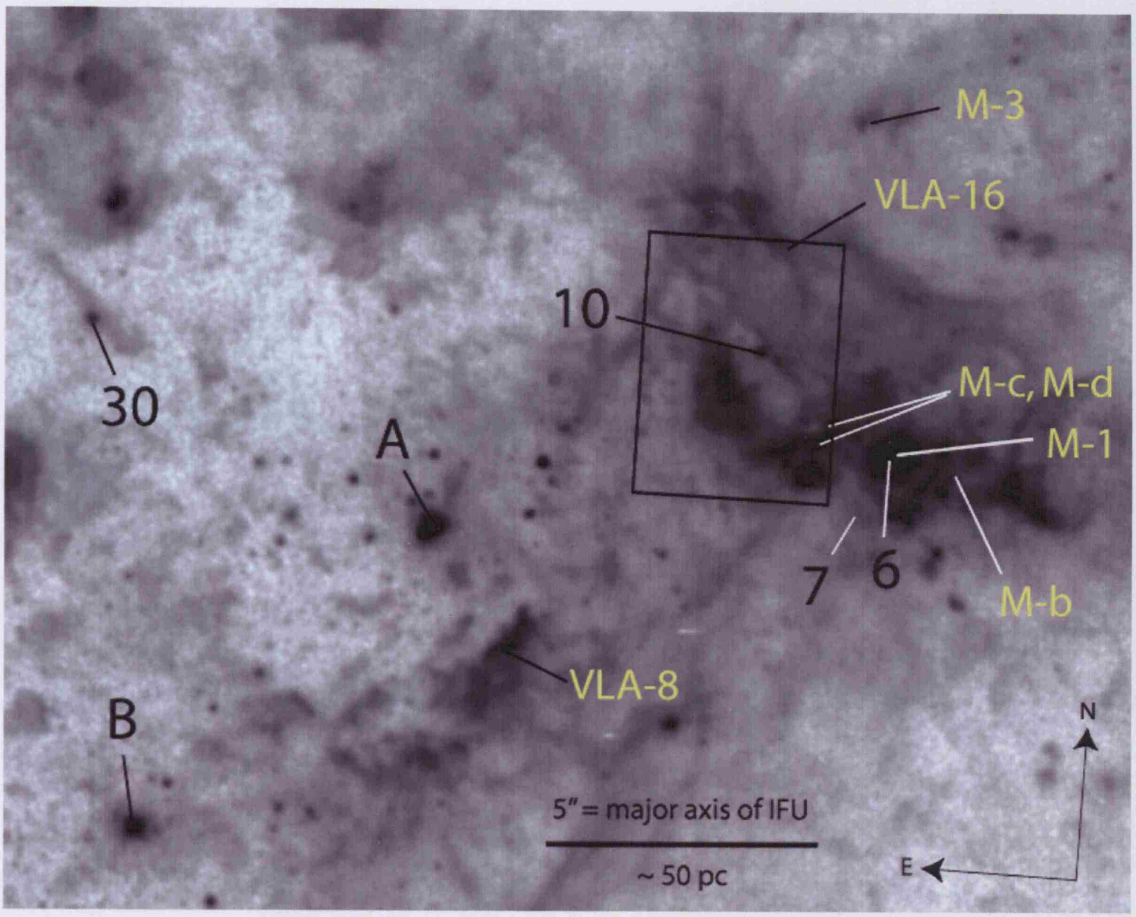

Figure 7.1: *HST*/WFPC2 Planetary Camera image taken through the F656N filter of the central region of NGC 1569 showing the position of the IFU field. A number of the most prominent star clusters (Hunter *et al.* 2000) and radio continuum sources (Greve *et al.* 2002*a*) are labelled in black and white respectively. (Adapted from the figure in Chapter 5.)

HST images. Fig. 7.2 (left panel) shows an *HST* ACS/HRC F555W image of the region covered in our IFU pointing. In the centre we show a virtual V-band image reconstructed from our IFU data by convolving the spectrum from each spaxel with a V-band filter function. The similarity between the two images is obvious once the resolution of each is taken into account (ACS/HRC = 0.″026 pixel^{-1}; GMOS IFU = 0.″18 spaxel^{-1} but seeing limited at ~0.″8). The fact that the ACS F555W filter contains contamination from nebular [O III] emission must be borne in mind, which is why a certain amount of nebulosity is seen surrounding cluster 10. The right-hand plot is of the same field but restricted in wavelength to cover the continuum only (6645–6660 Å). Overlaid is an outline of the 24 spaxels summed to create a spectrum of cluster 10 (see Section 7.1).

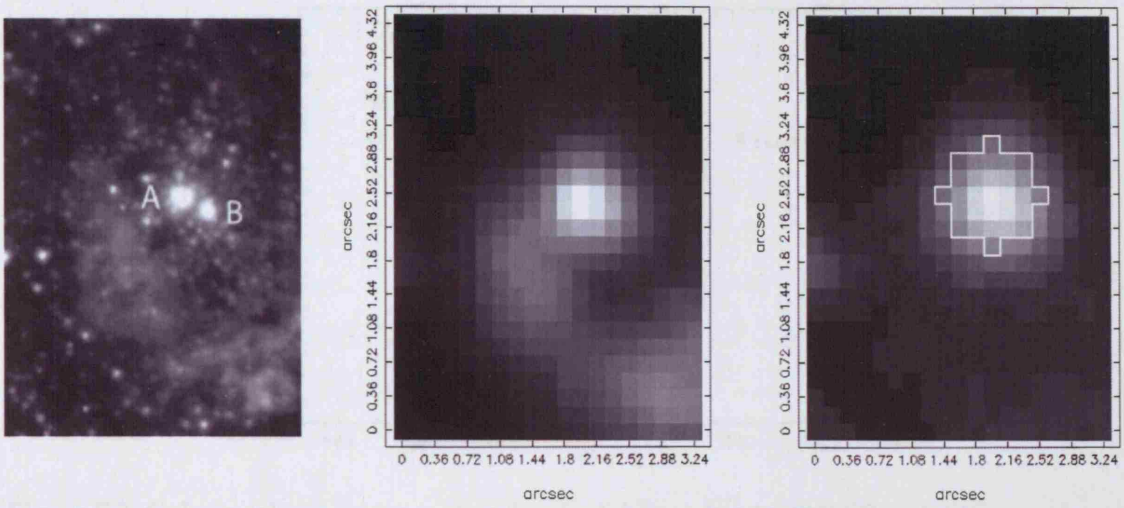

Figure 7.2: *Left:* HST/ACS HRC F555W image of the region covered by the IFU pointing. The two components of cluster 10 are labelled. *Centre:* IFU data convolved with a V-band filter function. *Right:* flux map in the continuum only (6645–6660 Å), showing the position of cluster 10 and the spaxels extracted to form the cluster spectrum. North is up and east is left.

7.1 Cluster 10

Cluster 10 is the third visually brightest cluster identified by (Hunter *et al.* 2000) but, as can be seen from Fig. 7.2 (left panel), it is in fact a double cluster. Because of the close proximity of the two sources, previous studies (*e.g.* Hunter *et al.* 2000) have treated cluster 10 as one object. Fitting the light profiles across the length and breadth of the IFU field with a Gaussian profile yields a average FWHM of 4.7 spaxels or 0.″84. This corresponds to the maximum seeing disc size at the time of observation, meaning that the two sub-clusters are not resolved.

From the F555W ACS/HRC image, we measure the separation of cluster 10 and it's companion as 0.″346 (3.69 pc). The coordinates of the two sources are given in Table 7.2 at the end of this section. Measurement of the size of the two clusters was made on the WFPC2 F439W image, and was achieved using ISHAPE (Larsen 1999) together with the TINYTIM package (Krist 2004) to correct for the point-spread function (PSF; the HRC images were not used to fit the size since a sufficiently accurate PSF model has yet to be developed for this detector). Using a circular Moffat function with a power index of 1.5, and a fit radius of 0.″2 gives an effective radius, $R_{\rm eff}$, of 0.88 ± 0.05 pc for the north-eastern component (hereafter cluster 10A; see Fig. 7.2 left panel), and $R_{\rm eff} = 0.60 \pm 0.15$ pc for the

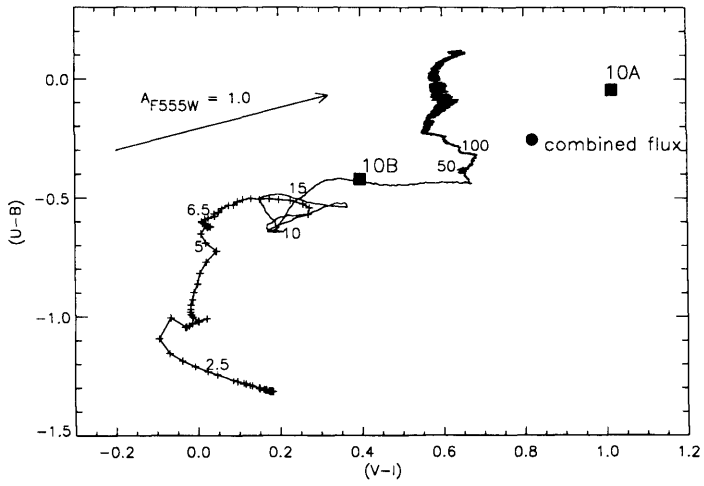

Figure 7.3: Colour-colour diagram showing (solid line) STARBURST99 instantaneous burst models for $Z = 0.004$. Crosses mark age points on the evolutionary curve from 5–7 Myr only; some significant age steps are labelled (units of Myr). The arrow represents the extinction vector for $A_{F555W} = 1.0$. Solid squares show the colours of the two clusters (cluster 10A and 10B); the solid circle shows the colour of the two combined, derived from the sum of the flux from both sources.

south-western component (hereafter cluster 10B). Due to this very small separation, and the crowding of the field around cluster 10 with other fainter sources, standard aperture photometry is not possible (and we cannot measure absolute magnitudes). However if all that is needed is relative magnitudes, then small-radius aperture photometry is sufficient. Using a radius of 4 pixels for the HRC images (F333W, F555W and F814W) and 2.5 pixels for the WFPC2 image (F439W) and suitable background annuli, we measure (F555W–F814W) = 1.12 and (F330W–F439W) = −0.27 for the cluster 10A, and (F555W–F814W) = 0.42 and (F330W–F439W) = −0.90 for cluster 10B.

Fig. 7.3 shows the evolutionary path of a $Z = 0.004$ STARBURST99 (SB99; Leitherer *et al.* 1999) instantaneous burst evolutionary-synthesis model with a standard Kroupa initial mass function (IMF) formulation in $U - B$, $V - I$ colour space, together with the colours that have been determined for both cluster 10 components. Also plotted is the colour of the summed flux from both annuli to compare to parameters derived from the spectrum, since the spectrum is derived from a convolution of the light from both components. SB99 does not give outputs in terms of *HST* filters, so the observed photometry was converted from *HST* to Johnson magnitudes using the conversion factors given by Holtzman *et al.* (1995) for the WFPC2 data, and Sirianni *et al.* (2005) for the ACS data. From the diagram we can

now derive an approximate age and an estimate of the reddening for each of the cluster components simultaneously. Assuming a extinction value sufficient to deredden each point until it intercepts the model track results in the following: for cluster 10A, $A_V \approx 0.8$ corresponds to an age of 50–100 Myr, whereas $A_V \approx 1.2$–2.0 gives an age of 5–20 Myr; for cluster 10B, zero extinction would imply an age of ~20 Myr, $A_V \approx 0.3$ intercepts the track at ~7–15 Myr, whereas an $A_V \approx 0.8$ implies an age of ~5 Myr. The extinction required for the combined point to cross the track at ~5–7 Myr is $A_V \approx 1.6$.

Adopting a Galactic foreground reddening of $A_V = 1.64$ [$E(B-V) = 0.53$] (following Origlia *et al.* 2001; Relaño *et al.* 2006), we can immediately rule out ages requiring reddening values less than this value. We therefore conclude that 10A must have an age of 5–7 Myr (with a foreground corrected reddening of $A_V \approx 0.0$–0.4), and 10B an age of $\leq$ 5 Myr (consistent with zero reddening after foreground correction). For the colour of the combined point to match these age determinations, the reddening value required is consistent with purely Galactic effects.

A further test to obtain an estimate of the cluster age is to compare the equivalent width of the Hα emission line to the predictions of evolutionary synthesis models. We measure the equivalent width from our spectrum of H$\alpha = 91 \pm 1$ Å. For the same SB99 model as used above ($Z = 0.004$, Kroupa IMF), this gives an upper limit to the age of ~6.5 Myr, and is consistent with the values derived above.

Buckalew *et al.* (2000) conducted a study of NGC 1569 using *HST* WFPC2 narrow-band imaging of the He II λ4686 line. They discovered fifteen He II emitting sources across the galaxy, of which five were associated with stellar clusters, including cluster 10 (specifically only the south-western component, 10B). They attribute the emission as nebular in origin (after Kobulnicky & Skillman 1997, who found wide-spread nebular He II emission in this region). However He II is also strongly emitted from the expanding winds of Wolf-Rayet (WR) stars of both WC and WN type. Buckalew *et al.* comment that *if* the emission they detect in cluster 10 was attributed fully to WR stars, it would correspond to the equivalent of three WNL-types (using the calibration of Vacca & Conti 1992). WR stars exist in clusters between ages of approximately 3–5 Myr, so in light of our age estimates for the two cluster components derived above, a WR origin for the He II emission in cluster 10B is perfectly reasonable.

Now we have an estimated age, we can derive an estimate for the mass by comparing the absolute magnitude, M_{F555W}, to evolutionary synthesis models. As mentioned above,

we cannot measure an absolute magnitude of the individual sub-clusters, but using an aperture large enough to include both, we find a combined $M_{\mathrm{F555W,cluster10}} = -9.61$ mag. Converting to Johnson magnitudes, we find $M_V \approx -9.2$ mag. A SB99 6 Myr, $1 \times 10^6\ M_\odot$ model predicts an absolute $M_v = -15.63$ mag, so comparing our measurements to this results in a mass of 2–5 $\times\ 10^4\ M_\odot$ (depending on the IMF formulation used) for the combined mass of both sub-clusters. Since there are uncertainties involved in transforming from the *HST* to Johnson magnitude system, we compared our measured M_{F555W} to the absolute magnitudes predicted by the equivalent Bruzual & Charlot (2003) model. The derived mass is 7–13 $\times\ 10^3\ M_\odot$ (depending on IMF), which is in general agreement with the SB99 result. This mass means that neither of the clusters can be defined as a 'super star cluster' in the generally accepted definition.

7.1.1 Cluster spectrum

To extract the spectrum of cluster 10, we summed 29 spaxels (covering an area with an equivalent diameter to the FWHM of the cluster measured from the IFU continuum image) centred on the continuum source as shown on the right-hand plot of Fig. 7.2. The resulting spectrum is shown in Fig. 7.4.

The spectrum is dominated by strong emission lines arising from the nebula surrounding the cluster, but also contains a broad emission feature that we identify with C IV $\lambda\lambda$5801,5812 arising from WC-type Wolf-Rayet stars. We also detect a large number of weak stellar absorption lines, diffuse interstellar bands (DIBs) and interstellar absorption lines. The detection of a red WR-bump is not unsurprising considering the age we find for cluster 10B, and strengthens the argument for a WR origin for the He II emission detected by Buckalew *et al.* (2000). Further evidence of the young nature of cluster 10 comes from the high ratio of [O III] to Hβ (see Fig. 7.4, lower line), and the presence of strong [S III] emission, indicating a high level of ionization in the surrounding H II region which can only arise in the presence young O stars.

Simultaneously fitting the WR feature with the overlaid absorption lines, we measure the bump to have a FWHM of ~130 Å, a total luminosity of 2.5×10^{37} erg s^{-1} (assuming a distance of 2.2 Mpc and $A_V = 1.64$), and an equivalent width of 12 ± 2 Å. This measured FWHM is unusually broad compared to canonical measurements (Crowther *et al.* 1998), and is likely to result from inaccuracies in the fit due to contamination from the superposed DIB absorption lines. Crowther & Hadfield (2006) present measurements of WR

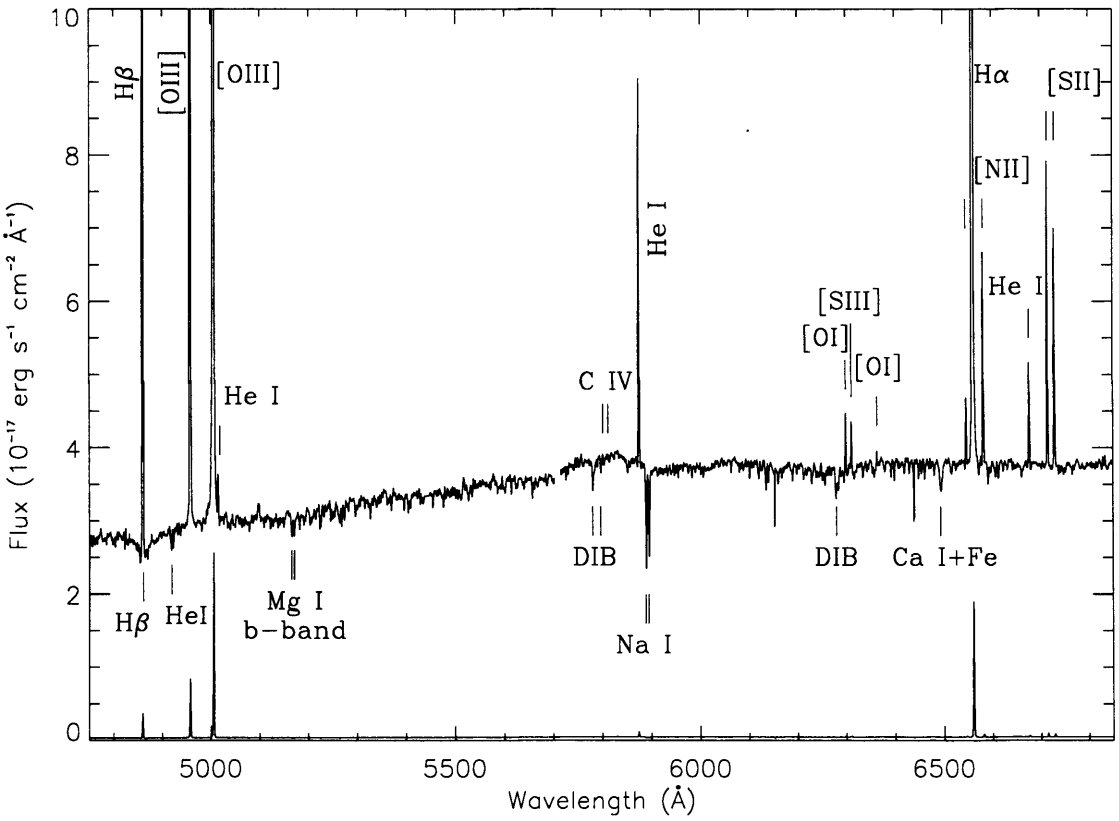

Figure 7.4: Plot of the extracted spectrum of cluster 10 (smoothed by 5 Å). All identified absorption and emission features are labelled. The lower line corresponds to a $\times 80$ reduction of the main plot to illustrate the the spectrum with a full flux range. Notice the strength of the [O III]λ5007 emission compared to the hydrogen recombination lines.

bump fluxes for a number of WC4 type stars in the LMC (the closest galaxy containing a significant population of WR stars at low metallicity – $Z = 0.008$) which can be used to determine the equivalent number of stars in our observation. They find one LMC WC4 star to have a red WR bump luminosity of $3.3 \pm 1.6 \times 10^{36}$ erg s^{-1}, thus the luminosity equivalent number of WC4 stars in our observed bump is estimated to be 10 ± 5, once all the uncertainties have been taken into account. For comparison, González-Delgado *et al.* (1997) find a luminosity equivalent of 20 ± 10 WNL stars in SSC A by measuring the flux in the blue WR bump.

By fitting Gaussian profiles to all the other emission and absorption lines present in the spectrum, we measured the central velocity and FWHM of each, and present them in Table 7.1. The average radial velocity of the nebular emission lines is -82 ± 4 km s^{-1}. Since our cluster spectrum only contains blended photospheric absorption lines, it is not possible

to measure an accurate velocity of the stellar component. The evolutionary synthesis models of Bruzual & Charlot (2003) provide a set of spectral energy distributions (SEDs) calculated for similar input ranges as the SB99 models, and although being less accurate at predicting very young ages, their SEDs are derived from actual observed spectral libraries rather than model stellar atmospheres. Their inclusion of observed stellar spectra at high resolution therefore make them ideal for comparing with our spectrum to derive a cluster velocity. Using a 0.25 $Z_{\odot}$, 5 Myr instantaneous burst model in the wavelength range 5100–5600 Å (where many faint stellar absorption lines are present), we find a match at -85 ± 5 km s^{-1}. A good correlation at this velocity is also found at the position of the Ca I+Fe blend at 6494 Å, which is thought to be photospheric in origin (Heckman *et al.* 1995). As well as stellar absorption lines, we detect the interstellar (IS) absorption lines of Na I $\lambda\lambda$5890,5896 and a number of DIBs (Herbig 1995; Heckman & Lehnert 2000). Their velocities are given in Table 7.1, and are consistent with being Galactic in origin (average velocity -40 ± 5 km s^{-1}), although the Na I profiles also show blue wings presumably associated with IS absorption within NGC 1569.

Determining the proper heliocentric systemic velocity, $v_{\rm sys}$, of NGC 1569 has proven to be a difficult task due to its irregular and disturbed morphology. The first study of NGC 1569's H I gas distribution by Reakes (1980) concluded a $v_{\rm sys} = -77$ km s^{-1}. CO observations by Taylor *et al.* (1999) find the same value, whilst Tomita, Ohta & Saito (1994) and Heckman *et al.* (1995) find an Hα $v_{\rm sys}$ of -90 km s^{-1} and -68 km s^{-1} respectively from their long-slit data. A more recent, high resolution H I study of the NGC 1569 system was made by Mühle *et al.* (2005), who find the peak of the H I profile at the position of cluster 10 to have a velocity of -80 km s^{-1} (S. Mühle, private communication). Thus, since our measurements of the ionized gas and cluster velocities are also consistent with this value, we adopt a systemic velocity for the cluster 10 region of $v_{\rm sys,10} = -80$ km s^{-1}.

Another check on the value of reddening for the combined light of both cluster components can be made by comparing the observed Hα/Hβ flux ratio with the intrinsic case B values from Hummer & Storey (1987). We derive an absorption-corrected reddening of $E(B-V) = 0.54 \pm 0.15$ mag from Gaussian fits to the Hα emission and Hβ emission and absorption lines. This value is consistent with both the adopted value of Galactic foreground reddening and with the extinctions derived from the colour-colour plot analysis given above. We therefore conclude that cluster 10 only suffers from Galactic foreground reddening; very little of its light is attenuated by material in NGC 1569 itself.

Table 7.1: Absorption and emission line measurements for cluster 10 (all lines are emission unless otherwise stated). Widths are corrected for instrumental contribution and velocities are quoted in the heliocentric frame of reference. Typical errors on the velocities of the emission lines are ~5–10 $\mathrm{km\,s^{-1}}$, and on the widths ~0.5–5 $\mathrm{km\,s^{-1}}$. Errors for the absorption lines are listed individually.

Line	λ_{air} (Å)	Velocity ($\mathrm{km\,s^{-1}}$)	FWHM ($\mathrm{km\,s^{-1}}$)
Hβ	4861.33	−84.4	50.7
Hβ abs[a]	4861.33	−55 ± 40	
He I abs[a]	4921.93	−84 ± 8	
[O III]	4958.92	−79.0	44.7
[O III][b]	5006.84	−75.1	31.6
He I[c]	5015.68	−74.7	42.3
Mg I abs	5167.32	−77 ± 7	180 ± 15
Mg I abs	5172.68	−89 ± 6	100 ± 15
DIB	5780.5	−40.9 ± 10	160 ± 35
DIB	5797.0	−47.5 ± 20	70 ± 25
He I	5875.67	−82.7	33.9
Na I abs	5889.95	−38 ± 8	
Na I abs	5895.92	−34 ± 8	
DIB	6283.9	−41.0 ± 10	110 ± 20
[O I]	6300.30	−84.9	32.8
[S III]	6312.10	−82.0	50.5
[O I][a]	6363.78	−80.1	
[N II]	6548.03	−81.4	28.3
Hα[b]	6562.82	−89.1	38.8
[N II]	6583.41	−82.8	44.5
He I	6678.15	−81.6	44.1
[S II]	6716.47	−85.1	40.8
[S II]	6730.85	−84.4	46.5

[a] Line too weak or confused to measure an accurate FWHM
[b] Narrow component (C1) only
[c] Blended with [O III]

The flux ratio of single Gaussian fits to the [S II]$\lambda\lambda$6717,6731 emission lines gives a value of $1.25^{+0.02}_{-0.01}$ hence an electron density, $n_e = 175^{+18}_{-20}$ $\mathrm{cm^{-3}}$ (assuming an electron temperature, $T_e = 10^4$ K). These results are summarised in Table 7.2.

7.2 Properties of the ionized gas

We now discuss the IFU data relating to the ionized gas in the environment of cluster 10. The signal-to-noise and spectral resolution of these data are sufficiently high to resolve multiple Gaussian components to each emission line in each of the 500 spectra across the field-of-view. Before discussing our findings, we first describe the methods used to fit the

Table 7.2: Observed and derived properties for cluster 10.

	Cluster component	
Parameter	10A	10B
Adopted systemic velocity ($km\,s^{-1}$)	-85	
Distance (Mpc)	2.2†	
Coordinates (J2000)	$04^h\,30^m\,47^s.16$	$04^h\,30^m\,47^s.12$
	$+64°\,51'\,00''.8$	$+64°\,51'\,00''.6$
(F555W–F814W)	1.12	0.42
(F330W–F439W)	-0.27	-0.90
Half-light radius, R_{eff} (pc)	0.88 ± 0.05	0.60 ± 0.15
Total $E(B-V)$	0.55 ± 0.15	
Electron density, n_e (cm^{-3})	175^{+18}_{-20}	
Age (Myr)	5–7	≤ 5
M_{F555W} (mag)	-9.61	
Mass ($M_\odot$)	$7 \pm 5 \times 10^3$‡	
No. of equiv. WC4 stars	10 ± 5	
Radial velocity ($km\,s^{-1}$)	-85 ± 5	

† Israel (1988)

‡ Depending on whether a Salpeter or Kroupa IMF is used

spectral line profiles and visualise the results.

7.2.1 Decomposing the line profiles

The automated fitting of multiple profiles to 500 spectra each containing eight emission lines has proved challenging. For this task we have adopted an IDL-based, general-purpose curve-fitting package, called PAN (Peak ANalysis; Dimeo 2005). This package and the techniques we employed to determine how many Gaussian components best fit an observed profile are described in detail in Chapter 6.

To obtain the correct errors in the profile fit parameters, the spectra read into PAN had to contain accurate associated error arrays. These error arrays were calculated by taking the square-root of the raw counts in the pre flux-calibrated and throughput-corrected data, converting this to a percentage of the total raw counts, and applying this to the final reduced and calibrated data in order to obtain the uncertainty equivalent to the Poissonian noise. This step was included when converting from FITS to PAN input format.

Each line in each of the 500 spectra was fitted using a single, double and triple Gaussian component initial guess where line fluxes were constrained to be positive and widths to be greater than the instrumental contribution. The wavelength limits used in fitting each line are given in Chapter 6 (Table 6.1). In general, the shape of the emission line profiles is a convolution of a bright, narrow component overlying a faint, broad component (most

obvious in high S/N lines, *e.g.* Hα). This is consistent with what Heckman *et al.* (1995) found for the central regions. For the double component fits, the initial guess was always made with the first Gaussian as the narrow component (hereafter referred to as C1), and the second Gaussian as the broader component (hereafter C2). For the triple component fit, the additional component (C3) was specified with a initial guess assigning it to a supplemental narrow line at the same wavelength as the main narrow line. This consistent approach helped limit the confusion that might arise during analysis as to which Gaussian fit belonged to which component of the line, as well as aiding the χ^2 minimisation process.

Fig. 7.5 shows two example Hα line profiles, each from a different spaxel, with their corresponding Gaussian fits and residual plots shown (see Chapter 6 for a description of how the residuals are calculated). The upper example represents an instance where two Gaussian components are needed to fit the profile –with the inclusion of a second Gaussian the fit, χ^2 is dramatically reduced and the residuals fall within the ± 1 guidelines. The lower plots show an example of a profile which is best fit with a triple Gaussian model. The addition of a second narrow, bright component as well as the broad, faint component causes a significant reduction in the χ^2 and again the residuals fall within the ± 1 guidelines.

The bright [O III]λ5007 line also exhibits the general line profile shape described above (narrow bright component with underlying fainter broad component), but unfortunately due to an instrumental artefact present at low levels in the blue wing of the line, we have not been able to characterise the shape of the secondary components accurately. The flux, width and velocity maps of the main bright [O III]λ5007 component (C1) look very similar to the equivalent Hα maps, so we do not show them here. Measurements of the [O III]λ4959 line also result in similar flux, FWHM and velocity distributions, but since it is a weaker line we cannot fit the low intensity broad component with any confidence.

In order to determine an accurate measurement of the instrumental contribution to the line broadening, we selected spectral lines from a wavelength calibrated arc exposure that were close to the Hα and [O III]λ5007 lines in wavelength, and sufficiently isolated to avoid blends. We then fitted these lines for all 750 apertures using PAN and took the average. The instrumental broadening at [O III] is 74 ± 5 km s^{-1} and at Hα is 59 ± 2 km s^{-1}.

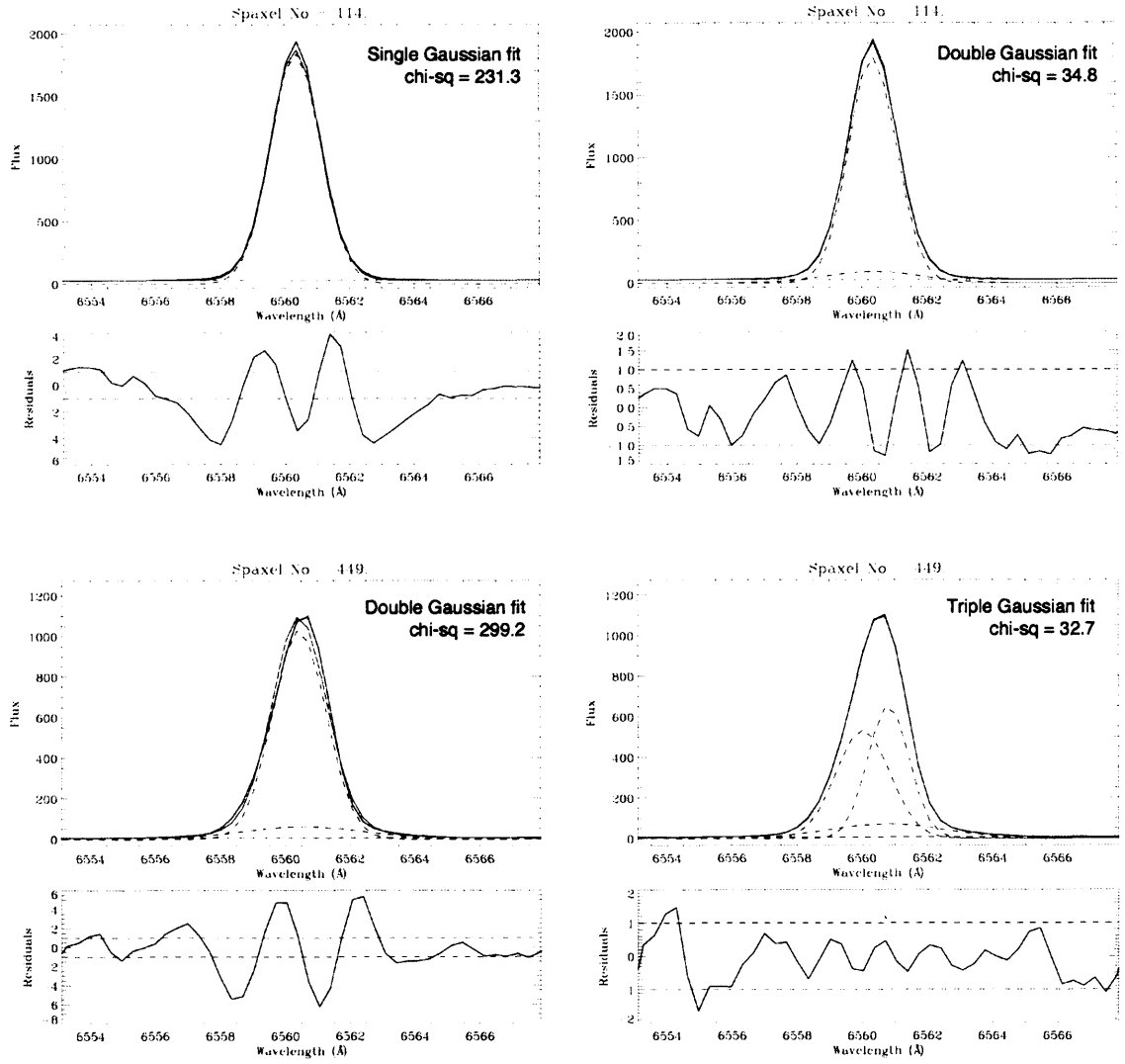

Figure 7.5: Examples of Hα line fits made by PAN comparing a single and double Gaussian fit for spaxel 114 and a double and triple fit for spaxel 449 (y-axis in arbitrary flux units, but note the difference in scale). The solid line is the observed data and the dashed lines represent the individual Gaussian components. Below each graph is a plot of the residuals (in units of σ) with dashed guidelines plotted at ± 1 (see Chapter 6 for an explanation of how the residuals are calculated). By comparing the ratios of the χ^2 values, the significance of a higher number of fit components can be tested.

7.2.2 How well can we fit each component?

The χ^2 minimisation algorithm used by PAN is very sensitive to the uncertainties associated with the input spectra. Because of this, we paid special attention to creating accurate Poissonian error arrays from the raw un-calibrated spectra, that we then associated with the fully reduced spectra for the purposes of fitting (see above and Chapter 6).

For a consistency check on the variability of the instrumental profile, we performed Gaussian fits to the unresolved [O I]λ5577 telluric emission line on pre-sky-subtracted spectra. The spatial distribution of the fit components clearly show no systematic variability across the IFU field indicating that the line profile shape is very stable. We also find that the telluric line is well fit by a single Gaussian, and shows no evidence for broad wings. The [O I] line fluxes have a standard deviation, s.d. $= 15 \times 10^{18}$ erg s^{-1} cm^{-2} arcsec^{-2}, the FWHM s.d. $= 4.5$ km s^{-1} and radial velocity s.d. $= 1.9$ km s^{-1}.

We now turn to the uncertainty estimates on each line component's Gaussian properties (line centre, flux and width). Unfortunately, the errors that PAN quotes on its fit results are derived simply from the formal errors on the χ^2 minimisation, and we have found these to be an under-estimate of the true uncertainties. More realistic errors have been estimated through visual inspection of the fit quality taking into account noise in the continuum (*i.e.* S/N of line) and the number of fitted components. For the Hα line flux, the percentage error varies between 0.5–10 per cent for C1 (for high-low S/N lines), 8–15 per cent for C2 and 10–80 per cent for C3. The addition of multiple Gaussian components always increases uncertainties; we estimate that where we can fit a third component, the errors in the flux of C1 and C2 increase by 5–10 per cent. For estimation of the FWHM and radial velocity errors, we have compared fits to the two lines of the [O III]$\lambda\lambda$4959,5007 doublet where possible. We find the FWHM errors vary between 0.25–2 km s^{-1} for high-low S/N C1 lines respectively, 4–15 km s^{-1} for C2 and 15–20 km s^{-1} for C3. For the radial velocity, the error in C1 varies between 0.1–3 km s^{-1}, 2–5 km s^{-1} for C2 and 10–30 km s^{-1} for C3. We estimate that the addition of a third component (where required) increases the errors in the C1 and C2 FWHM by $\sim$5 km s^{-1} and the central velocity by $\sim$3 km s^{-1}.

7.2.3 Visualisation of the data products

A major hurdle in the analysis of IFS is the visualisation of the data products. To this end, we have developed a PERL/PGPLOT based plotting and analysis package that has

enabled us to map out the results that we have obtained from our dataset. We have already shown one such visualisation in Fig. 7.2. The program allows the user to correct for DAR (currently not implimented), correct the measured FWHMs for the intrinsic instrumental profile (via simple FWHM^2 subtraction), deredden the data using the intrinsic Hα/Hβ ratio method, convert wavelengths and FWHM into velocities, create a number of ratio combinations, and then to visualise the results. There are options to allow the user to select the colour range (linear or log) for each plot, and to overplot using contours.

7.3 Emission line maps

Figs. 7.6–7.8 show maps of the fitted Gaussian properties (flux, FWHM and radial velocity) for each Hα line component (we show maps for measurements of the Hα line only for the reasons given above) over the whole field. Note, the systemic velocity, $v_{\rm sys} = -80$ km s^{-1}, has been removed in every radial velocity map. The grids represent that of our cubed data, not the original GMOS configuration, and the position of the cluster is overlaid with flux contours on selected maps to aid description and interpretation. As described in Section 7.2.1, in general we find a bright, narrow component overlaid on fainter, broad emission. This Hα broad component reaches a corrected FWHM of $\sim$300 km s^{-1} in places, indicating that this may be associated with the hot, fast moving cluster winds. In a number of spaxels we have been able to fit a third component (C3), which has approximately the same width as C1 implying that it may be associated with expanding shell- or bubble-like structures in the ionized gas.

7.3.1 Hα maps

Component 1 (C1)

From Fig. 7.6, it is immediately obvious that C1 and C2 do not originate in the same place, *i.e.* the flux maps show strikingly different spatial distributions. The two main knots of emission in C1, located near the middle and south-west of the field (south of the cluster), correspond to the pattern of diffuse emission seen in both the WFPC2 F656N (Fig. 7.1) and ACS F555W (Fig. 7.2, left) images. These knots lie just to the south of cluster 10 and mark the easternmost extent of the large ionized complex seen in Fig. 7.1 (H II region 2; Waller 1991). The width of C1 shown in Fig. 7.7 (left) ranges from a FWHM

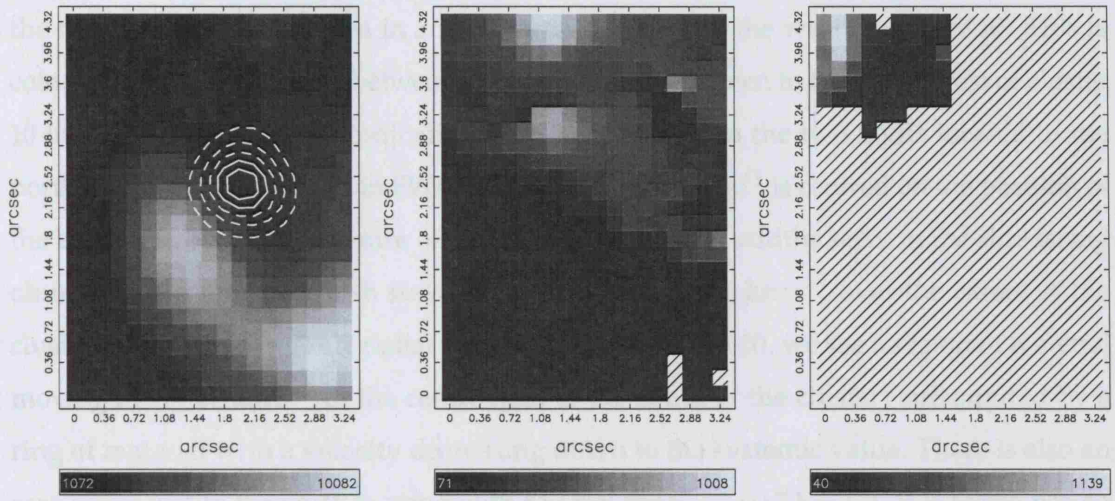

Figure 7.6: *Left:* Flux map in Hα component 1 (C1; bright, narrow); *centre:* flux map in Hα component 2 (C2; faint, broad); *right:* flux map in Hα component 3 (C3; narrow, second peak). Non-detections are represented as hatched spaxels, the x and y scales are in arcseconds offset from the lower-left spaxel, and a scale bar is given for each plot in units of 10^{-15} erg s^{-1} cm^{-2}. North is up and east is left. The higher levels in the continuum image are plotted as contours on the left-hand map, identifying the position of cluster 10.

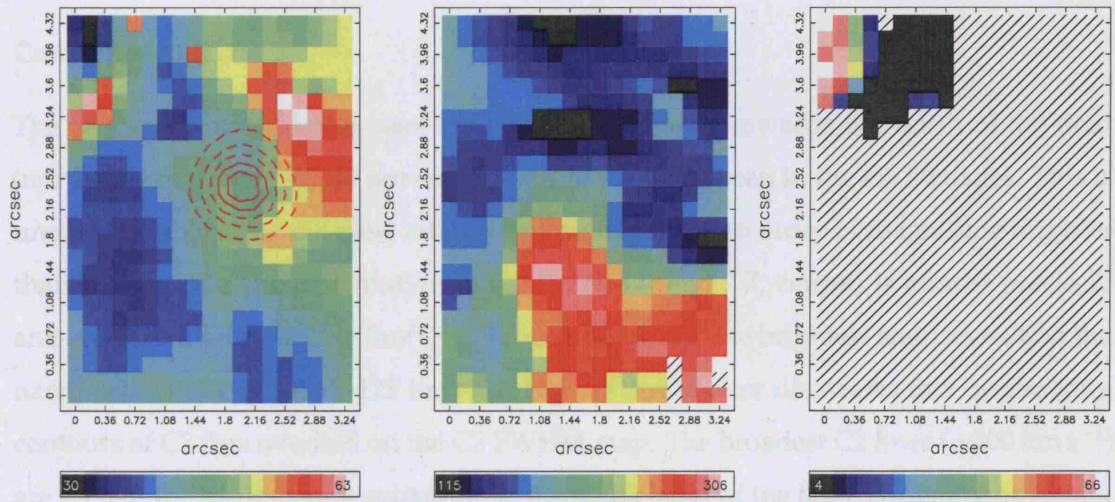

Figure 7.7: *Left:* FWHM map in Hα C1; *centre:* FWHM map in Hα C2; *right:* FWHM map in Hα C3. A scale bar is given for each plot in units of km s^{-1}, corrected for instrumental broadening. North is up and east is left, and the position of cluster 10 is identified on the left-hand map.

of ~30–40 km s^{-1} (corrected for instrumental broadening) towards the eastern side of the field, to ~60 km s^{-1} seen in a region arcing round to the west of cluster 10. This is coincident with the strip in-between two linear filaments seen to the north-west of cluster 10 in Fig. 7.1, and may be indicative of an influence from the two SNRs located to the north of the FoV. A gradient in FWHM from ~35 to 45 km s^{-1} is centred on the position of the bright Hα knot in the centre of the field, with broader widths seen on the side facing cluster 10, but the line width stays constant to within ~5 km s^{-1} over the extent of the cluster. As shown by the C1 radial velocity map (Fig. 7.8, left), we see a region of material moving at ~−10 km s^{-1} in the centre (just to the south of the cluster) surrounded by a ring of material with a velocity decreasing down to the systemic value. There is also an area of gas just to the north moving with a radial speed of ~+7 km s^{-1}. It is worth noting that these regions of negative and positive velocities are located either side of the position of the cluster at approximately equal distances. The fastest radially approaching C1 gas is seen in the south-west, moving at 10–15 km s^{-1}(coincident with the small dense knot seen in the *HST* Hα image), and the fastest receding gas is found along the eastern edge, increasing to ~15–20 km s^{-1} (off the colour scale for this plot) in the far north-east. It should be borne in mind that the total C1 radial velocity range observed across the whole field is only ~35 km s^{-1}.

Component 2 (C2)

The two small bright knots seen in C2 (Fig. 7.6, centre) towards the north of the field (north-east of cluster 10) do not correspond to anything seen in the HST images. This is understandable since the most intense emission in C1 is an order of magnitude brighter than that in C2. The distribution of C2 FWHMs (Fig. 7.7, centre) is almost precisely anti-correlated with the line flux (Fig. 7.6, centre), where the brightest features exhibit the narrowest line width (115–125 km s^{-1}). Fig. 7.9 (left) better illustrates this by showing contours of C2 flux overlaid on the C2 FWHM map. The broadest C2 lines (~300 km s^{-1}) are seen in the south-centre extending to the south-west of the field, corresponding well with the position of the brightest knots seen in C1 (Fig. 7.6, left) and the WFPC2 image. This again is illustrated clearly in Fig. 7.9 (right), where contours of C1 flux are overlaid on the C2 FWHM map. The C2 velocity field (Fig. 7.8, centre) covers the same overall range as the C1 gas; material approaching us at velocities of ~15 km s^{-1} (shown in blue) is located near the northern face of the bright C1 knot in the centre of the field, in between the

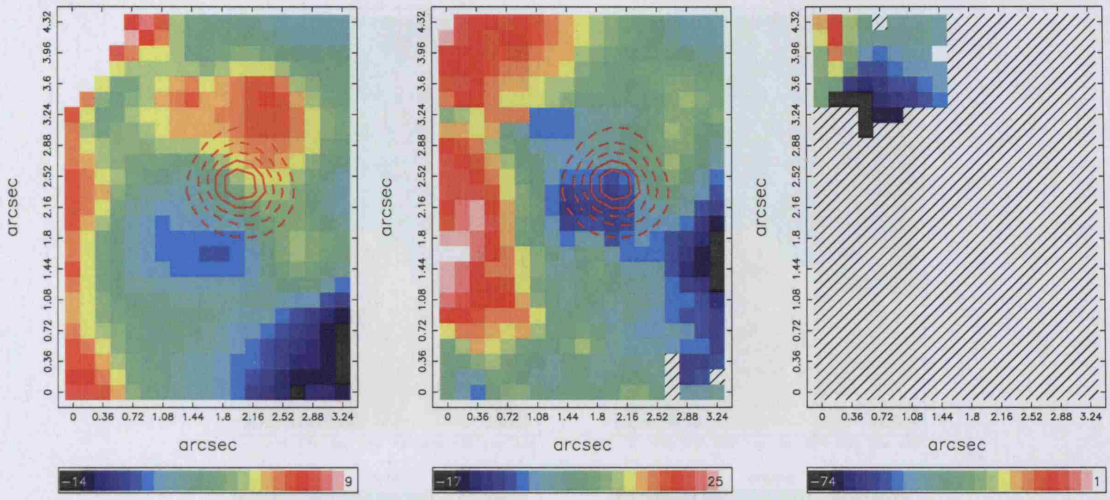

Figure 7.8: *Left:* radial velocity map in Hα C1; *centre:* radial velocity map in Hα C2; *right:* radial velocity map in Hα C3. A scale bar is given for each plot in units of km s^{-1} (heliocentric) relative to the systemic velocity of the region (-80 km s^{-1}). The position of cluster 10 is identified on the first two maps for comparison.

negative and positive velocity regions in C1, and almost coincident with cluster 10. This area of approaching gas also extends towards the west, reaching a maximum approaching velocity of 20 km s^{-1}. The fastest receding C2 velocities (red) are found along the eastern edge of the field at $\sim$20–25 km s^{-1} relative to the average. The spatial distribution of this region of redshifted gas mimics that of the redshifted C1 gas, but extends further to the west. Note the distribution of C2 radial velocities does not correlate with either of the C1 or C2 flux maps, however we do tentatively point out a possible radial velocity difference of $\sim$25 km s^{-1} between the two bright C2 knots seen in the flux map (Fig. 7.6, centre).

Component 3 (C3)

A third component to the Hα line profile fit was required in a small region located in the north-east of the field. The flux map (Fig. 7.6, right) shows it is brightest in the far north-eastern corner and has a FWHM range (Fig. 7.7, right) similar to C1. The radial velocity map (Fig. 7.8, right) indicates that the C3 gas has a larger velocity towards our line-of-sight than any of the C1 or C2 gas (up to $\sim$70 km s^{-1}), but the associated uncertainties are large (see Section 7.2.2). Since our only detection of this third component is very near the edge of the field, it is difficult to estimate its extent or role from just these maps. Perhaps more interesting is non-detection of a third component in locations where signatures of

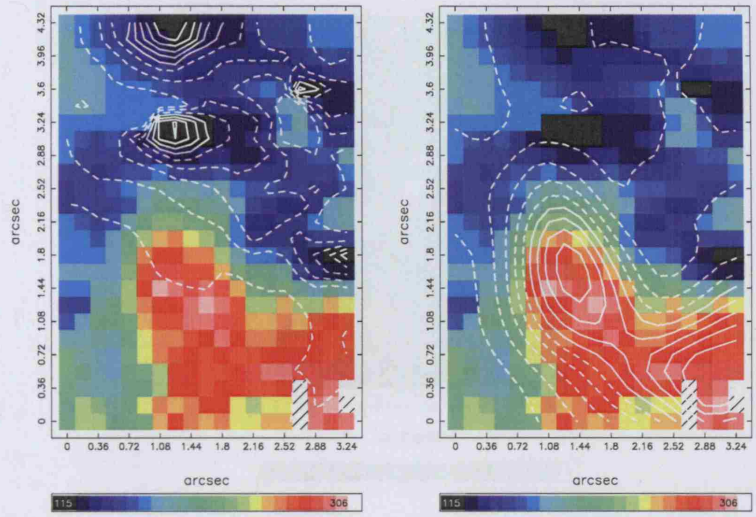

Figure 7.9: *Left:* contours of C2 flux overlaid on the C2 FWHM map. Solid contours represent levels above the mean of the range, and dashed below the mean. Notice the precise correlation between areas of high flux and low FWHM in the north. *Right:* contours of C1 flux overlaid on the C2 FWHM map. Here the correlation between the bright Hα knots seen in C1 and the broadest C2 lines can be seen clearly.

expanding structures might be expected from looking at Fig. 7.1.

7.3.2 Flux ratio maps

Electron Density

Fig. 7.10 shows a plot of the spatial variation of electron density, n_e, as derived from the ratio between single Gaussian fits to the [S II]$\lambda\lambda$6713, 6731 lines, assuming an electron temperature, T_e, of 10^4 K (the S/N of these lines is not high enough to fit multiple line components). There are two distinct regions of higher density seen in the map: in the south-west of the field, n_e reaches $\sim$250 cm^{-3} and is spatially coincident with the south-western bright knot seen in Hα C1 (Fig. 7.6, left), and the small distinct knot seen in the *HST* F656N image. A second high density region is coincident with the north-eastern part of the central bright Hα C1 knot and the position of cluster 10, and peaks at $\sim$270 cm^{-3}. We derived the electron density of the H II region surrounding cluster 10 in Section 7.1, and found $n_e = 165^{+18}_{-20}$ cm^{-3}. Our peak value of 270 cm^{-3} is entirely consistent with this value since the spectrum for cluster 10 was created by summing 29 spaxels centred on this central density peak, and hence includes some dilution from the surrounding lower density gas. These values are also consistent with Heckman *et al.* (1995), who find densities

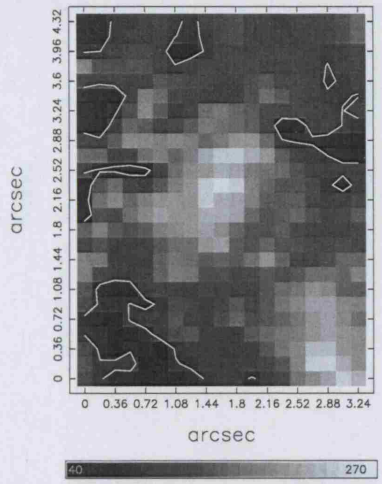

Figure 7.10: Map of the electron density, n_e, calculated from the ratio of single Gaussian fits to the the [S II]λ6716, 6731 lines. The scale is in units of cm^{-3}. A single contour level marks the 100 cm^{-3} low density limit.

of up to 200 ± 100 cm^{-3} in the central 15″ of NGC 1569. Only a small proportion of the gas is at or below the low density limit ($\sim$100 cm^{-3}; Osterbrock 1989, shown by the single contour level on the map).

Diagnostic diagrams

Our wavelength range gives us access to a number of important optical diagnostic lines. These can be used to constrain the properties of the emitting gas. The flux ratio of [O III]/Hβ is a good reddening-free indicator of the mean level of ionization (hardness) and temperature of the gas, whereas [S II]/Hα or [N II]/Hα are indicators of the number of ionizations per unit volume (Veilleux & Osterbrock 1987). A greyscale representation of the observed C1 flux ratio of [O III]λ5007/Hβ overlaid with contours of the [S II](λ6717+λ6731)/Hα C1 flux ratio is shown in Fig. 7.11. The ratio of log([S II]/Hα) is lowest (-1.7; shown by dashed contours) where the flux in Hα C1 is highest (see Fig. 7.6, left), *i.e.* where the central bright knot is located. The peak of the [O III]/Hβ ratio is also near to the central bright Hα knot, but offset by $\sim$4.″5 to the south-east. Numerically, the field average ratio of log([S II]/Hα) = -1.29 ± 0.17, log([N II]/Hα) = -1.62 ± 0.16, and log([O III]/Hβ) = 0.87 ± 0.05 (one σ errors), showing that the variations in the ratios are really only small. Plotting these values on the standard diagnostic diagrams of the type first first proposed by Veilleux & Osterbrock (1987), shows that all the points lie tightly

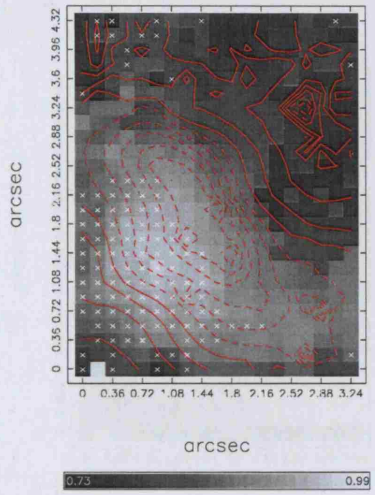

Figure 7.11: Flux ratio of log([O III]λ5007/Hβ) C1 (greyscale; scale bar shown) with contours of the ratio log([S II](λ6717+λ6731)/Hα) C1 (12 linearly spaced levels from -1.7 to -0.9). Spaxels marked with a cross indicate non-photoionized emission according to the maximum starburst line of Kewley *et al.* (2001).

clustered in the upper-left of the starburst-H II region distribution. Comparing these values with the Mappings-III photoionization models of Dopita *et al.* (2000) for an instantaneous burst of star-formation whose SED is given by SB99 (Leitherer *et al.* 1999), the gas is of low metallicity ($\sim$0.2 $Z_{\odot}$) and has a high ionization parameter ($q \simeq 10^8$). Buckalew & Kobulnicky (2006) use *HST*/WFPC2 narrow-band imaging to calculate the ratios of [O III]/Hβ and [S II]/Hα, and use the theoretical 'maximum starburst line' derived by Kewley *et al.* (2001) to set a threshold to determine the difference between photoionized and non-photoionized emission. Using this criterion on our de-reddened line ratios, we find a total of 118 spaxels containing non-photoionized emission, the location of which are plotted on Fig. 7.11 with white crosses. The distribution corresponds well to the maps of Buckalew & Kobulnicky (2006), with the majority of points in the south-east of the field. Since SSC A is located only 7″ away in this direction, Buckalew & Kobulnicky (2006) associate these points with an 'arc' of non-photoionized gas resulting from a possible wind-wind interaction between the two clusters. However, since our derived ratios only just fall above the maximum starburst line, we cannot be sure that non-photoionization processes play a significant part in the observed ionization levels (see Calzetti *et al.* 2004).

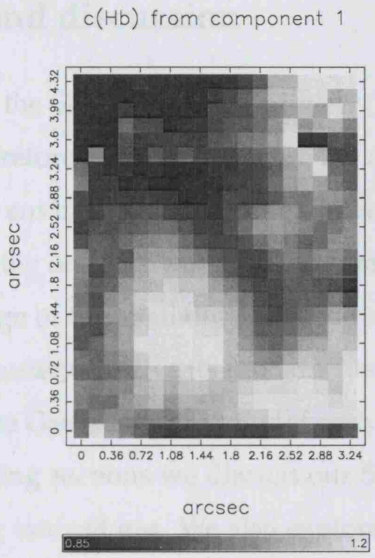

Figure 7.12: A c(Hβ) map calculated from the C1 flux ratio of Hβ/Hα.

Reddening map

De-reddening with our visualisation and analysis package uses the Galactic law of Howarth (1983, $R_V = 3.1$) and the intrinsic H I ratio of Hα/Hβ = 2.85 (Storey & Hummer 1995, for gas at $T_e = 10^4$ K and $n_e = 100$ cm^{-3}). A reddening map, computed using only C1 of Hα and Hβ, is shown in Fig. 7.12. The mean and standard deviation for c(Hβ) for C1 over the field-of-view is 1.01 ± 0.16 (compared to 1.15 when summing the flux in all components for the H I lines). In this, we are assuming most of the reddening comes from a Galactic foreground screen (a valid assumption; Israel 1988; Origlia *et al.* 2001, Section 7.1). The distribution of extinction is consistent with the location of the central and south-western bright knots seen in C1, where these knots exhibit the highest extinction [c(Hβ) = 1.3 $\equiv E(B-V) = 0.8$]. Interestingly, high values are also found in the north-west of the field, not correlating with any feature on any of the other maps. The lowest reddening [c(Hβ) = 0.75 $\equiv E(B-V) = 0.5$; equivalent to the Galactic foreground level; Relaño *et al.* 2006] is found in the north-east of the field, coincident with the location of the group of spaxels containing C3.

7.4 Interpretations and discussion

At the distance of NGC 1569, the GMOS IFU field-of-view (FoV) covers ~50 × 35 pc with an 8 pc resolution, and is therefore ideal for studying the detailed relationship between young star clusters and their environment. To this end, we have observed a region near the centre of the galaxy covering one such young, bright star cluster and the surrounding ionized gas. Taking advantage of the spatially resolved nature of IFU observations, we extracted a spectrum of the cluster to derive its fundamental properties, and created well-defined, high S/N maps of the Gaussian properties of each observed Hα line component across the FoV. In the following sections we discuss our findings relating to the cluster itself and to the surrounding ionized gas. We also explore possible theories that might give rise to the observed broad emission profiles and discuss their consequences.

7.4.1 Cluster 10

As clearly seen on the high-resolution *HST*/ACS images (*e.g.* Fig. 7.2), cluster 10 is composed of two individual clusters which we denote 10A and 10B. We measure their projected separation to be ~3.7 pc and their sizes to be $R_{\rm eff,A} = 0.88$ and $R_{\rm eff,B} = 0.60$ pc, and a combined photometric mass of $7\pm5 \times 10^3\ M_\odot$. By comparing the relative photometry of each cluster we find them to have very similar ages: 10B is the youngest (<5 Myr) and 10A a little older (5–7 Myr). The combined spectrum of the two clusters extracted from our IFU data shows that one (or both) of these clusters has a significant population of WR stars.

The unusually compact nature of these two clusters is reminiscent of R136 in the LMC. This equally young cluster has an $R_{\rm eff} \approx 1.7$ pc and mass of a few $\times\ 10^4\ M_\odot$ (Hunter *et al.* 1995; Bosch *et al.* 2001). R136 contains a large number of massive stars that power and maintain the ~100 pc-diameter giant H II region 30 Dor.

Our age estimates of the two clusters show that their formation was approximately coeval with SSC A, and that vigourous star-formation has certainly occurred recently in NGC 1569. Cluster 10 is located within the bright H II region No. 2 (Waller 1991) which is found to emit a powerful thermal radio signature (Greve *et al.* 2002*a*) and bright mid-IR forbidden-line and continuum emission (Tokura *et al.* 2006). These observations imply that this whole area is a large embedded star-formation complex being fuelled by the neighbouring molecular CO cloud (Taylor *et al.* 1999).

We do not see evidence for a compact individual H II region surrounding the cluster in the Hα flux maps or the extinction map. This is probably because the winds and supernova events have blown away the surrounding gas. The electron density map, however, does show an enhancement at the location of cluster 10, indicating that perhaps there is some associated gas. Our IFU FoV contains a great deal of ionized material that is both influenced by cluster 10 and by the relatively distant, but more massive, SSCs A and B. It is not clear if the source of ionization for H II region 2 is solely cluster 10 or whether other starburst regions contribute.

7.4.2 Ionized gas

The turbulent ISM and the narrow component (C1)

The integrated H I velocity dispersion for the disc of NGC 1569 is $\sigma \approx 15\,\mathrm{km\,s^{-1}}$ (FWHM $\approx$ $35\,\mathrm{km\,s^{-1}}$) indicating that the neutral ISM is very disturbed (Mühle *et al.* 2005), presumably due to the combined effects of stellar winds and supernovae. This value is consistent with the broad line widths also found in H I clouds associated with nearby giant H II regions (Viallefond *et al.* 1981). We would thus expect the H II gas in NGC 1569 to have similar or higher velocity dispersions to the H I.

In Fig. 7.13 we plot the heliocentric radial velocity against line width for all identified line components across the FoV, whilst in Fig. 7.14 we plot the line flux against line width. This latter plot was used successfully as a diagnostic tool by Muñoz-Tuñón *et al.* (1996) to examine the physical origin of the broadening mechanisms in giant H II regions. Plotting the line characteristics in this way highlights a number of trends within and between the components.

Fig. 7.13 shows that components C1 and C3 (FWHM = 35–65 $\mathrm{km\,s^{-1}}$) are easily distinguished from component C2 (FWHM = 120–300 $\mathrm{km\,s^{-1}}$). Furthermore, in the bottom panel of Fig. 7.14, there is a distinct $\sim$35 $\mathrm{km\,s^{-1}}$ lower limit to the C1 FWHM (which we label as FWHM$_0$). After correction for thermal broadening ($\sim$20 $\mathrm{km\,s^{-1}}$), this becomes 29 $\mathrm{km\,s^{-1}}$ (or $\sigma \approx 12\,\mathrm{km\,s^{-1}}$)[1]. This measured value of sigma is in agreement with the H I line widths of Mühle *et al.* (2005). We therefore suggest that the width of C1 largely reflects the random turbulent motions of a very disturbed NGC 1569 ISM which is now seen in both neutral and ionized gas. We note that the C1 line width does not correlate

[1]for $T_{\mathrm{gas}} = 10^4$ K, the sound-speed is $\sim$10 $\mathrm{km\,s^{-1}}$.

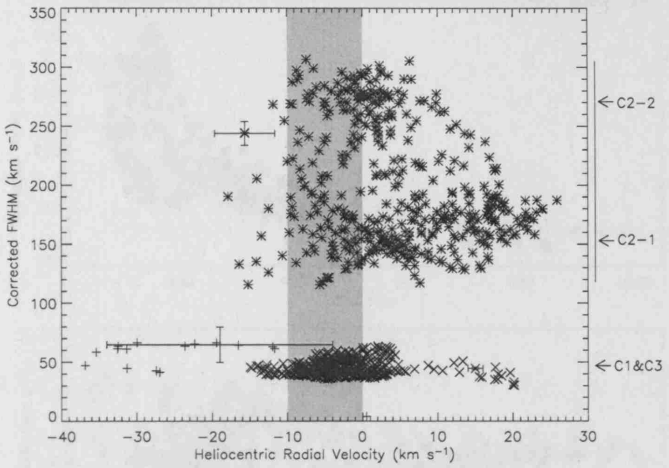

Figure 7.13: Hα line width (FWHM, corrected for instrumental but not thermal broadening) *vs.* radial velocity (heliocentric, relative to the systemic velocity of the region, $v_{\rm sys} = -80$ km s^{-1}). C1 is plotted with crosses ($\times$), C2 with asterisks ($*$) and C3 with plus symbols (+); a representative error bar has been plotted for each of the three components on one selected data point. The shaded region represents the velocity (including the error) of cluster 10 (see Section 7.1). By the right-hand axis are labels marking the three regimes in FWHM discussed in the text.

strongly with line flux, unlike the broad component which we discuss below.

The red velocity tail of C1, seen clearly on the left-hand side of Fig. 7.13, between radial velocities of +10–20 km s^{-1}, corresponds spatially to the extreme north-east of the field where we also see a blueshifted component (C3; see *e.g.* Fig. 7.5, lower panels). The velocities of these double-peaked emission lines are distributed evenly to the red and blue of the cluster radial velocity (shown as a grey strip), providing the only signature of classical shell expansion in the field.

Broad line widths have been observed in many young star-forming regions *e.g.* 30 Dor or NGC 604. A search through the literature uncovers a number of alternative theories that could account for the observed broad emission-line widths, but we find them not to apply, or apply to a lesser degree than what we concluded above, in the case of NGC 1569. The proposed mechanisms are: electron scattering of nebular emission; multiple unresolved expanding shells integrated along the line-of-sight; or gravitational broadening through either virial motions of ionized gas clouds.

Electron scattering can be immediately ruled out, as unphysical electron densities are required to produce the observed widths (see Roy *et al.* 1992). Multiple unresolved

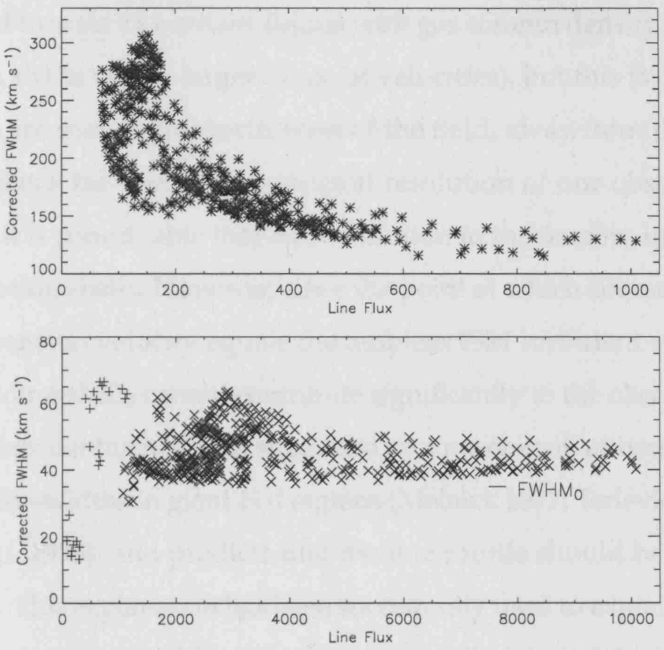

Figure 7.14: Hα line width (FWHM, corrected for instrumental but not thermal broadening) *vs.* flux (arbitrary scale). The selected axis ranges show C1 and C3 in the lower panel, and C2 in the upper panel (note in particular the factor 10 difference in flux range). C1 is plotted with crosses, C2 with asterisks and C3 with plus symbols. The distinct lower limit to the FWHM of C1, FWHM$_0 \approx 35$ km s^{-1}, is marked.

expanding shells integrated along the line-of-sight was an explanation proposed by Chu & Kennicutt (1994) to explain their observed broad line widths in the giant H II region 30 Dor. A follow up study of the same region by Melnick, Tenorio-Tagle & Terlevich (1999), but at very high spatial- and spectral-resolution (0.″6 seeing and 0.067 Å pix^{-1}), allowed shells to be resolved down to their resolution limit of 0.13 pc. At this resolution, the line-widths of the myriad discrete shell components are much narrower, thus validating this explanation for observations made at insufficient spatial/spectral-resolution. However an analytical model for this effect first developed by Dyson (1979) and analysed in detail by Tenorio-Tagle *et al.* (1996) predicts that the the resulting line profiles are always flat-topped if the age distribution of the stars powering the expanding shells is greater than the timescale for gravitational collapse of the parent cloud (an obvious physical requirement). Furthermore, Tenorio-Tagle *et al.* (1996) find that to have a collection of unresolved shells capable of producing a supersonic line-width over a large range of densities, implies a great many low-energy winds with properties similar to those typical for low-mass stars. If multiple shells are responsible for the observed broadening in our case, then the level of broadening

would be expected to scale to a certain degree with gas column density (a large volume of gas could contain shells with a larger range of velocities), but this is not observed. The broadest C1 lines are seen in the north-west of the field, away from the bright knots in the field centre. Since the spatial and spectral resolution of our observations is ~9 pc and 0.34 Å pix^{-1}, it is conceivable that a contribution to the narrow-line width is due to unresolved expanding shells. However, since the point at which coherent shells break up is when their expansion velocity equals the ambient ISM turbulent velocity (FWHM$_0$), unresolved expanding shells cannot contribute significantly to the observed widths of C1.

Gravitational broadening has been suggested by a number of authors as an explanation for the observed line-widths in giant H II regions (Melnick 1977; Terlevich & Melnick 1981; Tenorio-Tagle *et al.* 1993), and predicts that the line profile should be approximated by $\sigma_{\rm virial} = \sqrt{GM/R}$. This explanation has been successfully used to explain and calibrate the $R \propto \sigma$ and $L \propto \sigma$ relations found for giant H II regions (Terlevich & Melnick 1981; Melnick *et al.* 1988), and explain the supersonic widths found in NGC 604 (Muñoz-Tuñón *et al.* 1996; Yang *et al.* 1996). Although NGC 1569 cannot be likened to a single giant H II region, we can make a crude estimate of the expected virial broadening by taking the mass to be the total H I mass of the galaxy ($M_{\rm HI} \sim 10^8\ M_\odot$; Mühle *et al.* 2005) and an isophotal radius of ~4 kpc (de Vaucouleurs *et al.* 1991; Mühle *et al.* 2005). This results in a broadening of $\sigma_{\rm virial} \approx 11$ km s^{-1}, in surprising agreement with our measured FWHM$_0$.

Overall, we find that the C1 line velocity widths correspond to mildly supersonic speeds relative to ionized gas. We conclude that C1 represents the turbulent ISM, where its motions result from a convolution of both the underlying gravitationally induced virial motions inherent in the gas and the general stirring effects of the starburst. It is also possible that an additional minor contribution to its width may originate from unresolved shell components along the line-of-sight.

The broad component (C2)

We now turn our attention to the intriguing broad component. In the following discussion, we will attempt to understand what the conditions of the emitting gas are, and what mechanism(s) are acting to give it such a broad width. Firstly, we can use Figs 7.13 and 7.14 to identify a number of trends to help constrain the physical properties of this component. Fig. 7.13 shows that the group of C2 points can be split into two further sub-groups. The narrower group (≈ 150 km s^{-1}; labelled C2-1 on the plot) is associated

with the regions of higher C2 flux (compare the central panels of Fig. 7.6 with Fig. 7.7), whereas the close grouping of high-FWHM C2 measurements ($\approx$280 km s^{-1}; labelled C2-2) correspond (to a high degree of correlation) with the most intense C1 emission (*i.e.* the two bright knots; compare Fig. 7.6, left, with Fig. 7.7, centre). Disregarding the red tail of the C1 velocity distribution, there is an average redward offset of only $\sim$10 km s^{-1} between C1 and C2, implying that C2 does not originate from gas with large-scale bulk motions. Fig. 7.14 clearly demonstrates that the broadest C2 lines are also the faintest, where the average ratio of flux(C2)/flux(C1) over the FoV is 0.07. We can now assert that any theory explaining the origin of C2 must describe both how it remains existent over the entire FoV, and why its width is at once so highly correlated with the position of the bright knots seen in the narrow component, and so anti-correlated with its own flux?

Mechanisms proposed in the literature that can account for line widths of $>$100 km s^{-1} are quite varied, particularly from studies of more distant systems. Moreover, there are few studies that compare in terms of both the spatial-scale of the overall region (*i.e.* 30 Dor, for example, is clearly much smaller than the NGC 1569 starburst) and the spatial-resolution of the observations. This makes it harder to evaluate which mechanisms may be at work in NGC 1569.

Unresolved expanding shells have been cited as a possible cause of the broad component in a few studies, but it is difficult to envisage how smooth Gaussian profiles with widths of up to 300 km s^{-1} could be fully accounted for in this manner without showing some signs of velocity splitting. Heckman *et al.* (1995) observed Hα emission from NGC 1569 using two perpendicularly oriented long-sits intersecting at SSC A (see Chapter 5), and in positions where they were able to fit multiple Gaussians to the line profile, they found two distinct kinematic systems. Lines near to $v_{\rm sys}$ were found to have widths of FWHM $\approx$ 30–90 km s^{-1}, whereas broader lines with widths of up to 150 km s^{-1} were only identified at radial velocities of over 200 km s^{-1} relative to $v_{\rm sys}$. Heckman *et al.* proposed that this second, high-velocity system is the origin of the broad widths (30–50 Å at full-width zero-intensity) found in the summed Hα line profile of the area surrounding SSC A, since when integrating a larger spatial area, the discrete kinematic systems became blended together[2]. The level of broadening due to unresolved components is therefore dependent on *both* spatial- and spectral-resolution. This is illustrated by the study of

[2]In our data, we associate C3 with part of the high-velocity system described by Heckman *et al.*, and where detected, we resolve it at a sufficient level for it not to be confused with the broad C2.

Melnick *et al.* (1999), who, after Chu & Kennicutt (1994) found that multiple unresolved shells were likely to contribute significantly to the line-widths in 30 Dor, re-observed this object at very high spatial- and spectral-resolution. Although this allowed them to resolve individual components on scales down to 0.1 pc (as mentioned above), they were still able to identify a clear, underlying, broad component persisting in all sight lines.

Can the effects of high-energy photons and fast-flowing winds from the near-by clusters explain the origin of C2? Over the years, much work has been done examining these effects using complex hydrodynamical models (Hartquist *et al.* 1992; Klein *et al.* 1994; Suchkov *et al.* 1996; Pittard *et al.* 2005; Marcolini *et al.* 2005; Tenorio-Tagle *et al.* 2006). An exchange of energy and mass between the different hot and cold phases of the ISM can occur through four main processes: photoevaporation; conductively-driven thermal evaporation; hydrodynamic ablation; and turbulent mixing (for a review see Pittard 2006). Photoevaporation takes place in the presence of a strong ionizing radiation field, and conductive evaporation occurs when energetic electrons from a hot, surrounding medium, deposit their energy in the cloud surface. When the hot, tenuous medium is fast-flowing, as in the case of stellar or cluster winds, shearing between the high velocity flow and the cloud surface can set up a turbulent mixing layer that can drive further evaporation. The impacting wind can also physically strip (ablate) material off the clump surface, and entrain it into the flow.

Begelman & Fabian (1990) described a model for a turbulent mixing layer that forms between the hot, inter-cloud gas and the surface layers of cool or warm clouds in near-pressure equilibrium. The UV radiation emitted from the mixing layer photoionizes the cold gas in the cloud surface giving rise to optical emission lines (in a similar way to a shock precursor) with characteristic velocities of a fraction of the hot-phase sound speed. Slavin *et al.* (1993) expanded on this idea by modelling the cloud interface in detail. Including the effects of nonequilibrium ionization and self-photoionization allowed them to predict a number of optical, IR and UV line ratios, which they found to be in good agreement with the observed values at high latitudes in our Galaxy (for which this model was originally developed). Fig. 7.15 shows a schematic of their model: hot gas flows past a sheet of cold or warm gas inducing Kelvin-Helmholtz instabilities and the build-up of a turbulent mixing layer at the interface region. Thermal conduction between the layers results in a turbulent cascade down to the dissipative level, allowing the efficient exchange of energy between the media. This kind of system can attain a steady state when the

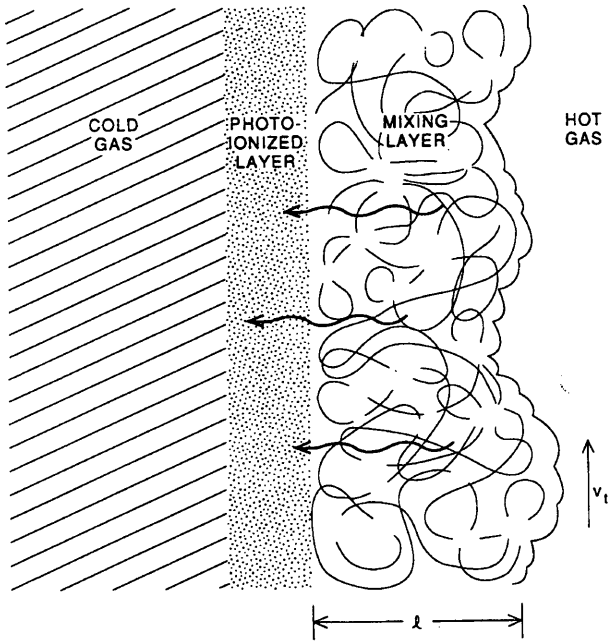

Figure 7.15: Schematic drawing of a turbulent mixing layer as proposed by Slavin *et al.* (1993). Hot gas moves at a transverse velocity v_t relative to the cloud surface, resulting in the build-up of a turbulent layer. Emission from this mixing layer photoionizes the surface of the cold cloud resulting in optical line emission.

energy flux into the layer is equal to the cooling rate per unit area. Their model predicts strong optical [O III] and Hα emission with non-Gaussian, broad-winged line profiles caused by the high levels of turbulence. Strong far-UV emission from C IV and O VI is also predicted. These predictions are qualitatively in good agreement with what we observe, and proves that the broad component can easily arise from such turbulent interface layers. However, the Slavin *et al.* model predicts [O III]/Hβ and [S II]/Hα nebular line ratios firmly in the shocked regime, far away from our observed ratios.

It is interesting to note that observations of CO (*e.g.* Falgarone & Phillips 1990), CH^+ (Crane, Hegyi & Lambert 1991) and H_2 2.1 μm (*e.g.* Geballe *et al.* 1986) in close-by Galactic molecular clouds have also revealed broad line profiles similar in shape to what we observe in our optical recombination and forbidden lines. To explain these observations, Hartquist *et al.* (1992) and Dyson *et al.* (1995) also developed turbulent boundary layer models, and found these broad molecular line widths could again be reproduced through the presence of shear induced turbulence, resulting from shocks in the cloud interface due to the viscous coupling between the fast wind and the clump gas. Melnick *et al.* (1999) were the first to suggest a connection with turbulent layers and erosion of dense

gas clumps in an extragalactic environment when discussing the persistent underlying broad line component identified from their high-resultion observations of 30 Dor.

We therefore find the most likely explanation of the origin of C2 is emission from a turbulent mixing layer formed at the surface of dense clouds resulting from the viscous coupling between the cool clump material and the hot, fast, winds from the surrounding clusters. Material is also removed from this layer through thermal evaporation and/or mechanical ablation, and mass-loads the flow. We know from X-ray studies that the hot, diffuse medium in NGC 1569 has a characteristic temperature around 0.7 keV ($\sim 10^7$ K) (Martin *et al.* 2002), implying that the sound speed in this hot phase is $\sim$500 km s^{-1}. The line-widths we measure are only a fraction of this value, meaning that the turbulent motions are firmly subsonic. This may provide a natural explanation for the lack of shock-excited line ratios in our data.

Although a shear induced turbulent mixing layer can theoretically attain a quasi-steady state (Slavin *et al.* 1993), the additional destructive effects of evaporation and/or ablation mean that gas clumps will only have a limited lifetime. How long could we therefore expect the clouds to survive? Unfortunately our knowledge of cloud disintegration is not yet developed enough to answer this question in detail. Simple hydrodynamical simulations of ablation predict that clouds enveloped in a supersonic (relative to the cloud temperature) wind have survival timescales typically less than 1 Myr (Klein *et al.* 1994; Marcolini *et al.* 2005). Clearly this cannot be the case since warm ionized gas is observed in superwinds out to heights of many kpc (*e.g.* Shopbell & Bland-Hawthorn 1998; Martin 1998; Devine & Bally 1999, Chapter 4). If this material has been transported from the disc, survival timescales of order $\sim$10 Myr (for typical observed speeds) are implied. Marcolini *et al.* (2005) find that the addition of thermal conduction and dynamical effects (such as cloud compression resulting from shocks) can act to reduce the evaporation rate and increase cloud survival times, particularly for larger cloud sizes. This is partly because the fragmentary effects of Rayleigh-Taylor and Kelvin-Helmholtz instabilities are strongly inhibited by thermal conduction. Furthermore, the fact that NGC 1569 is a low-metallicity environment means that the resultant stellar winds will be weaker than in the solar metallicity models run by Marcolini *et al.*, possibly extending the cloud survival times further.

Whether or not these mechanisms are all acting in our particular FoV, it is clear that the energetics are dominated by the interface layer at the surface of the gas clumps, and that

the principle influence on the gas state is external to the clouds, rather than embedded within the cloud, as would be the case for isolated giant H II regions. In other words, the properties of the Hα knots in our FoV are tied to the intrinsic state of the gas rather than the available energy supplies (the star clusters). This important difference may help to explain why the turbulent widths decrease away from the cloud surfaces. Cloud material remains intact and cool only for a limited length of time after it leaves the surface of the gas clump. Dense gas found near the surface of the cloud would be able to emit in Hα at higher velocities as it becomes entrained into the high-velocity flow than less dense gas, resulting in a broader line-width at the location of the cloud.

The motion of C2

The average width of C2 is much higher than the average radial velocity offset between C1 and C2 (obvious from comparing Figs 7.13 and 7.14), meaning that in our FoV, turbulent motions dominate over bulk flows. Tenorio-Tagle *et al.* (2006) develop 2D hydrodynamical models of the evolution of an H II region assuming that the medium surrounding the ionizing star cluster is composed of a large collection of clouds (*i.e.* a clumpy medium). Although their model is not specifically applicable to our case since the ionizing source is located within the cloud stratum, it illustrates a number of interesting results regarding the flow of material within the outer bounding shock front. In their simulations, the leading shock filters slowly through the gas clouds dissipating them one-by-one, leaving a highly turbulent, mass-loaded gas in its wake. The material interior to the leading shock moves in all directions resulting from the obstruction by the gas clumps, and possesses only a small net velocity in the outward direction. This is a very similar situation to what we observe, and shows that our FoV must be sampling gas well within the sonic point of the galactic wind, since as the flow becomes supersonic, turbulence is damped leaving only the bulk velocity component.

Final remarks

Despite all we have found so far, we still cannot unambiguously determine whether the primary source of energy for the broad line component in our FoV is cluster 10, SSC A or simply the combined effects of the ambient ionization field. The distribution of non-photoionized emission covering the whole of the south-eastern portion of the FoV (see

Fig. 7.11) would suggest that high-velocity gas is impacting from the south-east (*i.e.* the direction of SSC A), but without information on the three-dimentional distribution of the gas and velocity field, we cannot be sure.

Since the constraints to our model of the origin of C2 are only qualitative, further observations are clearly required. We predict that if the energetics are dominated by the interface region where the turbulence is proposed to originate, observations of emission originating from deep within the cloud would not show this line broadening. This would also apply to regions shielded from the wind impact, where only the ambient ISM turbulence would be evident. Furthermore, the models of Marcolini *et al.* (2005) predict strong soft X-ray emission from the bow-shock (reverse shock) produced as the wind hits the cloud. Whether the X-rays are primarily emitted from wind material or evaporated cloud material depends on the metallicity of the wind and the strength of the thermal conduction within the cloud. UV emission (or absorption) from C IV and O VI is also predicted to arise through collisional processes within the cloud material at the wind–cloud interface by both Slavin *et al.* and Marcolini *et al.*. Currently, O VI emitting gas is the highest temperature phase of an outflow that can be probed for which reliable velocities can also be measured (Heckman *et al.* 2001), making this transition a very important tool in the investigation of galactic winds.

In Chapter 8, we present the analysis of the other three IFU fields covering the central regions of NGC 1569. Following on from our analysis presented here, we first concentrate on the details of each field, then combine all the data in an attempt to constrain the general state of the ISM in the whole region.

7.5 Summary

The unique capabilities of the GMOS IFU have allowed us to map the detailed ionized gas properties of a region near the nucleus of NGC 1569 of only 5×3.5 arcsecs, and to relate the presence of a young star cluster located in the centre of the field-of-view to the surrounding gas.

Summing the spectra from an aperture centred on the position of the cluster has allowed us to measure and derive a number of fundamental characteristics of this object. We find:

- Cluster 10 is in fact composed of two sub-clusters denoted 10A and 10B, with sizes

$R_{\rm eff,A} = 0.88$ and $R_{\rm eff,B} = 0.60$ pc and a projected separation of 3.7 pc. Because of their proximity, they cannot be resolved in our IFU data.

- Using model colour-colour diagrams, we were able to estimate their ages to be 5–7 Myr for 10A and $\leq$5 Myr for 10B, with reddenings consistent with the Galactic foreground level (confirmed by measurements of the Hα/Hβ ratio).

- We derive a mass of $7 \pm 5 \times 10^3$ $M_\odot$ from the combined light of both sub-clusters. This result means that cluster 10 is not a super star cluster in the generally accepted definition.

- The presence of the red WR-bump (resulting from broad C IV emission) confirms the young age of at least one of the sub-clusters. From measuring the total luminosity of the feature, we estimate an equivalent population of 10 ± 5 WC4 stars in cluster 10. This is consistent with the narrow-band He II observations of Buckalew *et al.* (2000) who find a emission associated with 10B equating to a luminosity equivalent of 3 WNL stars.

The spatially resolved nature of our observations have allowed us to make a detailed analysis of the distribution of gas within the FoV. The most important findings are:

- We find bright emission over the whole field well characterised by a Gaussian function with mildly supersonic line widths (C1), and a distinct lower limit of FWHM$_0 \approx 35$ km s^{-1} (equating to $\sigma = 12$ km s^{-1} after correction for thermal broadening).

- We also measure a fainter line component (C2) with line widths of between $\sim$100–300 km s^{-1}, also found over the whole field.

- The width of the broad underlying emission is both highly correlated with the position of the bright narrow component emission (*i.e.* bright C1 $\propto$ broad C2), and anti-correlated with its own flux (*i.e.* bright C2 $\propto$ narrow C2).

- We conclude that C1 represents the turbulent ISM, where its motions result from the general stirring effects of the starburst (giving rise to the clear lower-limit to the line width, FWHM$_0$). However, it is possible that an additional minor contribution to its width may originate from unresolved shell components along the line-of-sight.

- We find the most convincing explanation for the broad component is that it represents a tenuous, highly turbulent, diffuse gas resulting from the turbulent mixing and thermal evaporation and/or ablation of clump material by the strong cluster winds found in the central regions of NGC 1569.

- The distribution of non-photoionized (shocked) gas as determined from nebular diagnostic line ratios supports evidence that the dominant source of wind energy/material is from SSC A, consistent with morphological indicators such as swept-back cones around dense Hα emitting knots that point towards this cluster. This does not mean, however, that the significant proportion of ionizing flux in this region does not come from the young cluster 10.

In Chapter 8, we will put our findings for this IFU position in context with the whole central region by analysing observations made with the three other IFU pointings.

CHAPTER 8

MAPPING THE ROOTS OF THE GALACTIC WIND IN NGC 1569 – II. LINKS BETWEEN THE INNER AND OUTER WIND ZONES

Following our detailed and in-depth analysis of one of the four Gemini/GMOS IFU positions in Chapter 7, this chapter de-focusses slightly. Here our primary aim is instead to explore the overall state of the ISM in the central regions of this galaxy and how this relates to the galactic outflow seen at larger radii. In pursuit of this goal, we begin in Section 8.1 by analysing the remaining three GMOS IFU positions located in the central 200 pc around SSC A, then in Section 8.2 we study the set of SparsePak observations introduced in Chapter 5 covering the outer environment of the galactic wind.

8.1 The environment of the inner-wind

The central ~200 pc around SSC A is highly disturbed. Clearly evident from Hα and H I imaging, a large cavity is being cleared around the central star clusters. This cavity is associated with a shell of ~20″ diameter surrounding SSCs A and B and expanding at ~40 km s^{-1} (Tomita *et al.* 1994; Martin 1998, catalogued as shell C), thus proving that these two clusters in particular are doing an effective job of clearing the surrounding gas. The highly clumped morphology and swept-back appearance of some of the remaining gas knots provide additional evidence of strong feedback effects.

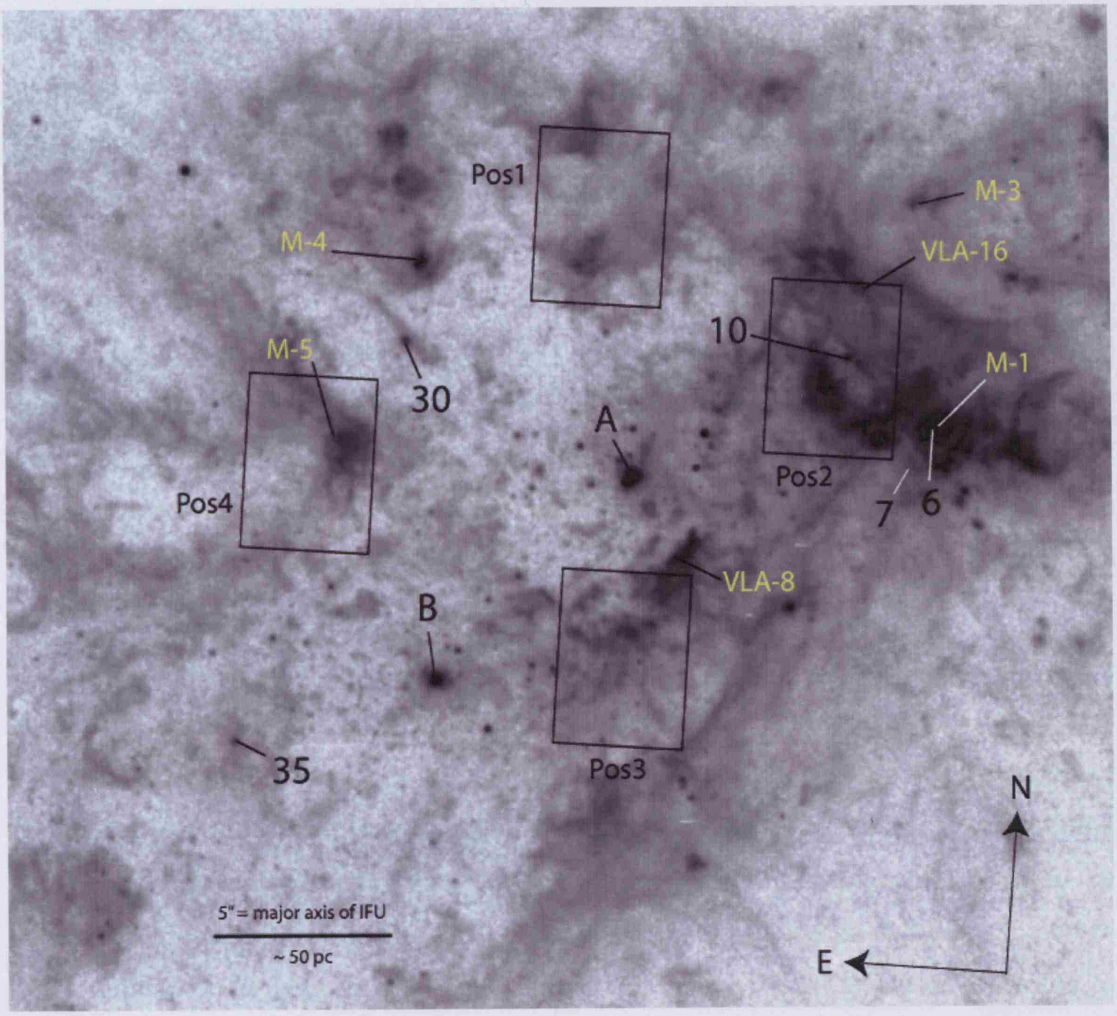

Figure 8.1: *HST*/WFPC2 F656N image of the centre of NGC 1569 showing the positions of the four IFU fields. A number of the most prominent star clusters (Hunter *et al.* 2000) and radio continuum sources (Greve *et al.* 2002*a*) have been labelled in black and white, respectively (figure reproduced from Chapter 5).

As described in Chapter 5, we obtained Gemini/GMOS IFU observations of four regions within 50–100 pc of SSC A covering a number of prominent gas knots, as shown in Fig. 8.1. These positions were chosen to cover areas that were thought likely to show signs of interaction between the cluster winds and the gas, in the hope of finding evidence of the very roots of the galactic-scale outflow. Although the IFU fields all cover what appear to be morphologically similar ionized regions, they are each sufficiently different and information-rich to warrant detailed individual analyses. Thus the first half of this section is devoted to describing the emission-line maps for IFU positions 1, 3 and 4 (position 2 was described in detail in Chapter 7), and interpreting what we find with reference to *HST* imaging and other multi-wavelength data. After discussing the individual characteristics of the three fields, we relate what we have learned to the wider context of the general state of the ISM in this central region. As we found in our analysis of IFU position 2, the relationships between the different line components and their properties are key to understanding the state of the gas. We will therefore search for and try to comprehend any correlations between the line components and properties within and between these four fields, to gain further insights into the overall nature of the ISM and the ionized gas conditions at the base of the galactic outflow.

The emission-line profiles of each of the observed lines in each spaxel for each field were modelled with PAN using the Gaussian-fitting method described in Chapter 6. This has given us a considerable set of measurements with which to investigate the properties of the ionized gas – the four fields together contain 2000 individual spectra, each containing six bright nebular lines many of which are composed of multiple components. We find the general profile shape prevalent in position 2 (a narrow, bright component that we refer to as C1, with an underlying, fainter, broad component referred to as C2) is also applicable to the other three fields. On the whole, if a further component (C3) is present, it has a similar width to the main brightest component, but is fainter and offset in velocity space. Once the fitting procedure was complete, we mapped out the properties of each line component for each field using the visualisation package DAISY (also described in Chapter 6). Hα and [O III]λ5007 are the highest S/N lines observed, but since their properties are found to closely follow that of one another, and we primarily compare our observations to Hα imaging, we focus on Hα only in the following sections.

8.1.1 Expected features

The morphology of the central regions of NGC 1569 is dominated by the effects of strong cluster winds. For example, Anders *et al.* (2004) identified 168 clusters in the inner parts of the galaxy, most with ages of only ~25 Myr. This many young clusters, coupled with the expected strength of the winds from the largest clusters (SSCs A and B), imply that the ISM is highly turbulent and contains many expanding, overlapping and interacting bubbles, much like a scaled-up version of a giant H II region such as 30 Dor.

Shell expansion is evident spectroscopically through split line profiles, where the individual components represent the near- and far-sides of the shell walls. In the ideal case of a single shell expanding into a uniform medium, the expansion is spherically symmetric, and its velocity can be estimated by calculating half the difference in radial velocities between the two components at the geometric centre of the structure. A spatially-resolved bubble will therefore show up as a circularly-symmetric peak in the velocity map with equal and opposite amplitudes in both components, and since the redshifted one represents the far-side wall, it naturally will be fainter. However, this situation can become somewhat confused when the bubble is expanding in an inhomogeneous medium. Sections impacting denser gas are rapidly decelerated as energy is lost through strong emission, whereas unimpeded sections are allowed to expand freely without significant radiative losses. This can result in a severely distorted, highly non-spherical structure which can often be difficult to identify as a single object from imaging or spectroscopy. In reality, as for NGC 1569, it is likely that only the largest-scale bubbles still exhibit coherent characteristics, and that mostly we observe the ragged, distorted remains of bubbles, often in the form of discrete, high-velocity features. The width of the line emission from the bubble walls is primarily determined by the state of the gas being swept up. For example, more turbulent gas would be expected to exhibit broader profiles.

We should also note here that it is impossible to accurately define local rest velocities for each of our four positions since the reference H I gas is also highly disturbed. It is therefore important to recognise that any velocity offsets quoted are accurate only with respect to the field average, and are approximate with respect to the systemic velocity.

8.1.2 GMOS Position 1

Position 1, the most northerly of our four positions, coincides with two large knots of gas, around which it appears part of the central cavity around SSC A is being evacuated. This position was chosen in the hope of finding evidence of the interaction of cluster winds from the central region with the ISM gas. Figs 8.2–8.4 show maps of the emission-line properties (flux, FWHM and radial velocity) for each line component over the whole field-of-view (FoV). This is the only position for which we have required a third Gaussian to fit the integrated profile shape for a significant proportion of the field.

We begin this section by noting that the discontinuous region towards the central-north-west of the field seen in the C2 flux and FWHM maps is caused by the sudden change from fitting with triple- to double-Gaussian profiles. According to the F-test method (Chapter 6), the χ^2 ratio in this region became no longer sufficient to justify a triple-Gaussian fit. The artificially high flux and low FWHM in C2 has resulted from fitting two components to an intrinsically three-component profile since C2 now includes some contribution from the ignored third component. The continuous nature of the radial velocity maps (which are less affected by poor S/N) proves that the component assignments were correctly made over the whole field and that we can safely ignore only the discontinuous region in the maps in the following discussion.

The C1 flux map (Fig. 8.2, left panel) highlights the two gas condensations, which, without any dynamical information appear very similar. However, from the equivalent FWHM (Fig. 8.3, left panel) and radial velocity (Fig. 8.4, left panel) maps, it is clear that the two do not share the same characteristics. The southern knot stands out for having the broadest (350–400 $\mathrm{km\,s^{-1}}$) C2 widths of all the fields (see Fig. 8.3, centre panel) and for having strong associated emission in C3. However the peak in C3 emission (Fig. 8.2, right panel), found just to the west of this knot, does not have a counterpart in the *HST* F656N image. Between this bright area and the C1 knot, a faint semi-circular structure can be identified (indicated on Fig. 8.2 with a white line), with a concentric morphology centred on the southern C1 knot. The FWHM of C3 increases radially towards the southern knot following this concentric pattern, while its radial velocity decreases slightly resulting in a velocity difference between C1 and C3 at the knot's location of 45–55 $\mathrm{km\,s^{-1}}$. Fig. 8.5 shows two examples of Hα line profiles from in this position, including one from this bright C3 region (the location of the spaxels from which the profiles are from are marked

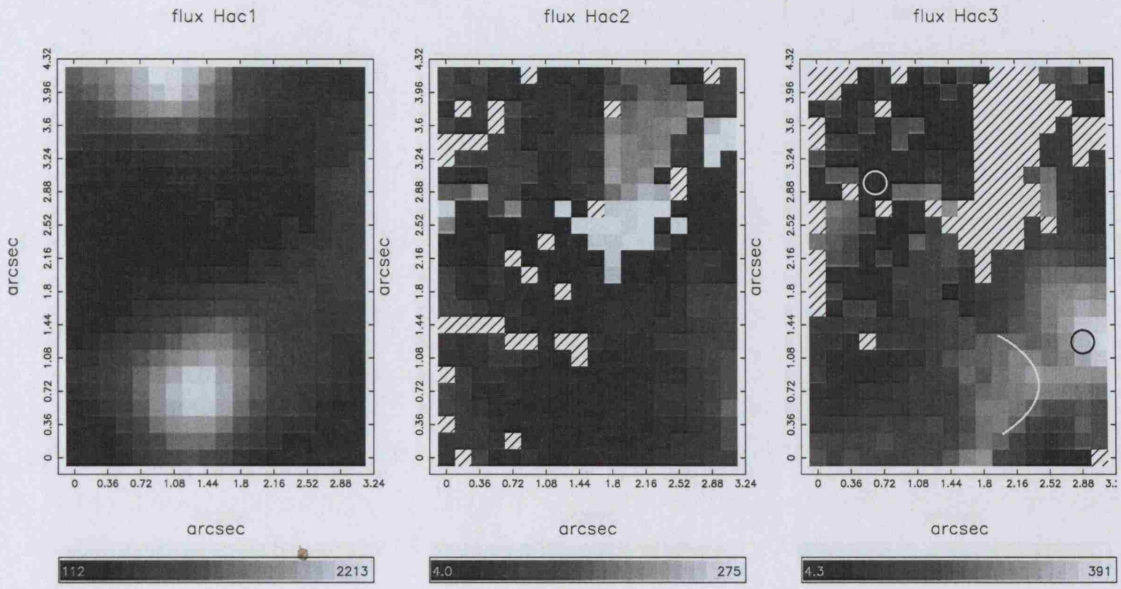

Figure 8.2: **Pos 1.** *Left:* Flux map in Hα C1 (range 112–2213); *centre:* flux map in Hα C2 (range 4–275); *right:* flux map in Hα C3 (range 4.3–391). Non-detections are represented as hatched spaxels, the x and y scales are in arcseconds offset from the lower-left spaxel, and a scale bar is given for each plot with units 10^{-15} erg s^{-1} cm^{-2} spaxel^{-1}. North is up and east is left. The spaxels from which the example spectra shown in Fig. 8.5 are marked with circles, and the semi-circular feature discussed in the text is outlined with a white line.

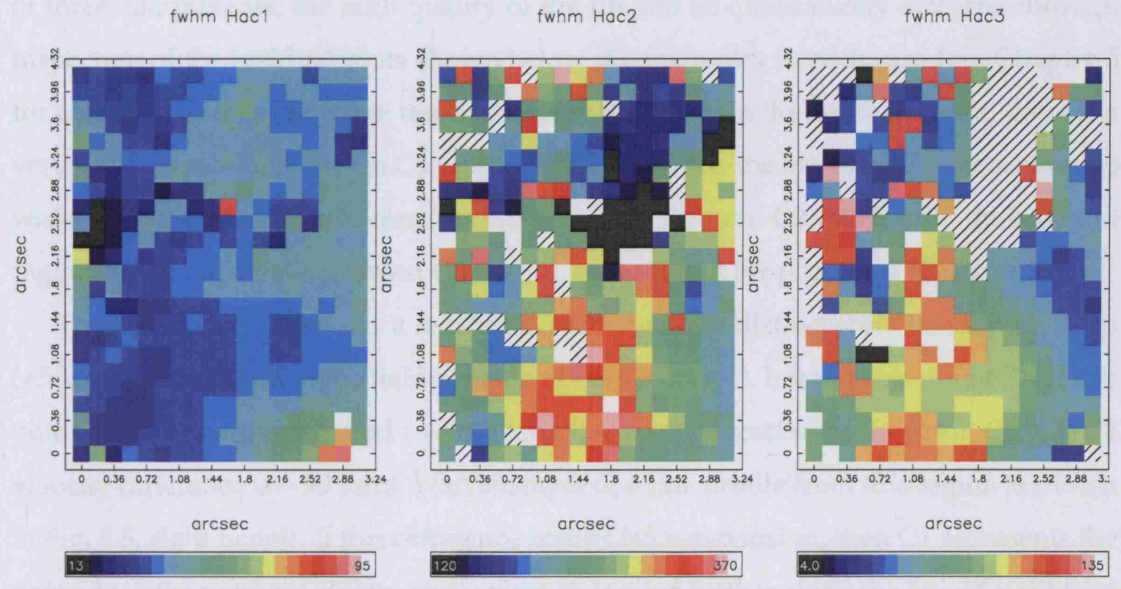

Figure 8.3: **Pos 1.** *Left:* FWHM map in Hα C1 (range 13–95); *centre:* FWHM map in Hα C2 (range 120–370); *right:* FWHM map in Hα C3 (range 4–135). A scale bar is given for each plot in km s^{-1}, and the measurements are corrected for instrumental broadening. North is up and east is left.

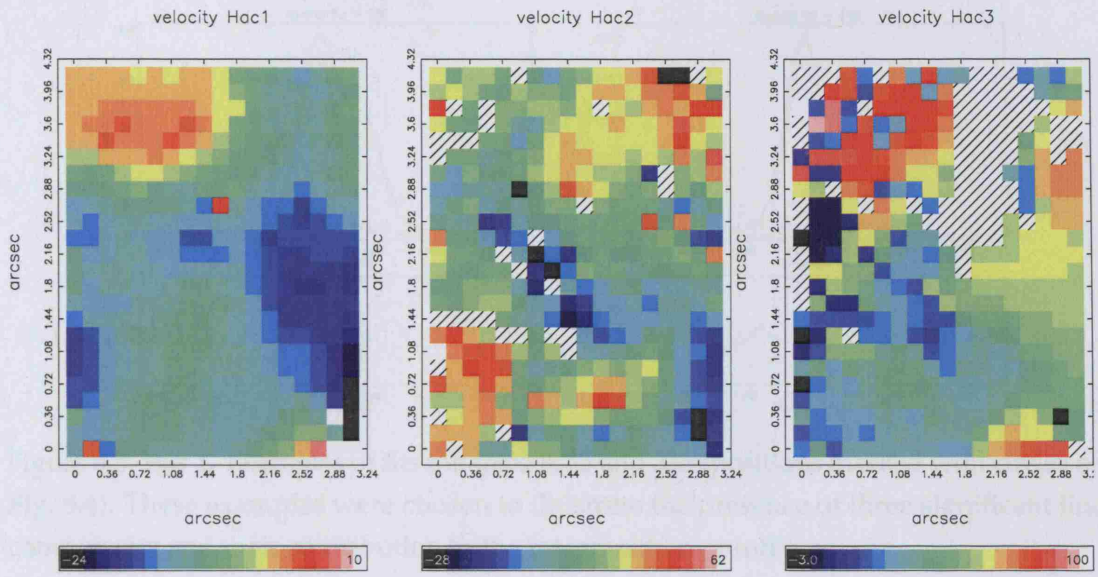

Figure 8.4: **Pos 1.** *Left:* radial velocity map in Hα C1 (range −24–10); *centre:* radial velocity map in Hα C2 (range −28–62); *right:* radial velocity map in Hα C3 (range −3–100). A scale bar is given for each plot in km s^{-1} (heliocentric, relative to the systemic velocity of the galaxy, $v_{\rm sys} = -80$ km s^{-1}). North is up and east is left.

with circles on the right-hand panel of Fig. 8.2). These examples clearly show the existence of three components; the high quality of the fits can be qualitatively assessed through inspection of the residual plots shown below the main plot in each case (see Chapter 6 for an explanation of how the residuals are calculated). In the southern knot, there is a very good correlation between C1 flux and C2 FWHM (*i.e.* the brightest C1 knots have the widest C2 FWHM), and anti-correlation between C2 flux and C2 FWHM (*i.e.* the brightest regions in C2 have the narrowest C2 width), as we found for position 2 (Chapter 7).

The northern C1 knot has a redshifted velocity quite distinct from its surroundings (+5 km s^{-1}, compared to the field average of $\sim$−15 km s^{-1}), but the velocity of C3 at this point is even more redshifted ($\sim$+100 km s^{-1}). At the location of the knot, the C1–C3 velocity difference is $\sim$90 km s^{-1} (an example of a line profile from this region is shown in Fig. 8.5, right panel). If this difference results from expansion, then C1 represents the nearside of the northern clump, and it must be located further along the line-of-sight than the southern knot and be expanding with a velocity, $v_{\rm exp} \approx 45$ km s^{-1} (half the C1–C3 velocity difference).

The properties of the inter-clump gas are generally fairly uniform. The only unusual relationship is that C1 has a blueshifted ($\sim$−15 km s^{-1}) mean velocity, whereas C2 and

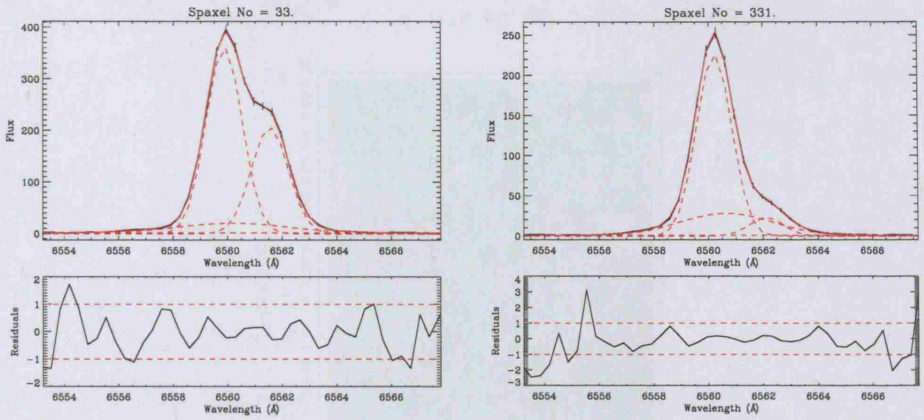

Figure 8.5: **Pos 1.** Examples of fits for spaxels 33 and 331 (positions marked with circles on Fig. 8.4). These examples were chosen to illustrate the presence of three significant line components and their contribution to the integrated line profile.

C3 are both redshifted relative to v_{sys} (+80 km s^{-1}). A region with distinctly different characteristics is found in the far south-west. Here the gas becomes rapidly redshifted in both C1 and C3, and is coincident with an area of very broad (∼100 km s^{-1}) C1 emission. This corner is faint in all three line components, and by comparing its location to the *HST* image, appears to be part of the low surface-brightness cavity surrounding SSC A.

The electron density of the ionized gas can be derived from the flux ratio of [S II] λ6713/λ6731. Unfortunately, the S/N of the [S II] lines in this field were too low to fit with anything but a single Gaussian, and since the densities implied fell near or below the low density limit across the whole field (100 cm^{-3}; Osterbrock 1989) we do not show the map here. This result shows that the compact nature of the two knots seen in the flux map of C1 is in fact misleading, and that the density of the gas in these condensations is actually quite low.

Line flux ratios can also be used to trace the ionization level of the emitting gas. In Fig. 8.6 we show the map of [S II]$\lambda\lambda$6717,6731/Hα, calculated from the sum of flux in all observed line components, since not all individual components could be identified in all lines. The lowest ratios are found towards the north-east of the field, corresponding to the northern Hα knot, and in the south-west, roughly coincident with the peak in Hα C3 emission. This ratio, when combined with [O III]λ5007/Hβ (not shown here because of the low S/N of the Hβ line) can be used to look for indications of shocks. Following the method described in Chapter 7 for position 2, we define points in [O III]/Hβ–[S II]/Hα

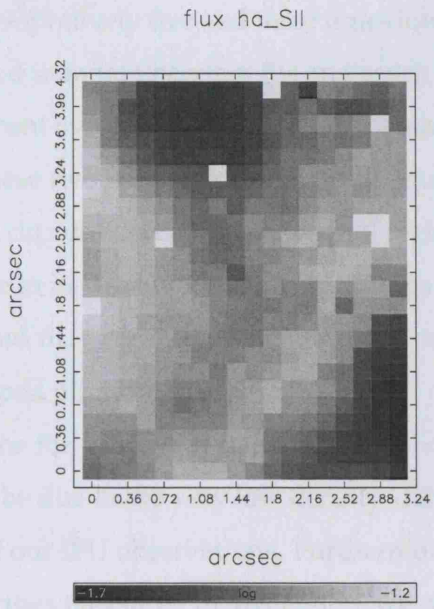

Figure 8.6: **Pos 1.** Map of the flux ratio of [S II]$\lambda\lambda$6717,6731/Hα (log range -1.7 to -1.2) calculated from the sum of flux in all identified line components.

space as containing a contribution from non-photoionization processes when they fall above the 'maximum starburst line' (Kewley *et al.* 2001). All points in this field lie below this line and are therefore consistent with pure photoionization.

Interpretation

This position covers two dynamically different gas knots that form part of the clumped medium around which the central cavity is being evacuated. The southern half of this field is similar to position 2 in that we see very broad (up to 350 km s^{-1}) C2 widths coincident with bright C1 emission. In Chapter 7 we discussed in detail what possible mechanisms might cause such broad emission coincident with brightly emitting knots, and concluded that the most likely explanation is a turbulent mixing layer at the surface of the gas cloud set up by the shear forces of the fast-flowing cluster winds. Thermal evaporation and/or mechanical ablation of clump material result in mass being stripped off the surface of the clouds and thus a highly turbulent velocity field pervades the whole area. Since the data for this southern knot are fully consistent with this explanation, we can extend our conclusions taking into account a number of other observations.

Firstly the gas is found to have a low density, possibly explaining why the average

intensity of C1 and C2 are respectively five and three times lower than in position 2. These low intensities have resulted in more uncertain fits and much noisier maps. Secondly, the width of the broad component over the whole field is on average 50 $\mathrm{km\,s^{-1}}$ larger than in position 2. We interpret these two facts to mean that this southern knot is undergoing a strong interaction with the cluster winds from the central region (particularly SSC A) and is at a more advanced stage in its dissolution than the clumps observed in position 2. The low density of the gas cloud may mean that the wind can penetrate more of the clump and material is being stripped off more easily.

We do not see evidence for the swept-back tail morphology seen in the *HST* Hα image, but this may again be due to the very low density, diffuse nature of the gas or the limited spatial-resultion of our IFU observations. Furthermore, as shown by the random distribution of radial velocities measured in this region, we cannot be sure which cluster or clusters are dominating the energetics in this region, so it is quite possible that what might appear to be a swept-back, bow-shaped seen region in the *HST* image is just another part of the ambient, clumped gas distribution.

Observing such a strong additional narrow component (C3) over the majority of the field is an indicator of the disturbed nature of this part of the inner 200 pc, however we defer a discussion of this component until Section 8.1.5 where we consider it in context with the whole central region.

8.1.3 GMOS Position 3 [1]

Position 3 is located just to the south of SSC A, in what appears to be a region of turbulent filamentary gas. The radio source VLA-8 is located near the north of the field at coordinates $\alpha = 4^{\mathrm{h}}\,30^{\mathrm{m}}\,48\overset{\mathrm{s}}{.}0$, $\delta = 64^{\circ}\,50'\,56\overset{''}{.}3$ (Greve *et al.* 2002*a*, see Fig. 8.1), and is thought to be an extended ($2'' \equiv 20$ pc), low surface brightness SNR. To the south and west, just beyond the IFU FoV, there is a large, prominent, semi-circular shell-like structure outlined by a string of non-photoioinized points (Buckalew & Kobulnicky 2006), indicating that this could be part of a fast, expanding bubble. Due to its close projected distance from SSC A, this region looks like it may bear the brunt of the impacting winds from the central star clusters.

The C1 intensity map (Fig. 8.7, left panel) shows a bright knot in the north-west corner,

[1] Note: this position has the shortest combined exposure time of the four fields: 63 mins rather than 107 mins for all the others.

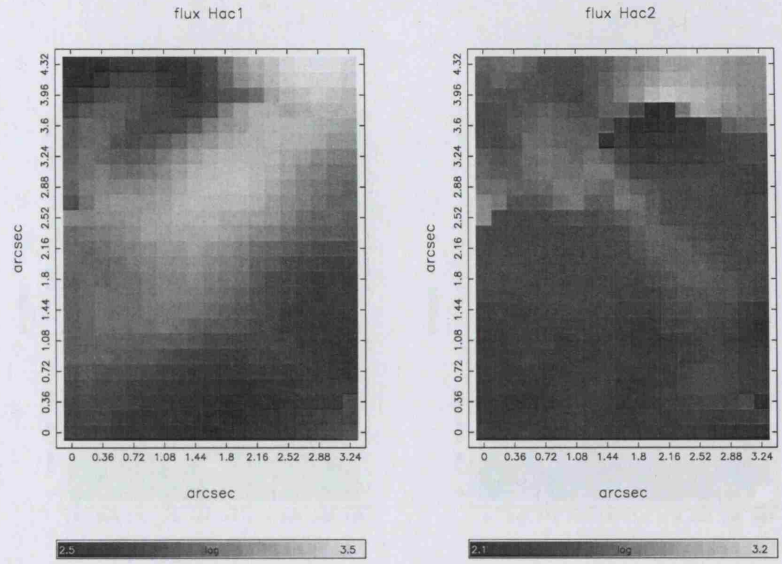

Figure 8.7: **Pos 3.** *Left:* Flux map in Hα C1 (log range 2.5–3.5); *right:* flux map in Hα C2 (log range 2.1–3.2). The x and y scales are in arcseconds offset from the lower-left spaxel, and a scale bar is given for each plot with units log 10^{-15} erg s^{-1} cm^{-2} spaxel^{-1}. North is up and east is left.

with a diffuse, extended area of emission spreading out towards the south-east. This diffuse emission corresponds to part of a highly clumped, ragged structure seen on the *HST* image of Fig. 8.1, which is unresolved in our IFU data. In the C2 flux map, the C1 velocity map and in both the C1 and C2 FWHM maps, this area is no longer smooth and diffuse, but rather surprisingly contains a compact region ($0\farcs8 \times 1\farcs4 \equiv 9 \times 16$ pc) with very different properties to the rest of the field. The FWHM of both C1 and C2 (Fig. 8.8) peak here at 70 km s^{-1} and 300 km s^{-1}, respectively (corrected for instrumental broadening), both corresponding to a strong redshifted peak in C1 ($\sim$25 km s^{-1} with respect to $v_{\rm sys}$; Fig. 8.7, left panel). In Fig. 8.10, we overplot the C1 FWHM and radial velocity maps (contours) on the C1 flux map (greyscale) to illustrate how this compact region, so clearly defined in the line dynamics maps, only roughly corresponds to the north-west of the diffuse emission mentioned above, and certainly not with the bright knot in the far corner. The rapid peaks in line-width and the contrasting nature of this knot indicate that this could be the position of the SNR VLA-8. It is of approximately the right extent, but since its centre is offset by $\sim$2″ (based on *HST* coordinates) from the location given by Greve *et al.* (2002*a*), we cannot confirm this scenario.

A faint diagonal strip in the C2 flux map runs from the north-east to south-west of

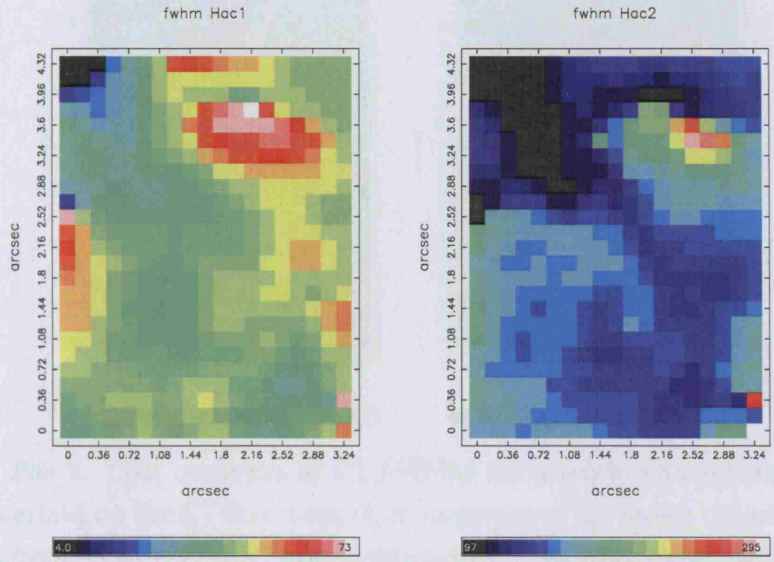

Figure 8.8: **Pos 3.** *Left:* FWHM map in Hα C1 (range 4–73); *right:* FWHM map in Hα C2 (range 97–295). A scale bar is given for each plot in km s^{-1}, with values corrected for instrumental broadening. North is up and east is left.

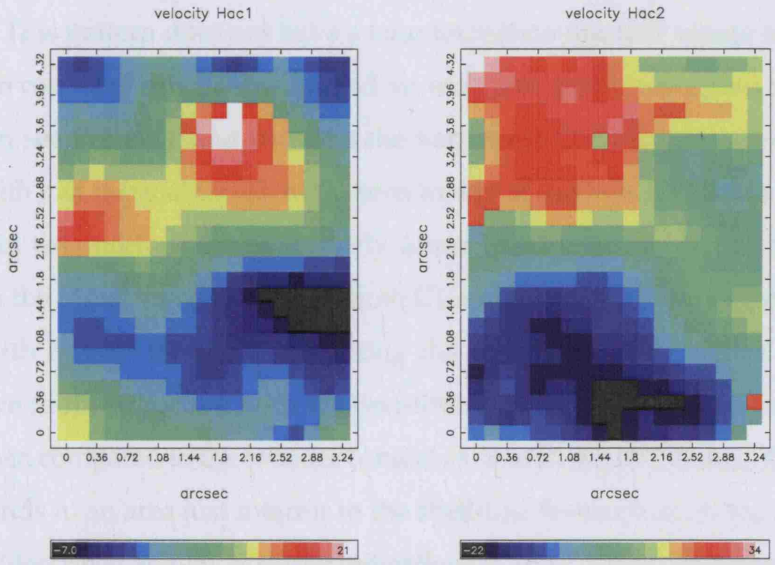

Figure 8.9: **Pos 3.** *Left:* radial velocity map in Hα C1 (range −7 to +21); *right:* radial velocity map in Hα C2 (range −22–34). A scale bar is given for each plot in km s^{-1} (heliocentric) corrected for the systemic velocity of the galaxy (−80 km s^{-1}).

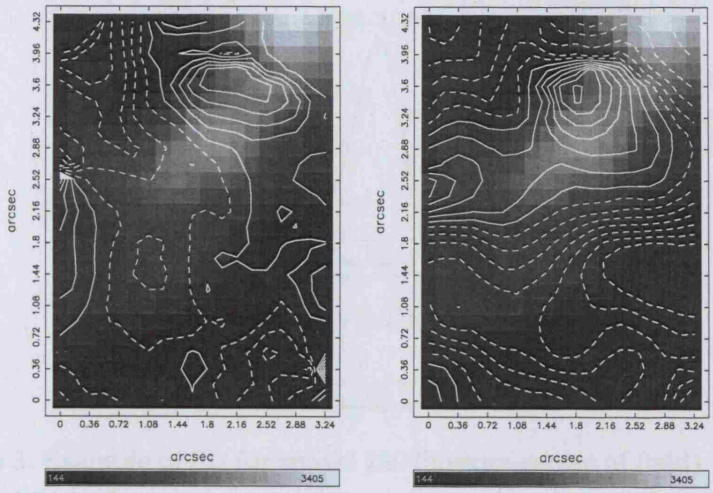

Figure 8.10: **Pos 3.** *Left:* contours of C1 FWHM (12 equally spaced levels from 4 to 73 km s^{-1}) overlaid on the C1 flux map; *right:* contours of C1 radial velocity (12 equally spaced levels from −7 to +21 km s^{-1}) overlaid on the C1 flux map. Solid contours represent levels above the mean of the range in each case, and dashed contours represent levels below the mean. These two maps illustrate the offset nature of both the regions of broad and redshifted emission with respect to the peak in the flux distribution.

the field in the opposite direction to the C1 morphology, wrapping around the unusual knot to the north and south, and is highly correlated with the distribution of narrowest C2 line-widths. This pattern does not have a counterpart on the *HST* image of Fig. 8.1. The north-eastern corner of this field is coincident with part of the evacuated region around SSC A (again see Fig. 8.1), and contains the narrowest C1 widths (as low as 5 km s^{-1}; consistent with just thermal broadening) seen in any of the four IFU fields.

The gas in the south of the field, fairly unremarkable in the flux or FWHM maps, stands out in the radial velocity maps of both C1 and C2 as being very blueshifted (∼10–20 km s^{-1} with respect to $v_{\rm sys}$; representing the most blueshifted C2 in all fields). A representative profile (together with the best-fitting model) from this region is shown in Fig. 8.11. When compared to the broader context as seen in the *HST* image, the blueshifted gas corresponds to an area just interior to the shell-like feature just off the south-west of the IFU FoV (described above), possibly indicating C1 and C2 are both associated with the near-side of this bubble.

Unlike positions 1 and 2, we do not see a correlation between C2 FWHM and C1 flux. Instead there is a strong anti-correlation between C2 FWHM and C2 flux (the maps appear almost morphologically identical), and to a lesser extent between C2 FWHM and C1

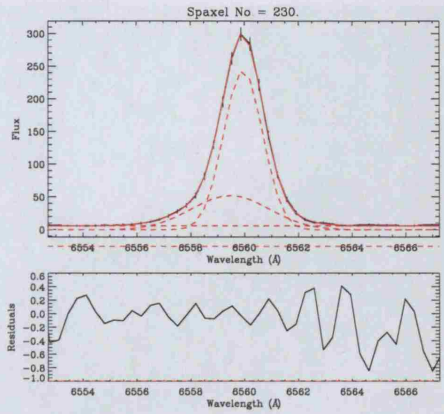

Figure 8.11: **Pos 3.** Example of fits for spaxel 230 (bottom-centre of field). This spaxel was chosen to exemplify the largest velocity difference between C1 and C2 of any of the fields.

FWHM, although the respective ranges in FWHM are dramatically different. A generally faint C1 results in this field having the highest average flux ratio of C2/C1 of ∼30 per cent.

Electron densities were derived from the flux ratio of [S II]λ6717/λ6731 but again fall near or below the low density limit (100 cm^{-3}) across the whole field, so we do not show the map here. The [S II]/Hα and [O III]/Hβ flux ratios are consistent with pure photoionization in every spaxel, with no evidence for shock-excited emission anywhere. This is a little unexpected considering the proximity of the SNR VLA-8, but could result from the low gas densities, since shocks are less likely to show up in low-density line-ratios.

Interpretation

The striking feature in position 3 is the unusual compact knot that dominates the C1 width and velocity maps, and the C2 flux and width maps. Fig. 8.12 shows a magnified version of the region surrounding this IFU position on which the location of the compact knot is shown by an orange ellipse. As we have suggested, the sudden peak in line-widths could indicate that this is the location of the SNR VLA-8 catalogued by Greve *et al.* (2002*a*), but since we see no evidence for shocked line-ratios (as would be expected if this was a SNR), and the fact that it is offset from the position quoted for VLA-8 make this explanation less tenable. Ergo, we can only conclude that this feature represents an isolated, unusually turbulent knot of faintly emitting, redshifted gas that happens to lie on this sight-line.

Except for at the location of this knot, the width of C2 does not exceed ∼200 km s^{-1}

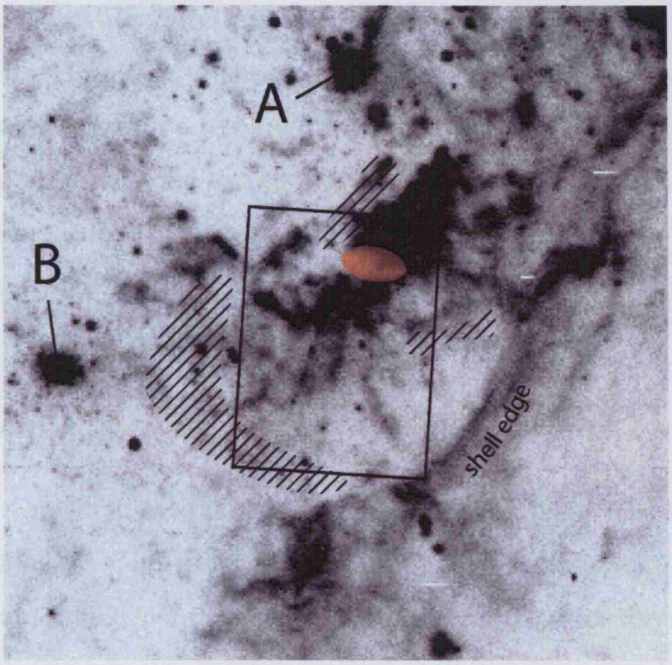

Figure 8.12: *HST* F656N image detail showing the region around IFU position 3. The white hatched areas encompass non-photoionized points found in the study of Buckalew & Kobulnicky (2006), and the orange ellipse marks the location of the unusual compact knot.

over the whole field, and falls as low as 100 km s^{-1} in the north-east quadrant. Away from the knot, the broadest widths are not associated with brightly emitting gas (as found in positions 1 and 2) implying that we are not seeing a strong interaction with the cluster winds in this position. The average ratio of C2/C1 for this position is the highest of all the fields, giving another indication that the physical conditions in this field are different to that of the other positions.

It would seem contradictory why at this close projected distance from SSCs A and B (~50 pc) the gas has not completely been blown away, since large swathes of material at similar projected distances have been completely evacuated. Can we explain this using the observations? We have already mentioned that we see little evidence for a clump–wind interaction in the form of broad line-widths or shocked line-ratios. Both C1 and C2 become gradually blueshifted with respect to v_{sys} towards the south of this field, peaking in an area coincident with the interior of the shell-like feature located just off the bottom of the field, if the string of non-photoionized points identified by Buckalew & Kobulnicky (2006) are included as part of the shell edge. Their non-photoionized points are shown in

Fig. 8.12 as hatched areas, and indicate that the eastern edge of this shell, although not identifiable from the Hα image, is shock-excited. This whole region, with the exception of the unusual isolated knot, may therefore be located at a different line-of-sight to the surrounding gas and be shielded to a certain extent from the effects of the strong cluster winds. This would explain the relatively quiescent line-widths, and was a result predicted for the turbulent mixing/ablation model described in Chapter 7, for regions not subject to the direct impact of cluster winds.

8.1.4 GMOS Position 4

Position 4 covers a bright knot of ionized gas to the east of SSC A that has a morphology somewhat resembling the southern knot in position 1. This condensation is coincident with the radio continuum source M-5 (a "non-thermal source with some thermal contribution"; Greve *et al.* 2002*a*), and appears to have an oval shell-like extension to the south in the *HST* F656N image.

Before discussing the emission-line maps for this position Figs 8.13–8.15, we first comment that since a third component is required in a small region on the east of the field, its presence has resulted in high uncertainties on the fits to C2 in this same region (for reasons discussed in Chapter 6). This has caused a spurious and erratic region in the C2 FWHM and radial velocity maps (outlined with a solid line on the following maps for clarity), so we ignore this section when discussing the properties of C2. Fig. 8.16 shows an example Hα line profile from this region showing the best-fitting Gaussian model profiles, and the fit residuals. In this particular spaxel, a third component is clearly required to accurately model the integrated line shape, but it is clear how the associated errors on the fit to C2 would increase as C3 becomes fainter thus leading to this area of inconsistent results.

The aforementioned bright knot shows up clearly in the C1 flux map (Fig. 8.13, left panel) as expected, but is only evident in the corresponding FWHM and radial velocity maps and the C2 flux map as part of a distinct arc of gas extending out of the FoV the north-east, and partly towards the south-east. This arc has a consistently low C1 FWHM ($\sim$40 km s^{-1}; Fig. 8.14, left panel), and is blueshifted by -10 to -15 km s^{-1} with respect to $v_{\rm sys}$ (Fig. 8.15, left panel), implying that the bright knot is dynamically associated with a larger gas filament extending out either side of the FoV.

The gas not associated with the filament is much fainter, and exhibits very different

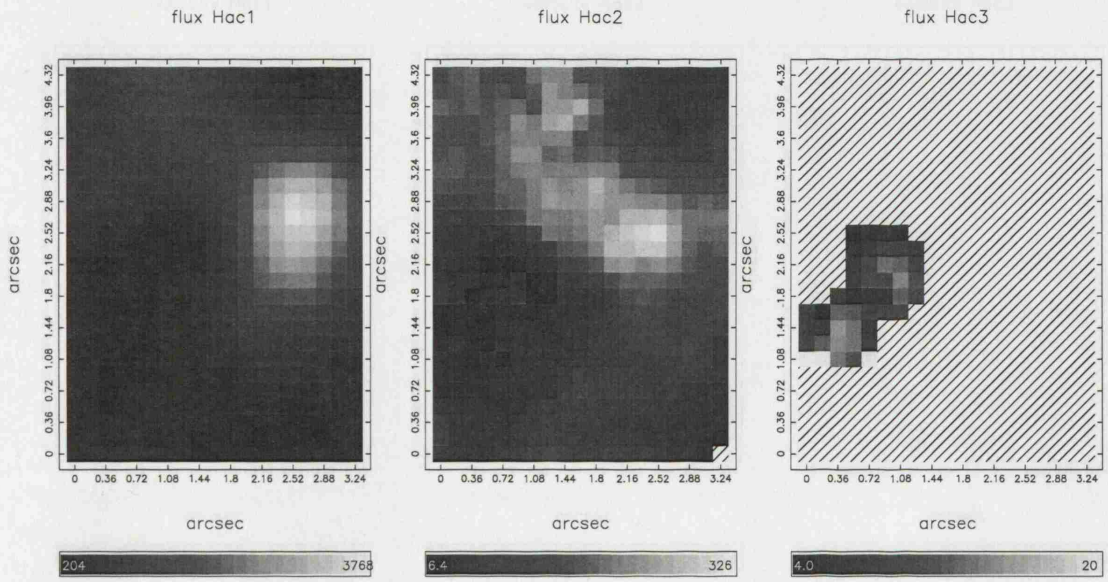

Figure 8.13: **Pos 4.** *Left:* Flux map in Hα C1 (range 204–3768); *centre:* flux map in Hα C2 (range 6.4–326); *right:* flux map in Hα C3 (range 4.0–20). Non-detections are represented as hatched spaxels, the x and y scales are in arcseconds offset from the lower-left spaxel, and a scale bar is given for each plot with units 10^{-15} erg s^{-1} cm^{-2} spaxel^{-1}. North is up and east is left.

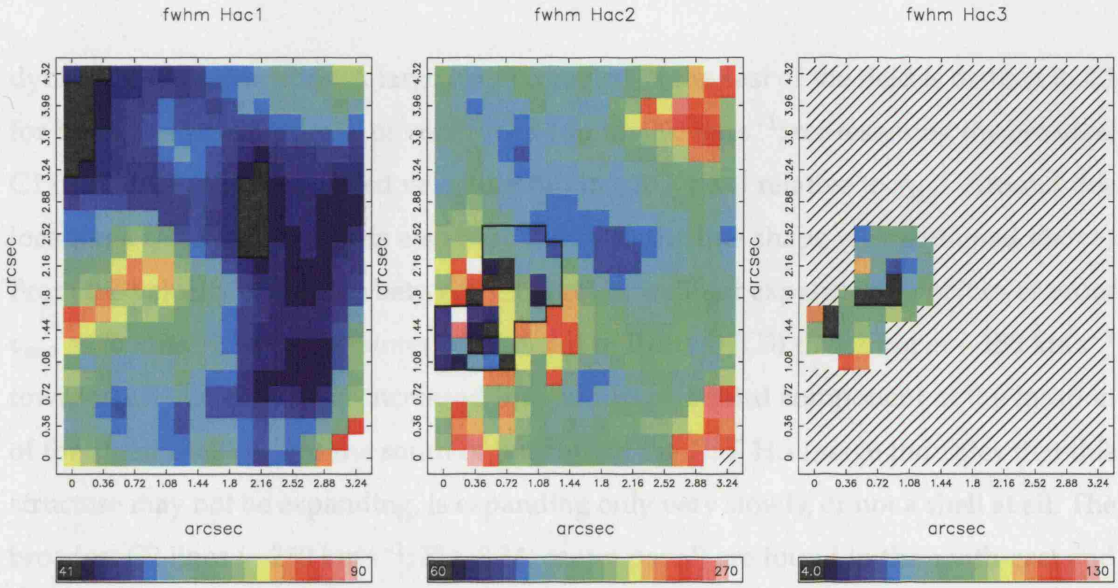

Figure 8.14: **Pos 4.** *Left:* FWHM map in Hα C1 (range 41–90); *centre:* FWHM map in Hα C2 (range 60–270); *right:* FWHM map in Hα C3 (range 4–130). The region outlined with a solid line in the C2 map indicates where the measurement errors are high due to the addition of a third Gaussian to the fit. A scale bar is given for each plot in units of km s^{-1}, with values corrected for instrumental broadening. North is up and east is left.

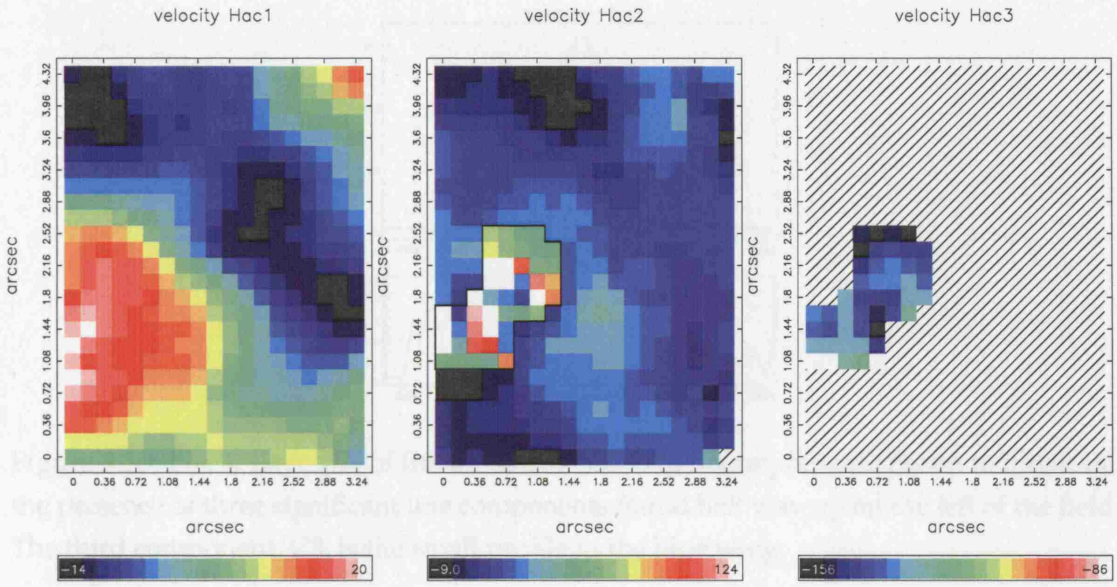

Figure 8.15: **Pos 4.** *Left:* radial velocity map in Hα C1 (range −14–20); *centre:* radial velocity map in Hα C2 (range −9–124); *right:* radial velocity map in Hα C3 (range −156 to −86). Again, the region outlined with a solid line in the C2 map indicates where the measurement errors are high due to the addition of a third Gaussian to the fit. A scale bar is given for each plot in km s^{-1} (heliocentric) corrected for the systemic velocity of the galaxy (−80 km s^{-1}).

dynamical characteristics. A large circular region in the east of the field is distinct in C1 for having coincident peaks of very broad (up to ∼90 km s^{-1}; representing the broadest C1 of all fields) and redshifted velocities (up to +20 km s^{-1} relative to $v_{\rm sys}$). Around this location a third component is also required to fit the line shape (as mentioned above). From the velocity difference between C1 and C3, we infer expansion velocities of order $v_{\rm exp} \approx 80$ km s^{-1}, with the fainter component of the two (C3) travelling at ∼150 km s^{-1} towards us. An absence of increased line-widths or a third component at the location of the small shell seen to the south of the knot in the *HST* Hα image indicates that this structure may not be expanding, is expanding only very slowly, or not a shell at all. The broadest C2 lines (∼250 km s^{-1}; Fig. 8.14, centre panel) are found in the south-east and north-west, and in both locations are associated with redshifted gas in C1 (+5–20 km s^{-1}). We mention this because these are sections of the IFU FoV that appear to be coincident with part of the evacuated cavity surrounding SSC A, and will be discussed later.

This field has a number of unexpected relationships between the components compared to the other positions. Firstly, this is the only position where the flux distribution of

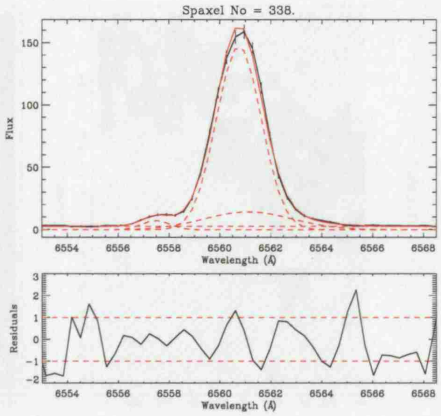

Figure 8.16: **Pos 4.** Example of fits for spaxel 338. This example was chosen to illustrate the presence of three significant line components found half way up on the left of the field. The third component, C3, is the small profile in the blue wing.

C2 (Fig. 8.13, centre panel) bears any resemblance to the corresponding C1 map and to the *HST* image. We show below how this can be explained by the unusually high density of the gas emitting C2. Secondly, the correlation between C2 FWHM and C1 flux is in the opposite sense to what we have seen in positions 1 and 2. Here the broadest C2 lines are coincident with the *faintest* C1 emission in the north-west, south-west and centre-east of the field.

This is the only position for which we have been able to make confident double-Gaussian fits to some of the [S II] lines, and derive the electron density for both components (mapped in Fig. 8.17). The density of the gas emitting C1 (left panel) is low, with only parts of the western edge coincident with the bright knot rising above the low density limit (indicated by the single contour). We are able to derive the density for C2 (centre panel) in a diagonal band stretching from the centre-west to the north-east, coincident with the band of bright C2 emission and blueshifted C1 gas in the north of the field. The density of C2 is on average much higher than that of C1, reaching up to $\sim$600 cm^{-3} in the north-east. Since the emission intensity of recombination lines is proportional to the gas density-squared, the unusually high densities in C2 may may explain why in this field the C2 emission morphology bears a close resemblance to the corresponding C1 morphology.

Also shown in Fig. 8.17 is the flux ratio of [S II](λ6717+λ6731)/Hα (right panel). The lowest ratios are found in the centre-west of the field, coincident with the bright Hα knot and the radio source M-5. Using the [O III]/Hβ–[S II]/Hα nebular diagnostic technique described in Chapter 7 and above, we find a significant number of spaxels over the

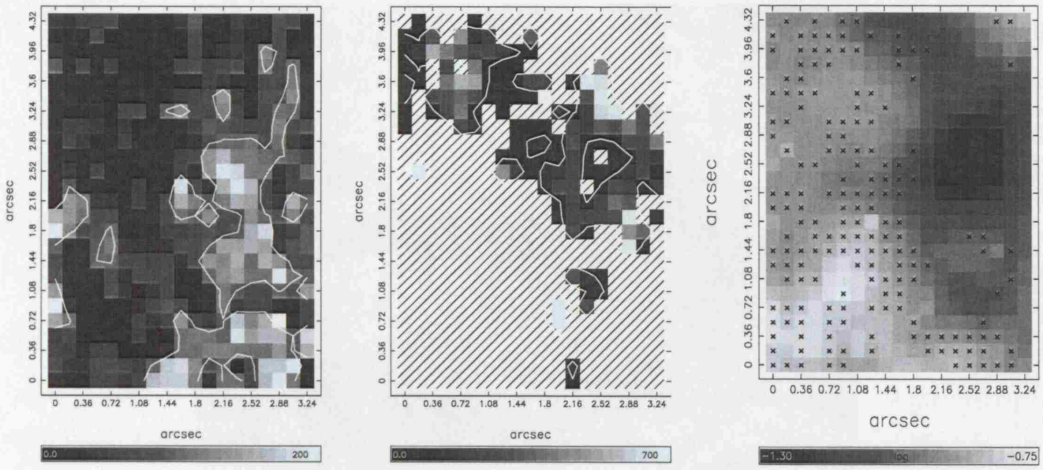

Figure 8.17: **Pos 4.** *Left:* Electron density map derived from the ratio of [S II]λ6717/λ6731 for C1 (range 0–200); *centre:* electron density map for C2 (range 0–700). A scale bar is given for each plot in units of cm^{-3}. A single contour level marks the 100 cm^{-3} low density limit (Osterbrock 1989) on both maps. *Right:* flux ratio of log([S II](λ6717+λ6731)/Hα) C1 (log range −1.3 to −0.75). Spaxels marked with a cross indicate non-photoionized emission according to the 'maximum starburst line' of Kewley *et al.* (2001).

whole eastern half of the field to contain a possible contribution from non-photoionization processes (presumably shock excitation; see Calzetti *et al.* 2004). However, the derived low flux ratios at the location of the bright knot do not support a SNR origin for M-5 unless it is highly embedded.

Interpretation

Evident in both the flux maps of C1 and C2, a band of material curves round from the north-east of the field to the south, including the bright knot near the western edge. In C1, this band has a consistently low FWHM and is blueshifted by 10–15 km s^{-1} with respect to $v_{\rm sys}$. In comparison, the ionized gas to the east of the field is significantly redshifted in C1, has a high-velocity ($\sim$150 km s^{-1}) blueshifted component, and a widespread non-photoionized contribution to the excitation.

Careful inspection of the *HST* image of Fig. 8.1 shows that this band may be the westernmost part of a fragmented shell extending out of the FoV to the east. Fig. 8.18 shows a blow-up of the *HST* F656N image around position 4. The hatched areas represent the regions of non-photoionized points found by Buckalew & Kobulnicky (2006), illustrating how the edges of this shell appear to be traced out by non-photoionized (shocked) emission.

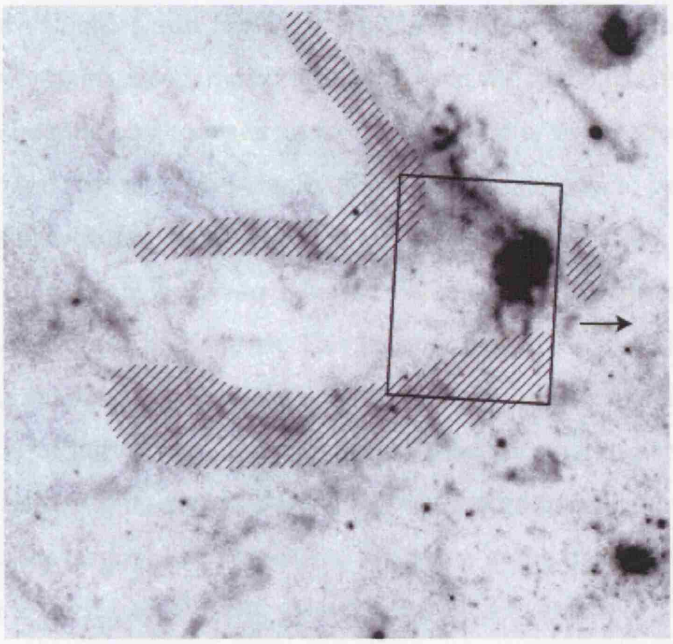

Figure 8.18: *HST* F656N image detail showing the region around IFU position 4. The hatched areas are non-photoionized points found in the study of Buckalew & Kobulnicky (2006), and the arrow indicates the direction of SSC A.

How can we relate this to our more wide-spread distribution of non-photoionized gas shown in Fig. 8.17? The methods used by Buckalew & Kobulnicky for the determination of their points are inherently luminosity weighted, in the sense that only where they actually detected emission at sufficient S/N could they measure the line ratios. The fact that our data go significantly deeper, combined with the advantages of actually being able to fit the individual emission lines (thus avoiding the uncertainties of continuum subtraction), has meant that we have been able to accurately measure the line ratios for much fainter gas. The distribution of non-photoionized gas we derive includes both their points arising from the brighter regions and additional points identified from the lower surface-brightess regions, implying that shock-excited emission is more widespread than previously observed.

We can now associate the emission to the east of the field with originating from within the expanding shell structure, where the near-side wall is represented by the high-velocity C3, and the far-side by the brighter redshifted region seen in C1. The velocities and brightness contrast between the two components can be explained if the far-side of the bubble is expanding into a dense medium, causing it to slow down rapidly and emit

brightly. The fast velocities and faint Hα emission of C3, imply that the near-side is expanding relatively unimpeded, meaning that an estimate of the true expansion velocity of the bubble can be made by comparing the radial velocity of the gas in the shell edge (the blueshifted band) to the high-velocity C3. We estimate $v_{\rm exp}$ to be $\approx$140 km s^{-1} by taking half the velocity difference between the two line components.

The width of C2 remains between 100 and 150 km s^{-1} in the blueshifted shell edge including the position of the bright knot. This lack of very broad lines may indicate that a direct wind–clump interaction is not taking place here. Recall that this clump contains the radio source M-5 emitting a mixture of thermal and non-thermal radiation. The presence of a thermal signature points towards an embedded photoionizing source (*e.g.* a young star cluster) being the origin of this emission. Emission in the thermal IR would support this scenario, but unfortunately the high-resolution observations of Tokura *et al.* (2006) did not cover this knot. There is very marginal evidence for continuum emission at the location of the bright knot in our IFU data, but since we cannot identify any discrete stellar features (*e.g.* a WR bump) we cannot prove the existence of an embedded stellar source.

8.1.5 The state of the ISM

So far we have examined the details of the ionized gas distribution in each field individually. However, there are insights to be gained from looking at the collective ionized gas properties of all four fields at once, so as to assess the general trends and systematic variations across the ~200 pc wide region centred on SSC A sampled by our IFU pointings. Figs 8.19, 8.20 and 8.21 plot the Gaussian flux, FWHM and radial velocity of the identified line components for all four positions in the three possible permutations. These, and the selected average properties listed in Table 8.1, are discussed in the following paragraphs in the context of understanding the general state of the ISM.

Fig. 8.20 shows that the trend found in position 2 whereby the broadest emission is the faintest, also applies to the entire data-set. This implies that the highly turbulent matter, which we believe is being entrained into the wind flow, does not emit strongly in Hα. Plotting all the data together also highlights the fact that the highest velocity gas is also the faintest (particularly obvious from Fig. 8.21). Position 2 is the brightest emitting field (as would be expected from the *HST* Hα image), whereas position 1 is overall the faintest. However, position 1 exhibits the broadest C2 widths, with an even spread extending up to ~400 km s^{-1}. As we have previously mentioned, this is likely to indicate that this position

Table 8.1: Selected average emission-line properties for the four IFU fields. The velocity measurements are quoted with a standard 1σ error.

IFU position	Line component	Gaussian property	Average value
all	C2/C1	Flux ratio	0.12
1	C2/C1	Flux ratio	0.11
2	C2/C1	Flux ratio	0.07
3	C2/C1	Flux ratio	0.30
4	C2/C1	Flux ratio	0.13
all	C1	FWHM[a]	46.9 ± 8.7
all	C2	FWHM	192.0 ± 47.3
all	C3	FWHM	53.1 ± 30.0
all	C1	Radial Velocity[b]	-1.8 ± 6.7
all	C2	Radial Velocity	$+13.4 \pm 17.4$
all	C3	Radial Velocity	-14.6 ± 24.3[c]
1	C1	Radial Velocity	-16.7 ± 6.0
2	C1	Radial Velocity	-2.5 ± 5.5
3	C1	Radial Velocity	-3.3 ± 5.9
4	C1	Radial Velocity	-0.1 ± 9.3
1	C2	Radial Velocity	$+19.5 \pm 21.9$
2	C2	Radial Velocity	$+4.4 \pm 8.7$
3	C2	Radial Velocity	$+4.4 \pm 14.4$
4	C2	Radial Velocity	$+25.3 \pm 24.7$

[a] FWHMs are in units of $\mathrm{km\,s^{-1}}$, corrected for instrumental, but not thermal broadening.
[b] Radial velocities are in units of $\mathrm{km\,s^{-1}}$, relative to v_{sys} ($= -80\ \mathrm{km\,s^{-1}}$).
[c] Average without position 4 $= +24.5 \pm 20.6\ \mathrm{km\,s^{-1}}$

covers gas that is experiencing the strongest interaction with the cluster winds. Position 3 has the most quiescent C2 widths, most likely resulting from the fact that the gas in this field is shielded to some extent from the direct influence of the outflowing cluster winds.

For position 2 (Chapter 7), the consistency in the width of C1, and its similarity to the integrated H I velocity dispersion for the whole of NGC 1569 of $\sigma \approx 15\ \mathrm{km\,s^{-1}}$ (FWHM $\approx$ $35\ \mathrm{km\,s^{-1}}$; Mühle *et al.* 2005), led us to conclude that it represents the disturbed, turbulent ISM that has been stirred up by the effects of the intense star-formation and supernova shocks. However, we could not rule out an additional minor contribution to its width from unresolved kinematical components along the line-of-sight. By plotting the FWHM results for all fields together (Figs 8.19 and 8.20), we find this consistency in line-width is mirrored across all positions, and that the widths of C1 fall in a very narrow band ($47 \pm 9\ \mathrm{km\,s^{-1}}$) extending over the full range of intensities observed. The C1 line-width therefore cannot be related to its emission strength. The clear lower-limit to the FWHM of C1 found in position 2, referred to as $\mathrm{FWHM_0}$, is also evident in the other fields. In positions 1 and 3, $\mathrm{FWHM_0} \approx 30$–$35\ \mathrm{km\,s^{-1}}$ (although is less well defined for position 3), and in position

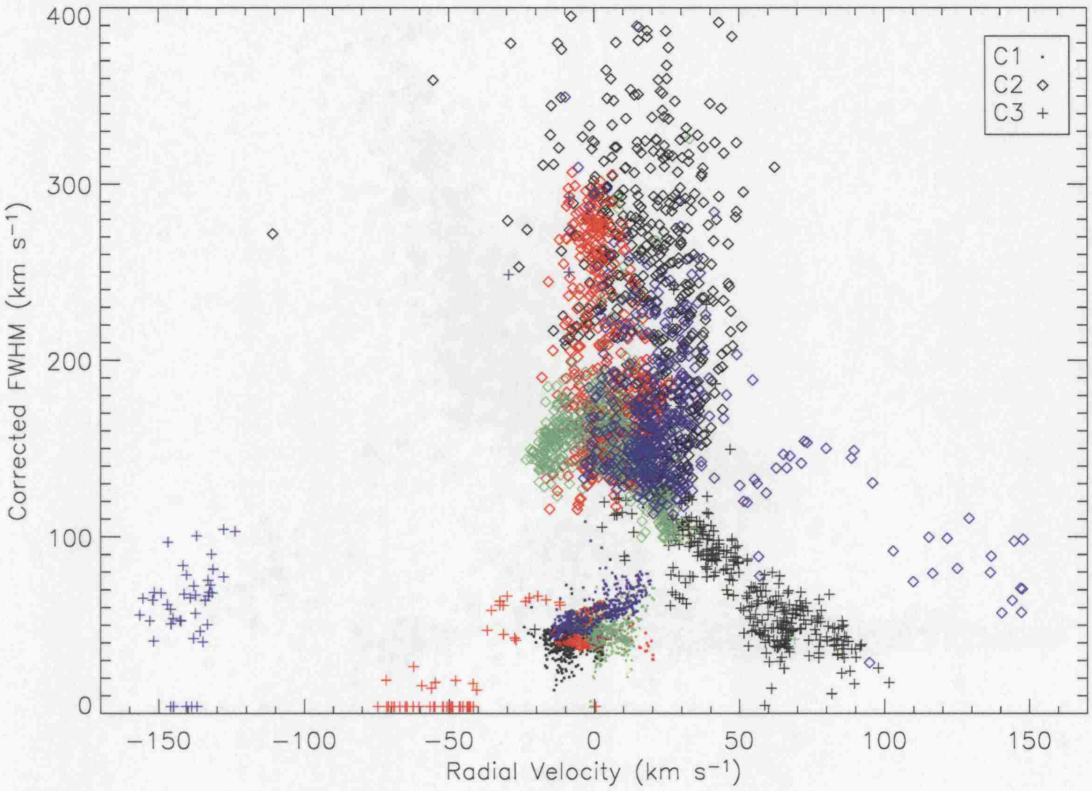

Figure 8.19: FWHM (corrected for instrumental broadening) *vs.* heliocentric radial velocity (with respect to v_{sys}) for all four IFU positions. Black symbols represent position 1, red position 2, green position 3, and blue position 4.

4, $FWHM_0$ is slightly higher at ≈ 45 km s^{-1}. This level of consistency therefore supports the conclusion that C1 simply represents the disturbed ISM. Although in places, C1 is associated with fast motion and/or expansion, its line-width is everywhere equal to or greater than the general turbulent width of the gas across the whole central regions.

We can identify a third component in positions 1, 2 and 4, and from Figs 8.19 and 8.20, we see that its FWHM is equivalent to that of C1 (within the uncertainties) in every case. This confirms the conclusion that where identified, C3 represents an additional narrow component associated with a secondary kinematical system. In position 4 its relation to shell expansion is clear, but in position 1 its significance is not so obvious. This component occupies a prominent diagonal band in Fig. 8.19, distinct from all the other components, between velocity = +100 km s^{-1}, FWHM = 20–30 km s^{-1}, and velocity = 30 km s^{-1}, FWHM = 100 km s^{-1}, implying that bulk motion and turbulence influence the dynamics of this component to differing degrees from one half of the field to the other. This behaviour is

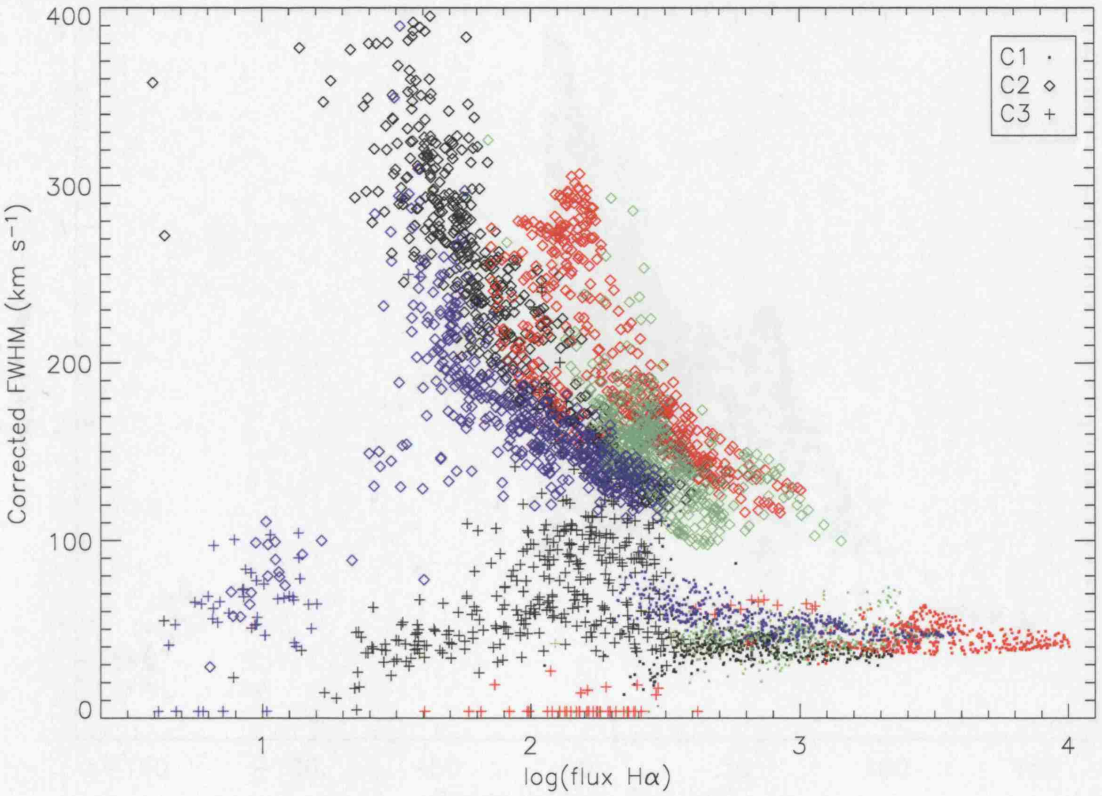

Figure 8.20: FWHM (corrected for instrumental broadening) *vs.* log(Hα flux) (arbitrary scale) for all four IFU positions. Symbol colours are the same as Fig. 8.19.

mirrored in Figs 8.20 and Fig. 8.21, where C3 of position 1 again occupies its own unique space. Its FWHM seems correlated with that of C2 at the position of the southern knot, implying that it is affected by the wind–clump interaction (unlike C1), however its velocity is spatially correlated with C1 only at the position of the northern knot. Consequently, we conclude that here, C3 represents a mix of overlapping kinematical systems originating from separate mechanisms. Where it exhibits a high comparative redshift (in the north), it may represent the the far-side of an expanding structure – its properties are consistent with being part of the high-velocity kinematic subsystem identified by Heckman *et al.* (1995). Where its velocity is similar to C1 (in the south), it is likely to be associated with the wind–clump interaction, since its FWHM is correlated with that of C2 (see Chapter 7).

As listed in Table 8.1, the average radial velocity of C2 is offset from the corresponding C1 average by only $\sim$+15 km s^{-1} over the four fields; the largest individual difference being in position 1 of $\sim$35 km s^{-1}. Furthermore, ignoring the high C3 velocities in positions 1 and 4, the total velocity spread across the four fields is only $\sim$70 km s^{-1} (see *e.g.* Fig. 8.19).

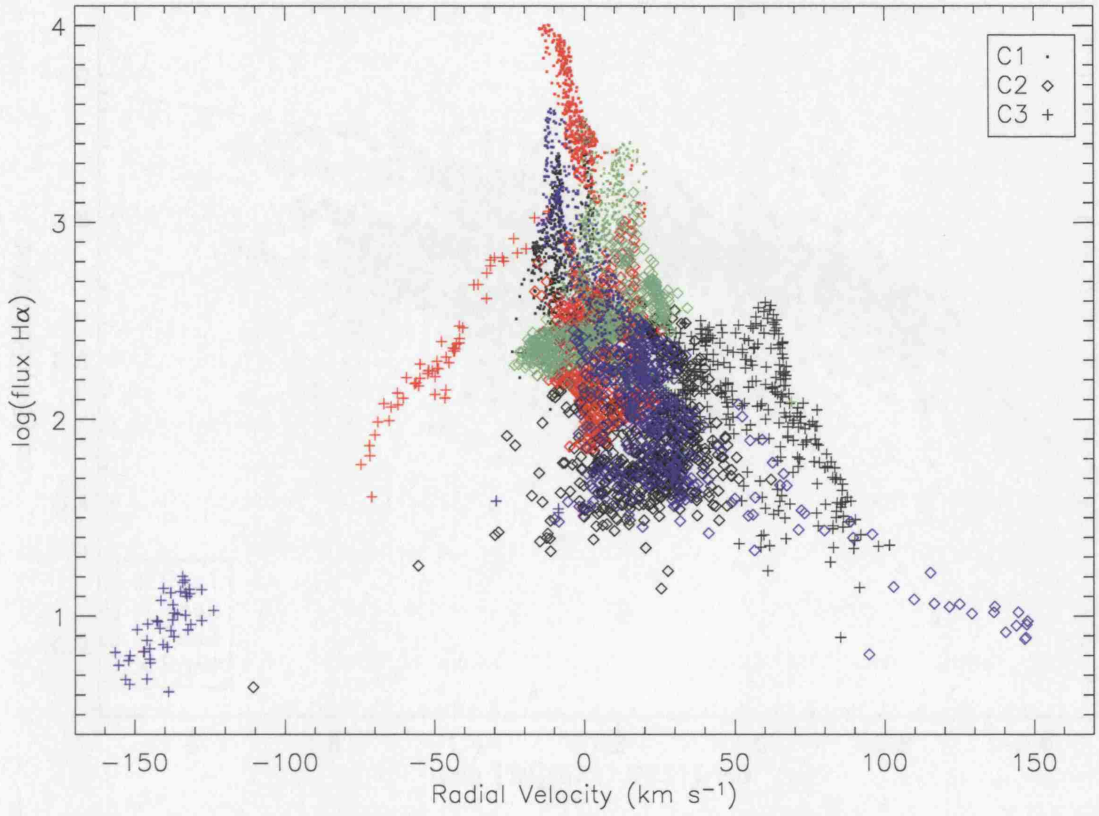

Figure 8.21: Heliocentric radial velocity (with respect to v_{sys}) *vs.* log(Hα flux) (arbitrary scale) for all four IFU positions. Symbol colours are the same as Fig. 8.19.

These values are smaller than even the narrowest line-widths measured, implying that turbulent velocities completely dominate over bulk motions in this whole 200 pc central region.

We began this study with the aim of looking for evidence of the 'roots' of the galactic wind, and to try and identify where and how the flow is accelerated and collimated. Heckman *et al.* (1995) and Martin (1998) identified large-scale expanding supershells surrounding the central regions of NGC 1569 that together form the large-scale galactic outflow (see Section 8.2). These authors find the velocity ellipses associated with shells A, B (on the western side) and E (on the north-eastern side) to have inner boundaries located at ∼10″, ∼30″ and ∼60″ away from SSC A, respectively, placing the start of the collimated flows at least ∼100 pc away from our IFU positions. We know that within the central 200 pc (as sampled by our observations), we do not see evidence for bulk motions consistent with the outflow. This must therefore mean that the collimation process occurs between radii of 100 to 200 pc from SSC A.

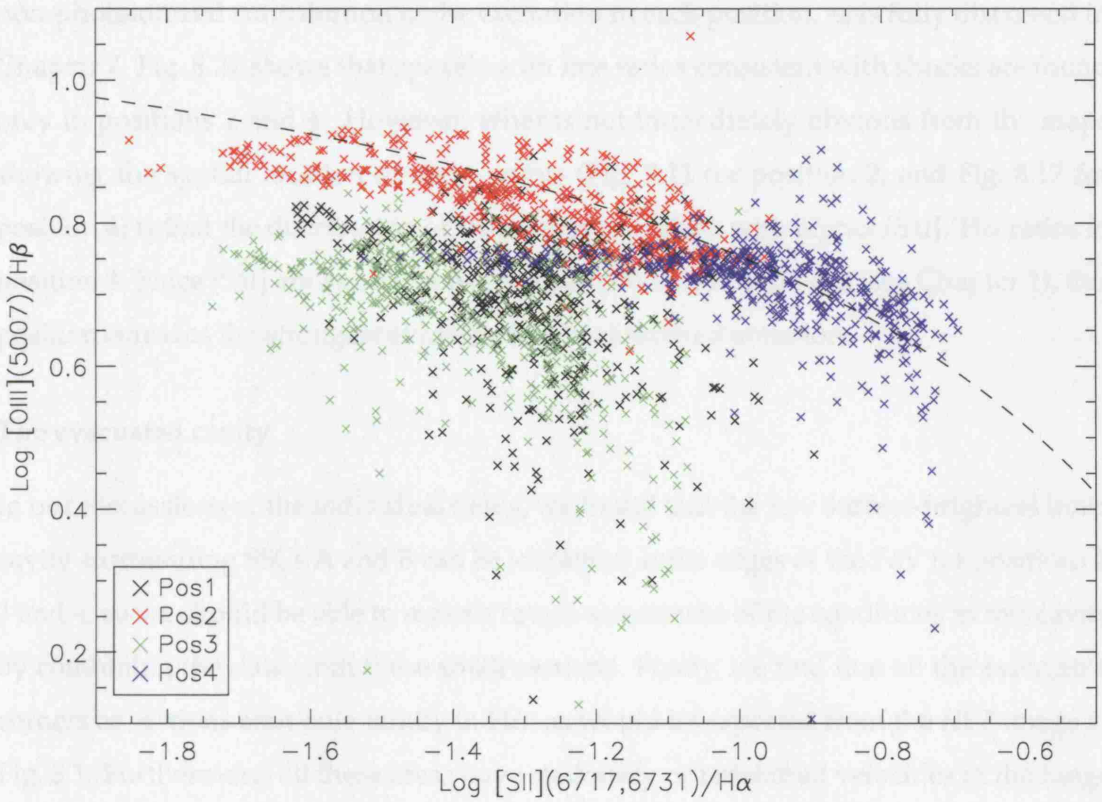

Figure 8.22: Dereddened C1 flux ratios of [O III]λ5007/Hβ *vs.* [S II]$\lambda\lambda$6717,6731/Hα for all four IFU positions. The maximum starburst line of Kewley *et al.* (2001) is plotted as a dashed line.

Are we then detecting the galactic wind roots? In Chapter 7 we discussed how our observations are reminiscent of the simulated gas motions within the outer bounding shock of an expanding zone as modelled by Tenorio-Tagle *et al.* (2006), in the presence of a highly clumped medium. The answer must therefore be yes, but in these inner regions, we are still well within the outflow's sonic point (equivalent in this case to the outer shock in the Tenorio-Tagle *et al.* models), and the gas has yet to develop into an organised flow capable of reaching into the galactic halo.

Finally we turn to Fig. 8.22, which shows the [O III]λ5007/Hβ *vs.* [S II]$\lambda\lambda$6717,6731/Hα nebular diagnostic diagram for all C1 measurements in all IFU positions. On this plot, we also show the 'maximum starburst line' derived by Kewley *et al.* (2001) that indicates the theoretical limit for pure photoionization. For points to exist above or to the right of this threshold, an additional contribution to the excitation from non-photoionization processes (*e.g.* shocks) is required. This criterion was used to define spaxels that should contain a

non-photoionized contribution to the excitation in each position, as is fully discussed in Chapter 7. Fig. 8.22 shows that spaxels with line ratios consistent with shocks are found only in positions 2 and 4. However, what is not immediately obvious from the maps showing the spatial location of these points (Fig. 7.11 for position 2, and Fig. 8.17 for position 4) is that the distribution of their ratios are offset, with higher [S II]/Hα ratios in position 4. Since [S II] emission can be strongly enhanced by shocks (see Chapter 1), this position contains the strongest evidence for shock-excited emission.

The evacuated cavity

In our discussions of the individual fields, we found that the low surface-brightess inner cavity surrounding SSCs A and B can be identified at the edges of the FoV for positions 1, 3 and 4, so we should be able to make a rough assessment of the conditions in this cavity by combining the data from these small sections. Firstly, we find that all the associated corners or sections emit only faintly in Hα, as would be expected from the *HST* image of Fig. 8.1. Furthermore, all these areas have stationary or redshifted velocities in the range 0–30 km s^{-1} with respect to $v_{\rm sys}$ (with the exception of C3 in the south-western corner of position 1, which has redshifted velocities of up to 100 km s^{-1}). This result is consistent with the evacuated nature of this region, implying that here we are seeing further into the galaxy to a region where the predominant gas motion is away from us.

In positions 1 and 4 on the north and west of SSC A, we observe very broad line widths in both C1 and C2 for areas associated with the cavity (up to 100 km s^{-1} in C1 and 250 km s^{-1} in C2), however the opposite is true in position 3, where we find the narrowest C1 line-widths of any field. Unfortunately, since our sample is very small and limited in spatial extent we cannot infer anything further. Additional observations are needed to better understand the gas conditions in this faint cavity.

8.1.6 Summary

From the *HST* F656N image of Fig. 8.1, it is clear that the central region of NGC 1569 is dominated by the effects of the cluster winds from SSCs A and B (see also Fig. 5.1). A large cavity ~200 pc in diameter has formed around these clusters due to the effects of their strong winds. This is exemplified by the 'swept-back', cometary-tail appearance of some of the remaining gas knots and the generally faint Hα emission from this region.

To the west of SSC A, a large, bright H II region complex (H II region 2; Waller 1991) dominates the emission intensity, and shows evidence for recent, on-going and embedded star- and cluster-formation, fuelled by the large near-by repository of molecular gas. Surrounding the western hemisphere of H II region No. 2 is a band of non-photoionized (shocked) points, demonstrating the strength of activity within this complex (Buckalew & Kobulnicky 2006). The small size of the GMOS IFU FoV (50 × 35 pc), coupled with the high spatial- and spectral-resolution, has meant that we have been able to examine each of the four fields in unprecedented detail, and relate the physical conditions of each field to the general state of the ISM in this central region.

It has become obvious, however, that the interpretation of emission-line properties at this resolution is not straightforward. We have encountered many confusing relationships and unexpected results within and between the four fields that have at first (and to some extent still) do not make sense. Further spatially-resolved data are needed to investigate the properties of the cavity immediately surrounding the central star clusters, to elucidate the nature of the unusual compact knot in position 3 and the possibly embedded source M-5 in position 4. The study of these four fields has left us in a much better position to judge where the strongest clump–wind interactions are taking place, meaning that future observations in this type of environment can be directed with a more informed approach.

We now summarise the main points arising from our in-depth study of the state of the ISM near SSC A in NGC 1569.

- We see knots and filaments of gas which appear to be located at different lines-of-sight and expanding in different directions, attesting to the highly disturbed and fragmented nature of the ISM in NGC 1569.

- We observe a narrow (∼35–100 $\mathrm{km\,s^{-1}}$) and broad (∼100–400 $\mathrm{km\,s^{-1}}$) component to the Hα line over all four regions with a total radial velocity spread of only ∼70 $\mathrm{km\,s^{-1}}$.

- We also identify a third, high-velocity component in some regions, which we can confidently associate with shell expansion in positions 2 and 4.

- We confirm and expand on our conclusions of Chapter 7 for the origins of the two main components. The most likely explanation of the narrow component (C1) is that it represents the general disturbed optically emitting ISM, stirred up by the effects

of the starburst. This gives a global characteristic turbulent width to C1 (referred to as $FWHM_0$), which is augmented by a varying contribution from unresolved kinematical components along the line-of-sight.

- We conclude that the broad component (C2) results from the highly turbulent velocity field associated with the interaction of the hot phase of the ISM with cooler gas clumps. Material that is photoevaporated or thermally evaporated from the surface of the clouds through the action of the strong ambient radiation field pervading the central regions of NGC 1569, gives rise to broad emission. However, the broadest emission appears to be associated with the direct impact of the hot, fast-flowing cluster winds, where turbulent mixing layers develop and mechanical ablation is taking place.

- We find surprisingly little evidence for shocked line ratios, which may be due to the low density of the gas throughout the regions observed. Positions 2 and 4 show the most convincing evidence for shocks, where in position 4 the emission is associated with a large expanding shell complex extending to the east of the FoV.

8.2 The environment of the outer-wind

In Chapter 5, Section 5.3, we introduced a set of SparsePak observations of the outer-wind regions in NGC 1569 and described the procedure followed to reduce these data. We now present the analysis of these observations and discuss our findings in context with what we have learned in the preceding sections and with the NGC 1569 starburst as a whole.

The positions of the SparsePak fibres for all four fields are shown in Fig. 8.23 (top panel) overlaid on a deep ground-based Hα image (reproduced from Hunter *et al.* 1993). As a reminder, the spectral dispersion of our set-up was 0.20 Å pix^{-1} (giving an average instrumental resolution of 30 km s^{-1}), each SparsePak fibre is 4.″69 in diameter, and the formatted field has approximate dimensions of 72 × 72 arcsecs. The four pointings were chosen to sample the outer galactic wind flow, to coincide with the main expanding shells identified by Heckman *et al.* (1995) and Martin (1998), and with regions of bright diffuse X-ray emission (Martin *et al.* 2002). An Hα and X-ray composite of the NGC 1569 system is reproduced in Fig. 8.23 (bottom panel), with the six large expanding supershells identified by Martin (1998) outlined with dashed lines. This figure highlights how soft

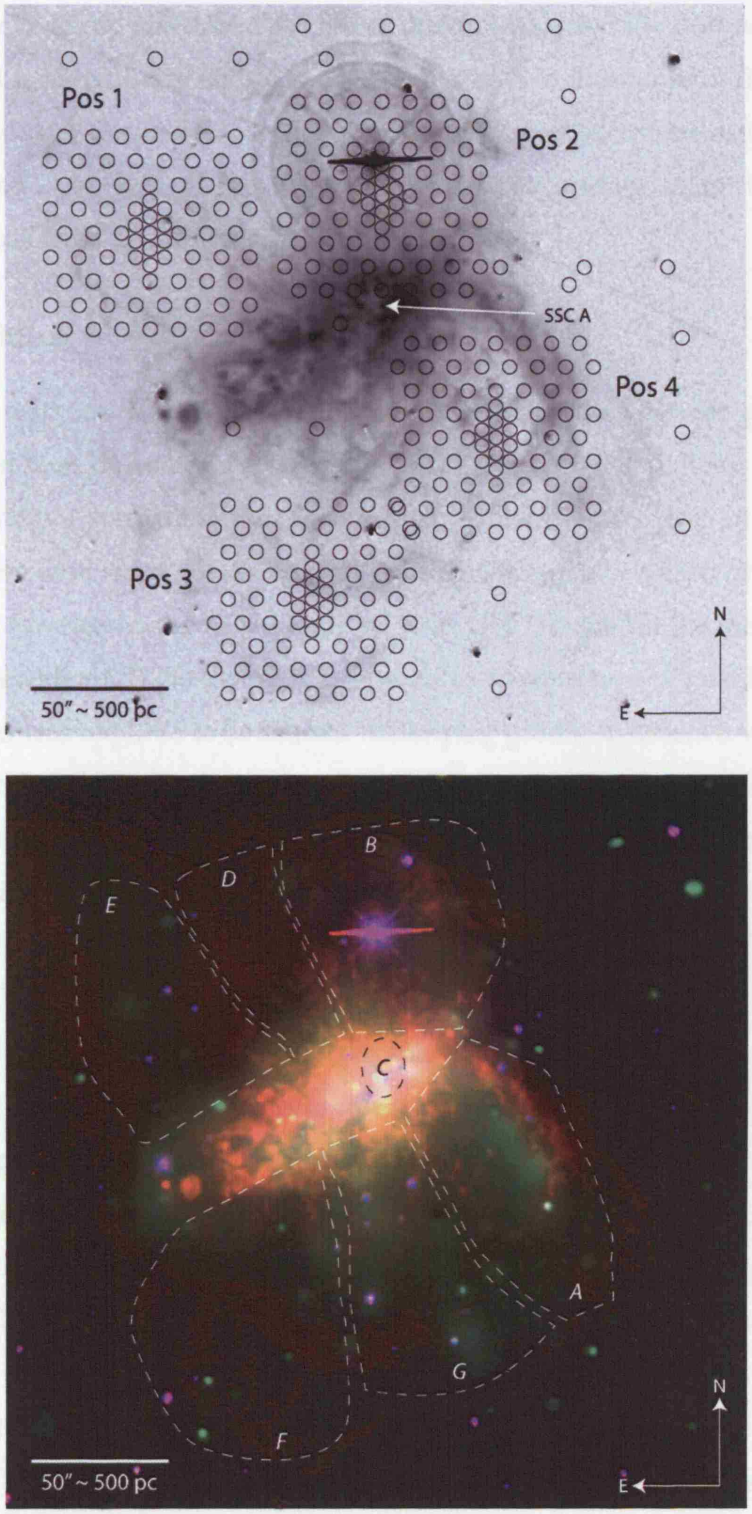

Figure 8.23: *Top:* SparsePak footprints overlaid on the Hα image from Hunter *et al.* (1993); *bottom:* composite optical (Hα, red; Hunter *et al.* 1993) and X-ray (green; Martin *et al.* 2002) image (courtesy of the Chandra X-ray Centre) highlighting the correspondence of X-ray emission with the Hα morphology. Outlines of the expanding shells identified by Martin (1998) are shown with dashed lines, and are labelled in her nomenclature.

X-ray emission is found interior to the Hα emission that generally outlines the walls of the shells, and is particularly obvious in shells A and G in the southern flow. The X-ray emission is thought to originate in the halo shock generated by the outflow, possibly from the mixing layers between the shock and the bubble interior, rather than the actual expanding shock front (Martin *et al.* 2002).

8.2.1 Line fitting

Following the methods described in Chapter 6, we fitted model Gaussian profiles to each of the emission lines detected in each spaxel of the four SparsePak fields using PAN. In order to maintain a consistent approach to help in the minimisation of the fit and in the analysis, the first component was always assigned to the brightest of any multiple-components encountered (hereafter referred to as C1). Thus with the second Gaussian component (hereafter C2), no distinction is made as to what type of profile it represents. In some cases it was required to fit a broad underlying profile, in others it was required to fit the fainter component of a split line, and in some cases it was not required at all. The final number of components fitted to each line was determined using a combination of visual inspection and the χ^2 fit statistic. We emphasise that since our observations are of considerably lower spatial-resolution and cover a much wider range of environments than our GMOS data, the physical origin of the line components may not be the same as that which we previously found. We discuss this in Section 8.2.3.

A range of example Hα line profiles from various spaxels are shown in Fig. 8.24, together with the individual Gaussian fits required to model the integrated line-shapes. The top four profiles were chosen to illustrate the main types of Hα line-shapes encountered over the four fields; the majority are similar to the top two examples, being composed of single- or double-Gaussians (most being simply double-peaked, but a good proportion exhibiting the broad underlying component). In only five fibres do we find a clear triple profile in Hα, two of these being of the type shown in the centre-left panel of Fig. 8.24, and three being of the type shown in the centre-right. For clarity, we do not show the third component in any of the following maps. The bottom two panels show example profiles that are discussed below.

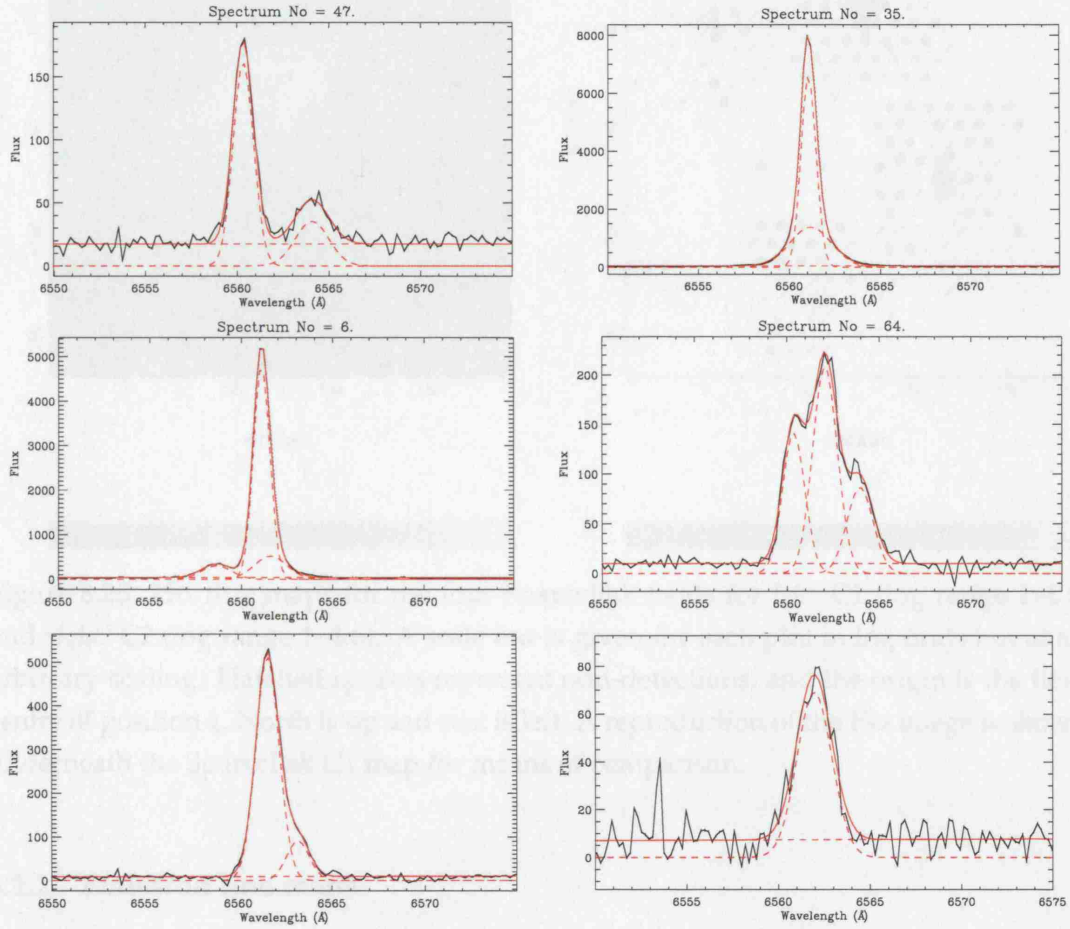

Figure 8.24: Example Hα line profiles chosen to represent the main types of profile shapes observed over the four fields (top four) and to aid explanation in the text (lower two). *Upper-left:* split line profile; *upper-right:* narrow, bright component with underlying, broad component; *centre-left:* split narrow profiles with underlying broad component (from N-E of position 4); *centre-right:* triple component line (from centre of shell B, position 2); *lower-left:* a spaxel from near the south-east of position 2 (30″ from SSC A) that does not show a broad underlying component, only two narrow components; *lower-right:* a low S/N line broadened by multiple unresolved components (from the north-west of position 2 on the edge of shell B). Observed data is shown by a solid black line, individual Gaussian fits by dashed red lines (including the straight-line continuum level fit), and the summed model profile in solid red. Flux units are arbitrary but on the same scale.

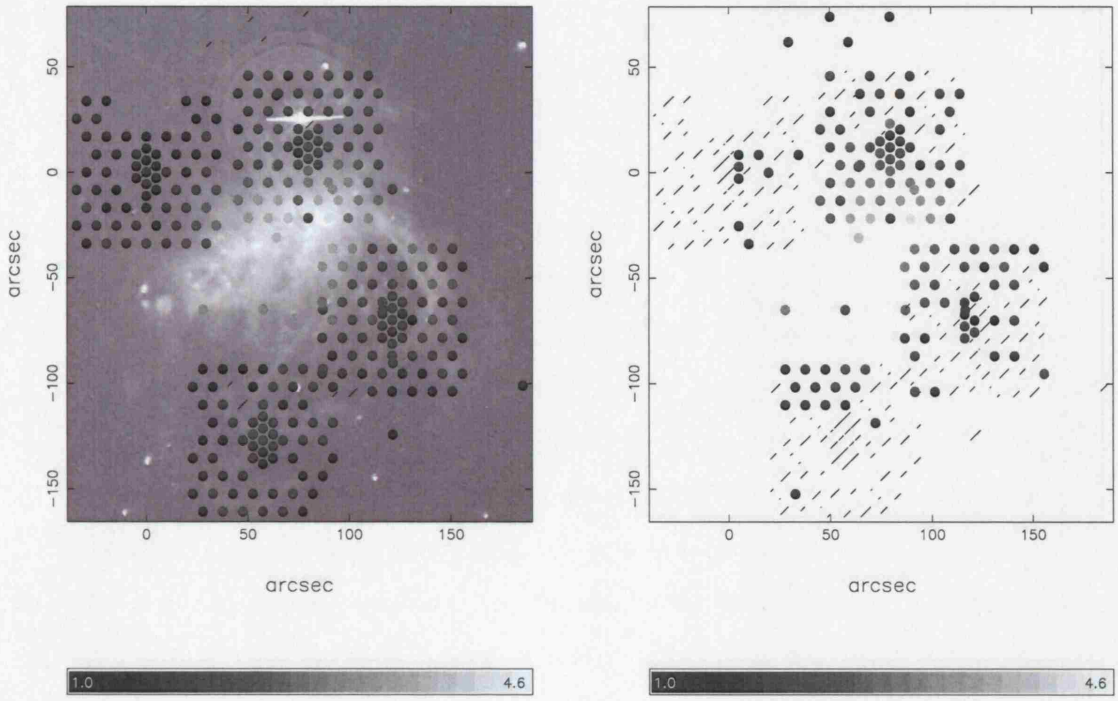

Figure 8.25: Hα flux maps for the four SparsePak fields for *left:* C1 (log range 1–4.6) and *right:* C2 (log range 1–4.6). A scale bar is given for each plot in log units but at an arbitrary scaling. Hatched spaxels represent non-detections, and the origin is the field centre of position 1. North is up and east is left. A reproduction of the Hα image is shown underneath the SparsePak C1 map for means of comparison.

8.2.2 Emission line maps

The spatial distribution of the properties of each Gaussian component were mapped using the visualisation tool, DAISY, in a similar fashion to the other IFU data-sets we have presented so far. Figs 8.25, 8.26 and 8.28 show the flux, FWHM and radial velocity maps of the Hα line for the four SparsePak positions, respectively. We detect Hα emission out to the extent of our spatial coverage – a maximum of 2.4 arcmins (1.5 kpc) away from SSC A.

Fig. 8.25 (left panel) shows the flux distribution of C1 (in log scale) seen by SparsePak, overlaid on the Hα image of Fig. 8.23 for comparison. It is clear that the two correspond very well, as would be expected. The corresponding flux distribution of C2, where detected, is shown in the right-hand panel of Fig. 8.25, and again matches the overall Hα brightness profile in a similar fashion to C1. An important quantity that we were able to derive in the GMOS data-set to give an estimation of the importance of the different components was the flux ratio of C2/C1. Unfortunately, the quality of this data-set is not

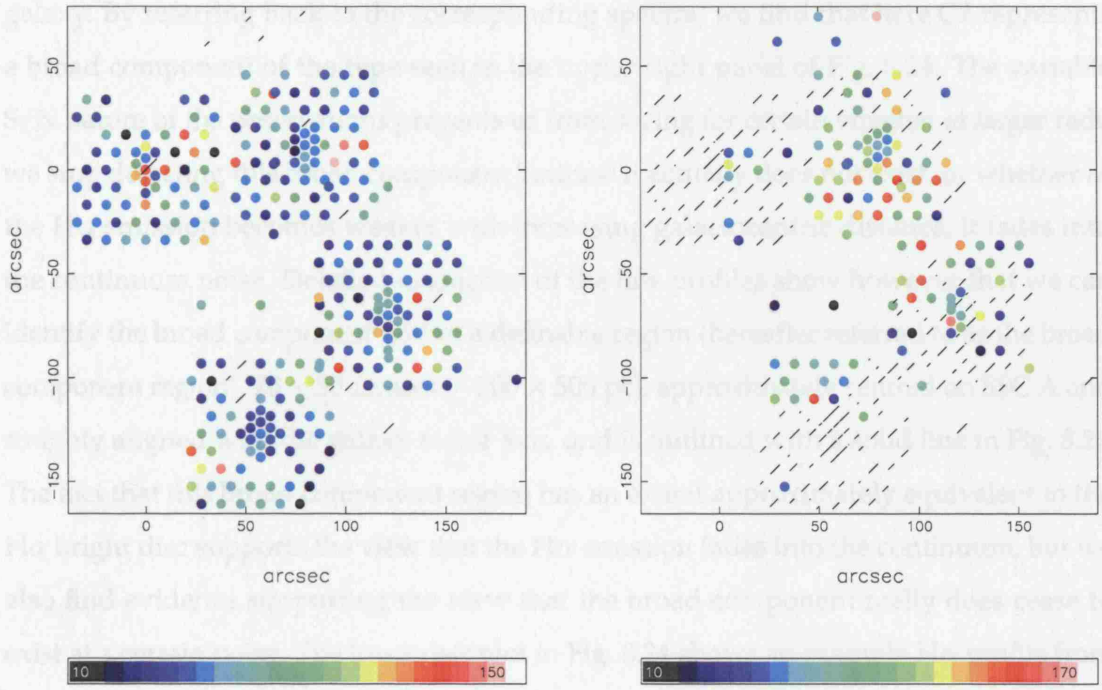

Figure 8.26: FWHM maps of the Hα line for the four SparsePak fields. *Left:* C1 (range 10–150) and *right:* C2 (range 10–170). A scale bar is given for each plot in km s^{-1} units corrected for instrumental broadening.

high enough to reveal any trends across the observed fields, only that the average ratio is $\sim 0.7 \pm 0.4$. This is considerably higher that that found in any of our GMOS IFU fields, and will be discussed in Section 8.2.3.

In Fig. 8.26, we plot the spatial variation of the FWHM of Hα. The line width of C1 (left-hand panel) remains fairly constant across the face of the galaxy, ranging over $\sim$20–70 km s^{-1} (corrected for instrumental contribution). In a number of places broad C1 lines are measured, but because these are almost all located adjacent or near to spaxels where multiple components are detected, these broad fits are likely to be caused by the convolution of many unresolved profiles. An example of a broad line from one of the outer-wind regions is shown in the lower-right panel of Fig. 8.24, illustrating how the low S/N has meant that only a single-Gaussian is required for a satisfactory fit to a profile that likely contains multiple kinematic components. The FWHM map for C2 is shown in the right-hand panel of Fig. 8.26. At large radii, where a second component is detected, it typically has a width similar to that of C1, and forms part of a classic split-line profile. The broadest lines (FWHM $\lesssim$ 160 km s^{-1}) are found within the central regions of the

galaxy. By referring back to the corresponding spectra, we find that here C2 represents a broad component of the type seen in the upper-right panel of Fig. 8.24. The variable S/N nature of the observations prevents us from saying for certain whether at larger radii we stop detecting this broad component because it actually does not exist, or whether as the Hα emission becomes weaker with increasing galactocentric distance, it fades into the continuum noise. Detailed inspection of the line profiles show however that we can identify the broad component within a definable region (hereafter referred to as the broad component region), 70×50 arcsecs ($\sim$700 $\times$ 500 pc), approximately centred on SSC A and roughly aligned with the galaxy major axis, and is outlined with a solid line in Fig. 8.27. The fact that this broad component region has an extent approximately equivalent to the Hα bright disc supports the view that the Hα emission fades into the continuum, but we also find evidence supporting the view that the broad component really does cease to exist at a certain point. The lower-left plot in Fig. 8.24 shows an example Hα profile from just outside this broad component region (distance from SSC A $\approx$ 330 pc), and clearly shows how it can be modelled with two Gaussians of similar narrow widths, with no requirement for a broad underlying component. Correspondingly, we find spaxels in a number of places just within the border of the outlined region with an equivalent S/N as the example shown, but clearly exhibiting the broad-line component. Therefore, although we cannot be completely certain, it appears that the broad line does physically cease to exist at the boundary of this region, rather than simply fading into the continuum noise. This has important consequences that we discuss below.

Fig. 8.28 shows the spatial variation of the Hα radial velocities. In general, the velocity of C1 (left-hand panel) appears consistent with the systemic velocity ($v_{\rm sys} = +80$ km s^{-1}), and remains fairly constant over the field, varying between -40 and +40 km s^{-1} relative to $v_{\rm sys}$. We do not find evidence for the east-west galactic rotation clearly seen in H I emission (Mühle *et al.* 2005). The C2 radial velocity map (Fig. 8.28, right panel) shows the velocity variation of the second Gaussian component. As described above, this is always the fainter of the two brightest components fitted, and either represents a broad underlying component or the other half of a split-line profile, depending on where the spaxel is located. Within the central $\sim$500 pc, inside the broad component region, the velocities measured are very similar to those found for C1. However, at larger radii, where C2 is the fainter component of any split-lines encountered, we see evidence for an ordered galactic wind outflow. In the north, the blueshifted component is stronger

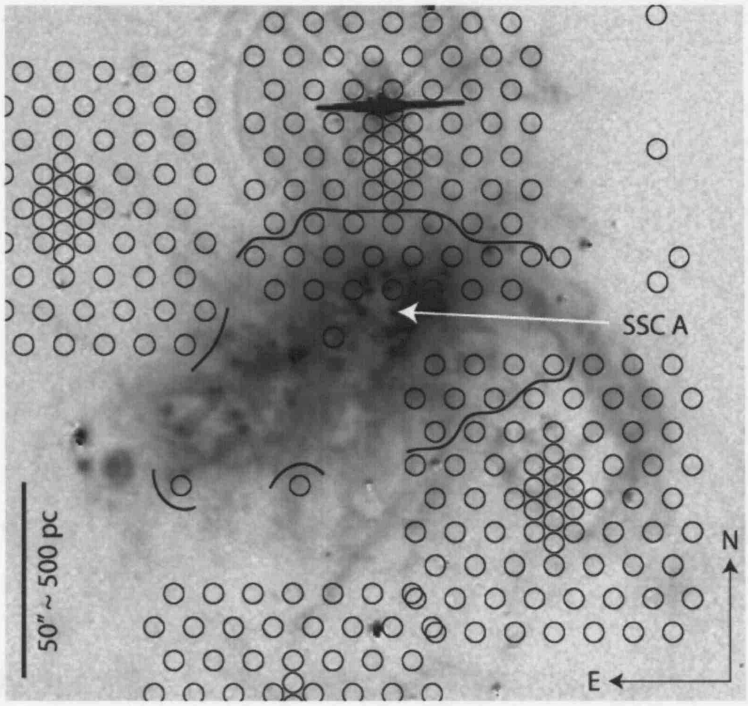

Figure 8.27: Spaxels with identifiable broad underlying Hα emission are all found within the solid line, shown here on this blow-up of Fig. 8.23.

(therefore in our convention assigned to C1), and has velocities ranging between -20 and 0 km s^{-1} (relative to $v_{\rm sys}$), whereas the redshifted component (C2) has velocities of up to +150 km s^{-1}. The maximum expansion velocity ($\sim$85 km s^{-1}; calculated as half the difference between the radial velocities of the two individual components) is found to the north-west of the polar axis corresponding to the centre of shell B, and agrees well with the measurements of Martin (1998). In the north-east, a small number of split-line detections are coincident with the position of shell E, implying expansion velocities of up to 50 km s^{-1}. In the south, the redshifted component is stronger (therefore assigned to C1) and exhibits velocities between 0 and +20 km s^{-1}. The blueshifted component (C2) has corresponding radial velocities of up to -160 km s^{-1}, giving a peak expansion velocity of 90 km s^{-1} to the south-west of SSC A, coincident with the centre of shell A (also agreeing well with the velocities quoted in Martin 1998). Blueshifted C2 velocities of -50 to -75 km s^{-1} are also seen in the northern half of position 3 coincident with shell F, implying expansion velocities of up to 100 km s^{-1}.

In three spaxels in position 2 (numbers 64, 73 and 76), coinciding with the centre and western edge of shell B, we detect three distinct Hα line components similar to the

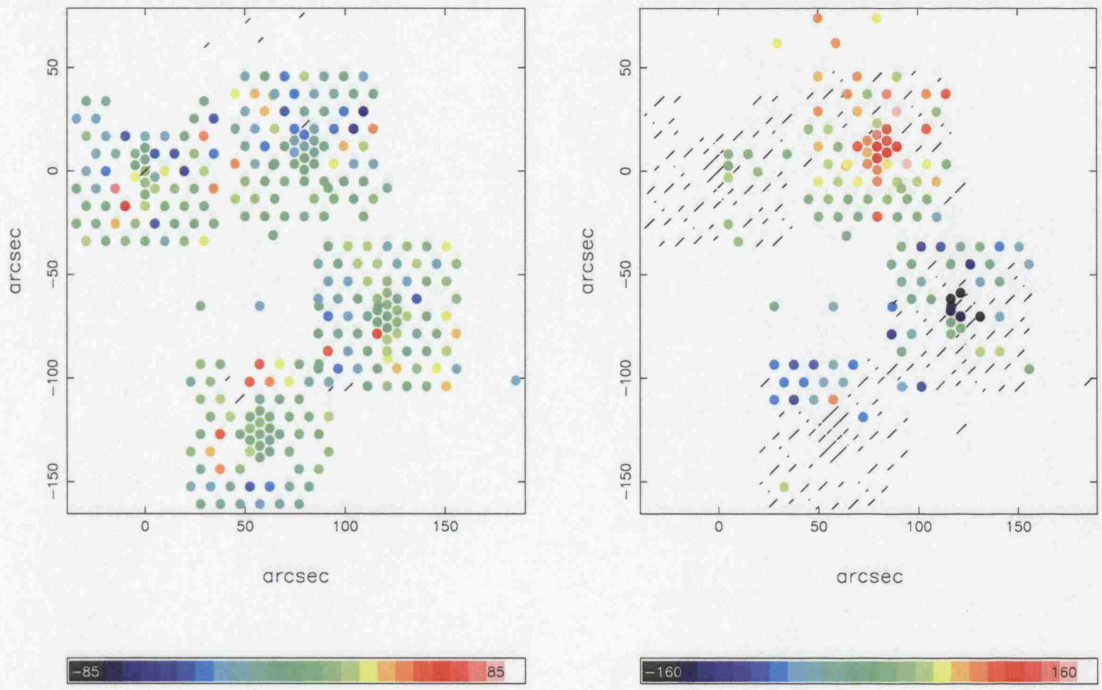

Figure 8.28: Radial velocity maps of the Hα line for the four SparsePak fields. *Left:* C1 (range −85 to +85) and *right:* C2 (range −160 to 160). A scale bar is given for each plot in heliocentric km s^{-1} units (with respect to $v_{\rm sys}$).

example shown in the lower-left panel of Fig. 8.24. The 'extra' component, with respect to the neighbouring double-component lines, lies at a velocity close $v_{\rm sys}$, so could represent quiescent halo gas or be associated with part of an as yet undetected shell.

The consistent reversal of strengths of the two major components of the split line from the north to south agrees well with previous studies (Heckman *et al.* 1995; Martin 1998), and demonstrates there is a definite preferred outflow direction in both the northern and the southern hemispheres. This strengthens the hypothesis that the actual axis of the NGC 1569 galactic outflow may be inclined to the observer (Stil & Israel 2002), rather than simply that the shells are randomly expanding out of the disc along paths of least resistance.

Electron Density

Fig. 8.29 shows a map of the electron density as derived from the flux ratio of the [S II] doublet, assuming $T_{\rm e} = 10^4$ K. [S II] emission is detected in all spaxels that also have bright Hα emission, but often the λ6717/λ6731 flux ratios measured imply a density below the

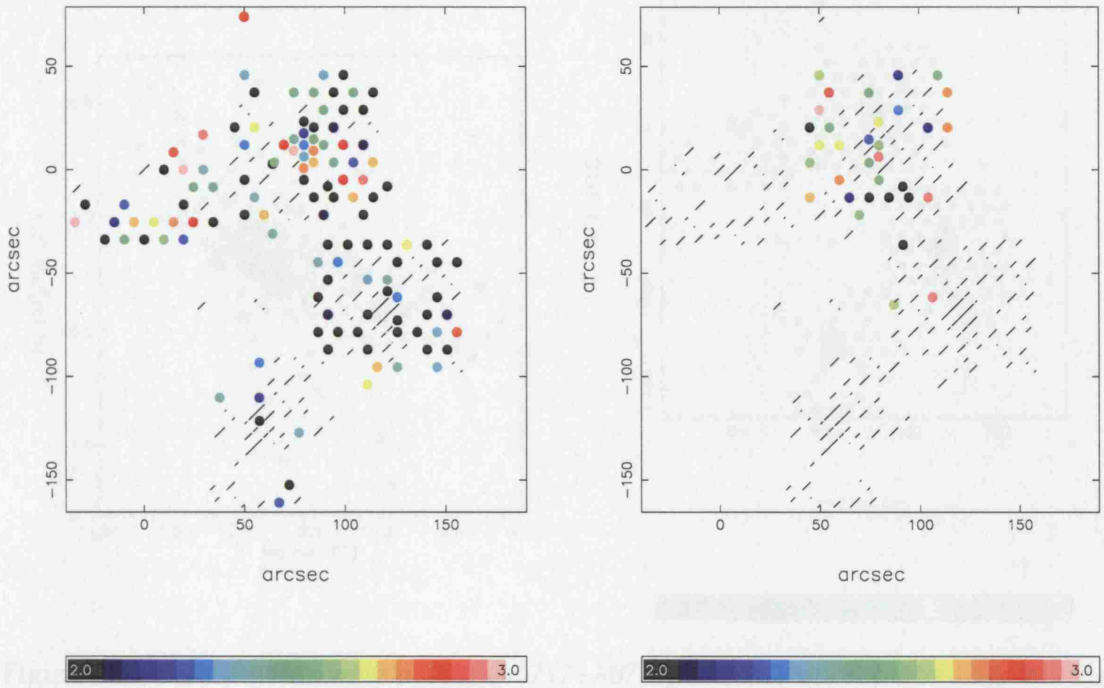

Figure 8.29: Spatial distribution of electron density (in units of log cm^{-3}) for the four SparsePak fields for *left:* C1 (range 2–3) and *right:* C2 (range 2–3), calculated from the flux ratio of the [S II] doublet. The colour map used is shown beneath each plot and ranges upwards from the low density limit of this indicator (∼100 cm^{-3}; Osterbrock 1989).

low density limit (∼100 cm^{-3}; Osterbrock 1989). Hence, we have set the minimum value of the colour map to 100 cm^{-3}, meaning that spaxels where [S II]$\lambda\lambda$6717,6731 emission was detected but imply densities below the low density limit are shown as black, whereas spaxels where [S II] is not detected or where an unphysical flux ratio is measured (resulting easily from the large errors) are represented by hatched lines.

The majority of the ionized gas in the outer-wind region is at or below the low density limit, as expected for a fast-moving expanding flow. Some regions in shell B (position 2) and shell E (position 1) exhibit measurable densities in C1 (left-hand panel) of order 500 cm^{-3}. In parts of position 2, and a few spaxels in position 4, we are able to detect two line components and measure the electron densities of both to be of the order ∼500 ± 300 cm^{-3}. The multi-component nature of the lines and the variable S/N have meant that the associated uncertainties on the measurements are quite high.

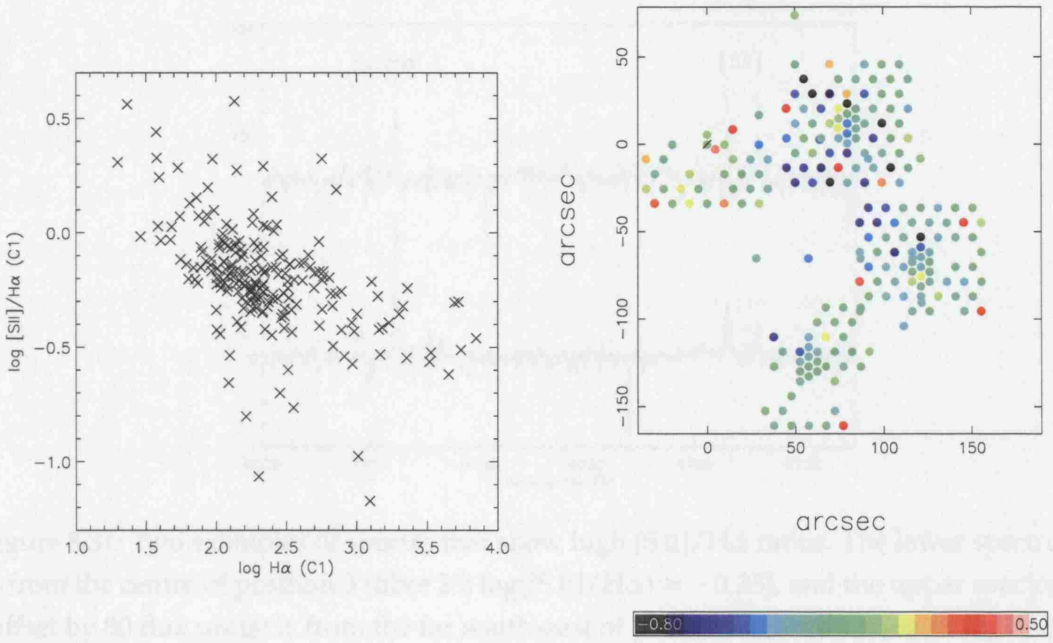

Figure 8.30: *Left:* the flux ratio of [S II](λ6717+λ6731)/Hα (C1 only) plotted against the flux of Hα C1; *right:* the spatial distribution of the [S II]/Hα ratio for the four SparsePak fields (C1 only; log range -0.8 to 0.5).

Nebular diagnostics

The flux ratio of [S II](λ6717+λ6731)/Hα can be used as an indicator of the ionization strength of the radiation field, and, as we have seen earlier in this chapter, can be used in conjunction with the [O III]λ5007/Hβ ratio to ascertain whether the gas has a shock-excited component. However, the instrument set-up chosen for these observations did not give us access to the [O III] and Hβ lines, so we can only infer approximate trends in the ionization field strength from the [S II]/Hα ratio. Another indicator commonly used is the ratio of [N II]λ6583/Hα, but the strength of [N II] is very weak compared to Hα (of order 2–5 per cent; Heckman *et al.* 1995) so could not be reliably measured in enough spaxels to determine any trends.

Fig. 8.30 shows both a graphical representation (left panel) and a spatial map (right-panel) of the [S II]/Hα ratios. The left-hand plot shows that the majority of spaxels have a log([S II]/Hα) ≈ -0.5 to 0, and that the highest ratios are generally associated with the faintest Hα flux whereas the lowest ratios are found where the Hα flux is highest. Moreover, the right-hand map shows this trend is associated with galactocentric distance, where log([S II]/Hα) increases from ~ -1 in the spaxels nearest SSC A, to >0 towards the

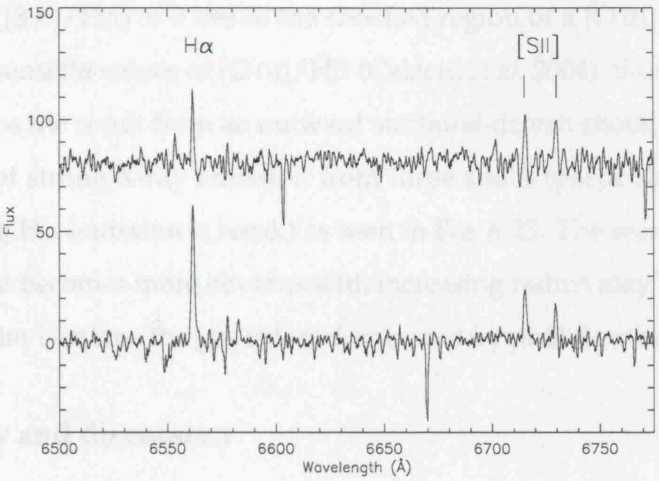

Figure 8.31: Two examples of spectra that show high [S II]/Hα ratios. The lower spectrum is from the centre of position 3 (fibre 25; log([S II]/Hα) ≈ -0.25), and the upper spectrum (offset by 80 flux units) is from the far south-east of position 1 (fibre 12; log([S II]/Hα) $\approx$ 0.20). Both are smoothed by 5 Å, and shown on an arbitrary but relative flux scale.

outer edges of the fields, up to 2.4 arcmins from SSC A.

These trends agree well with the measurements of Heckman *et al.* (1995), who mapped the [S II]/Hα ratio out to $\sim\pm 50''$ from SSC A using two perpendicular slits (see Fig. 5.2), except that they found values of log([S II]/Hα) ≈ -1.2 at the location of SSC A, increasing to ~ -0.5 at $\pm 50''$. In that paper, Heckman *et al.* did not mention whether or not they fit the [S II] lines with multiple Gaussians, so we cannot know whether they measured the flux ratio of the integrated line-flux, or that of just the brightest component. If the former was true, then a significant part of the discrepancy could arise from the varying contribution from the different line components. Furthermore, most of the central region covered by their slits is not well sampled by our SparsePak fibres, and we may easily have missed the very low ratios they find in the inner $20''$ or so. An additional factor is the decreasing S/N of the [S II] lines with increasing radius. Poorly determined [S II] fluxes are likely to be the cause of much of the scatter at low Hα intensities seen in Fig. 8.30 (left), but from close inspection of the actual data, there is no doubt that high ratios do exist. In Fig. 8.31 we plot two example spectra from the outer-wind regions illustrating high [S II]/Hα ratios. The upper spectrum has a [S II]/Hα ratio representative of the whole south-east of position 1 (shell E), where most of the highest ratios are found. However, high ratios are also found clustered in the centre of position 2 (shell B) and position 4 (shell

A). A ratio of $\log([\mathrm{S\,II}]/\mathrm{H}\alpha) > 0$ lies in the shocked region of a $[\mathrm{O\,III}]/\mathrm{H}\beta$ *vs.* $[\mathrm{S\,II}]/\mathrm{H}\alpha$ diagram, for any sensible values of $[\mathrm{O\,III}]/\mathrm{H}\beta$ (Calzetti *et al.* 2004), thus indicating that at least shell E may be the result from an outward starburst-driven shock. This is supported by the detection of strong X-ray emission from these shells (particularly shell E where the corresponding $\mathrm{H}\alpha$ emission is weak) as seen in Fig. 8.23. The reason why the shock excited component becomes more obvious with increasing radius may be because further from the central star clusters, the gas is less dominated by photoionization.

8.2.3 Summary and discussion

We have presented SparsePak "formatted field unit" data covering the outer galactic wind flow in NGC 1569 in four pointings with integration times of 4–4.5 hours per field. The large-scale coverage of these observations contrast with the small-scale, high-resolution GMOS data presented in the preceding sections: one SparsePak fibre is approximately the same diameter as the whole GMOS IFU, and each is separated by ∼100 pc, more than the average distance between our GMOS fields. The large diameter of the SparsePak fibres makes this instrument ideal for probing the faint ionized gas found in the haloes of galaxies. This light-collecting power allowed us to choose a high-resolution spectrograph set-up, enabling us to characterise the line profile shapes of the important nebular diagnostic lines of $\mathrm{H}\alpha$ and [S II] to an accuracy limited only by the S/N achieved. In general we find the emission-line profiles to be composed of a bright, narrow component with an underlying, broad component (FWHM $\lesssim 150\ \mathrm{km\,s^{-1}}$) within a distinct region, $\sim 700 \times 500$ pc in size, roughly centred on the location of SSC A. At larger radii, the profile shape is generally double-peaked, showing characteristics of shell expansion.

In Chapter 7 and the first half of this chapter, we discussed in detail the possible mechanisms that could produce the broad component we observe only in the central regions of the galaxy. We concluded that the most likely explanation is the turbulent velocity field resulting from the ablation/evaporation of gas from cloud surfaces through the action of the strong cluster winds. However these SparsePak observations are of considerably lower spatial-resolution, and cover a much wider range of environments than the data from which we derived these conclusions, meaning that the physical origin of the line components may not necessarily be the same.

An important indicator of the importance of the second component is the flux ratio of C2/C1. We have already mentioned that the quality of the data is not high enough

to identify any trends in this value across the observed fields, but the reason why we find such a high average value ($\sim$0.7) compared to our GMOS data deserves some attention. For all cases where C2 is one half of a split-line profile, C2/C1 should always be <1, since in our assignment convention C1 is by definition the brighter of the two components. Furthermore, since the intensity of the two profiles is similar (within an order of magnitude), a high C2/C1 ratio is understandable. A C2/C1 ratio of $\sim$0.2–0.7 is also representative of SparsePak spaxels within the broad component region, where from our GMOS observations of the gas immediately surrounding SSC A, C2/C1 never rises above 0.3. This is one indication that the physical origin of the two components may be different in this situation. In light of this, we re-examined a number of Hα profiles in the SparsePak spaxels closest to SSC A and our GMOS IFU fields, and found that a subtle extra component had been overlooked in some of these cases. Fig. 8.32 shows the Hα profile from fibre 50 of SparsePak position 2, and is the most obvious example of how, after close inspection, a three-component fit is found to be more appropriate (right panel) than the original, automatically determined double-Gaussian fit (shown in the left panel). The residuals shown below each plot clearly demonstrate the improvement in fit quality, even though the formal χ^2 improvement is not statistically significant. The effect of changing C2 of the double-Gaussian fit to C2 of the triple-Gaussian fit (now correctly assigned to a broad underlying component) is to increase its FWHM by 50 km s^{-1} to $\sim$150 km s^{-1}, and to decrease the C2/C1 flux ratio from 0.69 to 0.17 in this particular case, which is now in much better agreement with that found from the GMOS IFU fields. This mis-fitting also offers an explanation for why the widths of C2 near SSC A measured from our SparsePak data are much less than the average values measured from our GMOS observations.

Unfortunately, this kind of detailed fitting can only be done for the highest S/N spectra found near the centre of NGC 1569, so cannot be used reliably to track the C2/C1 ratio over the full extent of the broad component region. Where the S/N is lower, it is possible that one (or more) unresolved components, faint enough not to affect the fit to the bright C1, but strong enough to add a small amount of flux to the C2 fit, is the culprit of the high C2/C1 flux ratios.

Now that we have established that the properties of the broad line seen with SparsePak in the regions near to SSC A are in fact very similar to that found with our GMOS IFU data (after our more careful fitting), we can confidently associate this component with C2 from our GMOS data. However, the low spatial-resolution of SparsePak introduces a

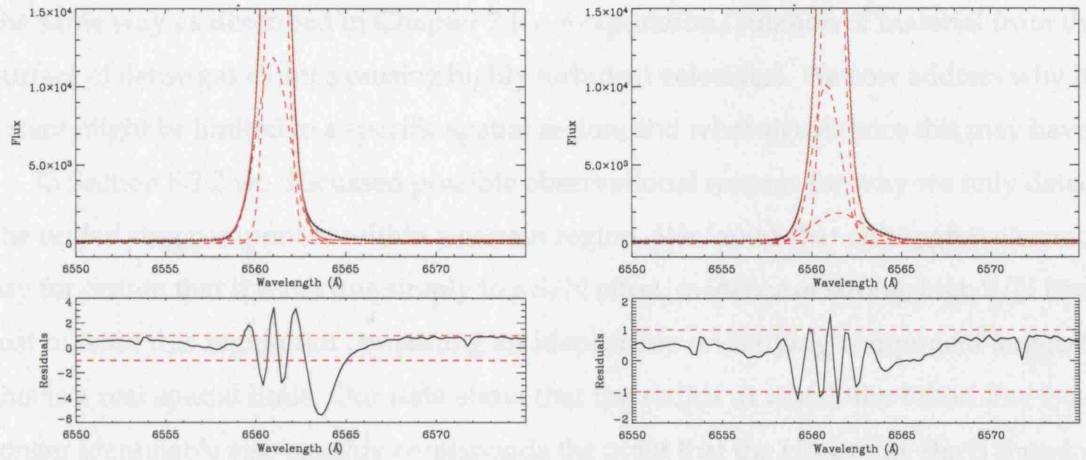

Figure 8.32: Hα profile from fibre 50 of SparsePak position 2, illustrating how a more careful modelling of the line profile reveals that a three-component fit (*right panel*) characterises the integrated shape more accurately than the automatically determined double-Gaussian fit (*left panel*). The addition of a third component and the correct assignment of the profiles results in the FWHM of C2 increasing from 100 to 153 km s^{-1} and the C2/C1 ratio changing from 0.69 to 0.17, now in much better agreement with the GMOS data for the same region. Observed data is shown by a solid black line, individual Gaussian fits by dashed red lines (including the straight line continuum level fit), and the summed model profile in solid red. Flux units are arbitrary but on the same scale. The fit residuals are shown below the spectrum in both cases.

greater degree of uncertainty in the level of contribution to the line width from unresolved kinematical components. As we have mentioned, one SparsePak fibre covers a similar area to the whole GMOS IFU FoV, and for example, we found C2 to have a velocity difference of >90 km s^{-1} in just one GMOS field (Section 8.1). The large size of the SparsePak fibres therefore makes the possibility of including multiple unresolved line-of-sight velocity components inevitable, and we must accept that all our FWHM measurements will include a certain contribution arising from this effect. However, the fact that we find C2 to have such a smooth and continuous distribution across the whole central region implies that unresolved components cannot contribute significantly to the width, and our high spectral-resolution has meant that whenever a sufficiently bright additional component does exist we were are able to confidently identify and fit it (exemplified by the few triple-Gaussian profiles found near the edge of the broad component region). We therefore conclude that in light of the underlying component's clear identification in the high-resolution GMOS IFU data, and its very similar properties found in near-by SparsePak fibres, it originates in

the same way as described in Chapter 7 (*i.e.* evaporation/ablation of material from the surface of dense gas clumps causing highly turbulent velocities). We now address why its extent might be limited to a specific spatial region, and what significance this may have.

In Section 8.2.2 we discussed possible observational reasons for why we only detect the underlying component within a certain region. We found that although we cannot say for certain that it is not due simply to a S/N effect, evidence of strong, high S/N lines just outside this region not containing an identifiable underlying component suggests this is a real spatial limit. Our data show that the radius at which the broad line is no longer identifiable also roughly corresponds the point that the Hα profile starts showing a secondary narrow kinematic component, indicating that this limit may represent an important point in the evolution of the galactic wind. We speculate that this radius marks the point where ordered expansion begins to dominate over turbulent motion, and may correspond to the sonic point (also referred to as the critical point), where the velocity of the outflows pass from the subsonic to supersonic regime. This possibly significant result warrants detailed further investigation at higher spatial resolution and S/N to better determine if this is the location of the critical point, and how this point in the flow is related to the existence of the broad component.

We now turn our attention to the narrow lines found in almost every spaxel over the combined FoV. At large radii we find two narrow components, each representing two halves of a split-line profile, and through measuring the velocity of both we have detected the previously catalogued supershells A, B, E and F (Martin 1998). We confirm the published expansion velocity, $v_{\rm exp}$ (calculated from the difference in the radial velocities between the two split-line components), of shells A and B, and derive new measurements for shells E and F of $v_{\rm exp} \sim 50$ km s^{-1} and $\lesssim$100 km s^{-1}, respectively. Martin (1998) interprets the fact that the velocity separation of the two line-components in shell A are still increasing when the fainter side fades below her detection limit as evidence that this bubble may have ruptured. However, our deeper observations show that this may not be the case, since we measure decreasing velocity separations in both shells A and B at the very edge of our combined FoV. In shell A, the expansion velocity peaks $\sim$330 pc south of SSC A, then begins to decrease until we can no longer detect Hα emission. In shell B, the expansion velocity peaks $\sim$375 pc north of SSC A, and our measurements are again consistent with a decrease in $v_{\rm exp}$ up to the edge of our FoV at distances of >500 pc (although the S/N at these radii is obviously quite low).

These conclusions do not, however, mean the fact that the shells may blow-out in the future. The best estimates for the escape speed in NGC 1569 are ~75–100 km s^{-1} (Martin 1998), implying that the Hα emitting gas in the shells is marginally bound at best. The fast-flowing, hot X-ray emitting phase cannot therefore be bound at all to the gravitational potential of NGC 1569.

The consistent reversal of strengths of the blue and red components in the northern and southern supershells provides evidence of a preferred outflow direction and thus a flattened gas distribution to the gas disc, but does this mean that we are observing a bi-polar M82-type outflow? The discreet nature of the supershells identified by Martin (1998) and the correspondence of soft X-ray emission with the individual shells, indicates that what has been previously interpreted as a galactic-scale wind may be more simply a collection of supershells blown out along paths of least resistance in the halo. In this interpretation, the outflow could be likened to a series of cannon bursts, where each explosive event (possibly the formation of a SSC or a collection of SSCs) has produced one of the expanding bubbles we observe today.

We see no evidence of east-west galactic rotation in either C1 or C2, but a careful comparison of the particular regions covered by our SparsePak pointings to the H I velocity map Mühle *et al.* (2005, their fig. 4), shows that in fact most of the equivalent H I gas is either consistent with being at $v_{\rm sys}$ or very disturbed with no systematic pattern. Moreover, no clear evidence for galactic rotation of the ionized gas is observed in either of the slits analysed by Heckman *et al.* (1995). It is likely therefore that any signature of rotation is either masked by the disturbed, strongly disrupted velocity field, or dominated by the effects of large-scale shell expansion.

In addition to characterising the Hα line profile, we have also measured [S II] derived electron densities, and an indication for the ionization field strength from the flux ratio of [S II]/Hα over the four fields. We find that much of the ionized gas in the broad component region and in the outer-wind regions is at or below the low density limit. Unfortunately the S/N of the [S II] lines was not high enough to determine any other definite trends, except that parts of shell B and E have higher densities in C1 of order a few hundred cm^{-3}, and that similar densities in C2 (here representing the far wall of the expanding bubble) are also observed in shell B.

The flux ratio of [S II]$\lambda\lambda$6717,6731/Hα suffers less from low S/N since it includes the combined flux from both lines of the [S II] doublet. We find the highest ratios are associated

with the faintest Hα flux and the largest galactocentric distances, whereas the lowest ratios are found nearest to SSC A in the galaxy centre. Although this trend agrees with previous measurements (Heckman *et al.* 1995), it begins and ends at considerably higher values. We find that the most likely explanation for this discrepancy is that previous studies have not decomposed the line profiles as accurately as was done here. The highest ratios ($\log([\mathrm{S\,II}]/\mathrm{H}\alpha) > 0$) are found in the south-east of position 1 corresponding to shell E, and in the centre of position 2 (shell B) and position 4 (shell A), indicating that in these shells the gas emission may be partly shock-excited. We cannot be surer than this since we are missing other key shock diagnostics such as [O III]/Hβ. Shocks are certainly expected in the outflow, since the hot superbubble will be expanding into preexisting H I gas and/or other halo material, which is effectively at rest with respect to the fast moving gas. The existence of shocks is also supported by the detection of strong X-ray emission associated with the main shells (Fig. 8.23; Martin *et al.* 2002).

8.3 Links between the small- and large-scales

One of the aims of this study was to attempt to identify any links between the small-scale GMOS observations of the inner-wind and the SparsePak observations of the halo environment. Fig. 8.33 shows the *HST* Hα image of Fig. 8.1 with the positions of the four GMOS IFU fields marked, together with the nearest SparsePak fibres from positions 1, 2 and 4. The large difference in scale between the two sets of observations becomes immediately clear: each GMOS IFU field covers an equivalent area as one SparsePak fibre, meaning that we can only compare the average properties for each GMOS field to the adjacent SparsePak fibres.

We find the average values to be broadly consistent between the two data-sets, but since the gas properties vary widely and rapidly down to our resolution limit of just one GMOS IFU field, a detailed comparison of the dynamics is futile. Furthermore the motions of the gas in these central regions are predicted to be highly turbulent, with only a very small net flow outwards, implying that a comparison would be meaningless anyway. We do find, however, that the FWHM of C1 is reasonably uniform within the broad component region, and is on average only just larger than FWHM_0 measured from our GMOS IFU fields. This provides evidence that the ISM within the whole Hα-bright disc is equally disturbed, and has been highly influenced on a global scale by the stirring

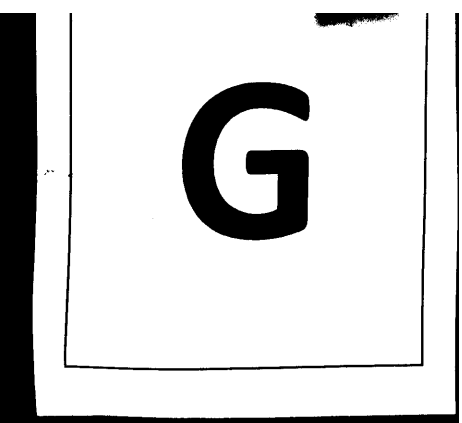
G

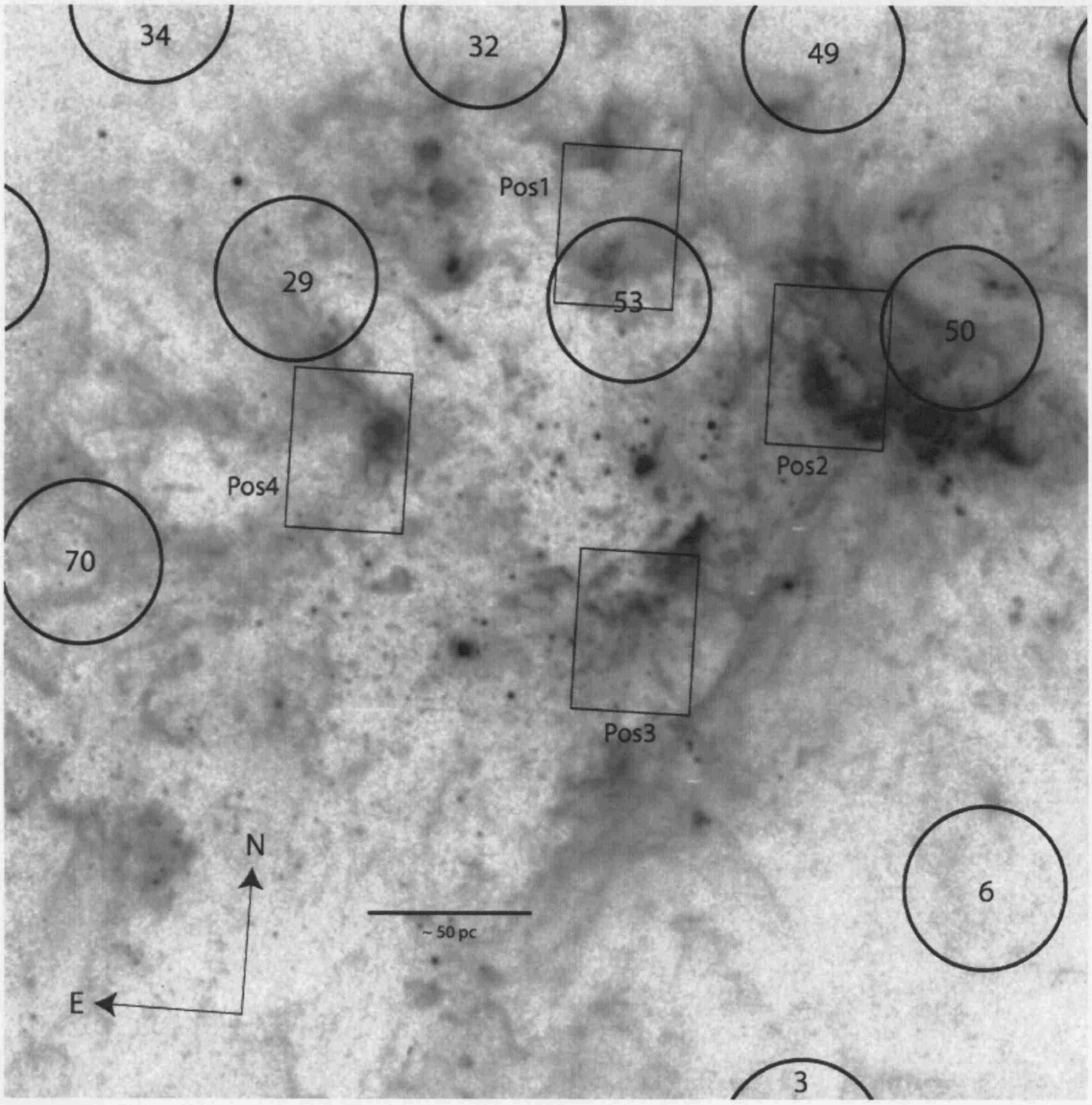

Figure 8.33: *HST* F656N image showing the whole central region of NGC 1569 with the positions of the four GMOS IFU fields and the nearest SparsePak fibres overlaid.

effects of the recent starburst.

A careful re-analysis of the Hα profiles in fibres 6 and 7 of position 4 (in the far south-western corner of Fig. 8.33) reveals very faint, high velocity (-110 to -160 km s^{-1}) blueshifted emission that was not identified with the original automatic fitting. The velocities are consistent with being part of near-side of shell C catalogued by Martin (1998), or with the beginnings of shell A extending out to the south-west. Beyond these two fibres, the high-velocity component is no longer identifiable, supporting the association with shell C rather than A.

CHAPTER 9

DISCUSSION AND CONCLUSIONS

Galactic-scale starburst-driven outflows are one of the most important evolutionary mechanisms of galaxies, and their correct interpretation has far-reaching consequences for both galaxy formation and cosmological models. Their truly multiphase nature, and the fact that they exhibit complexity on every scale, makes understanding them a difficult and time-consuming task. Furthermore, the connection between the emission or absorption lines through which we actually observe galactic winds (GWs) and the mechanisms through which they form are often unclear or ambiguous. We have seen that the hot, fast-flowing wind fluid itself is almost impossible to observe at any wavelength due to its low density and high temperature, so we are forced to observe the system at lower energies, where the wind can only be traced indirectly through its interaction with denser material.

The importance of studying winds in the local Universe where they can be easily resolved, also has ramifications for our understanding of high-redshift systems. As mentioned in Chapter 1, powerful winds are observed in many Lyman-break galaxies at $z > 1$, and if we are to understand their role in the evolution of the Universe (including re-ionization and IGM enrichment), then we must first know how feedback from star-formation occurs and develops locally.

In this thesis, we have presented and described the results of two intensive, multi-faceted, optical observing campaigns aimed at characterising the properties of the ionized gas in the starburst galaxies M82 and NGC 1569, two of the closest galaxies with large-scale GWs. Our goals were to further our understanding of how GWs are formed and driven,

where the material is accelerated, how they interact with their surroundings, and how they evolve to be what we see at large-scales.

M82 is the most extreme example of a starburst in the local Universe. The combination of a large gas reservoir and a nuclear bar to channel this material into the centre, has resulted in the rapid build-up of a very large number of massive star clusters packed into small, dense clumps that in turn, drive a powerful, bright and well collimated superwind to distances of many kiloparsecs. In contrast, the physical conditions of the NGC 1569 GW are driven by only a handful of massive star clusters, and the outflow is instead formed of multiple supershells that have expanded into the halo along paths of least-resistance, with only a hint of a preferred outflow direction.

The work of this thesis can be divided into three main themes. In the following sections we discuss the main themes of this thesis and the most important issues connected with each, followed by how they could be addressed further in future research.

9.1 Main themes

This section is split into three subsections, each focussing on one of the main themes of this thesis. In discussing each, we recapitulate our main conclusions without going into too much detail, and highlight a number of key outstanding issues that deserve further thought, investigation and observation. These are listed in bullet-points at the beginning of each subsection.

9.1.1 Star clusters as the driving sources of galactic winds

Key Issues:

- **The effects of the ISM densities on cluster evolution**
- **The spatial density and number of clusters**
- **The effects of metallicity on wind strength and evolution**
- **The interaction of winds between individual star clusters**

Young, massive star clusters are interesting in their own right in many ways (as discussed in Chapter 1). However, in this thesis we have primarily been concerned with the formation and evolution of GWs, and in order to realistically model the evolution of a superwind, we must know the fundamental parameters of the discrete sources (the star clusters) that drive it as accurately as possible. For this reason, we have focussed our

work on star clusters accordingly, and interpreted their fundamental properties (mass, age, size, mass function, metallicity, and spatial relationship – *i.e.* separations, clumping) in the context of GWs.

In this thesis, we have studied two such clusters in detail, M82-A1 and NGC 1569-10, both at either end of the cluster mass-scale and in two quite disparate systems, and have derived new estimates of some of the aforementioned parameters. However, the most striking result stems from the environmental differences between the media surrounding the clusters, and manifests itself most strongly through its effect on the clusters' ionized envelopes: at ~6.4 Myr, M82-A1 has a compact, high-density H II region, whilst NGC 1569-10, with an age of 5–7 Myr, seems to have already been able to blow away its natal gas cloud. This important finding provides clear evidence that the ambient density of the ISM must play a critical role in determining the evolution of clusters and hence the overall starburst. This result warrants a great deal more thought and investigation. How can the high gas densities in the cores of starburst clumps such as found in M82 be reconciled with the production of free-flowing cluster winds and hence a powerful superwind? Could the high interstellar densities somehow act to enhance the superwind much like a constricting pipe does to a gas flow?

9.1.2 Characterising the state of ionized ISM in starburst regions

Key Issues:

- **The consistent lower-limit to the width of the narrow component of the nebular emission lines**
- **The underlying broad component and its relation to mass-loading**
- **The energy injection zone and sonic point of the outflow**

One of the central aims of this thesis was to investigate the state of the ionized gas in starburst regions. We have used high-resolution narrow-band imaging, long-slit spectra and integral field spectra to investigate the optically emitting gas dynamics and energetics in M82 and NGC 1569. In general, we found the nebular emission-line profiles to be composed of a bright, narrow component with a fainter, very broad underlying component. We have mapped the properties of the individual components of the bright Hα line in particular, over the central regions of both galaxies, and our study of the relationship between the components has led us to investigate the mechanisms that might result in

the observed line broadening. Most significantly, we have proposed a new model for explaining the origin of the underlying broad lines.

We find that the narrow line most likely represents the turbulent ISM gas that has been stirred-up by the effects of the starburst. Although this stirring has resulted in a characteristic minimum line-width that applies across the whole central regions of the galaxy, an additional contribution to its width must inevitably come from the inclusion of multiple unresolved kinematic components along the line-of-sight as every observation is always limited to a finite spatial- and spectral-resolution. Our detailed investigations have led us to propose that the broad line results from a much stronger turbulent velocity field created as the hot, fast-flowing winds from the surrounding star cluster(s) flow past the surface of cool, dense gas clouds embedded in the ISM. This sets up a turbulent mixing layer at the interface region, and material begins to be thermally evaporated and/or mechanically ablated from the clump, resulting in the eventual dissolution of the cloud. In this model, the broad line is being emitted by material being entrained into the wind flow, hence it should be possible to trace the inner regions of superwinds *in the optical* by using the broad component as a proximate indicator.

Our study of the origin of the broad component engenders yet more questions: can the broad component truly be modelled using a Gaussian profile? Some studies find a non-Gaussian shape for the underlying emission (*e.g.* Mendez & Esteban 1997) whilst others maintain that it can be modelled satisfactorily using a single Gaussian profile (González-Delgado *et al.* 1994; Homeier & Gallagher 1999; this work). Why is this component sometimes only seen in recombination-lines and not forbidden-lines (*e.g.* Izotov *et al.* 1996)? Since "integrated emission line profile widths can result from very different physical processes, all of which are likely to act simultaneously with different weights according to the evolutionary status or history of region" (Melnick *et al.* 1999), can we determine which broadening mechanism(s) are likely to dominate in particular environments? When do the contribution from SNRs become significant? Can we disentangle the effects of photoevaporation, thermal evaporation, turbulent mixing, and mechanical ablation in high-energy starburst systems where the situation is intrinsically more complex than in near-by Galactic systems?

The ubiquitous presence of an underlying broad component in the starburst regions studied is an intriguing result, and its accurate characterisation has been one of the most important aspects of this thesis. In NGC 1569, we have seen how the extent of the

broad-line region may be correlated with the edge of the energy injection zone and the location of the sonic point. Does the sonic point represent the location at which random turbulent gas motions begin to form an ordered, directed flow? In M82, the conditions in the wind change rapidly around the points of infection in the minor-axis radial velocity measurements, which have led to the conclusion that this location corresponds to the sonic point (McKeith *et al.* 1995; Shopbell & Bland-Hawthorn 1998; Greve 2004). However, we have yet to determine how this is related to or controlled by the conditions within the starburst. We have tentative evidence from our DensePak observations of the M82 disc that the width of the broad component gets larger near the proposed sonic point. How, then, are the gas velocities related to the line widths at this point?

9.1.3 Characterising the small- and large-scale wind morphologies

Key Issues:

- **The large-scale distribution of halo material (including dust)**
- **Wind collimation mechanisms and their relationship to the energy injection zone**
- **The accurate modelling of wind outflows**

A significant proportion of this thesis has been devoted to describing and classifying the optical morphology of wind outflows, and making comparisons to multi-wavelength observations. Our data have covered a large range in spatial-scales and resolutions, from 0.05 arcsec-resolution *HST* imaging, to 0.8 arcsec-resolution IFU spectroscopy of discrete 5×3.5 arcsec regions, to overlapping 27×43 arcsec IFU fields, to contiguous formatted-field-unit observations covering a total of $\sim 3.5 \times 4$ arcmins, to mosaicked ground-based images covering $\sim 8 \times 5$ arcmins. This has given us tremendous scope to investigate the phenomenon of GWs and attempt to make links between the small-scale details and the large-scale characteristics.

Through the combination of deep, ground-based imaging, and high-resolution *HST* data, we have been able to, for the first time, track large-scale structures in the M82 wind back to individual features in the inner-flow, and to individual starburst clumps and star clusters in the galaxy centre. The medium spatial-resolution WIYN/DensePak observations of the M82 disc have proved critical in connecting the long-slit *HST*/STIS measurements to the larger-scale wind morphology, by providing high spectral-resolution over a large two-dimensional area. Following on from this detailed analysis, we have

been able to both independently develop and extend previously published models of the physical state within M82's starburst clumps and the distribution of these clumps within the galaxy. Our observations support the existence of a stellar bar with an inner Lindblad resonance, which seems to have significantly affected the evolution of the inner 500 pc of the galaxy. We find the cluster M82-A1 to be associated with the bar and the unique family of x_2-orbits oriented perpendicularly to the bar major-axis.

By comparison, the GW of NGC 1569 is at a very different evolutionary stage. While M82 hosts a powerful, well-collimated, bipolar outflow exhibiting a cornucopia of structure down to the resolution limit of our observations, the NGC 1569 outflow is composed of a series of faint, discrete supershells expanding in only a roughly bi-polar distribution. Because of the low surface-brightness of the shells, they are much better identified through their dynamical signatures, so we have studied the properties of the individual supershells through a set of mosaicked WIYN/SparsePak observations. However, because of the larger disparity in spatial-resolutions between these and our Gemini/GMOS observations of the galaxy centre, similar links between the large- and small-scales to what we found for M82 have been harder to make.

A number of important unanswered questions remain: how do galactic outflows evolve from the shell/supershell stage seen in systems such as 30 Dor or NGC 1569, to the large-scale winds seen in galaxies such as M82 or NGC 253? Presumably in powerful starburst systems, this happens over a very short timescale (*e.g.* for M82). Can starburst-driven superwinds really inject material into the IGM, or does it always remain bound to the galactic system? What is the escape fraction of ionizing photons from starbursts, and does the development of superwinds affect this value? These questions have important implications for our general understanding of the evolution of the Universe, as discussed previously. Our morphological analyses have highlighted the need for a multi-wavelength approach when trying to understand the evolution of such complex systems. Clearly, the distribution of cold, neutral halo gas and dust affects the large-scale morphology of outflows, whether that material is part of a preexisting halo, has been affected by external gravitational interactions, or has been dragged out there by the wind itself, but to what extent?

The accurate and realistic modelling of GW systems is key to understanding what the light we actually observe means. We have shown that identifying and characterising the morphology of GWs is essential in order to discern which simulations best predict

the reality. Hopefully the observations presented here will motivate and encourage new models to predict the critical inner-structure of superwinds, based on the ideas first developed by Tenorio-Tagle, Silich & Muñoz-Tuñón (2003) of a correct treatment of the discrete nature of the energy sources. However, it is unlikely that a model suitable for one GW system could be easily applied to another, due to the highly idiosyncratic nature of starbursts. For example, it would be very difficult to directly apply a model that accurately reproduces the observed characteristics of the M82 outflow to that of NGC 1569 and get sensible results.

9.2 Technical remarks

Much of the work done in this thesis could not have been accomplished without the advantages of spatially-resolved spectroscopy. For example, our detailed study of the ionized gas in the centre of NGC 1569 would have been very difficult to do without IFS techniques. In principle, the same effect could be achieved by stepping a single slit across a region many times, but IFU observations are far more time-efficient and technically easier to carry out. Furthermore, relationships between gas properties are much easier to identify and quantify when there is both continuous spatial coverage, and simultaneous access to fully spectrally-resolved emission lines over a large wavelength range.

However, with large spectral data-sets comes the need to accurately and automatically characterise the profile shapes of the emission/absorption lines. Although we have developed a fairly robust method for line-fitting, the process is still quite time-consuming and there are several stages where errors can be introduced. The variable and irregular nature of photoionized regions means that the line profile shapes often change rapidly over short scales, and since the results are highly dependent on the accuracy of the line-fitting, visual inspection of every profile fit is still necessary. Clearly, the synergy between spectral-resolution and S/N in the accurate quantification of line profiles implies that the best results will come from good spectrographs and long integration times.

9.3 Future work

In this section I will discuss what I believe to be some of the most important 'next steps' that could be taken following the work presented in this thesis, based on the key issues

emphasised above.

9.3.1 Observations

To further investigate the significance and location of the sonic point in galactic wind outflows, high velocity-resolution, spatially-resolved, spectroscopic observations need to be taken of regions both up and downstream of this critical transition. As we have shown, IFS techniques are well suited for the simultaneous measurement of large areas of interstellar gas, and provide a way to easily track relationships between the subsonic and supersonic gas flows. More specifically, a medium spatial-resolution IFU such as DensePak would be ideal for mapping the proposed boundary of the broad component region in NGC 1569. This kind of data could be used to explore its relationship to the sonic point, the transition to the classic split-line profiles found in the outer-wind, and whether the seemingly mutually exclusive existence of the broad and split-line profile types is significant. Of course, any observations would have to be deep enough so that the S/N of the broad-line is not in contention at any point.

To investigate the entrainment of gas and dust into the wind, and the importance of this material in affecting the wind's evolution, long wavelength observations are essential. The *Spitzer* images shown in Chapter 4 indicate that a great deal of dust in the M82 halo, and understanding whether its presence is due to the action of the wind, by tidal stripping, or was formed *in situ*, will be important for future wind formation models. An alternative way to investigate the dust content of the wind is through polarisation imaging. These notoriously difficult observations offer the potential of both probing the distribution of dust and the influence of magnetic fields on wind evolution. The intriguing results of Scarrott, Eaton & Axon (1991) for M82 certainly deserve further investigation, particularly in light of more recent observations, and our better understanding of the M82 starburst. They found Hα polarisation levels of 10–30 per cent throughout the wind (out to distances of 40″), forming a clear centro-symmetric pattern, and implying that Hα emission from the wind contains a certain contribution from reflection from the central starburst. They also found the symmetry of the polarisation pattern requires that the illuminating source is less than 4 arcsecs in diameter and located very near the IR emission peak associated with the nucleus. Unfortunately, this is one of very few polarisation studies that have been made of GW systems in the local Universe.

We have been granted observing time to obtain a set of Gemini/GMOS IFU obser-

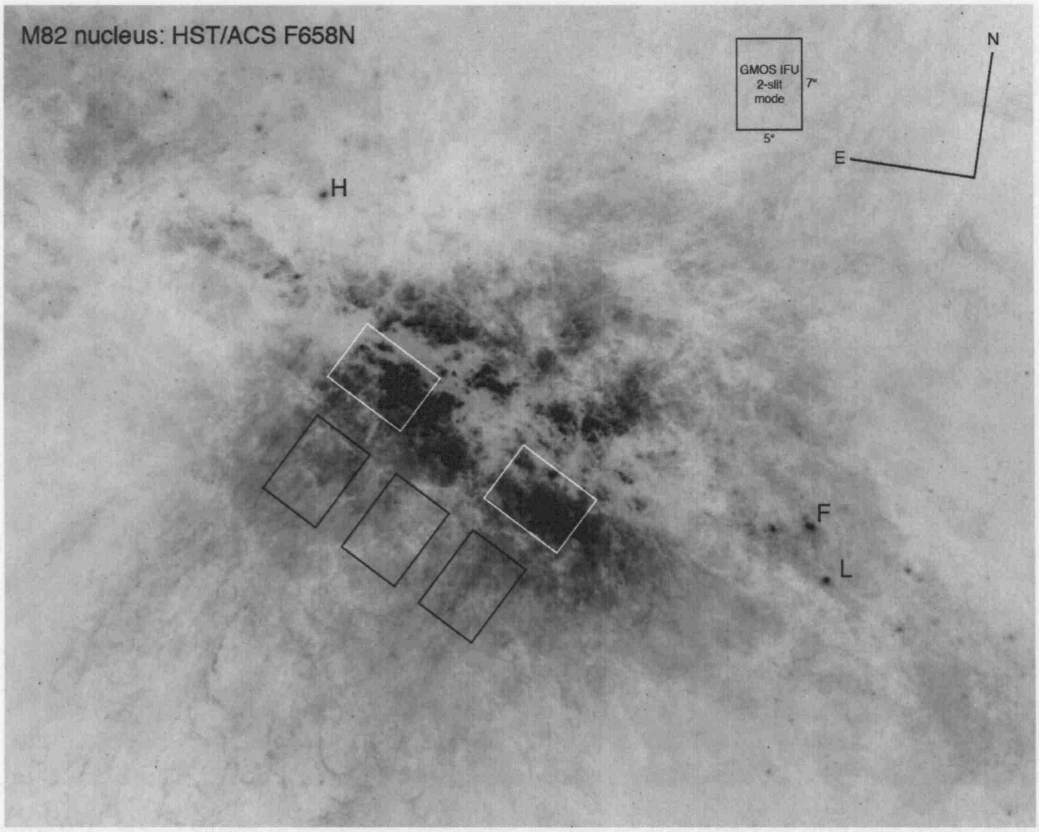

Figure 9.1: *HST*/ACS F658N image of the central region of M82 showing the positions of the five proposed Gemini/GMOS IFU pointings (5×7 arcsecs) for which we have recently been granted observing time.

vations of regions A and C and southern inner-wind of M82 (see Fig. 9.1). We hope to carry out a similar analysis to what we have presented here for NGC 1569, including measurements of line velocities, widths and electron densities/thermal pressures, and to look for shocks using the standard line diagnostics. These observations should significantly enhance our knowledge of the complexities of the brightest starburst clumps and inner-wind regions, particularly following our new proposed explanation for the broad-line component and our updated physical model of the M82 ISM within the starburst.

Can we isolate the direct effects of stellar/cluster winds from that of multiple unresolved kinematic components? It is unlikely that we will be able to with these GMOS data, since the core of M82 is a particularly dynamic and complex environment and it would require observations at spatial- and spectral-resolutions much higher than attainable with the GMOS instrument. However, as shown by Melnick *et al.* (1999), this can be done in near-by systems. To this end, we have recently obtained AAT/UCLES long-slit observa-

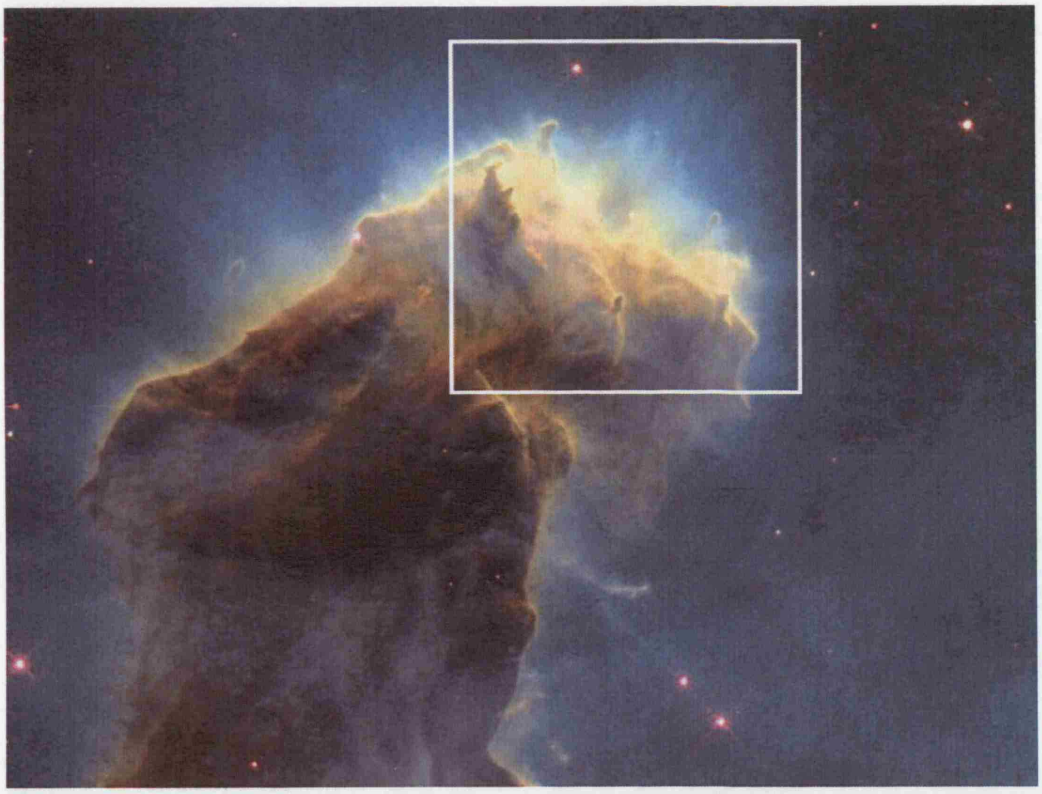

Figure 9.2: *HST*/WFPC2 colour-composite image of the head of one gas pillar in M16 (Credit: J. Hester & P. Scowen, NASA). Overlaid is the field-of-view of the 27 × 27 arcsecs VLT/VIMOS IFU illustrating how modern, large-format IFUs could be used to investigate gas evaporation/ablation from the surface of dense molecular clouds. (Note: VIMOS could not actually be used to observe M16 since the instrument and object are in opposite hemispheres. This figure is to illustrate the concept only.)

tions of NGC 346, a young, intense star-forming region in the SMC, to complement a recent *HST*/ACS observing campaign of this object (Nota *et al.* 2006). We hope to characterise the ionized gas surrounding the bright, young cluster down to scales of 0.1 pc, and to fully resolve the individual line-components. These observations will be used to address the efficiency of stellar wind feedback at low metallicity, and to study the complexity of the outflowing gas from a single, resolved cluster of stars in a similar fashion to what has been done for 30 Dor or NGC 604 (Chu & Kennicutt 1994; Yang *et al.* 1996).

Can we disentangle the effects of turbulent mixing from thermal evaporation and mechanical ablation and determine which is the most important mechanism in particular situations? So far, we have discussed these mechanisms in a fairly broad sense, since we have had no unambiguous way of isolating them with our current data-sets, but

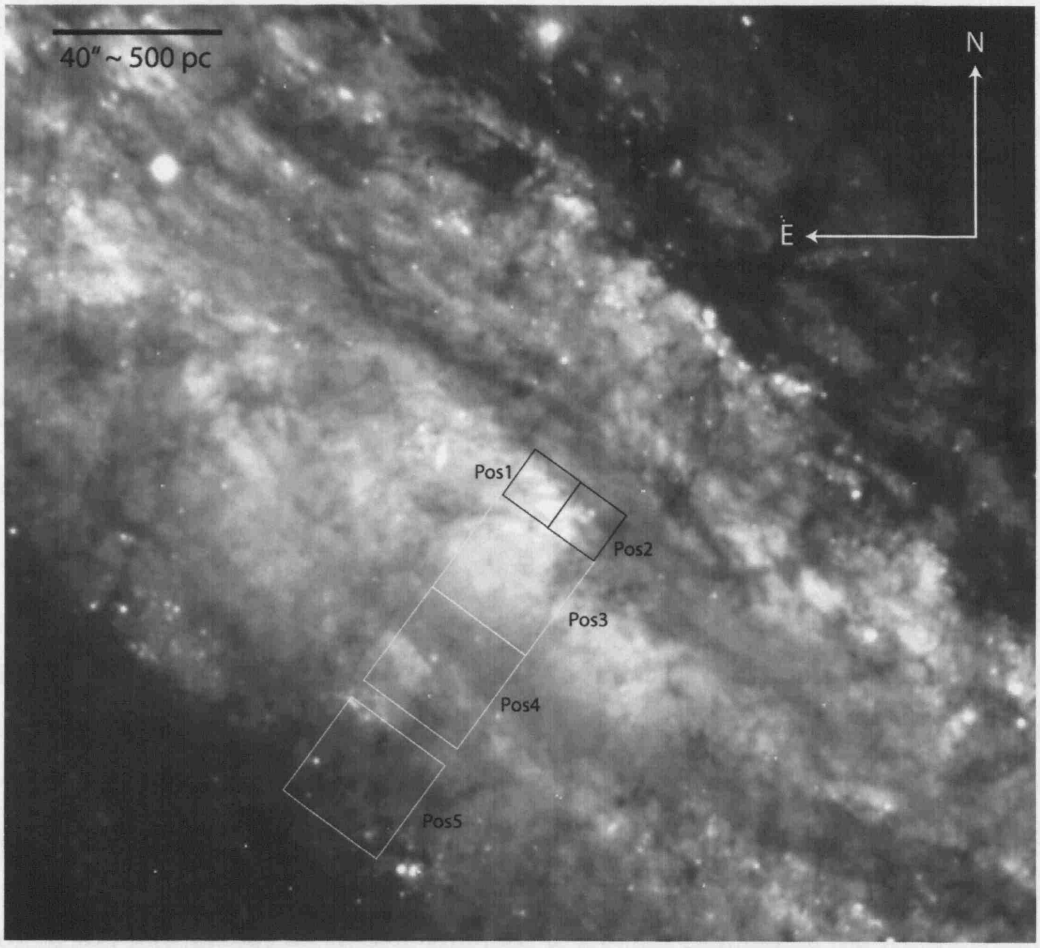

Figure 9.3: VLT/VIMOS IFU pointings overlaid on an archive mosaicked ESO 2.2 m/WFI *B*-band image of the central regions of NGC 253. The inner-most fields (Pos1 & 2) will be imaged by VIMOS in its high-spatial resolution 0.33″/fibre (13 × 13 arcsec) mode, while the outer fields will be in the 0.67″/fibre (27 × 27 arcsec) mode.

it would be interesting to see if their effects could be observed separately. Potentially, observations of an isolated molecular gas cloud in a near-by young star-forming region, where photo-evaporation and ablation are known to be occurring without the obfuscation of mixed, unresolved stellar sources and SNR, could yield these kind of results. Fig. 9.2 shows an example of how a large-format IFU such as VLT/VIMOS could easily capture a large section of the illuminated interface region of a molecular cloud in our own Galaxy.

In this thesis we have focussed on only two galaxies with known galactic-scale outflows, both being low-mass dwarfs. GWs are also observed in massive, metal-rich galaxies, and it is just as important to quantify their properties. To this end we will very soon be obtaining VLT/VIMOS IFU service observations (PI: M. Westmoquette) of the galactic

outflow in NGC 253, a near-by, massive, dust rich, high-inclination spiral galaxy hosting a nuclear starburst and possibly an AGN. Fig. 9.3 shows how we have made use of the multi-resolution capabilities of this instrument to propose five IFU pointings covering the nucleus (which contains known SSCs; Watson *et al.* 1996) and outflow along the minor-axis. In addition to extracting spectra of the individual star clusters over the wavelength range 6350–8600 Å from the high-resolution fields, we also hope to map the GW through the properties of the optical nebular emission lines from the point at which the wind is driven and collimated, out into the halo.

9.3.2 Modelling

Although it is outside the scope of this chapter to fully discuss the future of superwind modelling, it is clear that a correct treatment of the multiple discrete nature of the energy source in starbursts is important and justified. An emphasis in future models on predicting measurable quantities (line ratios, radial velocities, line widths) would be advantageous, so that they may easily be compared to the type of observations presented in this thesis. Furthermore, a realistic treatment of the ISM distribution, including an accurate account of the clumpiness, the level of molecular matter and dust, and how well the ionizing sources and ionized gas are mixed, will lead to a better estimate of the wind evolution and mass-loading factors.

Bibliography

Abbott, D. C. & Conti, P. S., 1987, *ArA&A*, **25**, 113

Achtermann, J. M. & Lacy, J. H., 1995, *ApJ*, **439**, 163

Adelberger, K. L., Steidel, C. C., Shapley, A. E. & Pettini, M., 2003, *ApJ*, **584**, 45

Aguirre, A., Hernquist, L., Schaye, J., Katz, N., Weinberg, D. H. & Gardner, J., 2001*a*, *ApJ*, **561**, 521

Aguirre, A., Hernquist, L., Schaye, J., Weinberg, D. H., Katz, N. & Gardner, J., 2001*b*, *ApJ*, **560**, 599

Allen, M. G., Dopita, M. A., Tsvetanov, Z. I. & Sutherland, R. S., 1999, *ApJ*, **511**, 686

Allington-Smith, J., Murray, G., Content, R., Dodsworth, G., Davies, R., Miller, B. W., Jorgensen, I., Hook, I., Crampton, D. & Murowinski, R., 2002, *PASP*, **114**, 892

Allington-Smith, J. R., Content, R. & Haynes, R., 1998, in S. D'Odorico (ed.), *Proc. SPIE Vol. 3355, p. 196-205, Optical Astronomical Instrumentation*, pp. 196–205

Alonso-Herrero, A., Rieke, G. H., Rieke, M. J. & Kelly, D. M., 2003, *AJ*, **125**, 1210

Anders, P., de Grijs, R., Fritze-v. Alvensleben, U. & Bissantz, N., 2004, *MNRAS*, **347**, 17

Arp, H. & Sandage, A., 1985, *AJ*, **90**, 1163

Arribas, S., Mediavilla, E., García-Lorenzo, B., del Burgo, C. & Fuensalida, J. J., 1999, *A&AS*, **136**, 189

Asplund, M., Grevesse, N., Sauval, A. J., Allende Prieto, C. & Kiselman, D., 2004, *A&A*, **417**, 751

Athanassoula, E., 1992*a*, *MNRAS*, **259**, 328

Athanassoula, E., 1992*b*, *MNRAS*, **259**, 345

Athanassoula, E. & Bureau, M., 1999, *ApJ*, **522**, 699

Bacon, R., Copin, Y., Monnet, G., Miller, B. W., Allington-Smith, J. R., Bureau, M., Carollo, C. M., Davies, R. L., Emsellem, E., Kuntschner, H., Peletier, R. F., Verolme, E. K. & de Zeeuw, P. T., 2001, *MNRAS*, **326**, 23

Baldwin, J. A., Phillips, M. M. & Terlevich, R., 1981, *PASP*, **93**, 5

Barden, S. C., Sawyer, D. G. & Honeycutt, R. K., 1998, in S. D'Odorico (ed.), *Proc. SPIE Vol. 3355, p. 892-899, Optical Astronomical Instrumentation,*, pp. 892–899

Bastian, N., Emsellem, E., Kissler-Patig, M. & Maraston, C., 2006*a*, *A&A*, **445**, 471

Bastian, N., Gieles, M., Efremov, Y. N. & Lamers, H. J. G. L. M., 2005, *A&A*, **443**, 79

Bastian, N. & Goodwin, S. P., 2006, *MNRAS*, **369**, L9

Bastian, N., Saglia, R. P., Goudfrooij, P., Kissler-Patig, M., Maraston, C., Schweizer, F. & Zoccali, M., 2006*b*, *A&A*, **448**, 881

Begelman, M. C. & Fabian, A. C., 1990, *MNRAS*, **244**, 26P

Bershady, M. A., Andersen, D. R., Harker, J., Ramsey, L. W. & Verheijen, M. A. W., 2004, *PASP*, **116**, 565

Binney, J. & Tremaine, S., 1987, *Galactic dynamics* (Princeton, NJ, Princeton University Press, 1987, p.747)

Bland-Hawthorn, J. & Cohen, M., 2003, *ApJ*, **582**, 246

Bosch, G., Selman, F., Melnick, J. & Terlevich, R., 2001, *A&A*, **380**, 137

Bregman, J. N., Schulman, E. & Tomisaka, K., 1995, *ApJ*, **439**, 155

Brouillet, N., Baudry, A., Combes, F., Kaufman, M. & Bash, F., 1991, *A&A*, **242**, 35

Bruzual, G. & Charlot, S., 2003, *MNRAS*, **344**, 1000

Buckalew, B. A., Dufour, R. J., Shopbell, P. L. & Walter, D. K., 2000, *AJ*, **120**, 2402

Buckalew, B. A. & Kobulnicky, H. A., 2006, *AJ*, **132**, 1061

Bureau, M. & Athanassoula, E., 1999, *ApJ*, **522**, 686

Calzetti, D., Harris, J., Gallagher, J. S., Smith, D. A., Conselice, C. J., Homeier, N. & Kewley, L., 2004, *AJ*, **127**, 1405

Cappellari, M. & Copin, Y., 2003, *MNRAS*, **342**, 345

Cardelli, J. A., Clayton, G. C. & Mathis, J. S., 1989, *ApJ*, **345**, 245

Castles, J., McKeith, C. D. & Greve, A., 1991, *Vistas in Astronomy*, **34**, 187

Cecil, G., Bland-Hawthorn, J. & Veilleux, S., 2002, *ApJ*, **576**, 745

Cecil, G., Bland-Hawthorn, J., Veilleux, S. & Filippenko, A. V., 2001, *ApJ*, **555**, 338

Chandar, R., Leitherer, C. & Tremonti, C. A., 2004, *ApJ*, **604**, 153

Chevalier, R. A. & Clegg, A. W., 1985, *Nature*, **317**, 44

Chu, Y.-H. & Kennicutt, R. C., 1994, *ApJ*, **425**, 720

Clark, J. S. & Negueruela, I., 2002, *A&A*, **396**, L25

Colina, L. & Arribas, S., 1999, *ApJ*, **514**, 637

Content, R., 1998, in A. M. Fowler (ed.), *Proc. SPIE Vol. 3354, p. 187-200, Infrared Astronomical Instrumentation*, pp. 187–200

Contopoulos, G. & Mertzanides, C., 1977, *A&A*, **61**, 477

Crane, P., Hegyi, D. J. & Lambert, D. L., 1991, *ApJ*, **378**, 181

Crowther, P. A., De Marco, O. & Barlow, M. J., 1998, *MNRAS*, **296**, 367

Crowther, P. A. & Hadfield, L. J., 2006, *A&A*, **449**, 711

de Grijs, R., Bastian, N. & Lamers, H. J. G. L. M., 2003, *MNRAS*, **340**, 197

de Grijs, R., O'Connell, R. W. & Gallagher, III, J. S., 2001, *AJ*, **121**, 768

de Grijs, R., Parmentier, G. & Lamers, H. J. G. L. M., 2005, *MNRAS*, **364**, 1054

de Grijs, R., Smith, L. J., Bunker, A., Sharp, R. G., Gallagher, J. S., Anders, P., Lançon, A., O'Connell, R. W. & Parry, I. R., 2004, *MNRAS*, **352**, 263

de Marchi, G., Clampin, M., Greggio, L., Leitherer, C., Nota, A. & Tosi, M., 1997, *ApJL*, **479**, L27+

de Vaucouleurs, G., de Vaucouleurs, A., Corwin, Jr., H. G., Buta, R. J., Paturel, G. & Fouque, P., 1991, *Third Reference Catalogue of Bright Galaxies* (Volume 1-3, XII, 2069 Springer-Verlag Berlin Heidelberg New York)

Devine, D. & Bally, J., 1999, *ApJ*, **510**, 197

Devost, D., Roy, J.-R. & Drissen, L., 1997, *ApJ*, **482**, 765

Dimeo, R., 2005, *PAN User Guide*
URL: *www.ncnr.nist.gov/staff/dimeo/panweb/pan.html*

Dolphin, A. E., 2002, in S. Arribas, A. Koekemoer & B. Whitmore (eds.), *The 2002 HST Calibration Workshop, Space Telescope Science Institute, October 17 and 18, 2002*, p. 301

Dopita, M. A., 1997, *ApJL*, **485**, L41

Dopita, M. A., Fischera, J., Sutherland, R. S., Kewley, L. J., Leitherer, C., Tuffs, R. J., Popescu, C. C., van Breugel, W. & Groves, B. A., 2006, astro-ph/0608062

Dopita, M. A., Groves, B. A., Fischera, J., Sutherland, R. S., Tuffs, R. J., Popescu, C. C., Kewley, L. J., Reuland, M. & Leitherer, C., 2005, *ApJ*, **619**, 755

Dopita, M. A., Kewley, L. J., Heisler, C. A. & Sutherland, R. S., 2000, *ApJ*, **542**, 224

Dopita, M. A. & Sutherland, R. S., 1995, *ApJ*, **455**, 468

Dyson, J. E., 1979, *A&A*, **73**, 132

Dyson, J. E., Hartquist, T. W., Malone, M. T. & Taylor, S. D., 1995, in S. Lizano & J. M. Torrelles (eds.), *Revista Mexicana de Astronomia y Astrofisica Conference Series*, p. 119

Elmegreen, B. G., Elmegreen, D. M., Chandar, R., Whitmore, B. & Regan, M., 2006, *ApJ*, **644**, 879

Elson, R. A. W., Fall, S. M. & Freeman, K. C., 1987, *ApJ*, **323**, 54

Evans, I. N. & Dopita, M. A., 1985, *ApJS*, **58**, 125

Falgarone, E. & Phillips, T. G., 1990, *ApJ*, **359**, 344

Fan, X., Narayanan, V. K., Lupton, R. H., Strauss, M. A., Knapp, G. R., Becker, R. H., White, R. L., Pentericci, L., Leggett, S. K., Haiman, Z., Gunn, J. E., Ivezić, Ž., Schneider, D. P., Anderson, S. F., Brinkmann, J., Bahcall, N. A., Connolly, A. J., Csabai, I., Doi, M., Fukugita, M., Geballe, T., Grebel, E. K., Harbeck, D., Hennessy, G., Lamb, D. Q., Miknaitis, G., Munn, J. A., Nichol, R., Okamura, S., Pier, J. R., Prada, F., Richards, G. T., Szalay, A. & York, D. G., 2001, *AJ*, **122**, 2833

Förster Schreiber, N. M., Genzel, R., Lutz, D., Kunze, D. & Sternberg, A., 2001, *ApJ*, **552**, 544

Förster Schreiber, N. M., Genzel, R., Lutz, D. & Sternberg, A., 2003, *ApJ*, **599**, 193

Freedman, W. L., Hughes, S. M., Madore, B. F., Mould, J. R., Lee, M. G., Stetson, P., Kennicutt, R. C., Turner, A., Ferrarese, L., Ford, H., Graham, J. A., Hill, R., Hoessel, J. G., Huchra, J. & Illingworth, G. D., 1994, *ApJ*, **427**, 628

Fruchter, A. S. & Hook, R. N., 2002, *PASP*, **114**, 144

Fujita, A., Martin, C. L., Mac Low, M.-M. & Abel, T., 2003, *ApJ*, **599**, 50

Gallagher, III, J. S. & Smith, L. J., 1999, *MNRAS*, **304**, 540

Galliano, F., Madden, S. C., Jones, A. P., Wilson, C. D., Bernard, J.-P. & Le Peintre, F., 2003, *A&A*, **407**, 159

Garnett, D. R., Kennicutt, Jr., R. C., Chu, Y.-H. & Skillman, E. D., 1991, *ApJ*, **373**, 458

Geballe, T. R., Persson, S. E., McGregor, P. J., Simon, T. & Lonsdale, C. J., 1986, *ApJ*, **302**, 693

Giavalisco, M., 1998, in M. Livio, S. M. Fall & P. Madau (eds.), *The Hubble Deep Field: Space Telescope Science Institute symposium series 11*, p. 121

Gnedin, O. Y. & Ostriker, J. P., 1997, *ApJ*, **474**, 223

Gómez, P. L., Nichol, R. C., Miller, C. J., Balogh, M. L., Goto, T., Zabludoff, A. I., Romer, A. K., Bernardi, M., Sheth, R., Hopkins, A. M., Castander, F. J., Connolly, A. J., Schneider, D. P., Brinkmann, J., Lamb, D. Q., SubbaRao, M. & York, D. G., 2003, *ApJ*, **584**, 210

González-Delgado, R. M., Cerviño, M., Martins, L. P., Leitherer, C. & Hauschildt, P. H., 2005, *MNRAS*, **357**, 945

González-Delgado, R. M., Leitherer, C., Heckman, T. & Cerviño, M., 1997, *ApJ*, **483**, 705

González-Delgado, R. M., Perez, E., Tenorio-Tagle, G., Vilchez, J. M., Terlevich, E., Terlevich, R., Telles, E., Rodriguez-Espinosa, J. M., Mas-Hesse, M., Garcia-Vargas, M. L., Diaz, A. I., Cepa, J. & Castañeda, H., 1994, *ApJ*, **437**, 239

Goodwin, S. P., 1997, *MNRAS*, **284**, 785

Götz, M., Downes, D., Greve, A. & McKeith, C. D., 1990, *A&A*, **240**, 52

Greggio, L., Tosi, M., Clampin, M., de Marchi, G., Leitherer, C., Nota, A. & Sirianni, M., 1998, *ApJ*, **504**, 725

Greve, A., 2004, *A&A*, **416**, 67

Greve, A., Tarchi, A., Hüttemeister, S., de Grijs, R., van der Hulst, J. M., Garrington, S. T. & Neininger, N., 2002*a*, *A&A*, **381**, 825

Greve, A., Wills, K. A., Neininger, N. & Pedlar, A., 2002*b*, *A&A*, **383**, 56

Hadfield, L. J., Crowther, P. A., Schild, H. & Schmutz, W., 2005, *A&A*, **439**, 265

Hanson, M. M., Luhman, K. L. & Rieke, G. H., 2002, *ApJS*, **138**, 35

Hartquist, T. W., Dyson, J. E. & Williams, D. A., 1992, *MNRAS*, **257**, 419

Heavens, A., Panter, B., Jimenez, R. & Dunlop, J., 2004, *Nature*, **428**, 625

Heckman, T., 2000, in P. Murdin (ed.), *Encylopedia of Astronomy and Astrophysics* (Institute of Physics Publishing)

Heckman, T. M., Armus, L. & Miley, G. K., 1990, *ApJS*, **74**, 833

Heckman, T. M., Dahlem, M., Lehnert, M. D., Fabbiano, G., Gilmore, D. & Waller, W. H., 1995, *ApJ*, **448**, 98

Heckman, T. M. & Lehnert, M. D., 2000, *ApJ*, **537**, 690

Heckman, T. M., Lehnert, M. D., Strickland, D. K. & Armus, L., 2000, *ApJS*, **129**, 493

Heckman, T. M., Sembach, K. R., Meurer, G. R., Strickland, D. K., Martin, C. L., Calzetti, D. & Leitherer, C., 2001, *ApJ*, **554**, 1021

Herbig, G. H., 1995, *ArA&A*, **33**, 19

Ho, L. C. & Filippenko, A. V., 1996, *ApJ*, **472**, 600

Holtzman, J. A., Burrows, C. J., Casertano, S., Hester, J. J., Trauger, J. T., Watson, A. M. & Worthey, G., 1995, *PASP*, **107**, 1065

Holtzman, J. A., Faber, S. M., Shaya, E. J., Lauer, T. R., Groth, J., Hunter, D. A., Baum, W. A., Ewald, S. P., Hester, J. J., Light, R. M., Lynds, C. R., O'Neil, Jr., E. J. & Westphal, J. A., 1992, *AJ*, **103**, 691

Homeier, N. L. & Gallagher, J. S., 1999, *ApJ*, **522**, 199

Hoopes, C. G., Heckman, T. M., Strickland, D. K. & Howk, J. C., 2003, *ApJL*, **596**, L175

Hoopes, C. G., Heckman, T. M., Strickland, D. K., Seibert, M., Madore, B. F., Rich, R. M., Bianchi, L., Gil de Paz, A., Burgarella, D., Thilker, D. A., Friedman, P. G., Barlow, T. A., Byun, Y.-I., Donas, J., Forster, K., Jelinsky, P. N., Lee, Y.-W., Malina, R. F., Martin, D. C., Milliard, B., Morrissey, P. F., Neff, S. G., Schiminovich, D., Siegmund, O. H. W., Small, T., Szalay, A. S., Welsh, B. Y. & Wyder, T. K., 2005, *ApJL*, **619**, L99

Howarth, I. D., 1983, *MNRAS*, **203**, 301

Hummer, D. G. & Storey, P. J., 1987, *MNRAS*, **224**, 801

Hunt, M. P., Steidel, C. C., Adelberger, K. L. & Shapley, A. E., 2004, *ApJ*, **605**, 625

Hunter, D. A. & Gallagher, III, J. S., 1997, *ApJ*, **475**, 65

Hunter, D. A., Hawley, W. N. & Gallagher, J. S., 1993, *AJ*, **106**, 1797

Hunter, D. A., O'Connell, R. W., Gallagher, J. S. & Smecker-Hane, T. A., 2000, *AJ*, **120**, 2383

Hunter, D. A., O'Connell, R. W. & Gallagher, III, J. S., 1994, *AJ*, **108**, 84

Hunter, D. A., Shaya, E. J., Holtzman, J. A., Light, R. M., O'Neil, Jr., E. J. & Lynds, R., 1995, *ApJ*, **448**, 179

Ichikawa, T., Yanagisawa, K., Itoh, N., Tarusawa, K., van Driel, W. & Ueno, M., 1995, *AJ*, **109**, 2038

Israel, F. P., 1988, *A&A*, **194**, 24

Izotov, Y. I., Dyak, A. B., Chaffee, F. H., Foltz, C. B., Kniazev, A. Y. & Lipovetsky, V. A., 1996, *ApJ*, **458**, 524

Kewley, L. J. & Dopita, M. A., 2002, *ApJS*, **142**, 35

Kewley, L. J., Dopita, M. A., Sutherland, R. S., Heisler, C. A. & Trevena, J., 2001, *ApJ*, **556**, 121

Kissler-Patig, M., Copin, Y., Ferruit, P., Pécontal-Rousset, A. & Roth, M. M., 2004, *Astronomische Nachrichten*, **325**, 159

Klein, R. I., McKee, C. F. & Colella, P., 1994, *ApJ*, **420**, 213

Kobulnicky, H. A. & Skillman, E. D., 1997, *ApJ*, **489**, 636

Koo, B.-C. & McKee, C. F., 1992, *ApJ*, **388**, 93

Krist, J., 2004, *The Tiny Tim User's Guide v. 6.3*

Kroupa, P., 2001, *MNRAS*, **322**, 231

Kulkarni, V. P., Fall, S. M., Lauroesch, J. T., York, D. G., Welty, D. E., Khare, P. & Truran, J. W., 2005, *ApJ*, **618**, 68

Larkin, J. E., Graham, J. R., Matthews, K., Soifer, B. T., Beckwith, S., Herbst, T. M. & Quillen, A. C., 1994, *ApJ*, **420**, 159

Larsen, S. S., 1999, *A&AS*, **139**, 393

Larsen, S. S., 2000, *MNRAS*, **319**, 893

Larsen, S. S., 2002, *AJ*, **124**, 1393

Larsen, S. S., 2004, The ISHAPE User's Guide

Larsen, S. S. & Richtler, T., 1999, *A&A*, **345**, 59

Lehnert, M. D., Heckman, T. M. & Weaver, K. A., 1999, *ApJ*, **523**, 575

Leitherer, C., Schaerer, D., Goldader, J. D., Delgado, R. M. G., Robert, C., Kune, D. F., de Mello, D. F., Devost, D. & Heckman, T. M., 1999, *ApJS*, **123**, 3

Lester, D. F., Gaffney, N., Carr, J. S. & Joy, M., 1990, *ApJ*, **352**, 544

Lisenfeld, U., Israel, F. P., Stil, J. M. & Sievers, A., 2002, *A&A*, **382**, 860

Lisenfeld, U., Wilding, T. W., Pooley, G. G. & Alexander, P., 2004, *MNRAS*, **349**, 1335

Loeb, A. & Barkana, R., 2001, *ArA&A*, **39**, 19

Lord, S. D., Hollenbach, D. J., Haas, M. R., Rubin, R. H., Colgan, S. W. J. & Erickson, E. F., 1996, *ApJ*, **465**, 703

Lynds, C. R. & Sandage, A. R., 1963, *ApJ*, **137**, 1005

Mac Low, M.-M. & McCray, R., 1988, *ApJ*, **324**, 776

Madau, P., Pozzetti, L. & Dickinson, M., 1998, *ApJ*, **498**, 106

Mao, R. Q., Henkel, C., Schulz, A., Zielinsky, M., Mauersberger, R., Störzer, H., Wilson, T. L. & Gensheimer, P., 2000, *A&A*, **358**, 433

Maoz, D., Ho, L. C. & Sternberg, A., 2001, *ApJL*, **554**, L139

Marcolini, A., Strickland, D. K., D'Ercole, A., Heckman, T. M. & Hoopes, C. G., 2005, *MNRAS*, **362**, 626

Markwardt, C. B., 2006
URL: *http://cow.physics.wisc.edu/~craigm/idl/fitting.html*

Marlowe, A. T., Heckman, T. M., Wyse, R. F. G. & Schommer, R., 1995, *ApJ*, **438**, 563

Martin, C. L., 1998, *ApJ*, **506**, 222

Martin, C. L., Kobulnicky, H. A. & Heckman, T. M., 2002, *ApJ*, **574**, 663

Martins, L. P., Delgado, R. M. G., Leitherer, C., Cerviño, M. & Hauschildt, P., 2005, *MNRAS*, **358**, 49

Mayya, Y. D., Carrasco, L. & Luna, A., 2005, *ApJL*, **628**, L33

Mazzuca, L. M., Sarzi, M., Knapen, J. H., Veilleux, S. & Swaters, R., 2006, *ApJL*, **649**, L79

McCrady, N., Gilbert, A. M. & Graham, J. R., 2003, *ApJ*, **596**, 240

McCrady, N., Graham, J. R. & Vacca, W. D., 2005, *ApJ*, **621**, 278

McKeith, C. D., Castles, J., Greve, A. & Downes, D., 1993, *A&A*, **272**, 98

McKeith, C. D., Greve, A., Downes, D. & Prada, F., 1995, *A&A*, **293**, 703

Melioli, C. & de Gouveia dal Pino, E. M., 2006, *A&A*, **445**, L23

Melnick, J., 1977, *ApJ*, **213**, 15

Melnick, J., Tenorio-Tagle, G. & Terlevich, R., 1999, *MNRAS*, **302**, 677

Melnick, J., Terlevich, R. & Moles, M., 1988, *MNRAS*, **235**, 297

Melo, V. P., Muñoz-Tuñón, C., Maíz-Apellániz, J. & Tenorio-Tagle, G., 2005, *ApJ*, **619**, 270

Mendez, D. I. & Esteban, C., 1997, *ApJ*, **488**, 652

Miller, B. W., Whitmore, B. C., Schweizer, F. & Fall, S. M., 1997, *AJ*, **114**, 2381

Muñoz-Tuñón, C., Tenorio-Tagle, G., Castaneda, H. O. & Terlevich, R., 1996, *AJ*, **112**, 1636

Mühle, S., Klein, U., Wilcots, E. M. & Hüttemeister, S., 2005, *AJ*, **130**, 524

Muxlow, T. W. B., Pedlar, A., Wilkinson, P. N., Axon, D. J., Sanders, E. M. & de Bruyn, A. G., 1994, *MNRAS*, **266**, 455

Norman, C. & Scoville, N., 1988, *ApJ*, **332**, 124

Nota, A., Sirianni, M., Sabbi, E., Tosi, M., Clampin, M., Gallagher, J., Meixner, M., Oey, M. S., Pasquali, A., Smith, L. J., Walterbos, R. & Mack, J., 2006, *ApJL*, **640**, L29

O'Connell, R., 2001, in *HST Proposal*, p. 5465

O'Connell, R. W., Gallagher, III, J. S., Hunter, D. A. & Colley, W. N., 1995, *ApJL*, **446**, L1

O'Connell, R. W. & Mangano, J. J., 1978, *ApJ*, **221**, 62

Oey, M. S., Dopita, M. A., Shields, J. C. & Smith, R. C., 2000, *ApJS*, **128**, 511

Ohyama, Y., Taniguchi, Y., Iye, M., Yoshida, M., Sekiguchi, K., Takata, T., Saito, Y., Kawabata, K. S. *et al.*, 2002, *PASJ*, **54**, 891

Oke, J. B., 1990, *AJ*, **99**, 1621

Origlia, L., Leitherer, C., Aloisi, A., Greggio, L. & Tosi, M., 2001, *AJ*, **122**, 815

Origlia, L., Ranalli, P., Comastri, A. & Maiolino, R., 2004, *ApJ*, **606**, 862

Osterbrock, D. E., 1989, *Astrophysics of Gaseous Nebulae and Active Galactic Nuclei* (University Science Books)

Pedlar, A., Muxlow, T. W. B., Garrett, M. A., Diamond, P., Wills, K. A., Wilkinson, P. N. & Alef, W., 1999, *MNRAS*, **307**, 761

Pettini, M., Madau, P., Bolte, M., Prochaska, J. X., Ellison, S. L. & Fan, X., 2003, *ApJ*, **594**, 695

Pettini, M. & Pagel, B. E. J., 2004, *MNRAS*, **348**, L59

Pettini, M., Shapley, A. E., Steidel, C. C., Cuby, J.-G., Dickinson, M., Moorwood, A. F. M., Adelberger, K. L. & Giavalisco, M., 2001, *ApJ*, **554**, 981

Pittard, J. M., 2006, astro-ph/0607310

Pittard, J. M., Dyson, J. E., Falle, S. A. E. G. & Hartquist, T. W., 2005, *MNRAS*, **361**, 1077

Pottasch, S. R., 1980, *A&A*, **89**, 336

Qian, Y.-Z. & Wasserburg, G. J., 2005, *ApJ*, **635**, 845

Reakes, M., 1980, *MNRAS*, **192**, 297

Relaño, M., Lisenfeld, U., Vilchez, J. M. & Battaner, E., 2006, *A&A*, **452**, 413

Rieke, G. H., Loken, K., Rieke, M. J. & Tamblyn, P., 1993, *ApJ*, **412**, 99

Rigby, J. R. & Rieke, G. H., 2004, *ApJ*, **606**, 237

Roy, J.-R., Aube, M., McCall, M. L. & Dufour, R. J., 1992, *ApJ*, **386**, 498

Rupke, D. S., Veilleux, S. & Sanders, D. B., 2005, *ApJS*, **160**, 115

Saito, M., Sasaki, M., Kaneko, N., Nishimura, M. & Toyama, K., 1984, *PASJ*, **36**, 305

Salpeter, E. E., 1955, *ApJ*, **121**, 161

Sánchez, S. F., 2004, *Astronomische Nachrichten*, **325**, 167

Sánchez, S. F., 2006, astro-ph/0606263

Sandage, A., 1961, *The Hubble atlas of galaxies* (Washington: Carnegie Institution, 1961)

Sandage, A. & Brucato, R., 1979, *AJ*, **84**, 472

Satyapal, S., Watson, D. M., Pipher, J. L., Forrest, W. J., Coppenbarger, D., Raines, S. N., Libonate, S., Piche, F., Greenhouse, M. A., Smith, H. A., Thompson, K. L., Fischer, J., Woodward, C. E. & Hodge, T., 1995, *ApJ*, **448**, 611

Satyapal, S., Watson, D. M., Pipher, J. L., Forrest, W. J., Greenhouse, M. A., Smith, H. A., Fischer, J. & Woodward, C. E., 1997, *ApJ*, **483**, 148

Sawyer, D., 1997, *DensePak Users Manual*

Scarrott, S. M., Eaton, N. & Axon, D. J., 1991, *MNRAS*, **252**, 12P

Schiano, A. V. R., 1985, *ApJ*, **299**, 24

Schwartz, C. M. & Martin, C. L., 2004, *ApJ*, **610**, 201

Seaquist, E. R. & Odegard, N., 1991, *ApJ*, **369**, 320

Seaton, M. J., 1979, *MNRAS*, **187**, 73

Shapley, A. E., Steidel, C. C., Pettini, M., Adelberger, K. L. & Erb, D. K., 2006, *ApJ*, **651**, 688

Shen, J. & Lo, K. Y., 1995, *ApJL*, **445**, L99

Shopbell, P. L. & Bland-Hawthorn, J., 1998, *ApJ*, **493**, 129

Sidoli, F., Smith, L. J. & Crowther, P. A., 2006, *MNRAS*, **370**, 799

Silich, S., Tenorio-Tagle, G. & Rodríguez-González, A., 2004, *ApJ*, **610**, 226

Sirianni, M., Jee, M. J., Benítez, N., Blakeslee, J. P., Martel, A. R., Meurer, G., Clampin, M., De Marchi, G., Ford, H. C., Gilliland, R., Hartig, G. F., Illingworth, G. D., Mack, J. & McCann, W. J., 2005, *PASP*, **117**, 1049

Slavin, J. D., Shull, J. M. & Begelman, M. C., 1993, *ApJ*, **407**, 83

Smith, L. J. & Gallagher, J. S., 2001, *MNRAS*, **326**, 1027

Smith, L. J., Westmoquette, M. S., Gallagher, J. S., O'Connell, R. W., Rosario, D. J. & de Grijs, R., 2006, *MNRAS*, **370**, 513

Sofue, Y., Reuter, H.-P., Krause, M., Wielebinski, R. & Nakai, N., 1992, *ApJ*, **395**, 126

Sofue, Y., Tomita, A., Tutui, Y., Honma, M. & Takeda, Y., 1998, *PASJ*, **50**, 427

Spergel, D. N., Verde, L., Peiris, H. V., Komatsu, E., Nolta, M. R., Bennett, C. L., Halpern, M., Hinshaw, G., Jarosik, N., Kogut, A., Limon, M., Meyer, S. S., Page, L., Tucker, G. S., Weiland, J. L., Wollack, E. & Wright, E. L., 2003, *ApJS*, **148**, 175

Stevens, I. R. & Hartwell, J. M., 2003, *MNRAS*, **339**, 280

Stevens, I. R., Read, A. M. & Bravo-Guerrero, J., 2003, *MNRAS*, **343**, L47

Stil, J. M. & Israel, F. P., 1998, *A&A*, **337**, 64

Stil, J. M. & Israel, F. P., 2002, *A&A*, **392**, 473

Storey, P. J. & Hummer, D. G., 1995, *MNRAS*, **272**, 41

Strickland, D. K., Heckman, T. M., Colbert, E. J. M., Hoopes, C. G. & Weaver, K. A., 2004, *ApJS*, **151**, 193

Strickland, D. K., Heckman, T. M., Weaver, K. A., Hoopes, C. G. & Dahlem, M., 2002, *ApJ*, **568**, 689

Strickland, D. K., Ponman, T. J. & Stevens, I. R., 1997, *A&A*, **320**, 378

Strickland, D. K. & Stevens, I. R., 2000, *MNRAS*, **314**, 511

Suchkov, A. A., Balsara, D. S., Heckman, T. M. & Leitherner, C., 1994, *ApJ*, **430**, 511

Suchkov, A. A., Berman, V. G., Heckman, T. M. & Balsara, D. S., 1996, *ApJ*, **463**, 528

Summers, L. K., Stevens, I. R., Strickland, D. K. & Heckman, T. M., 2003, *MNRAS*, **342**, 690

Taylor, C. L., Hüttemeister, S., Klein, U. & Greve, A., 1999, *A&A*, **349**, 424

Taylor, C. L., Walter, F. & Yun, M. S., 2001, *ApJL*, **562**, L43

Telesco, C. M., 1988, *ArA&A*, **26**, 343

Telesco, C. M., Joy, M., Dietz, K., Decher, R. & Campins, H., 1991, *ApJ*, **369**, 135

Tenorio-Tagle, G. & Muñoz-Tuñón, C., 1998, *MNRAS*, **293**, 299

Tenorio-Tagle, G., Muñoz-Tuñón, C. & Cid-Fernandes, R., 1996, *ApJ*, **456**, 264

Tenorio-Tagle, G., Muñoz-Tuñón, C. & Cox, D. P., 1993, *ApJ*, **418**, 767

Tenorio-Tagle, G., Muñoz-Tuñón, C., Pérez, E., Maíz-Apellániz, J. & Medina-Tanco, G., 2000, *ApJ*, **541**, 720

Tenorio-Tagle, G., Muñoz-Tuñón, C., Perez, E. & Melnick, J., 1997, *ApJL*, **490**, L179

Tenorio-Tagle, G., Muñoz-Tuñón, C., Pérez, E., Silich, S. & Telles, E., 2006, *ApJ*, **643**, 186

Tenorio-Tagle, G., Silich, S. & Muñoz-Tuñón, C., 2003, *ApJ*, **597**, 279

Tenorio-Tagle, G., Silich, S., Rodríguez-González, A. & Muñoz-Tuñón, C., 2005, *ApJ*, **620**, 217

Terlevich, R. & Melnick, J., 1981, *MNRAS*, **195**, 839

Terlevich, R., Melnick, J. & Moles, M., 1987, in E. E. Khachikian, K. J. Fricke & J. Melnick (eds.), *IAU Symp. 121: Observational Evidence of Activity in Galaxies*, p. 499

Terlevich, R., Tenorio-Tagle, G., Franco, J. & Melnick, J., 1992, *MNRAS*, **255**, 713

Thornley, M. D., Förster Schreiber, N. M., Lutz, D., Genzel, R., Spoon, H. W. W., Kunze, D. & Sternberg, A., 2000, *ApJ*, **539**, 641

Tokura, D., Onaka, T., Takahashi, H., Miyata, T., Sako, S., Honda, M., Okada, Y., Sakon, I., Tajiri, Y. Y., Kataza, H., Okamoto, Y. K., Yamashita, T. & Fujiyoshi, T., 2006, *ApJ*, **648**, 355

Tomisaka, K. & Ikeuchi, S., 1988, *ApJ*, **330**, 695

Tomita, A., Ohta, K. & Saito, M., 1994, *PASJ*, **46**, 335

Tremonti, C. A., Calzetti, D., Leitherer, C. & Heckman, T. M., 2001, *ApJ*, **555**, 322

Tsuru, T., Ozawa, M., Hyodo, Y., Matsumoto, H., Koyama, K., Awaki, H., Fujimoto, R., Griffiths, R., Kilbourne, C., Matsushita, K., Mitsuda, K., Ptak, A., Ranalli, P. & Yamasaki, N., 2006, astro-ph/0609623

Vacca, W. D. & Conti, P. S., 1992, *ApJ*, **401**, 543

van Dokkum, P. G., 2001, *PASP*, **113**, 1420

Vanzi, L. & Sauvage, M., 2004, *A&A*, **415**, 509

Veilleux, S., Cecil, G. & Bland-Hawthorn, J., 2005, *ArA&A*, **43**, 769

Veilleux, S. & Osterbrock, D. E., 1987, *ApJS*, **63**, 295

Veilleux, S. & Rupke, D. S., 2002, *ApJL*, **565**, L63

Viallefond, F., Allen, R. J. & Goss, W. M., 1981, *A&A*, **104**, 127

Waller, W. H., 1991, *ApJ*, **370**, 144

Walter, F., Weiss, A. & Scoville, N., 2002, *ApJL*, **580**, L21

Watson, A. M., Gallagher, III, J. S., Holtzman, J. A., Hester, J. J., Mould, J. R., Ballester, G. E., Burrows, C. J., Casertano, S., Clarke, J. T., Crisp, D., Evans, R., Griffiths, R. E., Hoessel, J. G., Scowen, P. A., Stapelfeldt, K. R., Trauger, J. T. & Westphal, J. A., 1996, *AJ*, **112**, 534

Weaver, R., McCray, R., Castor, J., Shapiro, P. & Moore, R., 1977, *ApJ*, **218**, 377

Weiß, A., Neininger, N., Hüttemeister, S. & Klein, U., 2001, *A&A*, **365**, 571

Whitmore, B. C., Zhang, Q., Leitherer, C., Fall, S. M., Schweizer, F. & Miller, B. W., 1999, *AJ*, **118**, 1551

Williams, R. J. R. & Dyson, J. E., 2002, *MNRAS*, **333**, 1

Wills, K. A., Das, M., Pedlar, A., Muxlow, T. W. B. & Robinson, T. G., 2000, *MNRAS*, **316**, 33

Wills, K. A., Pedlar, A. & Muxlow, T. W. B., 2002, *MNRAS*, **331**, 313

Wills, K. A., Redman, M. P., Muxlow, T. W. B. & Pedlar, A., 1999, *MNRAS*, **309**, 395

Yang, H., Chu, Y.-H., Skillman, E. D. & Terlevich, R., 1996, *AJ*, **112**, 146

Yorke, H. W., Tenorio-Tagle, G. & Bodenheimer, P., 1984, *A&A*, **138**, 325

Yun, M. S., Ho, P. T. P. & Lo, K. Y., 1993, *ApJL*, **411**, L17

Yun, M. S., Ho, P. T. P. & Lo, K. Y., 1994, *Nature*, **372**, 530

ACKNOWLEDGEMENTS

Writing this thesis has certainly been a long and arduous journey, but it would not have 'been' at all were it not for the help and support of a rather special group of people. People who I am honoured to call my friends.

I would like to begin by thanking my office mates, both past and current (you know who you are), for first getting me started, then providing such interesting and engaging conversation that I thought I would never get any work done, and finally putting up with me at the end when the going was toughest. I would also like to thank all those in my year (Tom Bell, Matt Callender, Antonio Hales, Chris King, and Chris Lintott), who I consider as part of my extended family. I would like to mention Tom in particular, with whom I spent many long evenings and weekends (before he abandoned UCL to go surfing in LA) exploring a varied mix of music supplied mostly by KJAZ.

Thank you Mum for being a constant source of inspiration (even in the darkest times), and thanks to both her and my sister, Kim, for their unwavering support throughout the years, even over time-zones. Also, thank you Emily, my housemate and best friend, for being there since the beginning.

I am indebted to Rob Dimeo at the The NIST Center for Neutron Research, U.S.A., for writing PAN, without which my life would have been so much harder. I would like to thank Nate Bastian for his help and general encouragement, and Katrina Exter for always being responsive to my incessant data reduction-related questions, her thorough editing skills, and particularly her hospitality on my visit to the IAC. I would also like to say a big thank you to Jay Gallagher for his hospitality on my visits to Madison, and for his consistently insightful and inspired comments on just about any subject you care to ask him about.

Finally, I would like to extend a special heart-felt thanks to my supervisor, Linda Smith, for all the advice, support, and wisdom she has imparted to me throughout the four years I have been working with her. I look forward to spending another 18 months under her guidance as a post-doc, and hopefully many more fruitful years of collaboration in the future.